DISS. ETH No. 24555

Thermocline Thermal Energy Storage: Advances and Applications to CSP, Compressed Air Energy Storage, and Solar Fuels

A thesis submitted to attain the degree of

DOCTOR OF SCIENCES of ETH ZURICH
(Dr. sc. ETH Zurich)

presented by

LUKAS GEISSBÜHLER
MSc ETH ME
born on 09.06.1989
citizen of Lauperswil (BE)

accepted on the recommendation of

Prof. Dr. Aldo Steinfeld, examiner
Prof. Dr. Ranga Pitchumani, co-examiner
Dr. Andreas Haselbacher, co-examiner

2017

Abstract

This thesis investigates high-temperature thermocline thermal energy storages (TES) that are based on packed beds of solid particles. Such storages are typically charged with hot heat-transfer fluid (HTF) from the top and discharged with cold HTF from the bottom. This creates a thermocline that is moved downwards and upwards during charging and discharging, respectively. A major drawback of this technology is thermocline degradation, which leads to smaller storage utilization factors and an outflow temperature increase during charging and an outflow temperature drop during discharging. Various concepts have been proposed to inhibit these negative effects, such as, e.g., adding small amounts of phase-change materials (PCMs) to the top or the bottom of the thermocline TES.

The aim of this thesis is on the one hand the assessment of existing concepts and the development of modified or novel concepts that address the issues related to thermocline degradation. On the other hand, this thesis aims at investigating the application of thermocline TES to concentrated solar power (CSP), advanced adiabatic compressed air energy storage (AA-CAES), and solar fuels.

A numerical heat-transfer model of the TES is developed for separate fluid and solid phases, variable thermo-physical properties and arbitrary geometries. The model is capable of simulating sensible-heat, latent-heat and combined sensible/latent-heat TES. The packed bed with the HTF is discretized in one dimension and the structure and the insulation in two

dimensions. The model is verified with analytical solutions.

The concept of combined sensible/latent TES is experimentally tested with a 42 kWh$_{th}$ laboratory-scale storage. The storage is based on placing a limited amount of steel-encapsulated AlSi$_{12}$ on top of a packed bed of rocks and is charged from the top with air at 595°C and discharged from the bottom with air at 20°C. Experimental results demonstrate the stabilization of the outflow temperature during discharging. Furthermore, experimental results are used to validate the numerical model, which is then applied to assess the performance of industrial-scale combined sensible/latent TES. Simulation results are compared to the performance of sensible-only TES and show that the combined storage can reduce the material costs for a given maximum outflow temperature drop during discharging. The simulations also demonstrate that the industrial-scale combined storage meets the goals of the U.S. Department of Energy's SunShot Initiative of exergy efficiencies greater than 95% and material costs below \$15/kWh$_{th}$.

Three thermocline-control (TCC) methods are assessed through simulations for a TES filled with a packed bed of rocks. Two methods, based on extracting or injecting HTF through ports, were published previously while the third method, based on mixing HTF streams, is novel. Results of a stand-alone TES with maximum allowed outflow temperature differences of 10% show that the mixing method with three ports leads to the largest utilization factors of 90.8% and 85.1% for molten salt and compressed air as HTF, respectively. These represent relative improvements of 38.8% and 73.4% compared to the baseline configurations without TCC. Simulations of a TES integrated into a CSP plant operating on a Rankine steam cycle and molten salt show that TCC increases the annually averaged plant efficiency.

The application of thermocline TES to AA-CAES is studied and experimental results of the world's first underground AA-CAES pilot plant are shown. The pilot plant aims at investigating the tightness of a mostly unlined rock cavern and studying the performance of a 12 MWh$_{th}$ TES that is filled with a packed bed of rocks and placed inside the cavern. Tests are carried out with charging temperatures up to 550°C and cavern gauge

pressures up to 7 bar. The numerical model of the TES is coupled to a simple cavern model and both show good agreement with the experimental results. Leaks from the unlined cavern are found to be small or negligible while leaks are traced mainly to the concrete plugs. Cycle energy efficiencies of the TES are determined to lie between 77% and 91%. The estimated round-trip efficiency of the AA-CAES plant is based on the measured TES performance while estimating the performance of the other components, yielding promising values of 63% to 74%.

Heat recovery of sensible-heat is essential to reach high efficiencies for solar-thermochemical fuel production based on temperature-swing redox cycles. A novel heat-recovery concept, the so-called dual-storage reactor, is proposed, which is based on two thermocline TES. Each thermocline TES has next to it a reaction zone with redox material. A gaseous HTF is employed to move the temperature profiles, such that the redox materials are alternately exposed to reduction and oxidation temperatures, while heat is inherently recovered within the thermocline TES. The potential of the dual-storage reactor is assessed with a numerical model. Simulation results of a laboratory-scale setup are compared to experimental results. Large-scale simulations with encapsulated non-stoichiometric ceria as redox material predict solar-to-fuel efficiencies of more than 35%, which is approximately twice as high as the maximum attainable efficiency without heat recovery. A second laboratory-scale dual-storage reactor setup is built and tested using encapsulated ceria in the reaction zone. With this setup, both heat recovery at temperatures up to 1500°C and the generation of CO from CO_2 are demonstrated successfully. The heat-recovery effectiveness ranges from 33% to 52%. The results of both numerical and experimental work are promising and represent an important step towards the industrial production of solar fuels.

ZUSAMMENFASSUNG

In dieser Arbeit werden Hochtemperatur-Festbett-Wärmespeicher untersucht. Diese Speicher werden typischerweise mit einem heissen Wärmetransportfluid von oben geladen und mit einem kühlen Wärmetransportfluid von unten entladen. Dabei entsteht eine sogenannte Temperatur-Sprungschicht zwischen den beiden Temperatur-Niveaus, welche während dem Laden nach unten und während dem Entladen nach oben geschoben wird. Ein Hauptnachteil dieser Technologie ist die Verbreiterung der Temperatur-Sprungschicht über die Zeit. Diese Verbreiterung führt zu einer verringerten Ausnutzung des Speichers und einem Temperaturabfall/-anstieg während dem Laden/Entladen. Es wurden verschiedene Konzepte zur Minderung dieser negativen Effekte vorgeschlagen, wie zum Beispiel die Zugabe von geeignetem Phasenwechselmaterial am oberen oder unteren Ende des Speichers.

Das Ziel dieser Arbeit ist einerseits die Bewertung und Entwicklung von Konzepten, die das Problem der Verbreiterung der Temperatur-Sprungschicht angehen. Anderseits untersucht diese Arbeit die Anwendung von Festbett-Wärmespeichern für Solarkraftwerke, Druckluftspeicher und solare Treibstoffe.

Ein numerisches Wärmetransfer-Modell des Speichers wird präsentiert. Es ist separat für Fluid- und Festkörper-Phasen formuliert und ist für variable thermo-physikalische Eigenschaften und beliebige Geometrien implementiert. Das Modell kann rein sensible, rein latente und kombiniert sensibel/latent Wärmespeicher modellieren. Die Energiegleichungen des Festbetts und des

Wärmetransportfluids werden ein-dimensional und die Energiegleichungen für die Struktur und die Isolation des Tanks zwei-dimensional gelöst. Das Modell wird verifiziert mit exakten analytischen Lösungen.

Das Konzept des kombinierten sensibel/latent Wärmespeichers wird experimentell getestet mit einem 42 kWh$_{th}$ Labor-Speicher. Der Speicher basiert darauf, dass eine geringe Menge von in Stahl eingekapseltem AlSi$_{12}$ auf einem Stein-Festbett platziert wird und von oben mit Luft bei 595°C geladen wird und von unten mit Luft bei 20°C entladen wird. Die experimentellen Resultate demonstrieren die Stabilisierung der Austritts-Temperatur beim Entladen. Ausserdem werden die experimentellen Resultate zur Validierung des Modells verwendet, welches dann benützt wird, um das Verhalten von industriellen kombinierten Wärmespeichern abzuschätzen. Die Simulations-Resultate werden mit jenen eines rein sensiblen Speichers verglichen und zeigen, dass der kombinierte Speicher die Materialkosten für einen vorgegebenen maximalen Temperaturabfall während dem Entladen verringern kann. Ausserdem zeigen die Simulationen, dass die Ziele der SunShot Initiative des amerikanischen Departementes für Energie erreicht werden können, mit Exergie-Effizienzen, die 95% übersteigen und Materialkosten, die \$15/kWh$_{th}$ unterschreiten.

Drei Methoden zur aktiven Beeinflussung der Temperatur-Sprungschicht werden mit Hilfe von Simulationen eines Stein-Festbett-Wärmespeichers beurteilt. Zwei Methoden, basierend auf einspritzen oder entnehmen von Wärmetransportfluid durch Anschlüsse auf verschiedenen Höhen des Tanks, wurden bereits publiziert, während die dritte Methode, basierend auf mischen von Wärmetransportfluid, neu ist. Resultate eines alleinstehend betrachteten Speichers, mit einer vorgegebenen maximalen Austritts-Temperaturschwankung von 10%, zeigen, dass die neue Methode zur grössten Speicherausnutzung führt, mit Werten von 90.8% und 85.1% für Flüssigsalz beziehungsweise Druckluft als Wärmetransportfluid. Diese Werte entsprechen Verbesserungen von 38.8% und 73.4% im Vergleich zur Konfiguration ohne aktive Beeinflussung der Temperatur-Sprungschicht. Simulationen eines Speichers, der integriert ist in ein Solarkraftwerk mit Rankine-Zyklus, zeigen, dass die aktive

Beeinflussung der Temperatur-Sprungschicht die jährliche Anlagen-Effizienz erhöht.

Experimentelle Resultate von der allerersten unterirdischen Pilotanlage eines adiabaten Druckluftspeichers werden präsentiert. Die Ziele der Pilotanlage sind das Untersuchen der Dichtheit der mehrheitlich nicht ausgekleideten Fels-Kaverne, sowie die Analyse der Leistungsfähigkeit eines 12 MWh_{th} Stein-Festbett-Wärmespeichers, welcher direkt in der Kaverne platziert ist. Es werden Versuche mit Lade-Temperaturen bis zu 550°C und Kavernen-Überdrücken bis zu 7 bar durchgeführt. Das numerische Modell des thermischen Speichers wird mit einem einfachen Kavernenmodell gekoppelt und ergibt gute Übereinstimmung mit den experimentellen Resultaten. Die gemessenen Zyklus-Effizienzen des Wärmespeichers liegen zwischen 77% und 91%. Die Effizienz der Pilotanlage des adiabaten Druckluftspeichers, geschätzt basierend auf der gemessenen Leistungsstärke des Wärmespeichers und unter Abschätzung der Leistungsfähigkeit der anderen Komponenten, beläuft sich auf Werte zwischen 63% und 74%.

Um hohe Effizienzen in der solar-thermochemischen Treibstoffherstellung zu erreichen, braucht es die Rückgewinnung von sensibler Wärme des Redox-Materials zwischen der Reduktions- und der Oxidationstemperatur. Ein neuartiges Konzept für Wärmerückgewinnung wird vorgestellt, welches auf zwei Festbett-Wärmespeichern basiert. Beide Wärmespeicher enthalten eine Reaktionszone, wo sich das Redox-Material befindet. Mit Hilfe eines gasförmigen Wärmetransportfluids werden die Temperaturprofile hinauf und hinunter geschoben, sodass die Redox-Materialien abwechselnd der Reduktions- und der Oxidationstemperatur ausgesetzt sind, während die Wärme durch die Speicherung in den Wärmespeichern zurückgewonnen werden kann. Das Potenzial des neuen Konzepts wird mit Hilfe eines numerischen Modells bewertet. Simulationsresultate eines Versuchsaufbaus werden mit experimentellen Resultaten verglichen. Die Simulation von einer industriellen Anlage mit nicht-stöchiometrischem Ceroxid prognostiziert Effizienzen von über 35%, was in etwa einer Verdoppelung der maximal erreichbaren Effizienz des Prozesses ohne Wärme-Rückgewinnung entspricht. Ein zweiter experimen-

teller Versuchsaufbau dieses Konzepts wird konstruiert und getestet, wo die Reaktionszone aus Ceroxid, welches in Röhren eingekapselt wird, besteht. In diesem Versuch wird die Wärmerückgewinnung bei bis zu 1500°C in Kombination mit der Produktion von CO aus CO_2 erfolgreich demonstriert. Die experimentellen Wärmerückgewinnungseffizienzen liegen zwischen 33% und 52%. Die Resultate der experimentellen Kampagnen und der numerischen Simulation sind vielversprechend und ein wichtiger Schritt in Richtung industrieller Produktion von solaren Treibstoffen.

Acknowledgements

First, I would like to thank Prof. Dr. Aldo Steinfeld for giving me the unique opportunity to perform my doctoral studies under his supervision in this exciting research field and for providing an outstanding research environment at the Professorship of Renewable Energy Carriers (PREC) at ETH Zürich.

I am very grateful to Prof. Dr. Ranga Pitchumani, Professor at Virginia Tech, USA, for serving as co-examiner of this thesis.

I am extremely thankful to my direct supervisor and co-examiner Dr. Andreas Haselbacher. Throughout my thesis he gave me excellent guidance and support. The countless fruitful discussions with him were of enormous value for this thesis.

Special thanks go to Dr. Giw Zanganeh and Luciano Serio from ALA-CAES S.A. for the very helpful discussions and their unmatchable commitment to the AA-CAES pilot plant.

I would like to thank Andrea Pedretti for the exciting collaboration, fruitful discussions and very valuable inputs on engineering issues.

I am grateful for the very pleasant collaboration with Prof. Dr. Maurizio Barbato and Simone Zavattoni from SUPSI.

Thanks go to Anoop Mathur from Terrafore LLC for the valuable discussions and his experienced advices.

I want to thank all former and present members of the PREC group at ETH for their support and the many useful discussions. Special thanks go to Viola Becattini, Dr. David Weibel, Dr. Stefan Ströhle, Tobias Betschart,

x

Dr. Jan Marti, Dr. Philipp Furler, Dr. Simon Ackermann and Dominik Herrmann.

I gratefully acknowledge the work done by the students Adrian Zbinden, Michael Kolman and Adrian Mularczyk, performing their Master theses, Bernhard Leistner, Stefan Zoller, Claudia Walser and Fadri Guetg, performing their Semester projects, and Marco Weibel and Kevin Frick, performing their Bachelor theses under my supervision.

Finally, I would like to express my sincere gratitude to my family and closest friends, especially my parents Annette and Samuel, my brothers Matthias, Stefan and Michael, as well as my girlfriend Catherine for their love and unconditional support.

Contents

5   Pilot-scale demonstration of advanced adiabatic compressed air energy storage: Plant description and tests with sensible thermal energy storage   **99**

6   Efficient solar-thermochemical fuel production using sensible heat recuperation in a dual-storage reactor   **131**

Nomenclature

Abbreviations

AA-CAES	Advanced adiabatic compressed air energy storage
CA	Compressed air
CSP	Concentrated solar power
D-CAES	Diabatic compressed air energy storage
DNI	Direct normal irradiation
GHG	Greenhouse gas
HHV	Higher heating value
HT	Heat transfer
HTF	Heat-transfer fluid
HX	Heat exchanger
LDC	Low-density concrete
LWC	Lightweight concrete
MFC	Mass-flow controller
MFM	Mass-flow meter
MS	Molten salt
PB	Power block
PCM	Phase-change material
PHS	Pumped hydroelectric storage
PPI	Pores per inch
RG	Reactant gas
RPC	Reticulated porous ceramic

RTD	Resistance temperature detector
SM	Solar multiple
TCC	Thermocline control
TES	Thermal energy storage
UHPC	Ultra-high-performance concrete

Greek characters

α	Exponent in analytical solution of cavern temperature	$-$
β	Volumetric thermal expansion coefficient	$1/\mathrm{K}$
γ	Heat capacity ratio	$-$
Δ	Difference	$-$
δ	Reduction extent, difference	$-$
ε	Effectiveness	$-$
ϵ	Emissivity	$-$
ζ	Storage utilization factor	$-$
η	Efficiency	$-$
θ	Tank wall inclination angle	$-$
μ	Dynamic viscosity	$\mathrm{kg/m\,s}$
ν	Kinematic viscosity	$\mathrm{m^2/s}$
Ξ	Exergy	J
ξ	Integration variable	$-$
π	Pressure ratio	$-$
ρ	Density	$\mathrm{kg/m^3}$
σ	Stefan-Boltzmann constant, $5.6704{\cdot}10^{-8}$	$\mathrm{W/m^2\,K^4}$
ϕ	Volume fraction	$-$

Latin characters

A	Area	$\mathrm{m^2}$
A	Case-dependent constant in Ergun's equation	$-$
a	Surface area per unit volume	$\mathrm{m^2/m^3}$
B	Case-dependent constant in Ergun's equation	$-$
C	Constant	$-$
C	Solar concentration ratio	$-$

c	Molar concentration	$\mathrm{mol/m^3}$
c	Specific heat capacity	$\mathrm{J/kg\,K}$
d	Diameter	m
E	Thermal energy	J
e	Specific thermal energy	$\mathrm{J/kg}$
f	Fraction	$-$
g	Gravitational acceleration, 9.81	$\mathrm{m/s^2}$
H	Height	m
H	Reaction enthalpy	$\mathrm{J/mol}$
h	Heat-transfer coefficient	$\mathrm{W/m^2\,K}$
h	Specific enthalpy	$\mathrm{J/kg}$
h_v	Volumetric heat-transfer coefficient	$\mathrm{W/m^3\,K}$
I	Solar irradiation	$\mathrm{W/m^2}$
i	Index	$-$
k	Thermal conductivity	$\mathrm{W/m\,K}$
M	Molar mass	$\mathrm{kg/mol}$
m	Mass	kg
N	Number of layers / units	$-$
n	Number of moles	mol
P	Power	W
p	Pressure	Pa or bar
Q	Heat flow rate	W
q	Volumetric heat flow rate	$\mathrm{W/m^3}$
R	Thermal resistance	$\mathrm{K/W}$
R	Universal gas constant, 8.314	$\mathrm{J/mol\,K}$
r	Radius, radial coordinate	m
S	Molar source term	$\mathrm{mol/m^3\,s}$
s	Specific entropy	$\mathrm{J/kg\,K}$
S_L	Longitudinal pitch between tubes	m
S_T	Transverse pitch between tubes	m
T	Temperature	K or °C
t	Thickness	m

t	Time	s
u	Interstitial velocity	m/s
u_0	Superficial velocity	m/s
V	Volume	m^3
W	Work	J
x	Axial coordinate	m
x	Molar fraction	–

Subscripts

0	Conditions of the free flow, reference/initial state
∞	Surroundings
c	Charging
d	Discharging
f	Fluid
g	Gas
p	Particle
s	Isentropic
s	Solid
t	Total (stagnation)
v	Volumetric
w	Wall
abs	Absorption
alt	Alternating
amb	Ambient
bot	Bottom
cav	Cavern
circ	Circumferential
comp	Compressor
cond	Conductive
cont	Contact
conv	Convective
cool	Cooling
eff	Effective

el	Electric
enc	Encapsulation
epcm	Encapsulation and PCM
est	Estimated
ex	Exergetic
exp	Experiment
ext	Extracted
fus	Fusion
gen	Generator
heat	Heating
hr	Heat recovery
in	Inside or in
ins	Insulation
int	Internal
l→r	From left to right
max	Maximum
mix	Mixing
mot	Motor
nc	No thermocline control
nom	Nominal
opt	Optical
out	Outside or out
ox	Oxidation
pc	Precharging
prev	Previous
r→l	From right to left
rad	Radiative
rec	Receiver
red	Reduction
ref	Reference
sf	Solar field
sim	Simulation

stg	Stagnant
str	Storage structure and insulation
sw	Southwest
tc	Thermocouple
th	Thermal
tot	Total
turb	Turbine
util	Utilized

Superscripts

$''$	Per unit area
$^-$	Average
$^{.}$	Flow rate
$^\sim$	Relative
*	Modified, threshold

<div align="right">

CHAPTER 1

</div>

<div align="right">

INTRODUCTION

</div>

1.1 The role of renewable energies and thermal energy storage

Global warming originates most likely from the observed increase in anthropogenic greenhouse gas (GHG) concentrations [1]. The most important anthropogenic GHG is carbon dioxide. It was shown that from 1006 A.D. until the beginning of industrialization, CO_2 concentrations were in the range 275-284 ppm [2]. Since 1950 A.D. the concentration increased from around 310 ppm to more than 400 ppm today. The primary source of this increase is the use of fossil fuels. In 2014, oil, coal and natural gas supplied 81% of the world primary energy [3].

To mitigate the substantial risks associated with global warming, the use of fossil fuels needs to be decreased drastically. Over the past decade, new renewable energy sources, in particular wind and solar, have been pushed to reduce the use of fossil fuels and ensure long-term energy supply. Despite

their exponential growth, up to now wind and solar remain relatively small contributors in the world primary energy supply. Among consumption sectors, the highest contribution of wind and solar energy is seen in the world electricity generation mix with shares of 3% and 1%, respectively [4]. The potential of further increasing their contribution is high, particularly for solar energy. Collecting the annual solar irradiation on 0.78% of the surface area of the Sahara would already provide the total world primary energy demand [5, 3]. However, due to the dilute nature of solar energy, large areas need to be covered with cost-effective solutions that convert sunlight into useful energy.

Another inherent drawback of both wind energy and solar energy is their intermittency. This intermittency can be compensated via energy storage. Among many energy storage technologies, one of the most cost-effective technologies is thermal energy storage (TES). It is the cost-effectiveness of TES that makes concentrated solar power (CSP) plants attractive [6, 7]. The working principle of CSP plants is shown in Fig. 1.1. CSP plants harvest solar energy via concentrating sunlight to heat a heat-transfer fluid (HTF) that is then used to generate electricity. During the day, excess thermal energy can be stored in the TES and during the night or cloudy periods, the TES can provide the thermal energy to continue generation of electricity. As an alternative to continuous operation, TES offers also the possibility to shift electricity generation to periods of high demand, making CSP dispatchable. Note that CSP is only one out of several applications of TES in context with renewable energies. Further applications are discussed in Section 1.4.
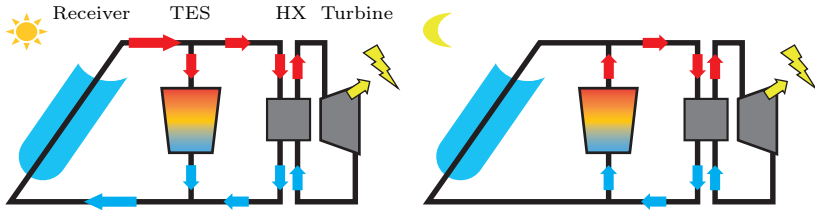
Figure 1.1: Working-principle of a CSP plant with TES during the day (left) and during the night (right). Red and blue arrows represent hot and cold fluid streams, respectively. HX denotes heat exchanger.

1.2 Thermal energy storage concepts

The specific application sets the performance requirements of the TES such as storage capacity, operation temperatures, heat fluxes, energy and exergy efficiencies and cost. Depending on these requirements, different TES concepts may be appropriate. Three different TES concept classifications are introduced in the following.

1. TES concepts can be divided into direct and indirect TES concepts [8]. Direct TES concepts employ a HTF which is at the same time also the storage medium. The HTF should therefore exhibit the characteristics of a good HTF and a good storage material. In indirect TES concepts, thermal energy is stored in a second medium, e.g., a packed bed of solid particles, which is charged and discharged by the HTF.

2. TES operate typically between a hot and a cold temperature level. These temperature levels can either be separated by two individual tanks, or they are separated in a single tank, where a temperature gradient evolves between the two temperature levels, a so-called thermocline. The single-tank system is also referred to as thermocline TES.

3. TES concepts can be classified as sensible-heat, latent-heat, sorption and thermochemical storage concepts [9]. Concepts based on sorption

and thermochemical storage have the highest storage densities, but they are also the least mature. Latent-heat storage concepts offer also relatively high storage densities, but they are based on relatively expensive phase-change materials (PCMs), which typically need to be encapsulated, complicating its technical realization. By contrast, concepts based on sensible-heat storage are the most mature and many sensible-heat storage materials are low-cost.

Various combinations of the different TES concepts of each classification are possible. The most common TES concepts in CSP plants are based on indirect or direct sensible-heat TES with two tanks as well as indirect sensible-heat thermocline TES [9].

All of the currently installed two-tank and thermocline TES systems in utility-scale CSP plants are based on sensible-heat storage materials [9].

1.3 Motivation for thermocline TES and further advancements

State-of-the art in CSP plants is currently the indirect sensible-heat two-tank concept with oil as HTF and molten salt as storage medium [10]. However, it has crucial disadvantages such as high cost [8] and restricted operating temperatures due to relatively high freezing points of the molten salts (120-240$°$C) and relatively low maximum operating temperatures ($<$600$°$C) [11]. Alternative concepts are under research mainly to achieve two improvements:

1. Higher maximum storage temperatures are needed to keep up with the trend towards higher temperatures in CSP plants, as they result in higher plant efficiencies [12].
2. Costs need to be reduced significantly to fulfill the goals from the U.S. Department of Energy's SunShot Initiative of specific costs below \$15/kWh$_{th}$ [13].

Both of theses improvements can be reached with thermocline TES:

1. Higher temperatures can be reached because there is no need of finding a storage HTF that has high storage densities and withstands the high temperatures. Instead, HTFs such as air can be employed, which have no or only little application temperature restrictions. Furthermore, many solid storage materials can resist temperatures above 700°C [8, 14, 15, 16]. Temperatures up to 1573-1873 K are common in regenerators used in the steel industry [17].

2. The cost breakdown of the current state-of-the art TES concept is such that the molten salt (49%), the two tanks (17%) and the heat exchangers (13%) together make up for 79% of the total cost of the concept [9]. With a thermocline TES, the cost for the heat exchanger between HTF and storage medium is avoided and only one tank is necessary. Furthermore, costs are reduced significantly by replacing the expensive molten salt either partly by filling the tank with low-cost storage filler material [18, 19] or entirely by replacing the molten salt with a a low-cost HTF and using a low-cost storage filler material.

However, thermocline TES have two major drawbacks. First, as thermocline TES are preferably filled with a packed bed of solid particles[1], thermal ratcheting is of concern, which occurs due to uneven expansion and contraction of the tank structure and filler particles [20]. To address this problem, previous work has suggested inclined storage walls to reduce the normal force on the walls during thermal expansion of the filler material [21, 22] and to maximize internal insulation [20].

The second drawback of thermocline TES is thermocline degradation, which means that the steepness of the thermocline decreases over time [23]. This decreases the utilizable storage capacity and leads to an outflow temperature increase/decrease during charging/discharging, which is unfavorable for downstream applications such as power cycles.

Several methods were proposed in previous work to reduce thermocline degradation and its consequences. Passive methods comprise combinations

---

[1]Packed beds offer favorable heat transfer rates and therewith high thermocline steepness [9].

of TES filler materials, e.g., combining sensible-heat with small volumes of latent-heat to decrease the outflow temperature drop during discharging [24, 25, 26], or cascading latent-heat [27, 28, 29, 30] or thermochemical [31] storage materials. Active methods, also referred to as thermocline control (TCC) methods, were also proposed, which are typically based on extracting and injecting HTF at certain positions of the thermocline TES to steepen the thermocline [32, 33, 34]. In this thesis, one passive and multiple active methods are studied in detail.

The selected passive method which is studied in this thesis is combined sensible/latent TES. Thanks to the small amount of required PCM, this method is interesting in terms of performance and material cost. An experimentally validated model is used to predict the exergetic performance and the material cost of industrial-scale thermocline storages that are based on combined sensible/latent TES. The resulting performance and cost are compared to the results from a sensible-only TES and to the goals from the SunShot initiative.

With respect to TCC methods, the literature lacks studies that assess and compare these methods based on their performance. In this thesis, two existing TCC methods and a novel TCC method are described and analyzed. The TCC methods are compared based on a numerical performance assessment of a stand-alone TES as well as of a TES that is incorporated in a CSP plant.

1.4   Further applications of thermocline TES

Apart from CSP plants, thermocline TES can be applied to several other technologies, e.g., to provide domestic hot water or industrial process heat. In this thesis, two additional applications are studied numerically and experimentally: (1) advanced adiabatic compressed air energy storage (AA-CAES) and (2) heat recovery for solar-thermochemical fuel production.
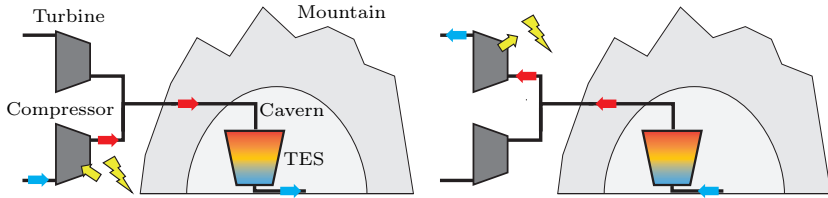
Figure 1.2: Working-principle of AA-CAES during compression with a compressor while charging of the TES and the cavern (left) and during expansion over a turbine while discharging the TES and the cavern (right). Red and blue arrows represent hot and cold air streams, respectively.

1.4.1   Advanced adiabatic compressed air energy storage

AA-CAES is an electricity storage technology that permits better integration of wind power into national grids and therefore increases their utilisation [35]. It is the only electricity storage technology with similar storage capacities as pumped hydroelectric storage (PHS), but has potentially lower costs and less geographic restrictions [36, 37, 38].

The working principle of AA-CAES is shown in Fig. 1.2. CAES plants use excess electricity from the grid to drive a compressor to compress ambient air. The compressed air is stored in a cavern, preferably underground, as for example in a rock cavern in the mountain. At times of high power demand, electricity is generated by expanding the compressed air in a turbine. In contrast to the utility-scale proven diabatic CAES (D-CAES), AA-CAES uses a thermal energy storage to store the compression heat and re-supply it before expansion. This avoids the need of a fossil fuel burner that pre-heats the air before expansion as required in D-CAES plants, and it increases round-trip efficiencies from around 45-50% to about 60-75% [39, 40].

In this thesis, results from the world's first underground pilot-scale AA-CAES plant are shown. A 12 MWh$_{th}$ thermocline TES is incorporated in a rock cavern. The TES is filled with a packed bed of rocks and charged with compressed air.
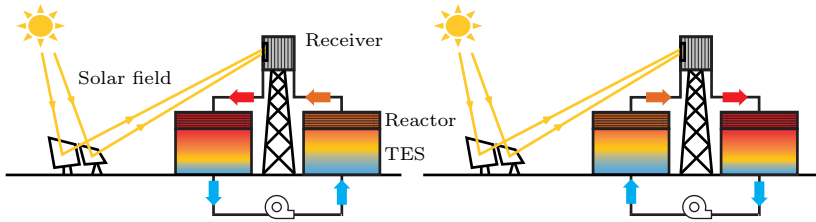
Figure 1.3: Working-principle of a dual-storage reactor for solar fuel production. In the left picture, the right and left reactors are at reduction and oxidation temperatures, respectively, and in the right picture reduction and oxidation temperatures are switched between the two tanks. Red and orange arrows represent hot HTF streams and blue arrows represent cold HTF streams.

1.4.2 Solar-thermochemical fuels

Liquid fuels can be produced from concentrated solar energy, H_2O, and CO_2 using a non-stoichiometric temperature-swing redox cycle [41]. To reach high solar-to-fuel efficiencies, heat recovery of the redox material between reduction and oxidation temperatures is essential [42]. Several heat recovery concepts were suggested in previous works [43, 44, 45, 46, 47], however all of them have either the need of moving high-temperature redox material or the need of pumping liquid metal as HTF.

In this thesis, a novel heat-recovery concept is proposed, the so-called dual-storage reactor. It avoids moving the redox material and is based on a gaseous HTF and two thermocline TES, see Fig. 1.3. Each thermocline TES has on top of it a reaction zone with redox material. The redox material can either be encapsulated or it can be in direct contact with the HTF. The HTF is pumped through the tanks from the cold ends. It allows moving of temperature profiles back and forth, such that the redox materials are alternately exposed to reduction and oxidation temperatures, while heat is recovered inherently within the thermocline TES. Concentrated solar energy heats the HTF in a solar receiver to compensate for thermal losses,

thermocline degradation and the endothermic reduction energy.

The novel dual-storage reactor concept is studied in detail. Two experimental laboratory-scale demonstration setups are built and tested. The first one focuses on the demonstration of heat recovery and results are compared to a numerical model. The numerical model is used to predict the solar-to-fuel efficiency of a large-scale dual-storage reactor. The second experimental laboratory-scale setup combines heat recovery and redox reaction.

1.5 Thesis outline

Chapter 2 introduces the numerical model for the sensible-heat and latent-heat sections. In Chapter 3 the experimental validation and the analysis of industrial-scale combined sensible/latent TES are shown. Chapter 4 presents the numerical assessment and comparison of various TCC methods. Chapter 5 is devoted to the AA-CAES pilot plant description, results and comparison with the numerical model. Chapter 6 describes the dual-storage reactor concept, the laboratory-scale experimental proof of concept of heat recovery and the large-scale simulations. Chapter 7 presents the experimental demonstration of the dual-storage reactor including both, heat recovery and chemical reaction. Chapter 8 provides an outlook with suggestions for future work.

HEAT-TRANSFER MODEL[1]

2.1 Introduction

Several types of numerical models of packed bed TES have been studied in literature. In [48] a comparison is shown between four basic types:

- Continuous solid phase models

- Models based on Schumann's two-phase analytical solution [49]

- Single phase models

- The thermal diffusion models or models with thermal gradients inside the particles

---

[1]Material in this chapter has been published in L. Geissbühler, M. Kolman, G. Zanganeh, A. Haselbacher and A. Steinfeld, "Analysis of industrial-scale high-temperature combined sensible/latent thermal energy storage," *Applied Thermal Engineering*, vol. 101, pp. 657-668, 2016. doi: 10.1016/j.applthermaleng.2015.12.031.

Numerical two-phase models based on the analytical solution presented by Schumann, which was actually solved before in [50], are widely used for simulating sensible-heat storage systems due to the significantly smaller computational time in comparison to the models that solve the thermal gradients inside the particles.

In this thesis, a numerical two-phase simulation model is developed to simulate sensible-heat storage, latent-heat storage, and combined sensible/latent-heat storage. The starting point is the model developed by [25], which is also based on Schumann's model. The quasi-one-dimensional heat-transfer model is formulated separately for the sensible- and latent-heat sections. Energy conservation equations are solved for the fluid and solid/molten phases, considering convective, conductive, and radiative heat transfer as well as losses through the top, bottom, and lateral walls of the storage. Thermo-physical properties are modeled to be temperature-dependent. The model developed in this thesis improves on that presented by [25] in three ways:

- Heat conduction is solved in the encapsulated PCM in the radial direction of the PCM. This is important for low-conductivity PCMs such as salts.

- The thermal inertia of the wall structure and insulation is considered and the corresponding energy equations are solved in two dimensions (axial and radial). This is particularly important for simulating laboratory-scale storages, where the heating of the insulation has a major effect on the results.

- To decrease the computational time, the model is solved implicitly in time and space derivatives are discretized with second-order accuracy.

In the following section the mathematical model is presented in detail. Section 2.3 describes the numerical implementation. The model is verified with analytical solutions in Section 2.4 and a summary and conclusions are given in Section 2.5. Model adaptations for the simulation of TCC methods and the dual-storage reactor are given in Appendices A and E, respectively.
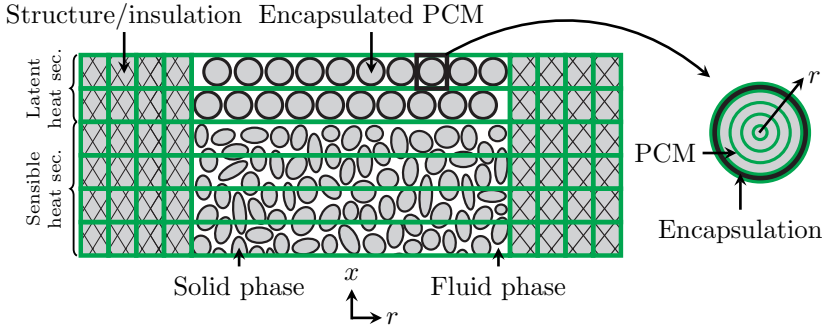
Figure 2.1: Schematic of the combined sensible/latent-heat storage with coordinates x and r. Note that the coordinate r is used for both the radial direction in the tank and the radial direction in the encapsulated PCM tube/sphere. The discrete control volumes are shown schematically in green.

2.2 Mathematical model

Figure 2.1 shows schematically the structure/ insulation and the sensible- and latent-heat sections. The corresponding energy conservation equations are presented in the following.

2.2.1 Sensible-heat section

The conservation equations for the fluid and solid phases are

$$(1 - \phi_s) \frac{\partial(\rho_g e_g)}{\partial t} + (1 - \phi_s) \frac{\partial(u \rho_g h_g)}{\partial x} = h_{v,\text{rocks}}(T_s - T_g)$$
$$+ q_{\text{loss,cover}} + q_{\text{loss,bottom}} + a_w h_{w,\text{conv}}(T_w - T_g), \quad (2.1)$$

$$\phi_s \frac{\partial(\rho_s e_s)}{\partial t} = \frac{\partial}{\partial x}\left(k_{\text{eff}} \frac{\partial T_s}{\partial x}\right) + h_{v,\text{rocks}}(T_g - T_s) + a_w h_{w,\text{cond-rad}}(T_w - T_s), \quad (2.2)$$

where all symbols are defined in the nomenclature. Temperature-dependent rock and air properties are taken from [22, 51, 52]. The volumetric heat-

transfer coefficient $h_{v,\text{rocks}}$ of the packed bed of rocks is determined from
the correlation of [53],

$$\text{Nu}_{\text{rocks}} = \frac{h_{\text{rocks}} d_p}{k_g} = \frac{2.06}{1 - \phi_s} \text{Re}_0^{0.425} \text{Pr}_g^{1/3} \quad \left[90 \lesssim \text{Re}_0 \lesssim 4000, \text{Pr}_g \approx 0.7 \right],$$

using

$$h_{v,\text{rocks}} = \frac{6\phi_s}{d_p} h_{\text{rocks}}. \tag{2.3}$$

The Reynolds number Re_0 is based on the mean rock diameter d_p and
the superficial velocity. For stagnant flow (during idle time), the analytical
Nusselt correlation for a sphere is used, $\text{Nu}_{\text{rocks}} = 2$. The lateral wall
convective heat-transfer coefficient $h_{w,\text{conv}}$ and the conductive-radiative wall
heat-transfer coefficient $h_{w,\text{cond-rad}}$ are taken from [54] and [55], respectively.
The effective thermal conductivity k_{eff} is calculated using the correlation
of [56] which is applied as described in [22]. The terms $q_{\text{loss,cover}}$ and
$q_{\text{loss,bottom}}$ model the volumetric thermal losses from the top and bottom of
the storage to the environment and are defined in Section 2.2.4.

The pressure drop in the packed bed is determined from Ergun's equa-
tion [57]. The sphericity of the packed-bed material is 0.6 for rocks and 1
for spheres. The case-dependent constants appearing in Ergun's equation
are set to $A = 217$ and $B = 1.83$ for the rocks, as reported by [58], where
randomly shaped gravel of similar size and void fraction was used.

2.2.2 Latent-heat section

Because PCMs can have low thermal conductivities, Biot numbers may be
larger than 0.1. Therefore, the encapsulated PCM is discretized in the radial
direction to account for thermal conduction inside the PCM. Spherical and
cylindrical encapsulations are considered. Temperature-dependent PCM and
encapsulation properties are given in Section 3.2.1.

Fluid

For the fluid phase, the energy conservation equation is

$$(1 - \phi_{\text{epcm}}) \frac{\partial(\rho_g e_g)}{\partial t} + (1 - \phi_{\text{epcm}}) \frac{\partial(u \rho_g h_g)}{\partial x}$$
$$= a_w h_{w,\text{conv}}(T_w - T_g) + q_{\text{enc},g} + q_{\text{loss,cover}} + q_{\text{loss,bottom}}, \quad (2.4)$$

where ϕ_{epcm} is the volume fraction of the encapsulated PCM and $q_{\text{enc},g}$ accounts for the convective heat transfer between the gas and encapsulation and is specified in the next section. The pressure drop for spherical encapsulations is calculated from Ergun's equation using case-dependent constants of $A = 150$ and $B = 1.75$.

Encapsulation

The energy conservation equation for spherical encapsulations is

$$\phi_{\text{enc}} \frac{\partial(\rho_{\text{enc}} e_{\text{enc}})}{\partial t} = \frac{\partial}{\partial x}\left(k_{\text{eff,pcm}} \frac{\partial T_{\text{enc}}}{\partial x}\right)$$
$$+ a_w h_{w,\text{cond-rad}}(T_w - T_{\text{enc}}) - q_{\text{enc},g} + q_{\text{pcm,enc}}, \quad (2.5)$$

where ϕ_{enc} is the volume fraction of the encapsulation. The effective thermal conductivity $k_{\text{eff,pcm}}$ for spherical encapsulations is calculated from [56], applying the relation given by [59],

$$\text{Pe}_{d_{\text{p}},\text{eff}} = \frac{\dot{m}'' c_{p,g} d_p}{k_{\text{eff}}} = \frac{\text{Pe}_{d_p,g}}{0.5 \text{Pe}_{d_p,g} + k_{\text{eff,stg}}/k_g}, \quad (2.6)$$

where $k_{\text{eff,stg}}$ is the stagnant bed effective thermal conductivity.

For cylindrical encapsulations,

$$\phi_{\text{enc}} \frac{\partial(\rho_{\text{enc}} e_{\text{enc}})}{\partial t} = -q_{\text{enc},g} + q_{\text{cond,enc}} + q_{\text{rad,enc}} + q_{\text{pcm,enc}}$$
$$+ \frac{a_w f_{\text{cont},w} k_{\text{enc}}}{(r_{\text{tank}} - t_{\text{enc}}) \ln[r_{\text{tank}}/(r_{\text{tank}} - t_{\text{enc}})]}(T_w - T_{\text{enc}}), \quad (2.7)$$

where $f_{\text{cont,w}} = 0.002$ is the estimated fraction of the circumferential tank area in physical contact with the tubes and $q_{\text{enc,g}}$ represents the volumetric heat transfer between the fluid phase and the encapsulation considering convective and conductive resistances.

The volumetric heat-transfer contributions are based on the cell volumes of the quasi-one-dimensional model. Therefore, it is necessary to introduce the subscript i to indicate the axial location in the grid associated with the model. For the cell with axial index i and volume V_i the volumetric heat transfer between encapsulation and gas is given by $q_{\text{enc},g,i} = (T_{\text{enc},i} - T_{g,i})/V_i(R_{\text{cond},i} + R_{\text{conv},i})$. The conductive thermal resistances for spherical and cylindrical encapsulations are given by the standard expressions in which the numbers of spheres or tubes in cell i are taken into account. The conductive resistance is based on the mean length of the cylindrical tubes in a given row. For spherical encapsulations, $h_{v,\text{enc},i}$ is calculated from Eq. 2.3 (appropriately modified) and from the correlation of [60],

$$\text{Nu}_{\text{enc}} = \frac{h_{\text{enc}}d_p}{k_g} = 2.0 + 2.031\text{Re}_0^{1/2}\text{Pr}_g^{1/3} + 0.049\text{Re}_0\text{Pr}_g^{1/2} \quad [\,\text{Re}_0 < 5000\,]. \tag{2.8}$$

For cylindrical encapsulations, $h_{v,\text{enc},i}$ is determined from $h_{v,\text{enc},i} = a_{s,i}h_{\text{enc},i}$ with $a_{s,i}$ being the calculated surface area of the tubes divided by the total volume of the cell (including the volume of encapsulation, PCM, and gas) and the heat-transfer coefficient per unit area h_{enc} is calculated from the correlation of [61],

$$\text{Nu}_{\text{enc}} = \frac{h_{\text{enc}}d_{\text{tubes}}}{k_g} = 0.51C_{\text{row}}\text{Re}_{\text{max}}^{1/2}\text{Pr}_g^{0.37}\left(\frac{\text{Pr}_g}{\text{Pr}_s}\right)^{1/4}$$
$$[\,40 < \text{Re}_{\text{max}} < 1000\,],$$

where $C_{\text{row}} = 0.95$ (for four staggered tube rows as in the experimental setup described below), Re_{max} is based on $u_{\text{max}} = S_t u_0/(S_t - d_{\text{tubes}})$ with S_t denoting the transversal pitch, Pr_g is the gas Prandtl number evaluated at the gas temperature, and Pr_s is the gas Prandtl number evaluated at the solid temperature.

The conductive and radiative heat transfer for one row of tubes is approximated as

$$q_{\text{cond,enc},i} = \frac{f_{\text{cont,enc}}}{\Delta x}\left[\left(k_{\text{enc}}\frac{\partial T_{\text{enc}}}{\partial x}\right)_{i+\frac{1}{2}} - \left(k_{\text{enc}}\frac{\partial T_{\text{enc}}}{\partial x}\right)_{i-\frac{1}{2}}\right],$$

$$q_{\text{rad,enc},i} = \frac{\sigma\phi_{\text{epcm}}}{(2/\epsilon_{\text{enc}}-1)\Delta x}\left(T_{\text{enc},i+1}^4 - 2T_{\text{enc},i}^4 + T_{\text{enc},i-1}^4\right),$$

where $f_{\text{cont,enc}} = 0.05$ is the estimated fraction of the cross-sectional area for which the tubes are in contact with each other.

The conduction heat transfer between PCM and encapsulation can be expressed as

$$q_{\text{pcm,enc},i} = \frac{T_{\text{pcm},i} - T_{\text{enc},i}}{V_i(R_{\text{cond,pcm},i} + R_{\text{cond,enc},i})}, \tag{2.9}$$

using the appropriate thermal resistances for spheres or tubes.

PCM

The energy conservation of the PCM is

$$\frac{\partial(\rho_{\text{pcm}}e_{\text{pcm}})}{\partial t} = \frac{1}{r^n}\frac{\partial}{\partial r}\left(k_{\text{pcm}}r^n\frac{\partial T_{\text{pcm}}}{\partial r}\right) - q_{\text{pcm,enc}},$$

where $n = 1$ or 2 for cylindrical or spherical encapsulations, respectively, and $q_{\text{pcm,enc}}$ is non-zero only for the outermost PCM layer, see Eq. 2.9. For liquid PCM, the conductive resistance is neglected because it is dominated by natural convection [62].

2.2.3 Interface between sensible and latent sections

Between the sensible and latent sections, an effective conductivity is used for the spheres [56]. Radiative heat transfer is considered between the last row of tubes and the top cell of rocks,

$$Q_{\text{interface,rad}} = \frac{\sigma A_{N_{\text{tube-rows}}}\phi_{\text{epcm}}}{1/\epsilon_{\text{enc}} + 1/\epsilon_{\text{rocks}} - 1}\left(T_{\text{rocks},1}^4 - T_{\text{enc},N_{\text{tube-rows}}}^4\right).$$

2.2.4 Storage structure and insulation

Following [22], the volumetric cover and bottom losses are modelled as

$$q_{\text{loss,cover}} = h_{\text{cover,cond}} a_{\text{cover}} (T_{\text{surface}} - T_{g,\text{top}}), \qquad (2.10)$$

$$q_{\text{loss,bottom}} = h_{\text{bottom,cond}} a_{\text{bottom}} (T_{\infty,\text{bottom}} - T_{g,\text{bottom}}), \qquad (2.11)$$

where a_{cover} is given by the top area of the topmost cell divided by its volume, a_{bottom} is defined analogously, $h_{\text{bottom,cond}}$ is obtained through calculation of the thermal resistances of the bottom structure and insulation and a certain amount of soil (see Section 3.3.1), $T_{\infty,\text{bottom}}$ is assumed to be the ambient temperature, and $h_{\text{cover,cond}}$ takes into account conduction through the structure and the insulation, convection at the upper surface, and solar irradiation.

For the lateral wall, conduction through the structure and the insulation are included,

$$\frac{\partial(\rho_{\text{str}} e_{\text{str}})}{\partial t} = \frac{1}{r} \frac{\partial}{\partial r} \left(k_{\text{str}} r \frac{\partial T_{\text{str}}}{\partial r}\right) + \frac{\partial}{\partial x} \left(k_{\text{str}} \frac{\partial T_{\text{str}}}{\partial x}\right) + q_{\text{boundary}}, \quad (2.12)$$

where q_{boundary} is non-zero only at the boundaries and accounts for losses from the wall to the surface (similar to Eq. 2.10), to the bottom (similar to Eq. 2.11), and to the lateral environment. At the inner circumferential surface, q_{boundary} accounts for heat transfer between the wall and the fluid and between the wall and the solid, see, e.g., the last terms in Eqs. 2.1 and 2.2. The outer circumferential wall is exposed either to free convection (if the storage is above ground) or to conduction to the surrounding soil (if the storage is immersed in the ground). The latter is simulated by including the thermal inertia of part of the soil in the lateral wall section (see Section 3.3.1) and the former is modeled using [52],

$$\text{Nu}_x = \left(\frac{\text{Gr}_x}{4}\right)^{1/4} \frac{0.75 \text{Pr}_g^{1/2}}{(0.609 + 1.221 \text{Pr}_g^{1/2} + 1.238 \text{Pr}_g)^{1/4}}.$$

2.3 Numerical implementation

The finite-volume method is applied to solve the energy conservation equations. The discrete volumes are schematically indicated in green in Fig. 2.1. The equations are solved in space with second order accuracy and integrated in time with the backward Euler method. The enthalpy method [63] is used to solve the equations of the PCM. The specific enthalpy and specific thermal energy of the fluid are computed from $h_g = \int_{T_{g,\mathrm{ref}}}^{T_g} c_{p,g}(T)\,dT$ and $e_g = \int_{T_{g,\mathrm{ref}}}^{T_g} c_v(T)\,dT$, whereas the specific thermal energy of the encapsulation, PCM, and structure and insulation are determined from $e = \int_{T_{\mathrm{ref}}}^{T} c(T)\,dT$ with the appropriate specific heat. For ease of implementation and to exploit efficient solution methods, the energy equations of the packed bed, encapsulation, PCM, and structure and insulation are solved in separate tridiagonal and pentadiagonal systems. Convergence at each time step is achieved through an outer iteration. In each iteration, the systems are solved sequentially until the residual

$$R = \sqrt{\frac{1}{N} \sum_{i=1}^{N} \left(\frac{T_i^{n+1,m} - T_i^{n+1,m-1}}{T_i^{n+1,m-1}} \right)^2}$$

reaches a user-specified tolerance. In the above equation, N is the total number of unknowns, n is the time step index, and m is the iteration index. In the simulations reported below, the convergence criterion was $R < 10^{-6}$, for which between two and five iterations were typically required.

2.4 Model verification

The model for the sensible section was verified with the exact solution obtained by neglecting axial conduction and wall losses and assuming constant properties and uniform initial and boundary conditions [50]. The simulation
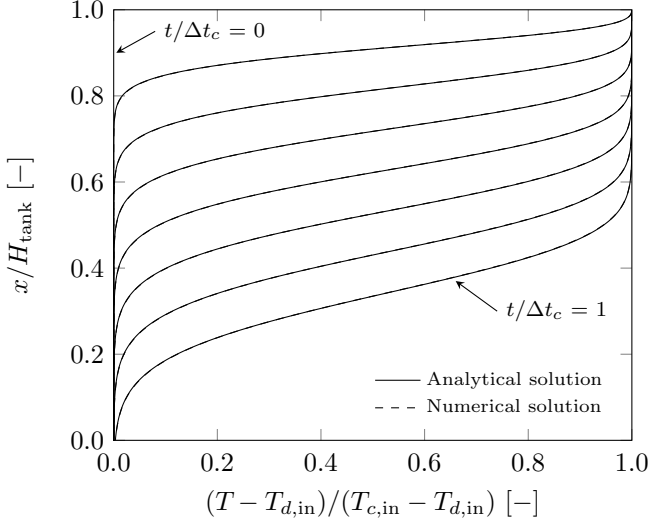
Figure 2.2: Comparison of numerical solution and analytical solution [50] for the solid temperature during the first charging. The thermocline evolution is shown every $t/\Delta t_c = 1/7$.

parameters were

$$\sigma\Gamma = \frac{\phi_s \rho_s c_s H_{\text{tank}}}{2\dot{m}'' c_{p,g} \Delta t} = 0.747,$$

$$\text{NTU} = \frac{h_v H_{\text{tank}}}{2\dot{m}'' c_{p,g}} = 54.8,$$

$$\text{Pe}_{H,\text{eff}} = \frac{\dot{m}'' c_{p,g} H_{\text{tank}}}{k_{\text{eff}}} \to \infty.$$

The simulation time step was $\Delta t = 5$ s and the grid spacing was $\Delta x = 0.016$ m. The comparison of the numerical and analytical solutions for the solid temperature during the first charging shown in Fig. 2.2 reveals excellent agreement.

In general, axial conduction in the solid phase cannot be neglected. However, no generally valid exact solution with non-negligible conduction is
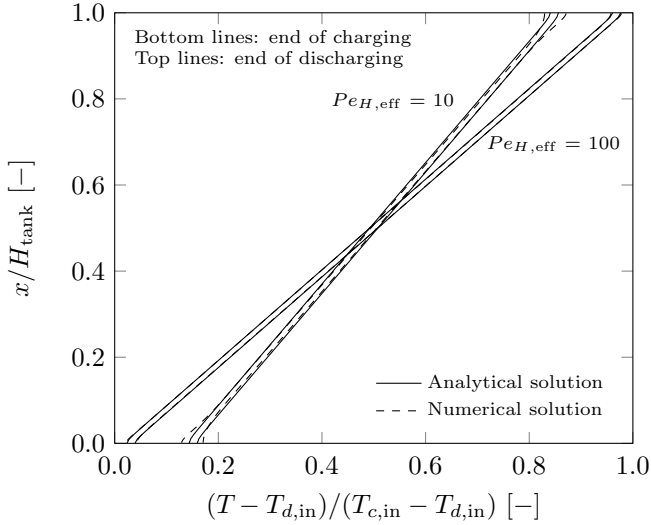
Figure 2.3: Comparison of numerical solution and analytical solution [64] for the solid temperature at steady cycling conditions.

known to the author. Under the assumption of steady cycling behavior, an analytical solution is available in the limit of fast switching times [64]. The numerical solution after 1500 cycles is compared with the analytical solution in Fig. 2.3 for $\sigma\Gamma = 31.4$, NTU $= 54.8$, and $\mathrm{Pe}_{H,\mathrm{eff}} = 10$ and $\mathrm{Pe}_{H,\mathrm{eff}} = 100$. The simulation time step and the grid spacing were $\Delta t_{\mathrm{sim}} = 5$ s and $\Delta x = 0.016$ m, respectively. The overall agreement is seen to be excellent, with the exception of the inflow and outflow regions for $\mathrm{Pe}_{H,\mathrm{eff}} = 10$, which may be caused by the numerical treatment of the boundary conditions.

2.5 Summary and conclusions

A two-phase numerical heat-transfer model was developed for the simulation of sensible-heat and latent-heat thermal energy storage. One-dimensional energy conservation equations are solved for the fluid and solid/molten

phases inside the TES, while two-dimensional energy equations are solved in the storage structure and insulation. Spatial derivatives are discretized with second-order accuracy and time integration is performed implicitly with the backward Euler method.

The model was verified with two exact analytical solutions. First, for the case of no axial conduction, no wall losses, and assuming constant properties and uniform initial and boundary conditions, which yielded excellent agreement. Second, for the case of non-negligible axial conduction, steady cycling behavior, and in the limit of fast switching times. The agreement was excellent except for the inflow and outflow regions of one set of parameters, which was attributed to the numerical treatment of the boundary conditions.

The successful verification of the model is an important step. However, before the model can be applied to predict the performance of real TES, it needs to be validated with experimental data. In this thesis, the model was validated with multiple experimental setups and concepts, see Sections 3.2, 5.4.2 and 6.3.3.

Analysis of Industrial-Scale High-Temperature Combined Sensible/Latent Thermal Energy Storage[1]

3.1 Introduction

The integration of thermal energy storage (TES) improves the efficiency and economics of concentrated solar power (CSP) plants [65]. A thermocline TES based on a packed bed of rocks as sensible heat storage material and air as heat-transfer fluid (HTF) is well-suited for CSP plants, yielding 95% overall (charging-discharging) thermal efficiency [66, 22, 67]. However, unless the storage is oversized, sensible heat thermocline systems suffer from decreases in the HTF outflow temperature during discharging, reducing the efficiency

[1]Material in this chapter has been published in L. Geissbühler, M. Kolman, G. Zanganeh, A. Haselbacher and A. Steinfeld, "Analysis of industrial-scale high-temperature combined sensible/latent thermal energy storage," *Applied Thermal Engineering*, vol. 101, pp. 657-668, 2016. doi: 10.1016/j.applthermaleng.2015.12.031.

of the power block. Obviously, oversizing the storage increases costs and is
therefore undesirable.

In principle, temperature decreases during discharging can be avoided
with packed beds of encapsulated phase-change materials (PCMs). Several
studies have concluded that packed beds composed of a single PCM do not
offer clear benefits [68, 69, 70], however. Cascaded latent heat storage [71, 72]
appears promising, but requires additional experimental and numerical
investigation. In particular, further research into characterization, phase-
segregation and subcooling, compatibility of phase-change and encapsulation
materials [73], cycling performance, and heat-transfer enhancement [10] are
needed, especially at the high temperatures required for CSP [74, 75].

These considerations prompt the investigation of combined sensible/
latent-heat storage [76, 24, 25, 51, 26]. In prior work, such a combined
storage was investigated numerically and experimentally at the laboratory
scale. Placing 5% by volume of encapsulated $AlSi_{12}$ on top of a packed bed
of rocks was found to be sufficient to stabilize the outflow temperature for
approximately 90 minutes during discharging [25, 51]. This allows a combined
storage to be smaller than a sensible storage for the same temperature drop
during discharging. The associated reduction in material offsets at least
partially the increased cost of the PCM compared to the rocks. To the
author's knowledge, this offset has not been studied so far. The study of
this offset is particularly relevant for industrial-scale TES where reduced
material costs are an important contribution to lowering the levelized cost
of the electricity produced by CSP plants [23].

Therefore, the objective of this chapter is to compare industrial-scale
sensible and combined storage in terms of the exergy efficiency and specific
material costs for a specified temperature drop of the HTF during discharging.
Using the temperature drop during discharging as the basis for comparison is
natural because the temperature of the HTF entering the power block has a
direct impact on the efficiency of the power block. The comparison is based
on a numerical model (see Chapter 2) that is validated with experimental
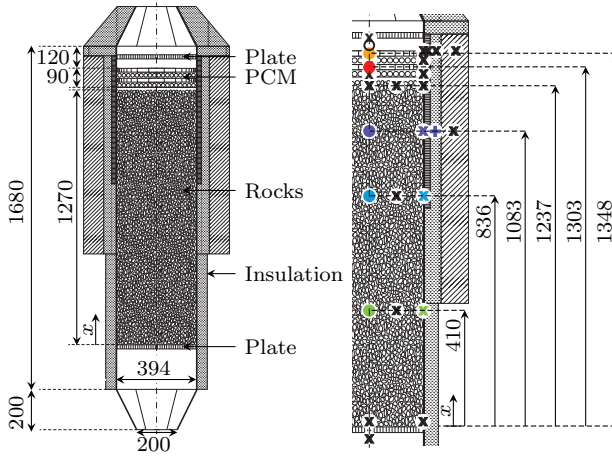data from a laboratory-scale combined storage.

Figure 3.1: Schematic of the laboratory-scale combined sensible/latent-heat storage (left) with thermocouple positions indicated by circles and crosses (right). All dimensions in mm.

3.2 Model validation

The models of the sensible- and latent-heat sections were validated with data from [22] and [59], respectively. For combined sensible/latent-heat storage, limited experimental data are available. To gain insight into combined sensible/latent-heat storage and to allow further validation of the model, an experimental study of combined sensible/latent-heat storage was conducted.

3.2.1 Experimental configuration

Experiments were performed with a cylindrical laboratory-scale combined storage of 42.4 kWh$_{\text{th}}$ capacity consisting of a packed bed of rocks and encapsulated AlSi$_{12}$ on top of the bed, see Fig. 3.1. The alloy AlSi$_{12}$ was chosen as PCM because its melting temperature is suitable for CSP plants and because of its high heat of fusion, high thermal conductivity, and comparatively low price [74]. The storage was charged from the top with air at up to 595 °C

Table 3.1: PCM and encapsulation properties (temperature in °C).

Quantity	Units	$T < 573$	$573 < T < 577$	$T > 577$	Source
$c_{\mathrm{AlSi_{12}}}$	J/kgK	1070	116500	1170	[51]
$\rho_{\mathrm{AlSi_{12}}}$	kg/m^3	2650	2650	2650	[51]
c_{enc}	J/kgK	535	581	590	[52]
ρ_{enc}	kg/m^3	8238	8238	8238	[52]

Table 3.2: Insulation thicknesses for laboratory-scale storage (in mm, x is defined in Fig. 3.1).

Position	Microtherm®	Felt	Rockwool
$1405 < x$	–	160	–
$775 < x < 1405$	20	40	100
$425 < x < 775$	–	60	100
$x < 425$	–	50	–

and discharged from the bottom with air at room temperature (20 °C). Compared to previously reported experiments [51], more thermocouples and additional insulation were used and the air temperature at the top of the storage was measured with a shielded thermocouple.

The packed bed consisted of rocks such as limestone, gabbro, quartzite, and sandstone. The mean diameter of the rocks was 32 mm. The total mass of the rocks was $m_{\mathrm{rocks}} = 245$ kg. Additional properties are given in [22, 51]. The PCM was encapsulated in steel tubes (AISI 316) with an inner diameter of 16 mm and a wall thickness of 1 mm (see Fig. 5 in [51]). Four bundles of 17 tubes each were stacked at angles of 45°. The total masses of the PCM and encapsulation were $m_{\mathrm{pcm}} = 9.27$ kg and $m_{\mathrm{enc}} = 13.17$ kg, respectively. The specific area per storage volume was $a_{\mathrm{enc}} = 103.45$ m^2/m^3. The heat capacities and densities of the PCM and the encapsulation are summarized in Table 3.1. The temperature-dependent thermal conductivity of the encapsulation is given in [52] and the thermal conductivity of AlSi$_{12}$

Table 3.3: Material properties for laboratory- and industrial-scale storages. Ranges indicate temperature-dependent properties.

Material	c [J/kgK]	ρ [kg/m^3]	k [W/mK]	Source
Steel AISI 304	468-591	7900	14.6-23.5	[52]
Microtherm®	1020	250	0.025-0.038	[77]
Felt	1000	130	0.055-0.157	[78]
Rockwool	840	100	0.038	[79, 80]
UHPC	500	2500	1.63-2.19	[81]
LDC	663	1500	0.37-0.66	[81]
LWC	663	850	0.244	[81, 82]
Foamglas®	840	120	0.05	[81]
Soil	1840	2050	0.5	[52]

was $k_{\mathrm{AlSi_{12}}} = 160$ W/mK [74]. The heat of fusion of AlSi$_{12}$ was measured to be $h_{\mathrm{fus}} = 466$ kJ/kg with a melting range of $\Delta T_{\mathrm{fus}} = 4$ K [51]. In Table 3.1, the specific heat capacity of AlSi$_{12}$ within the melting range is reported as the pseudo specific heat capacity $h_{\mathrm{fus}}/\Delta T_{\mathrm{fus}}$.

The tank was made of 3 mm thick stainless steel (AISI 304) and insulated with Microtherm®, felt, and rockwool. The insulation thicknesses are given in Table 3.2 and thermal conductivities, heat capacities, and densities are given in Table 3.3. The values of the temperature-dependent properties are listed for the range of applied temperatures. Two 20 mm thick steel plates perforated with 221 circular holes of 10 mm diameter were used to homogenize the flow at the top and bottom of the storage.

The positions of the K-type NiCr-Ni thermocouples are marked by circles and crosses in Fig. 3.1. Because of the high temperatures, a radiation correction was applied to the air inflow temperature measured by a shielded thermocouple [83]. The emissivity of the thermocouple was approximated by $\varepsilon_{\mathrm{tc}} = 0.7$ [84] and the convective heat-transfer coefficient h_{tc} was determined from a correlation [85] in which Re$_{\mathrm{tc}}$ was based on the thermocouple diameter $d_{\mathrm{tc}} = 1.5$ mm.
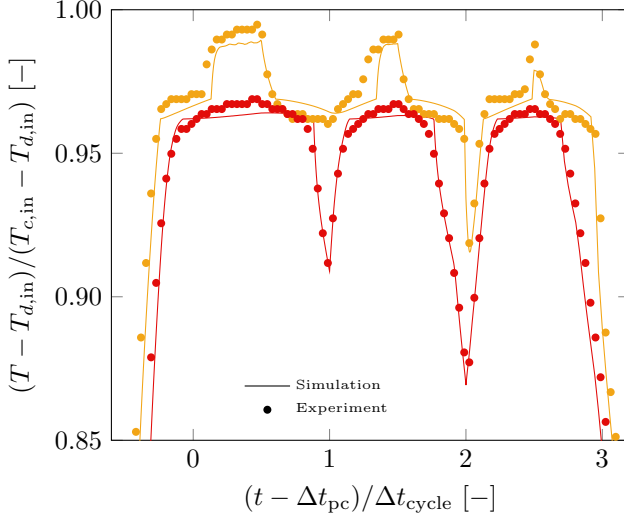
Figure 3.2: Comparison of simulated and measured PCM temperatures as a function of time for three charge-discharge cycles of the laboratory-scale combined storage.

3.2.2 Comparison of experimental and numerical results

The measured insulation temperatures at the height of the topmost PCM row at four radial positions, see Fig. 3.1, were used as boundary conditions for the simulation. In the energy equation for the topmost PCM row, the radiative power emitted by the perforated plate was included,

$$Q_{\text{top,rad}} = \frac{\sigma A_{\text{plate}} \phi_{\text{plate}}}{1/\epsilon_{\text{plate}} + 1/\epsilon_{\text{enc}} - 1} \big(T^4_{\text{plate,bottom}} - T^4_{\text{enc},1} \big),$$

where $\phi_{\text{plate}} = 0.858$, $T_{\text{plate,bottom}}$ was measured during the experiment, and $\epsilon_{\text{plate}} = 0.79$ for steel oxidized at 593 °C [86].

Because the ratio of tank diameter to mean rock diameter was only 12.3, a bypass fraction of 7.5% was used in the model of the sensible-heat section. This value was derived from two-dimensional simulations of the same tank filled only with rocks of the same properties as used during the experiments.
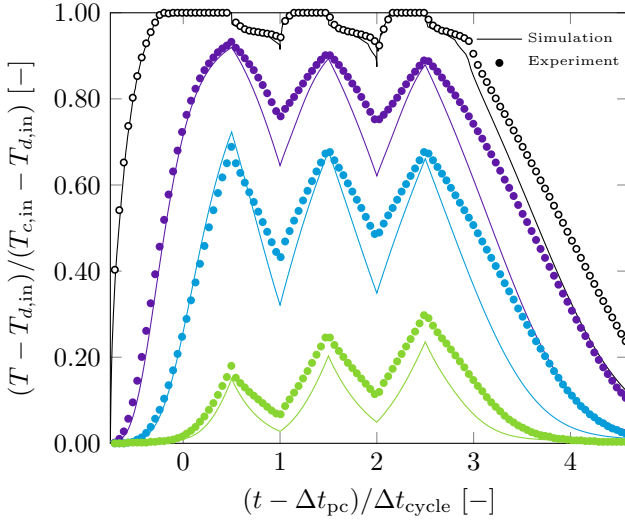
Figure 3.3: Comparison of simulated and measured rocks and air temperatures as a function of time for three charge-discharge cycles of the laboratory-scale combined storage.

In the presented experimental results, the storage was pre-charged for $\Delta t_{\text{pc}} = 2.26$ h to better represent steady-cycling conditions. A complete cycle took $\Delta t_{\text{cycle}} = 3$ h with equal charging and discharging durations.

In Figs. 3.2 to 3.4, the non-dimensional temperatures predicted by simulations for the latent section, the sensible section, and the structure and insulation are compared to measurements for three charge-discharge cycles. The colors correspond to the thermocouple positions indicated by the colored symbols in Fig. 3.1. Given the simplicity of the model, the agreement is considered to be good, in particular for the temperatures in the latent section and the air temperature above the latent section. These temperatures indicate clearly that the air outflow temperature during discharge can be stabilized.

A comparison of the simulated and measured thermoclines as a function
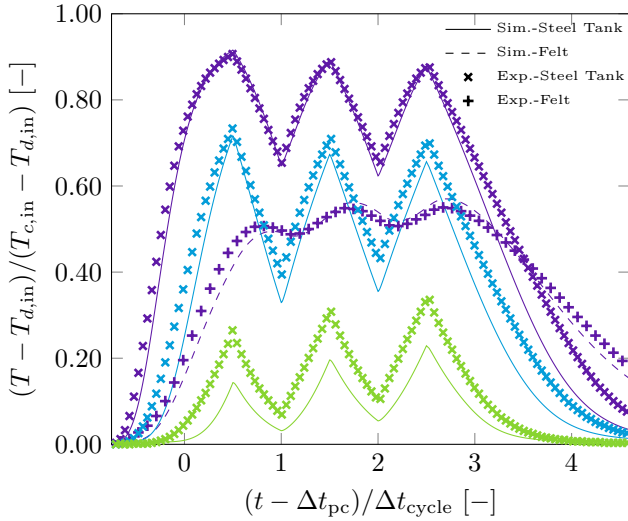
Figure 3.4: Comparison of simulated and measured tank and insulation temperatures as a function of time for three charge-discharge cycles of the laboratory-scale combined storage.

of the axial coordinate and time during one charge-discharge cycle is presented in Fig. 3.5. The shaded region corresponds to the latent section of the storage and the dashed vertical line indicates the PCM melting temperature. The measurements show that radial temperature gradients are non-negligible because of the small ratio of tank diameter to mean rock diameter. Nevertheless, the one-dimensional model agrees well with the measurements, particularly during charging. Because radial gradients diminish for increasing storage diameters, one-dimensional simulations are expected to be more accurate for industrial-scale storage units.
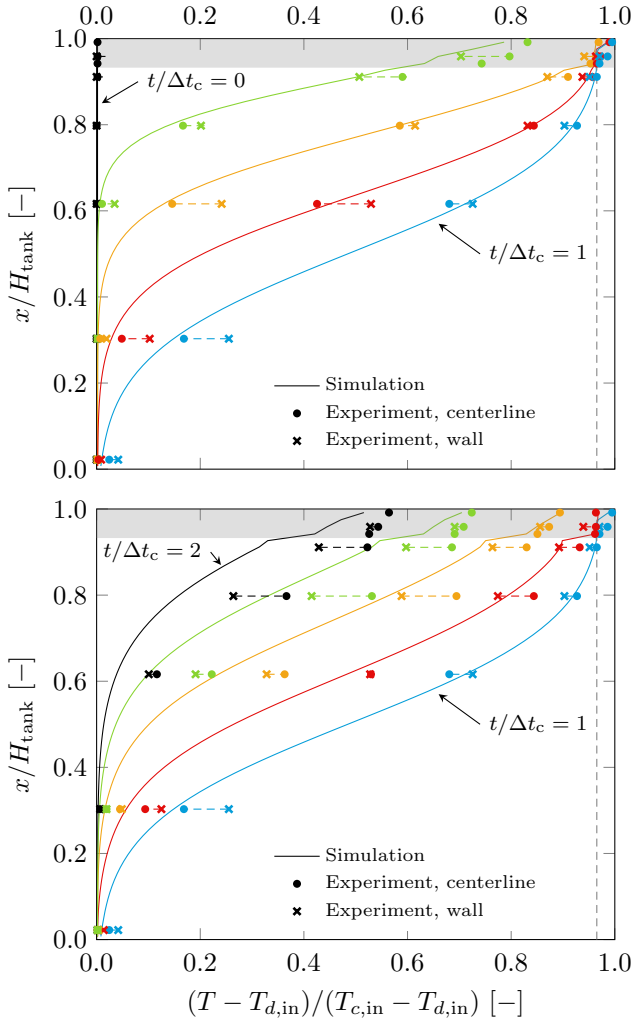
Figure 3.5: Comparison of simulated thermocline with measured centerline and wall temperatures as a function of axial position at selected times during charging (top) and discharging (bottom) for the laboratory-scale combined storage. The shaded region indicates the latent section and the dashed vertical line corresponds to the PCM melting temperature.

3.3   Efficiency and cost assessment

3.3.1   Reference configurations and operating conditions

Combined sensible/latent storage is motivated by the stabilization of the outflow temperature during discharging and the potential for reducing material costs. With the model validated at the laboratory scale, attention was turned to using the model to assess the potential reduction in material costs for two industrial-scale storage units. The first was based on the industrial-scale packed-bed storage in Ait Baha, Morocco [87], which is shaped like a truncated hollow concrete cone with a height of 4 m and top and bottom diameters of 12 m and 10 m, respectively, and which provides an energy output of 23 MWh_{th} per cycle. The second unit was sized to have a discharging capacity of about 1000 MWh_{th}, similar to the molten-salt storage of the Andasol CSP plant [88]. This unit was assumed to be constructed as a truncated hollow concrete cone also. The cone angle was set to be identical to that for the Ait Baha storage. To avoid large decreases in the exergy efficiency due to pumping work, the ratio of height to mean diameter was chosen to be smaller than for the Ait Baha storage. Because the top diameter is limited to less than 40 m for construction reasons, the second storage unit was therefore split into three sub-units with a discharging capacity of 333 MWh_{th} each. The height of the sub-units was chosen such that the maximum and minimum outflow temperatures during charging and discharging, respectively, were similar to those of the Ait Baha storage, resulting in a height of 4.5 m. In the following, the above-described units are referred to as the reference configurations.

For each reference configuration, two storage concepts were compared: (1) a sensible-heat storage consisting of a packed bed of rocks and (2) a combined sensible/latent-heat storage consisting of a packed bed of rocks with encapsulated $AlSi_{12}$ on top of it. The mean diameter of the rocks was 32 mm. Spherical AISI 316 stainless steel shells with 30 mm inner diameter and 1 mm wall thickness were used as encapsulation. The void fractions of

the packed bed of rocks and encapsulated PCM were taken as 0.342 (average bulk void fraction given by [22]) and 0.37 [59], respectively.

The dimensions and operational parameters of the two reference configurations are listed in Table 3.4. The charging and discharging temperatures were adapted from the Ait Baha unit so that the charging temperature is well suited to the melting temperature of $AlSi_{12}$: If the charging temperature is too close to the melting temperature, the PCM melts insufficiently; conversely, if the charging temperature is much higher than the melting temperature, the PCM cannot stabilize the outflow temperature during discharging to be close to the charging temperature. For these reasons, the charging and discharging temperatures were set to 595 °C and 220 °C instead of 640 °C and 280 °C, respectively.

The CSP plant incorporating the storage units was assumed to be operated such that the air fed to the storage is always at the design outflow temperature of the solar field. To account for the variable solar input, the mass flow rate was ramped during charging and discharging in a sinusoidal manner over half an hour [25]. The charging, discharging, and idle times are those of the Ait-Baha plant. Up to 200 cycles were simulated to reach steady cycling conditions for each configuration.

The storage structure and insulation consisted of ultra-high performance concrete (UHPC), low-density concrete (LDC), light-weight concrete (LWC), Microtherm®, and Foamglas®, see Fig. 3.6. The concrete and insulation thicknesses listed in Table 3.5 are based on the storage unit at the Ait Baha plant. For simplicity, the same thicknesses were used for the simulations of both storage configurations. Due to the considerably higher price of Microtherm® compared to Foamglas®, see Table 3.6, Microtherm® was applied only in the upper quarter where Foamglas® would be heated beyond its upper limit of 480 °C. The storage units were assumed to be immersed in the ground and therefore conduction through 1.0 m of soil below and around the units were included in the simulation, see Section 2.2.4. Concrete, insulation, and soil properties are given in Table 3.3.

Table 3.4: Simulation parameters for comparison of industrial-scale sensible and combined storage configurations. For the Andasol storage unit, the charging and discharging mass flow rates are reported per sub-unit.

Quantity	Ait Baha	Andasol	Units
$E_{d,\text{net}}$	23	1000	MWh
$H_{\text{tank,ref}}$	4	4.5	m
$d_{\text{tank,top,ref}}$	12	36.25	m
$d_{\text{tank,bottom}}$	10	34	m
θ_{tank}	14	14	°
$\dot{m}_{c,\text{max}}$	6.3	132	kg/s
$\dot{m}_{c,\text{max}}$	15	132	kg/s
Δt_c	10	7	h
Δt_d	4.5	7	h
Δt_{idle}	9.5	10	h
$T_{c,\text{in}}$	595	595	°C
$T_{d,\text{in}}$	220	220	°C
T_∞	25	25	°C
η_{fan}	0.95	0.95	–
η_{Rankine}	0.35	0.35	–

Table 3.5: Thicknesses of structure and insulation layers in industrial-scale storage units (in m).

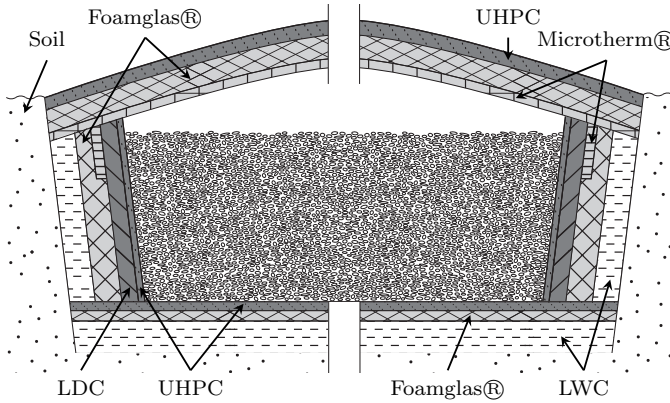|	UHPC	LDC	Microtherm®	Foamglas®	LWC
Cover	0.1	0.0	0.075	0.225	0.0
Wall	0.02	0.28	0.075/0.0	0.225/0.3	0.3
Bottom	0.05	0.0	0.0	0.05	0.45

Figure 3.6: Schematic of structure and insulation of the industrial-scale storages (not to scale).

3.3.2 Comparison and assessment strategy

The sensible and combined storage configurations described above were compared in terms of the normalized maximum outflow temperature drop during discharging,

$$\widetilde{\Delta T}_{d,\mathrm{max}} = \frac{T_{c,\mathrm{in}} - T_{d,\mathrm{out},\mathrm{min}}}{T_{c,\mathrm{in}} - T_{d,\mathrm{in}}}. \tag{3.1}$$

It should be noted that the sinusoidal decrease of the mass flow rate causes the outflow temperature to decrease considerably in the final few minutes of discharging. This final decrease in temperature was neglected because the energy extracted from the storage during this period is of the order of 0.1% of the total energy extracted during discharging.

For sensible-only storage, the temperature drop during discharging can be reduced by oversizing the storage. In the simulations, this was achieved by increasing the height, starting from the reference height given in Table 3.4. Because the cone angle was kept constant, the top diameter changed accordingly. The bottom diameter was kept constant. For the combined storage, the temperature drop during discharging can be reduced by increasing the

amount of PCM on top of the packed bed. In the simulations, an increase in the amount of PCM was compensated by a reduction of the height of the sensible section to keep the total storage height equal to the reference height.

Sensible and combined storage units with the same temperature drop during discharging were assessed in terms of their exergy efficiency and specific material costs. The exergy efficiency was defined as [89, pp. 312]

$$\eta_{\mathrm{ex}} = \frac{\Xi_{d,\mathrm{net}} - \Xi_{\mathrm{th,pump}}}{\Xi_{c,\mathrm{net}}}, \tag{3.2}$$

where $\Xi_{c,\mathrm{net}}$ and $\Xi_{d,\mathrm{net}}$ are the net exergies of the air supplied to the storage during charging and extracted from the storage during discharging, respectively, and $\Xi_{\mathrm{th,pump}}$ is the thermal exergy required for pumping for one charge-discharge cycle. The net exergy output during discharging was defined as

$$\begin{aligned} \Xi_{d,\mathrm{net}} &= \Xi_{d,\mathrm{out}} - \Xi_{d,\mathrm{in}} \\ &= \int_0^{\Delta t_\mathrm{d}} \dot{m} \big\{ h_g(T_{d,\mathrm{out}}) - h_g(T_{d,\mathrm{in}}) - T_0 \left[s_g(T_{d,\mathrm{out}}) - s_g(T_{d,\mathrm{in}}) \right] \big\} \, dt, \end{aligned} \tag{3.3}$$

where the reference state was taken as the ambient. An analogous definition holds for $\Xi_{c,\mathrm{net}}$. The specific entropy was calculated as a function of temperature based on values given by [52], neglecting entropy generation through pressure variations.

The electricity required for pumping was assumed to have been generated by the CSP plant, whose power block was assumed to be based on a Rankine cycle. The fraction of electricity required for pumping was calculated from [22],

$$\begin{aligned} f_{\mathrm{electric,pump}} &= \frac{W_{\mathrm{electric,pump}}}{W_{\mathrm{electric,tot}}} \\ &= \frac{1}{\eta_{\mathrm{Rankine}} E_{d,\mathrm{net}} \rho_g(T_{d,\mathrm{in}}) \eta_{\mathrm{fan}}} \int_0^{\Delta t_{\mathrm{cycle}}} \dot{m} \Delta p \, dt, \end{aligned} \tag{3.4}$$

where $E_{d,\mathrm{net}}$ is the net thermal energy extracted from the storage during discharging,

$$E_{d,\mathrm{net}} = E_{d,\mathrm{out}} - E_{d,\mathrm{in}} = \int_0^{\Delta t_d} \dot{m} \left[h_g(T_{d,\mathrm{out}}) - h_g(T_{d,\mathrm{in}}) \right] \, dt, \qquad (3.5)$$

which was assumed to be provided to the turbine without losses. The fan efficiency η_{fan} and Rankine cycle efficiency η_{Rankine} are given in Table 3.4 and are assumed to be constant. The fraction of the thermal exergy needed for pumping was assumed to be equal to the fraction of electricity needed for pumping, leading to

$$\Xi_{\mathrm{th,pump}} = f_{\mathrm{electric,pump}} \Xi_{d,\mathrm{net}}. \qquad (3.6)$$

The exergetic losses arising from thermal losses through the insulation (which is inherently reflected in $\Xi_{d,\mathrm{net}}$) were determined from

$$\Xi_{\mathrm{loss}} = \int_0^{\Delta t_{\mathrm{cycle}}} \int \left(1 - \frac{T_0}{T} \right) \delta Q_{\mathrm{loss}} \, dt. \qquad (3.7)$$

To estimate the material costs of a storage unit, the volume of each material shown in Fig. 3.6 was multiplied by its cost per unit volume, see Table 3.6. Specific material costs were then calculated as costs per net energy output per cycle, which was defined as

$$E_{\mathrm{out,cycle,net}} = E_{d,\mathrm{net}} - E_{\mathrm{th,pump}}, \qquad (3.8)$$

where $E_{\mathrm{th,pump}}$ is the additional thermal energy required to generate the electricity consumed by the pump, determined from

$$E_{\mathrm{th,pump}} = f_{\mathrm{electric,pump}} E_{d,\mathrm{net}}.$$

3.3.3 Results

The results presented below were obtained by increasing the height of the sensible storage units, starting from the reference height given in Table 3.4, or

Table 3.6: Material costs per unit volume, obtained from supplier quotes
and [90, 91].

Material	Cost [$/m^3]
UHPC	3421
LDC	737
LWC	188
Microtherm®	4269
Foamglas®	616
Rocks	66
AlSi$_{12}$	6015
Steel AISI 316L	25744

by adding encapsulated PCM for the combined storage units at constant total
storage height, and recording the computed $\widetilde{\Delta T}_{d,\mathrm{max}}$ under steady cycling
conditions. For the combined storage, there is a lower limit on $\widetilde{\Delta T}_{d,\mathrm{max}}$
because of the melting point of the chosen PCM, which lies 20 °C below
$T_{c,\mathrm{in}}$. There is also an upper limit, which is imposed by the required height
of the PCM being smaller than the diameter of the spherical encapsulation.
For all simulations, the maximum increase in $T_{c,\mathrm{out}}$ was found to be less
than 15%, which was considered to be acceptable for the purposes of this
study.

23 MWh$_{\mathrm{th}}$ Storage

Figure 3.7 shows a comparison of the outflow temperatures during discharging
for the sensible reference configuration and a combined storage with sufficient
PCM to limit the temperature drop to about 5%. Following an initial
reduction in which the PCM is cooled to its melting temperature, the
combined storage can deliver heat at an almost constant temperature for
the remainder of the discharging period.

    In Fig. 3.8, the steady cycling thermoclines of the sensible reference stor-
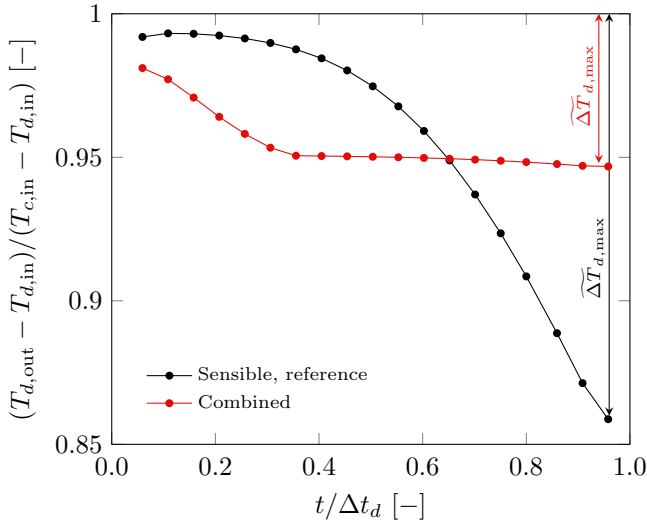
Figure 3.7: Steady cycling outflow temperature during discharging for the 23 MWh$_{\mathrm{th}}$ sensible-only reference storage and the combined storage with $\widetilde{\Delta T}_{d,\max} = 5\%$.

age, the combined storage and the sensible storage with doubled tank height are shown. The thermoclines are seen to occupy nearly the entire heights of the storages. This is in agreement with the analytical approximation of the steady cycling solution proposed by [64]. Nevertheless, the temperature drop during discharging as well as the temperature rise during charging are smaller with a larger sensible storage in comparison to the sensible reference storage. The combined storage reaches a significant decrease in the temperature drop during discharging with only a small amount of PCM and without increasing the storage volume.

The volumes of the sensible and combined storage units, normalized by the volume of the reference configuration, are compared in Fig. 3.9 as a function of the non-dimensional temperature drop during discharging. Here, 'volume' denotes the total volume that is occupied by the sensible and latent sections,
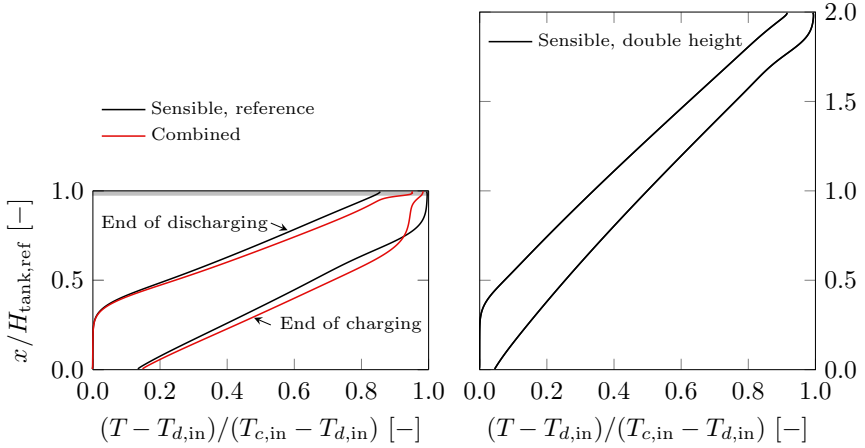
Figure 3.8: Steady cycling thermoclines at the end of charging and discharging for the 23 MWh$_{\text{th}}$ sensible-only reference storage and the combined storage with $\widetilde{\Delta T}_{d,\text{max}} = 5\%$ (left) and the sensible-only storage with doubled height (right). The shading indicates the latent section of the combined storage.

including the void space and, for the latent section, the encapsulation. For the combined storage, the total volume is constant: the height of the sensible section is reduced to compensate for an increase in the height of the latent section. It can be seen that with as little as 1% of encapsulated PCM by volume, the maximum temperature drop during discharging is approximately halved compared to the reference storage. Increasing the amount of encapsulated PCM reduces the drop further. The maximum temperature drop of the combined storage cannot be made arbitrarily small, however, because $T_{c,\text{in}} - T_{d,\text{out}} \approx T_{c,\text{in}} - T_{\text{fus}}$ is fixed by the operating conditions and the melting temperature of the PCM. For the sensible storage, the maximum temperature drop can be reduced by increasing the height and therefore the volume. Figure 3.9 shows that the volume increases are considerable: To reduce the maximum temperature drop from 15% to about
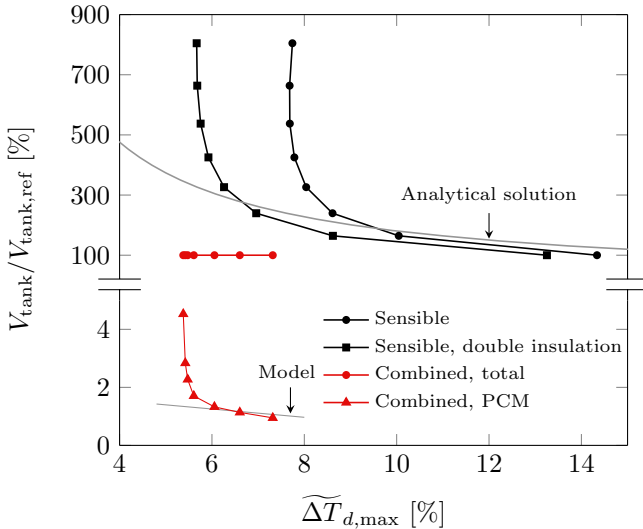
Figure 3.9: Storage volume and PCM volume as function of $\widetilde{\Delta T}_{d,\max}$ for the 23 MWh$_{\text{th}}$ storage. The model for the required PCM volume is described in [92].

8%, the storage volume must be nearly three times larger than that of the reference configuration. For drops below approximately 8%, further reductions are negligibly small because of growing thermal losses through the increasing storage surface area. As indicated by the figure, further reductions can be achieved by increasing the thickness of the insulation. The gray lines in Fig. 3.9 denote the estimated volume of the sensible storages using the analytical solution given by [64] and the estimated volume of the PCM in the combined storages calculated from the model described in [92], respectively.

The exergy efficiency as a function of the maximum temperature drop is presented in Fig. 3.10 for the sensible storage, the sensible storage with doubled insulation, and the combined storage. The reference configuration of the sensible storage attains an efficiency of about 96%. Reductions in the maximum temperature drop result in a significant decline in efficiency.
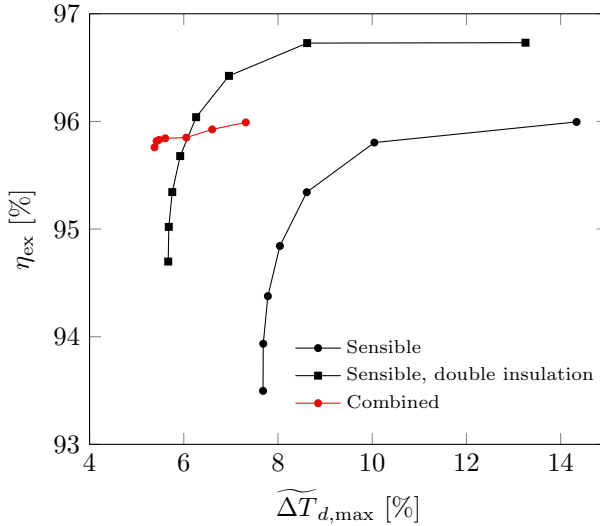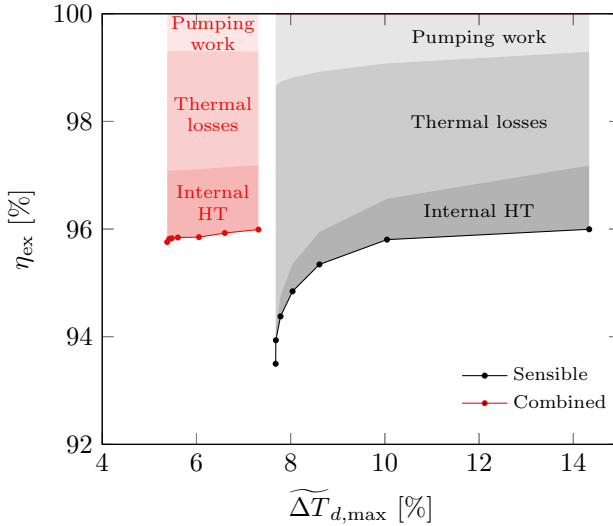
Figure 3.10: Exergy efficiency at steady cycling conditions as a function of $\widetilde{\Delta T}_{d,\max}$ for the 23 MWh$_{\text{th}}$ storage.

Doubling the insulation of the sensible storage is seen to increase the exergy efficiencies, but the significant decline for smaller temperature drops remains. By contrast, the exergy efficiency of the combined storage is only weakly dependent on the maximum temperature drop. Furthermore, the combined storage fulfills the target of 95% exergy efficiency by the U.S. Department of Energy's SunShot Initiative [23] independent of the maximum temperature drop.

In Fig. 3.11, the exergy losses due to pumping work, thermal losses, and internal heat transfer are plotted as a function of the maximum temperature drop during discharging for the sensible and the combined storages. The figure shows that the significant decrease in the exergy efficiency of the sensible storage for smaller temperature drops is caused by a large increase in the thermal losses and a smaller increase in the pumping work. The increased thermal losses are caused by the increased surface area of the

Figure 3.11: Exergy efficiency and exergy loss breakdown at steady cycling conditions as a function of $\widetilde{\Delta T}_{d,\max}$ for the 23 MWh$_{\text{th}}$ storage.

storage as the temperature drop decreases, see Fig. 3.9. The increased pumping work is a result of the increased height of the packed bed as the temperature drop decreases. Figure 3.11 also shows that for the combined storage, the pumping work, thermal losses, and internal heat transfer do not change significantly with the maximum temperature drop during discharging.

The material costs per net energy output over one cycle, see Eq. 3.8, is presented as a function of the maximum temperature drop during discharging in Fig. 3.12. Thanks to the smaller volumes, the estimated material costs for the combined configurations are lower than for the sensible configurations for a given temperature drop. In other words, although the costs per unit volume of the PCM and the encapsulation are considerably higher than those of the concrete and the insulation, see Table 3.6, the small volumes required by the PCM and encapsulation compensate for the higher costs per unit volume. Furthermore, it should be noted that the material costs of all combined
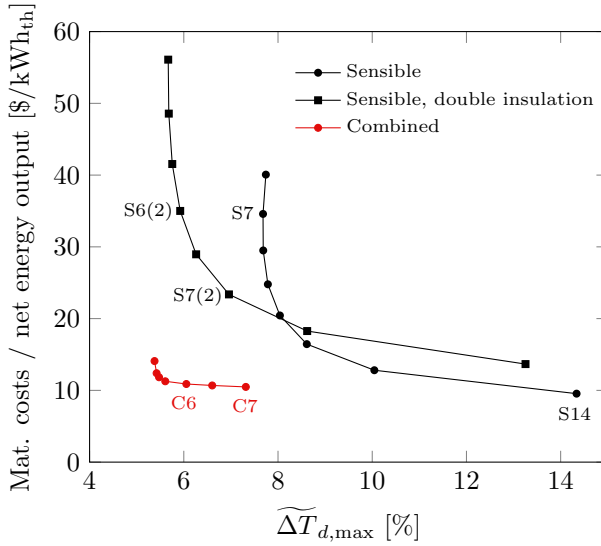
Figure 3.12: Storage material costs per net energy output of one cycle as a function of $\Delta T_{\mathrm{d,max}}$ for the 23 MWh$_{\mathrm{th}}$ storage.

storage configurations meet the SunShot Initiative target of \$15/kWh$_{\mathrm{th}}$ [23]. The fractional material costs for the configurations indicated in Fig. 3.12 are presented in Table 3.7. For all configurations, the costs are seen to be dominated by the concrete and insulation. The fractional cost of the latent-heat section does not exceed 13% for the two shown configurations.

1000 MWh$_{\mathrm{th}}$ Storage

Figure 3.13 presents the exergy efficiency and exergy-loss breakdown as a function of the maximum temperature drop during discharging. The exergy efficiency of the combined storage is again only weakly dependent on the temperature drop and above 96%. The exergy efficiency of the sensible storage is strongly dependent on the temperature drop and is lower than the efficiency of the combined storage irrespective of the temperature drop. The

Table 3.7: Fractional material costs in percent for the configurations in Fig. 3.12.

Configuration	Concrete	Insulation	Rocks	PCM	Encapsulation
S14	49.5	43.0	7.6		
S7	45.0	41.1	13.9		
S7(2)	33.2	59.5	7.3		
S6(2)	32.4	58.9	8.7		
C7	45.0	39.1	6.8	4.7	4.3
C6	43.5	37.8	6.6	6.4	5.8
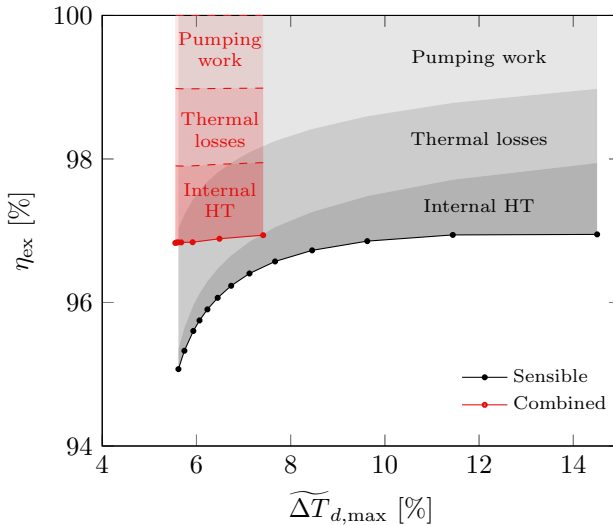
Figure 3.13: Exergy efficiency and exergy loss breakdown at steady cycling conditions as a function of $\widetilde{\Delta T}_{d,\max}$ for the 1000 MWh$_{\text{th}}$ storage.

significant decrease of the exergy efficiency of the sensible storage is seen to be caused by rapidly increasing pumping work.

The material costs per net energy output over one cycle are shown in
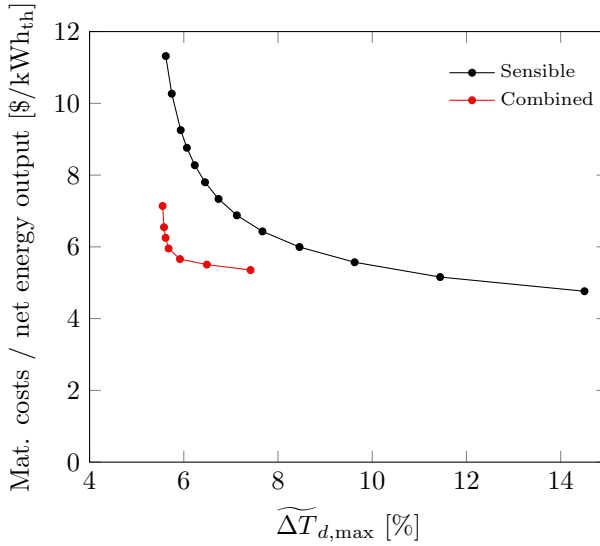
Figure 3.14: Storage material costs per net energy output of one cycle as a function of $\widetilde{\Delta T}_{d,\max}$ for the 1000 MWh$_{\text{th}}$ storage.

Fig. 3.14. The specific material costs for the combined storage are again lower than those of the sensible storage for a given maximum temperature drop during discharging, though the difference is not as pronounced as for the 23 MWh$_{\text{th}}$ storage. Furthermore, the specific material costs are not only smaller than $15/kWh$_{\text{th}}$, they are also lower than the estimated cost of $14/kWh$_{\text{th}}$ for the salt only in a two-tank molten-salt system, calculated from the salt mass for the Andasol storage and cost data from [18].

3.4 Conclusions

Combined sensible/latent heat storage based on a packed bed of rocks and steel-encapsulated AlSi$_{12}$ was investigated using an experimental-numerical approach. Exact solutions and experimental data from a 42 kWh$_{\text{th}}$ laboratory-scale combined storage were used to verify and validate an unsteady one-

dimensional heat-transfer model. The agreement with experimental data was good considering the radial gradients and bypass effects that are known to be less pronounced for larger-scale storages. Simulations of 23 MWh_{th} and 1000 MWh_{th} industrial-scale combined storages showed that exergy efficiencies are increased and that material costs can be reduced compared to sensible storages for a given maximum outflow temperature drop during discharging. The cost reduction is made possible by the small volumes of $AlSi_{12}$ required by the combined storages to reduce the temperature drop compared to the considerably larger volumes of rocks required by the sensible storages to reach the same temperature drop. The small volumes of $AlSi_{12}$ required thus compensate for its much larger cost per unit mass compared to the rocks. The total storage material costs were dominated by the costs of the insulation and the concrete. Exergy losses were found to be dominated by pumping and thermal losses, explaining why the exergy efficiencies of oversized sensible storages drop considerably in comparison with combined storages. The simulations indicated that the industrial-scale combined storages surpass the goals of the U.S. Department of Energy's SunShot Initiative of exergy efficiencies greater than 95% and material costs below \$15/kWh_{th}. Combined sensible/latent thermal energy storage is thus an attractive option to contribute to lowering the levelized cost of electricity produced by CSP plants.

An Assessment of Thermocline-Control Methods for Packed-Bed Thermal Energy Storage in CSP Plants[1]

4.1 Introduction

Concentrated solar power (CSP) plants with thermal-energy storage (TES) offer dispatchable electricity from intermittent solar energy and are therefore expected to play an important role in the future electricity-generation mix. To reduce the levelized cost of the electricity generated by CSP plants, efficient and cost-effective TES solutions are required. Two-tank molten-salt TES systems are currently the state-of-the-art [9]. In the last two decades, single-tank thermocline TES systems filled with a packed bed of low-cost

---

[1] Material in this chapter is to be submitted as L. Geissbühler, A. Mathur, A. Mularczyk, A. Haselbacher and A. Steinfeld, "An assessment of thermocline-control methods for packed-bed thermal-energy storage in CSP plants," *Solar Energy*, to be submitted for publication, 2018.

filler material have attracted significant interest because they cost less than two-tank systems [18, 19].

The lower costs of thermocline TES are accompanied by several challenges. It was stated in [23] that "the biggest technoeconomic challenge of thermocline TES systems is temperature degradation". Temperature degradation, also known as thermocline degradation, refers to the flattening of temperature gradients in the TES with successive charging-discharging cycles. Thermocline degradation has several negative consequences. One is an increase of the heat-transfer fluid (HTF) outflow temperature during charging relative to the inflow temperature during discharging and a decrease of the HTF outflow temperature during discharging relative to the inflow temperature during charging. The maximum changes in the HTF outflow temperatures can be expressed in non-dimensional form as

$$\Delta \widetilde{T}_{c,\text{out,max}} = \frac{T_{c,\text{out,max}} - T_{d,\text{in}}}{T_{c,\text{in}} - T_{d,\text{in}}} \,, \tag{4.1}$$

$$\Delta \widetilde{T}_{d,\text{out,max}} = \frac{T_{c,\text{in}} - T_{d,\text{out,min}}}{T_{c,\text{in}} - T_{d,\text{in}}} \,, \tag{4.2}$$

where $T_{c,\text{out,max}}$ is the maximum outflow temperature during charging, $T_{d,\text{out,min}}$ is the minimum outflow temperature during discharging, $T_{c,\text{in}}$ is the inflow temperature during charging, and $T_{d,\text{in}}$ is the inflow temperature during discharging. The maximum outflow temperature change during charging is typically constrained by temperature restrictions of other CSP plant components such as piping, pumps, valves, and the receiver [30, 93, 19]. Conversely, the maximum outflow temperature change during discharging is typically constrained by operating restrictions of the power block, in particular the desire for high efficiencies [94, 30, 93, 19].

Another negative consequence of thermocline degradation is a limited utilization factor, which is defined as [95, 96]

$$\zeta = \frac{\text{utilized storage capacity}}{\text{maximum storage capacity}} \,. \tag{4.3}$$

The smaller the utilization factor, the larger the specific material cost of the storage, i.e., the material cost per utilized capacity. Thermocline degradation

is thus seen to make a storage both less efficient and more expensive. The motivation for understanding the causes of thermocline degradation and finding methods to prevent it are therefore clear.

The causes of thermocline degradation are well known and include (1) limited convective heat transfer between the HTF and the storage material, (2) axial heat conduction and radiation in the storage, (3) heat exchange between the storage material/HTF and the storage container/insulation, (4) mixing of HTF at different temperatures due to vortical flows at the inlet/outlet, and (5) mixing of HTF at different temperatures due to bypass flows adjacent to the container wall.

Much research has focused on finding methods that reduce thermocline degradation or mitigate its negative consequences. While some research has been directed at decreasing the changes in the outflow temperatures, other research has been directed at increasing the utilization factor. These research directions are not independent because the utilization factor and the changes in the outflow temperatures are related. Figure 4.1 shows the utilization factor as a function of the maximum allowed change in the outflow temperatures, determined from simulations of a packed-bed storage that uses rocks as storage material and compressed air as HTF and has a maximum capacity of 1789 MWh$_{\text{th}}$. Clearly, the smaller the maximum allowed changes in the outflow temperatures, the smaller the utilization factor.

Methods that reduce thermocline degradation or mitigate at least some of its negative consequences can be classified as passive or active methods. Passive methods focus on the design of the storage, i.e., on its geometry and materials. Active methods, by contrast, focus on the operation of the storage, e.g., altering the flow of the HTF through the storage.

Passive methods include:

1. Increasing the height-to-diameter ratio of the storage while keeping its volume constant and/or increasing the heat-exchange surface area (e.g., by decreasing the particle diameter): This increases convective heat transfer and can decrease axial heat transfer at the expense of increased pumping work and increased thermal losses due to higher
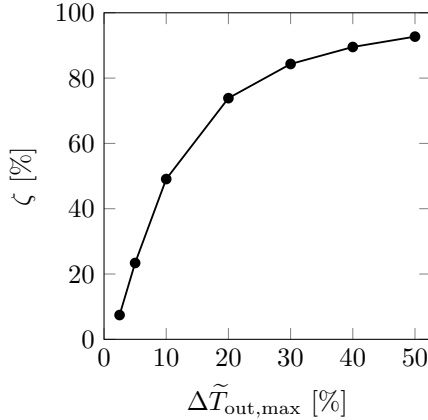
Figure 4.1: Simulated utilization factor ζ as a function of the maximum allowed change in outflow temperatures $\Delta \widetilde{T}_{\text{out,max}} = \Delta \widetilde{T}_{c,\text{out,max}} = \Delta \widetilde{T}_{d,\text{out,max}}$ for a packed-bed storage using rocks as storage material and compressed air as HTF and a maximum capacity of 1789 MWh$_{\text{th}}$. More information on the storage is provided in Section 4.3.1.

surface-to-volume ratios [67]. It should be noted that the storage height is usually limited for construction reasons [94].

2. Using phase-change materials (PCMs) at the top and/or at the bottom of the storage to stabilize the outflow temperatures [24, 25, 26, 97]: Although encapsulated PCMs are typically significantly more expensive than low-cost sensible storage materials, cost reductions are possible due to the small amounts of PCM required for temperature stabilization [97].

3. Cascaded latent storage [27, 28, 29, 71, 30, 98]: Using encapsulated PCMs that melt at different temperatures as filler materials can give higher utilization factors.

4. Cascaded thermochemical storage [31]: Using filler materials that react at different temperatures can result in high utilization factors. Material cyclability and cost can be issues.

Furthermore, the use of a floating barrier to separate hot and cold HTF was suggested [21, 99, 100, 101, 102, 103], but it is incompatible with the use of filler materials.[2] Increasing the height of the storage while keeping its diameter constant is also not considered as a method for decreasing the maximum changes in the outflow temperatures because it leads to a decrease of the utilization factor [97].

Active methods, which are called thermocline-control (TCC) methods in this thesis, include:

1. Flushing: Periodically, the storage is discharged completely, i.e., the thermocline is expelled during discharging. One drawback is that part of the energy expelled during flushing is at low temperatures and might therefore be unusable for the power block. In CSP plants, the low-temperature energy could be used to protect against freezing of HTFs such as molten salts or synthetic oils [93].

2. Segmented storage [104]: The packed bed is divided into multiple segments with ports between adjacent segments. The inlet port is switched to maintain thermal stratification in the case of variable inlet temperatures. During charging, ports whose temperature is higher than the inlet temperature are skipped. Similarly, during discharging, ports whose temperature is lower than the inlet temperature are skipped.

3. Sliding flow [105, 106, 33, 107]: The packed bed is divided into multiple segments that are charged successively. Once a given segment is charged, the inlet and outlet ports are changed to charge the next segment. Originally, this method was introduced to increase the exergy efficiency by partially decoupling the pressure drop from heat transfer, but it can also be used for TCC.

4. Extracting, upgrading, and returning [34]: The packed bed is again divided into multiple segments. The outlet port is switched and HTF is extracted at intermediate temperatures, upgraded, and returned to

---

[2]The barrier reduces axial radiative and conductive heat transfer. Achieving an effective seal between the storage walls and the barrier is challenging.

the top of the TES, leading to a local steepening of the thermocline.[3] This method is particularly interesting for CSP plants because if the extracted temperature is high enough the upgrade could be performed with thermal energy collected during periods of low insolation.

5. Siphoning [32]: HTF is extracted at the position of the thermocline through a port while hot and cold HTF are supplied simultaneously from the top and bottom of the storage, respectively. Similar to flushing, the energy extracted during siphoning is at an intermediate temperature and might therefore be unusable for the power block.

6. Using a thermochemical section at the top of the storage to control the outflow temperature [108]: The thermochemical storage material is encapsulated in tubes placed on top of the packed bed. By adjusting the pressure in the tubes, the heat released during discharging and therefore the outflow temperature of the HTF can be controlled.

This chapter aims at reducing the negative effects of thermocline degradation in a sensible-heat storage containing a packed bed of a low-cost filler material such as rocks. Because the attention is restricted to sensible-heat storage, the only passive method of avoiding thermocline degradation is to adjust the height-to-diameter ratio and/or increase the heat-exchange surface area. In the following, it is assumed that this method was applied during the design of the storage and that TCC is required to further improve the storage performance. To the best knowledge of the author, no systematic assessment of various TCC methods is available in the literature. Filling this gap in the literature is the main objective of this chapter. Because the flushing and siphoning methods lead to potentially unusable low-temperature thermal energy, this chapter focuses on assessing (1) the extracting, upgrading, and returning method, (2) a method based on injecting HTF, and (3) a new method based on mixing HTF streams.

The assessment is based on simulations of stand-alone storages as well

---

[3]We use "steepening" to indicate increases in the magnitude of the temperature gradient $|dT/dx|$, where x is the axial coordinate.

as storages integrated into a CSP plant. The simulations are carried out using the model presented in Chapter 2 that assumes one-dimensional temperature distributions in the packed bed and two-dimensional temperature distributions in the storage structure and insulation. The assumption of one-dimensional temperature distributions in the packed bed is justified for large-scale storage units without TCC. With TCC, the assumption may not be justified near the locations where HTF is injected or extracted. Therefore, the assessment presented in this chapter should be considered to be a first step in deciding which TCC methods merit further investigations. These investigations will require simulations using models with two- and/or three-dimensional temperature distributions as well as experiments.

The performance of the TCC methods applied to stand-alone storages is assessed at the quasi-steady state, i.e., the state in which the thermoclines at the ends of successive charging and discharging cycles become identical. For the storages integrated into a CSP plant, the performance of the TCC methods is assessed in terms of the annual electricity production of the plant.

4.2 Description of TCC methods

This section describes the three TCC methods that are assessed in this chapter. Because the assessment will consider a storage without TCC as a baseline, first a brief description of the operation of a thermocline storage without TCC is presented.

4.2.1 No TCC

The operation of a thermocline storage without TCC is depicted schematically in Fig. 4.2. In this and the subsequent schematic figures, the abscissa is the non-dimensional HTF temperature

$$\widetilde{T} = \frac{T - T_{d,\mathrm{in}}}{T_{c,\mathrm{in}} - T_{d,\mathrm{in}}} \tag{4.4}$$

and the ordinate is the non-dimensional axial coordinate $\widetilde{x} = x/H$, where H is the height of the storage. The dotted lines indicate $\widetilde{T}_{c,\mathrm{out,max}}$, the

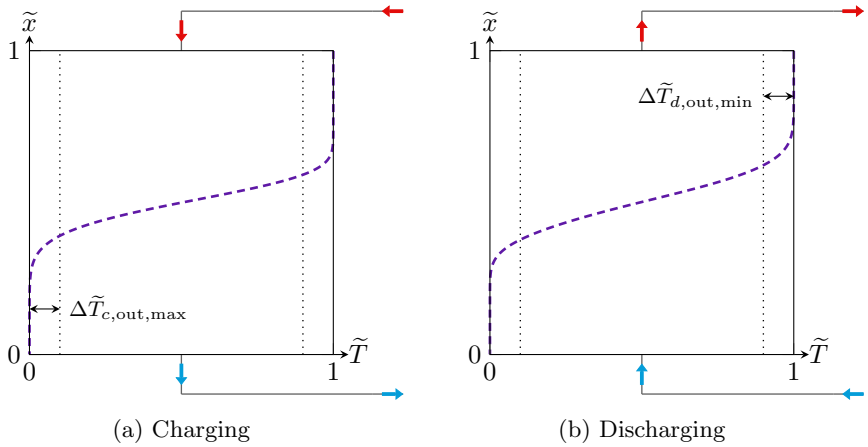(a) Charging   (b) Discharging

Figure 4.2: Schematic depiction of the operation of a thermocline storage without TCC during charging and discharging. The dashed purple lines represent the thermoclines halfway through the charging and discharging phases. The dotted lines indicate $\widetilde{T}_{c,\mathrm{out,max}}$, the maximum HTF outflow temperature during charging, and $\widetilde{T}_{d,\mathrm{out,min}}$, the minimum HTF outflow temperature during discharging. Red arrows indicate the flow direction of HTF with temperatures of $\widetilde{T} \geqslant \widetilde{T}_{d,\mathrm{out,min}}$. Blue arrows indicate the flow direction of HTF with temperatures of $\widetilde{T} \leqslant \widetilde{T}_{c,\mathrm{out,max}}$.

maximum non-dimensional HTF outflow temperature during charging, and $\widetilde{T}_{d,\mathrm{out,min}}$, the minimum non-dimensional HTF outflow temperature during discharging. The non-dimensional changes in the outflow temperatures defined by Eqs. (4.1) and (4.2) are also shown.

During the charging phase, the storage is supplied from the top with hot HTF, as indicated by the red arrows, at a temperature of $\widetilde{T}_{c,\mathrm{in}} = 1$. The thermocline represented by the dashed purple line moves downwards and cold HTF leaves the storage at the bottom, as indicated by the blue arrows. As long as the thermocline is not close to the bottom, the outflow temperature is close to $\widetilde{T}_{d,\mathrm{in}} = 0$. As the thermocline approaches the bottom, however, the outflow temperature begins to increase. The charging phase

is terminated when the increase in the outflow temperature reaches the specified limit of $\Delta \widetilde{T}_{c,\text{out,max}}$.

Conversely, during the discharging phase, the storage is supplied from the bottom with cold HTF at a temperature of $\widetilde{T}_{d,\text{in}} = 0$. The thermocline moves upwards and hot HTF leaves the storage at the top. As long as the thermocline is not close to the top, the outflow temperature is close to $\widetilde{T}_{c,\text{in}} = 1$. As the thermocline reaches the top, however, the outflow temperature starts to decrease. The discharging phase is terminated when the decrease in the outflow temperature reaches the specified limit of $\Delta \widetilde{T}_{d,\text{out,min}}$.[4]

4.2.2   Extracting Method

The first method investigated in this chapter is the extracting, upgrading, and returning method [34]; for brevity, it is referred to as the extracting method. It is assumed that the extracted HTF is upgraded in the receiver of the CSP plant and returned to the top of the storage.

The operation of the storage with the extracting method is explained in Fig. 4.3. To simplify the explanation, the attention is restricted to the case in which HTF is extracted through only one port that is located at the mid-height of the storage. The restriction to one port will be lifted in the assessment of the TCC methods in Section 4.3.

At the beginning of the charging phase, hot HTF is supplied to the storage at the top and extracted through the port, see Fig. 4.3(a). The black lines indicate the thermoclines produced by the extracting method just before port switching. The dashed purple lines show the thermoclines produced without TCC at the same instant. As soon as the HTF outflow temperature at the port reaches $\widetilde{T}_{c,\text{out,max}}$, the HTF outlet is switched from the port to the bottom, see Fig. 4.3(b). (If there are multiple ports, the

---

[4]In this description, we have assumed that the height and diameter of the storage are given and that the maximum allowed changes in the outflow temperatures determine the durations of the charging and discharging phases. If the durations of the charging and discharging phases are given instead, the maximum allowed changes in the outflow temperatures can be used to determine the height and diameter of the storage.
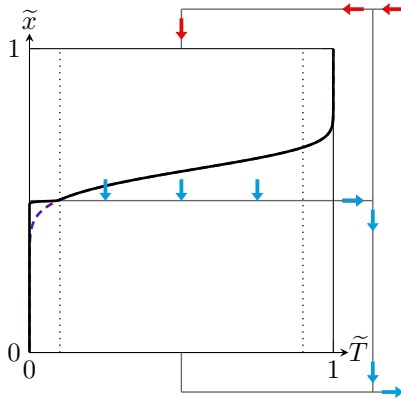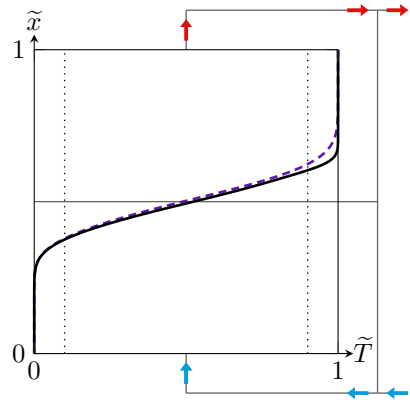
(a) Charging: before port switching
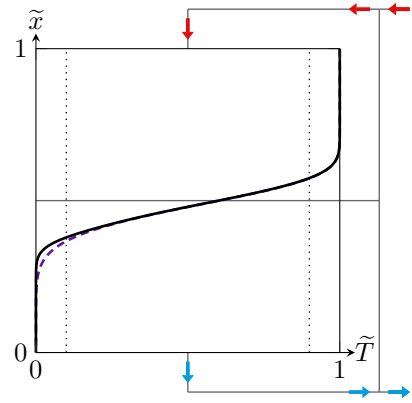
(b) Charging: after port switching
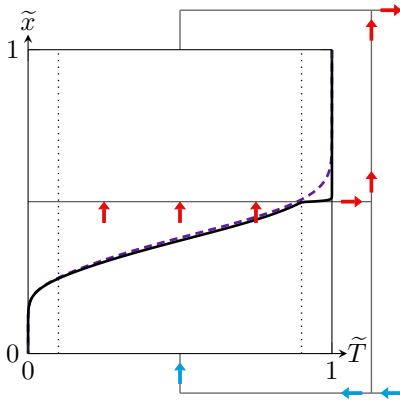
(c) Discharging: before port switching

(d) Discharging: after port switching

Figure 4.3: Schematic depiction of the operation of a thermocline storage with the extracting method using one port located at the storage mid-height. The left/right plots represent the thermoclines just prior to/after port switching. The black lines represent the thermoclines resulting from the extracting method at representative instants during the charging and discharging phases. The dashed purple lines represent the thermoclines without TCC at the same instants. The other lines and arrows are explained in the caption of Fig. 4.2.

outlet is switched to the port located immediately below that through which HTF is being extracted.)

The operation during the discharging phase is analogous. Cold HTF is supplied to the storage from the bottom and extracted through the port, see Fig. 4.3(c). Once the HTF outflow temperature at the port drops below $\widetilde{T}_{d,\mathrm{out,min}}$, the HTF outlet is switched to the top, see Fig. 4.3(d). (If there are multiple ports, the outlet is switched to the port located immediately above that through which HTF is being extracted.)

Comparing the black and dashed purple lines in Fig. 4.3 shows that the extracting method does indeed lead to a steepening of the thermocline, but also suggests that the impact of the method is limited. The limited impact is explained by the fact that the thermoclines shown in the figure represent simulation results during the first charging and discharging phases. As will be shown in Section 4.3, at the quasi-steady state the impacts of all the TCC methods investigated in this chapter are substantial.

4.2.3 Injecting Method

As implied by its name, the injecting method can be viewed as the opposite of the extracting method: Instead of extracting HTF, it is injected into the storage. The operation of the storage with the injecting method and one port is illustrated in Fig. 4.4, where the lines have the same meanings as in Fig. 4.3.

At the beginning of the charging phase, hot HTF enters the storage from the top and cold HTF leaves from the bottom as shown in Fig. 4.4(a) just as without TCC. When certain switching criteria that will be discussed below are fulfilled, the supply of hot HTF is switched from the top to the port, see Fig. 4.4(b), where the arrows indicate the flow of the HTF after switching. In Fig. 4.4(a) it can be seen that the HTF temperature at the port position is significantly lower than $\widetilde{T}_{d,\mathrm{out,min}}$. In Fig. 4.4(b), some time after switching, the HTF temperature at the port position has risen to $\widetilde{T}_{c,\mathrm{in}} = 1$.

The operation of the storage during the discharging phase is analogous. Prior to port switching, as indicated in Fig. 4.4(c), cold HTF enters the

(a) Charging: before port switching

(b) Charging: after port switching

(c) Discharging: before port switching
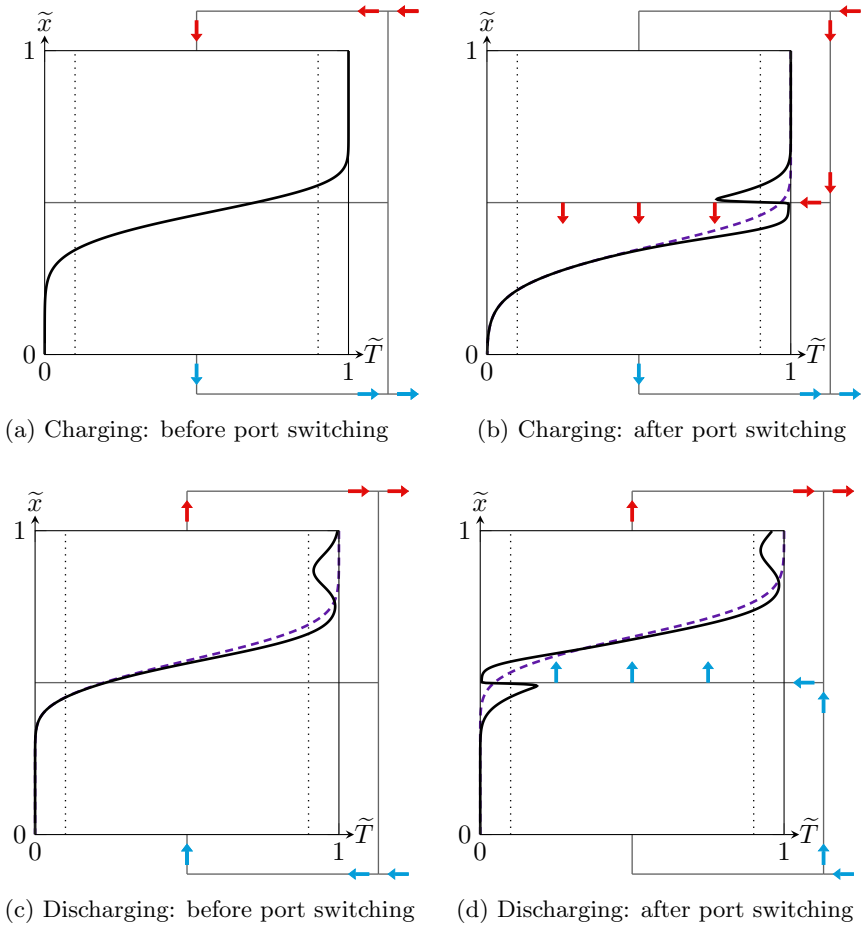
(d) Discharging: after port switching

Figure 4.4: Schematic depiction of the operation of a thermocline storage with the injecting method using one port located at the storage mid-height. The left/right plots represent the thermoclines just prior to/after port switching. The black lines represent the thermoclines resulting from the injecting method during the charging and discharging phases. The dashed purple lines represent the thermoclines without TCC at the same instants. The other lines and arrows are explained in the caption of Fig. 4.2.

storage from the bottom and hot HTF leaves at the top just as without TCC. When the switching criteria are satisfied, the supply of hot HTF is switched from the bottom to the port. Some time after switching, the HTF temperature at the position of the port has dropped to $\widetilde{T}_{d,\text{in}} = 0$, see Fig. 4.4(d).

Two observations can be made about Fig. 4.4(d). First, by comparing the black and dashed purple lines, it becomes clear that the injecting method leads to a steepening of the thermocline. Second, the thermocline exhibits an oscillation near the top of the storage. This oscillation is caused by switching the supply of hot HTF from the top to the port during the charging phase, see Fig. 4.4(b). Axial dispersion (due to limited convective heat transfer, conduction, and radiation) reduces the amplitude and increases the axial extent of the oscillation. As the oscillation approaches the top of the storage during discharging, $\widetilde{T}_{d,\text{out}}$ becomes oscillatory. It should be noted that during the charging phase that follows the discharging phase depicted in Fig. 4.4(d), $\widetilde{T}_{c,\text{out}}$ will be oscillatory also.

Ensuring that the amplitudes of the oscillations in $\widetilde{T}_{c,\text{out}}$ and $\widetilde{T}_{d,\text{out}}$ remain below $\Delta\widetilde{T}_{c,\text{out,max}}$ and $\Delta\widetilde{T}_{d,\text{out,min}}$, respectively, is the objective of the port-switching criteria. Finding effective port-switching criteria is not straightforward. The criteria used in this chapter are based on the ratio of two thermal energies between the current inlet and the proximate (downstream) port, where "inlet" refers to either the usual inlets at the top and bottom of the storage or a port. In the following, the axial positions of the current inlet and the proximate port are danoted by x_i and x_{i+1}. The first thermal energy is the actual thermal energy stored between the current inlet and the proximate port,

$$E_i(t) = \int_{x_i}^{x_{i+1}} A(x) \int_{T_{d,\text{in}}}^{T(x,t)} \left[(1 - \phi_s)\rho_f(\xi)c_{p,f}(\xi) + \phi_s\rho_s(\xi)c_s(\xi)\right] d\xi \, dx,$$

(4.5)

where $A(x)$ is the cross-sectional area of the TES, ϕ_s is the solid volume fraction of the packed bed, ρ_f is the density of the HTF, ρ_s is the density of the filler material, $c_{p,f}$ is the specific heat capacity at constant pressure
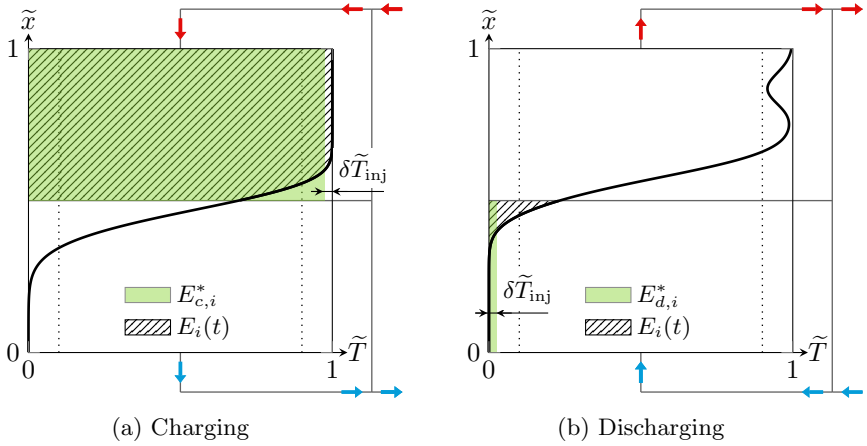
Figure 4.5: Schematic depiction of the port-switching criterion with the injecting method during charging (left) and discharging (right). The schematic shows the instant when the criterion is just met, i.e., when $E_i(t)/E_{c,i}^* = 1$ during charging and $E_i(t)/E_{d,i}^* = 1$ during discharging. Note that the highlighted areas correspond only qualitatively to the respective energies, see Eqs. (4.5), (4.6), and (4.8) for the precise expressions.

of the HTF, and c_s is the specific heat capacity of the filler material. The second thermal energy is the so-called threshold thermal energy. During the charging phase, the threshold thermal energy is defined as

$$E_{c,i}^* = \int_{x_i}^{x_{i+1}} A(x) \int_{T_{d,\mathrm{in}}}^{T_{c,\mathrm{in}}-\delta T_{\mathrm{inj}}} \left[(1-\phi_s)\rho_f(\xi)c_{p,f}(\xi)+\phi_s\rho_s(\xi)c_{p,s}(\xi)\right] \mathrm{d}\xi \, \mathrm{d}x,$$

(4.6)

where δT_{inj} is a specified temperature difference. The threshold energy can be interpreted as the net thermal energy between the temperatures $T_{d,\mathrm{in}}$ and $T_{c,\mathrm{in}}-\delta T_{\mathrm{inj}}$ stored in the volume between the current inlet and the proximate port. Using these two thermal energies, the port-switching criterion during the charging phase can be expressed as

$$\frac{E_i(t)}{E_{c,i}^*} \geqslant 1.$$

(4.7)

This criterion is illustrated in Fig. 4.5(a), where $E_i(t)$ and $E_{c,i}^*$ are indicated by the hatched and green areas, respectively. The black line shows the thermocline at the instant when the criterion is just met, i.e., when $E_i(t)/E_{c,i}^* = 1$.

Conversely, during the discharging phase the threshold energy is defined as

$$E_{d,i}^* = \int_{x_i}^{x_{i+1}} A(x) \int_{T_{d,\text{in}}}^{T_{d,\text{in}}+\delta T_{\text{inj}}} \left[(1-\phi_s)\rho_f(\xi)c_{p,f}(\xi) + \phi_s\rho_s(\xi)c_{p,s}(\xi) \right] \mathrm{d}\xi \, \mathrm{d}x \tag{4.8}$$

and the port-switching criterion is

$$\frac{E_i(t)}{E_{d,i}^*} \leqslant 1, \tag{4.9}$$

as illustrated in Fig. 4.5(b).

For constant cross-sectional area, densities, and specific heat capacities, Eqs. (4.7) and (4.9) simplify to $\overline{T}_i \geqslant T_{c,\text{in}} - \delta T_{\text{inj}}$ and $\overline{T}_i \leqslant T_{d,\text{in}} + \delta T_{\text{inj}}$, respectively, where $\overline{T}_i$ is the average temperature between x_i and x_{i+1}. In Eqs. (4.6) and (4.8), it was assumed for simplicity that the temperature differences δT_{inj} are identical. The value of δT_{inj} that results in a desired utilization factor depends on the rate of thermocline degradation and on the number of ports and must either be chosen a priori or be determined by simulations.

4.2.4 Mixing Method

The operation of the storage with the mixing method and one port during the charging phase is illustrated in Fig. 4.6. At the beginning of the charging phase, HTF is supplied to the storage from the top and extracted from the port, just like for the extracting method, see Fig. 4.6(a). The extracting and mixing methods differ once the temperature of the HTF extracted through the port exceeds $\widetilde{T}_{c,\text{out,max}}$. Rather than switching the outlet to the bottom of the storage, HTF is extracted simultaneously from the port

(a) Charging: before port switching

(b) Charging: after port switching

(c) Discharging: before port switching

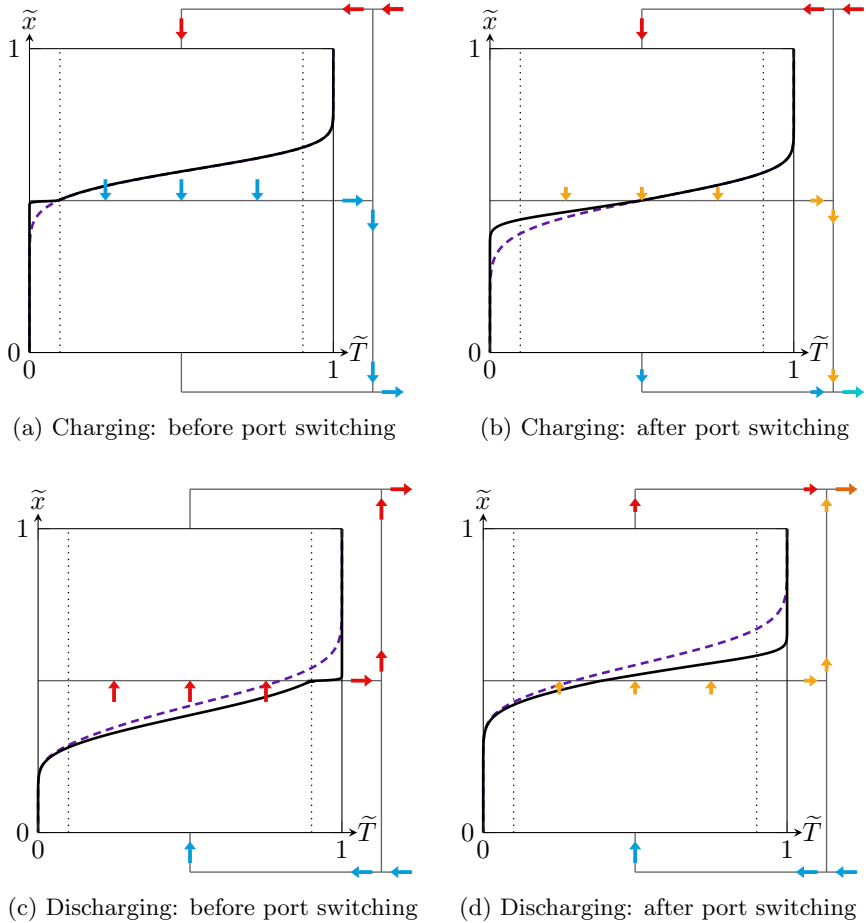(d) Discharging: after port switching

Figure 4.6: Schematic depiction of the operation of a thermocline storage with the mixing method using one port located at the storage mid-height. The left/right plots represent the thermoclines just prior to/after the port switching. The black lines represent the thermoclines resulting from the mixing method during the charging and discharging phases. The dashed purple lines represent the thermoclines without TCC at the same instants. Yellow arrows indicate the flow direction of HTF with temperatures of $\widetilde{T}_{c,\mathrm{out,max}} < \widetilde{T} < \widetilde{T}_{d,\mathrm{out,min}}$. The other lines and arrows are explained in the caption of Fig. 4.2.

and the bottom, see Fig. 4.6(b).[5] The two streams are mixed such that the temperature of the mixed HTF equals $\widetilde{T}_{c,\text{out,max}}$. For the case of only one port, the time-dependent mass flow rate at the bottom of the storage, denoted by $\dot{m}_{\text{bot}}(t)$, is determined from

$$\left(\dot{m}_{\text{top}} - \dot{m}_{\text{bot}}(t)\right) \int_{T_{\text{ref}}}^{T_{\text{ext}}(t)} c_{p,f}(\xi)\, d\xi + \dot{m}_{\text{bot}}(t) \int_{T_{\text{ref}}}^{T_{c,\text{out}}(t)} c_{p,f}(\xi)\, d\xi$$
$$= \dot{m}_{\text{top}} \int_{T_{\text{ref}}}^{T_{c,\text{out,max}}} c_{p,f}(\xi)\, d\xi,$$

where $\dot{m}_{\text{top}}$ is the mass flow rate supplied to the storage at the top and T_{ref} is an arbitrary reference temperature. If the specific heat is constant, one obtains

$$\frac{\dot{m}_{\text{bot}}(t)}{\dot{m}_{\text{top}}} = \frac{T_{\text{ext}}(t) - T_{c,\text{out,max}}}{T_{\text{ext}}(t) - T_{c,\text{out}}(t)}.$$

Because $\dot{m}_{\text{bot}}(t)/\dot{m}_{\text{top}} \leqslant 1$, the part of the thermocline below the port moves slower than that above the port, thereby contributing to the steepening of the thermocline as a whole.

During discharging with the mixing method, the storage is operated in an analogous manner, see Fig. 4.6(c) and (d). Instead of reducing the mass flow below the port, the mass flow above the port is reduced. Comparing the purple dashed and the black lines indicates that the mixing method steepens the thermocline.

If there are multiple ports, the two active outlets where HTF is extracted during charging are chosen as follows: The primary outlet is the one closest downstream of the thermocline and that has a temperature that is still below $T_{c,\text{out,max}}$. The secondary outlet is the one immediately upstream of the primary outlet, where $T \geqslant T_{c,\text{out,max}}$. If the secondary outlet would correspond to the inlet, then only the primary outlet is active. The criterion is defined analogously during discharging.

Note that for the mixing method that is assessed in this work, the inlet remains at the top/bottom during the entire charging/discharging phase.

---

[5] As for the other methods, if there are multiple ports, first the proximate port is used instead of that at the bottom.

To decrease the pressure drop, the inlet could be switched as well, similar to the injecting method.

4.2.5   Discussion

Combining the extracting and injecting methods would result in a method with some similarities to the sliding-flow method [109, 33, 106, 107]. There are several important differences between the sliding-flow method and a combined extracting/injecting method, however. First, the objective of the sliding-flow method is not to control the thermocline, but rather to reduce the pumping work and thereby achieve higher exergy efficiencies. Second, the port-switching criterion used in the sliding-flow method is based on the temperature rather than on the ratio of thermal energies as in Eqs. (4.7) and (4.9). Third, the sliding-flow method as described in [106] operates with two active ports that straddle an inactive port and fully charges the storage segment below the upper active port. Finally, and most importantly, it is unlikely that using a combined extracting/injecting method would further steepen the thermocline compared to using either the extracting or the injecting method. To see why, consider the thermocline shown in Fig. 4.4(b). If the thermocline in the subsequent discharging phase would be extracted as in Fig. 4.3(c), one would extract precisely that part of the thermocline that had been steepened in the previous charging phase, and thereby actually decrease the thermocline steepness.

4.3   Assessment of TCC for stand-alone TES

The three TCC methods are assessed using simulations of a stand-alone thermocline TES that is filled with a packed bed of rocks and operated with either molten salt at 1 bar or compressed air at 10 bar. The main advantages of using compressed air compared to molten salt are zero material costs and no temperature limitations [110]. The main disadvantages are thermophysical properties that result in reduced heat-transfer rates and increased pumping work [110].

The objectives of the assessment are (1) to assess the performance of the TCC methods with molten salt and compressed air at the quasi-steady state and for given maximum outflow temperature differences and (2) to determine how the performance of the TCC methods is affected as the number of ports is varied between one and three.

The assessment is performed using simulations with a heat-transfer model [97] that resolves the packed bed in one dimension and the structure and insulation in two dimensions and that was adapted for TCC as described in Appendix A.

4.3.1 TES geometrical and operational parameters

The same TES design is used for both molten salt (MS) and compressed air (CA), see Table 4.1. Instead of the conventional cylindrical shape, the TES is shaped like a truncated cone to reduce the normal forces between the walls and the rocks as they expand and contract during thermal cycling [22]. The height, which is typically limited for construction reasons, was chosen to be $H = 14$ m following the design of the storages used in the Andasol CSP plant [111]. The top and bottom diameters d_{top} and d_{bottom} follow from the wall angle, chosen to be $\theta = 14°$, and the maximum capacity. The maximum capacity with molten salt was chosen as $E_{max} = 2549$ MWh$_{th}$, based on the CSP plant design presented in Section 4.4.1. With compressed air, the maximum capacity was $E_{max} = 1789$ MWh$_{th}$. The rocks were assumed to have a diameter of $d_{rocks} = 2$ cm. The void fraction was taken to be a function of the axial coordinate following measurements [22].

The structure is made of stainless steel AISI 304, which was reported to have good resistance to corrosion by molten salt [112]. The insulation consists of Microtherm® and Foamglas®. The bottom of the storage is reinforced with light-weight concrete (LWC). The steel thickness, chosen following [113], and the insulation thicknesses are given in Table 4.2.

The TES was operated with charging and discharging temperatures of $T_c = 600°$C and $T_d = 300°$C. The mass flow rates during charging and discharging were equal to the rated mass flow rate of $\dot{m} = 594$ kg/s

Table 4.1: Geometrical and operational parameters of the TES.

Parameters	Quantity	Value	Units
Geometrical	H	14	m
	d_{top}	33.78	m
	d_{bottom}	26.80	m
	θ	14	°
	d_{rocks}	2	cm
Operational	$T_{c,\text{in}}$	600	°C
	$T_{d,\text{in}}$	300	°C
	T_{amb}	25	°C
	$\Delta \widetilde{T}_{c,\text{out,max}}$	10	%
	$\Delta \widetilde{T}_{d,\text{out,min}}$	10	%
	η_{pump}	95	%

Table 4.2: Thicknesses of structure and insulation layers of the TES (in m).

	AISI 304	Microtherm®	Foamglas®	LWC
Cover	0.04	0.3	0.2	0.0
Wall	0.04	0.1	0.3	0.0
Bottom	0.04	0.0	0.2	0.2

of the turbine in the CSP plant design presented in Section 4.4.1. The charging phase was terminated when the outflow temperature increased above the maximum charging outflow temperature $T_{c,\text{out,max}}$. Similarly, the discharging phase was terminated when the outflow temperature dropped below the minimum discharging outflow temperature $T_{d,\text{out,min}}$. In this assessment, the outflow temperatures variations were limited to $\Delta \widetilde{T}_{c,\text{out,max}}$ = $\Delta \widetilde{T}_{d,\text{out,min}}$ = 10%.

The temperature differences used in the port-switching criteria of the injecting method are listed in Table 4.3.

Table 4.3: Temperature differences used in port-switching criteria of the injecting method.

HTF	N_{ports} [−]	δT_{inj} [°C]	$\delta \widetilde{T}_{\text{inj}}$ [%]
	1	6	2
MS	2	7.5	2.5
	3	9	3
	1	9.75	3.25
CA	2	11.625	3.875
	3	13.5	4.5

4.3.2 Assessment criteria

The performance of the TCC methods at the quasi-steady state was assessed through three criteria. The first criterion is the storage utilization factor

$$\zeta = \frac{E_{\text{util}}}{E_{\text{max}}} , \qquad (4.10)$$

where E_{util} is the utilized energy in one charge-discharge cycle,

$$
E_{\text{util}} =
$$
$$
\int_0^H A(x) \int_{T_{d,\text{in}}}^{T(x,t_c)} \Big[(1 - \phi_s)\rho_f(\xi)c_{p,f}(\xi) + \phi_s\rho_s(\xi)c_{p,s}(\xi) \Big] \, \mathrm{d}\xi \, \mathrm{d}x
$$
$$
- \int_0^H A(x) \int_{T_{d,\text{in}}}^{T(x,t_d)} \Big[(1 - \phi_s)\rho_f(\xi)c_{p,f}(\xi) + \phi_s\rho_s(\xi)c_{p,s}(\xi) \Big] \, \mathrm{d}\xi \, \mathrm{d}x,
$$
$$(4.11)$$

where t_c and t_d are final times of successive charging and discharging phases, respectively, and where E_{max} is the maximum storable energy,

$$
E_{\text{max}} = \int_0^H A(x) \int_{T_{d,\text{in}}}^{T_{c,\text{in}}} \Big[(1 - \phi_s)\rho_f(\xi)c_{p,f}(\xi) + \phi_s\rho_s(\xi)c_{p,s}(\xi) \Big] \, \mathrm{d}\xi \, \mathrm{d}x.
$$
$$(4.12)$$

The second criterion is the cycle exergy efficiency, defined as [97]

$$
\eta_{\text{ex}} = \frac{\Xi_{d,\text{net}} - \Xi_{\text{th,pump}}}{\Xi_{c,\text{net}}} , \qquad (4.13)
$$

where $\Xi_{d,\mathrm{net}}$ is the net exergy recovered by the HTF during discharging, $\Xi_{c,\mathrm{net}}$ is the net exergy supplied by the HTF during charging, and $\Xi_{\mathrm{th,pump}}$ is the thermal exergy required for pumping. The net exergy recovered is

$$
\begin{aligned}
\Xi_{d,\mathrm{net}} &= \Xi_{d,\mathrm{out}} - \Xi_{d,\mathrm{in}} \\
&= \int_0^{\Delta t_d} \dot{m} \big\{ h_f(T_{d,\mathrm{out}}) - h_f(T_{d,\mathrm{in}}) - T_0 \left[s_f(T_{d,\mathrm{out}}) - s_f(T_{d,\mathrm{in}}) \right] \big\} \, \mathrm{d}t,
\end{aligned}
\tag{4.14}
$$

where T_0 is taken to be the ambient temperature T_{amb} given in Table 4.1, $\dot{m}$ is the mass flow rate, and h_f and s_f are the specific enthalpy and entropy of the HTF, respectively.[6] The net exergy supplied during charging is defined analogously. The specific entropy is assumed to depend only on the temperature,

$$
s_f(T) = \int_{T_0}^{T} c_{p,f}(\xi) \frac{\mathrm{d}\xi}{\xi} .
\tag{4.15}
$$

The calculation of $\Xi_{\mathrm{th,pump}}$ is described in [97]. It is important to note that the thermal exergy required for pumping includes only the pressure drop through the packed bed. The pressure drops through the ports, pipes, and valves required for the TCC methods are neglected in this first assessment.

The final criterion are the specific material costs,

$$
\text{specific material costs} = \frac{\text{storage material costs}}{E_{\mathrm{out,net}}} ,
\tag{4.16}
$$

where $E_{\mathrm{out,net}}$, the net output energy per cycle, is

$$
E_{\mathrm{out,net}} = E_{d,\mathrm{net}} - E_{\mathrm{th,pump}} ,
\tag{4.17}
$$

and where $E_{d,\mathrm{net}}$ is the net energy discharged per cycle and $E_{\mathrm{th,pump}}$, the thermal energy required for pumping, is computed following [97]. The net energy discharged per cycle can be expressed as

$$
E_{d,\mathrm{net}} = E_{\mathrm{util}} - E_{d,\mathrm{loss}} = \zeta E_{\mathrm{max}} - E_{d,\mathrm{loss}} ,
\tag{4.18}
$$

---

[6]In the mixing method, exergy is destroyed by the mixing of two HTF streams. This additional exergy destruction is taken into account by using the adiabatic mixing temperature for $T_{d,\mathrm{out}}$.

where it should be noted that $E_{d,\text{loss}}$, the thermal losses during discharging caused by heat transferred from the storage material to the lateral wall, the cover, and the lid, are typically negative because the walls are hotter than the storage material.

The storage material costs in Eq. (4.16) include the costs of the rocks, the HTF, as well as the storage structure and insulation. The costs of ports, pipes, valves, and sensors needed for TCC are excluded because the costs depend on the as yet unavailable detailed design. Cost data for rocks, insulation, and concrete are taken from [97], whereas for molten salt and steel cost data are taken from [114].

4.3.3 Results

Thermoclines and outflow temperatures

Figures 4.7 and 4.8 show the solid-phase thermoclines at the ends of the charging and discharging phases without TCC and with the three TCC methods for MS and CA, respectively. The thermoclines are shown for all cycles until the quasi-steady state is reached. For the TCC methods, the number of ports is given in parentheses after the method name and the port positions are indicated by triangles on the right border of each plot. For each TCC method, the thermoclines are shown for the number of ports that resulted in the highest utilization factor.

We make five observations. First, the figures show that the thermoclines are generally steeper for MS than for CA. This is attributed to the higher thermal conductivity of MS, leading to higher convective heat-transfer rates.[7] Second, for both MS and CA, the mixing method is seen to lead to the steepest thermoclines while no TCC leads to the shallowest thermoclines. Third, there is an asymmetry between the steepness of the thermoclines at

---

[7]The higher thermal conductivity of MS also leads to higher axial heat transfer rates, which in general decreases the steepness of the thermocline. However, this effect is smaller than the effect of the increased convective heat transfer rates because the effective conductivity is dominated by the thermal conductivity of the rocks.
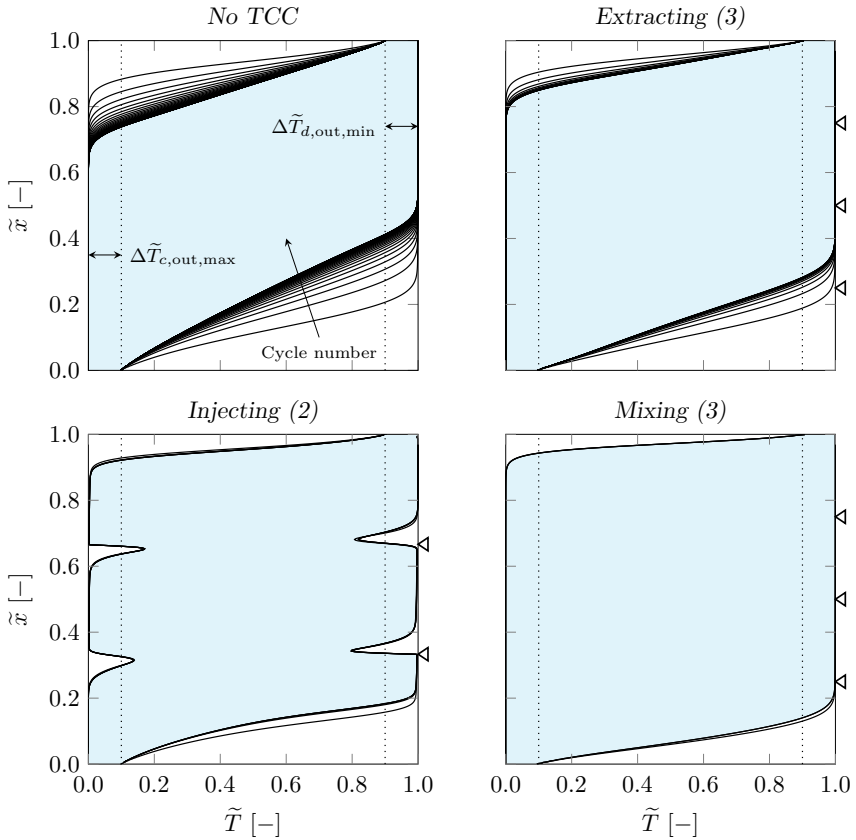
Figure 4.7: Thermoclines at the ends of charging and discharging phases until the quasi-steady state is reached for MS. The number of ports is given in parentheses after the method name and the position of the ports is indicated by triangles on the right border of each plot.

the top and at the bottom. This is attributed mainly to the truncated-cone shape of the TES and to the specific heat capacity of the rocks that increases with the temperature. Both lead to more energy being stored per unit height at the top than at the bottom and therefore to steeper thermoclines
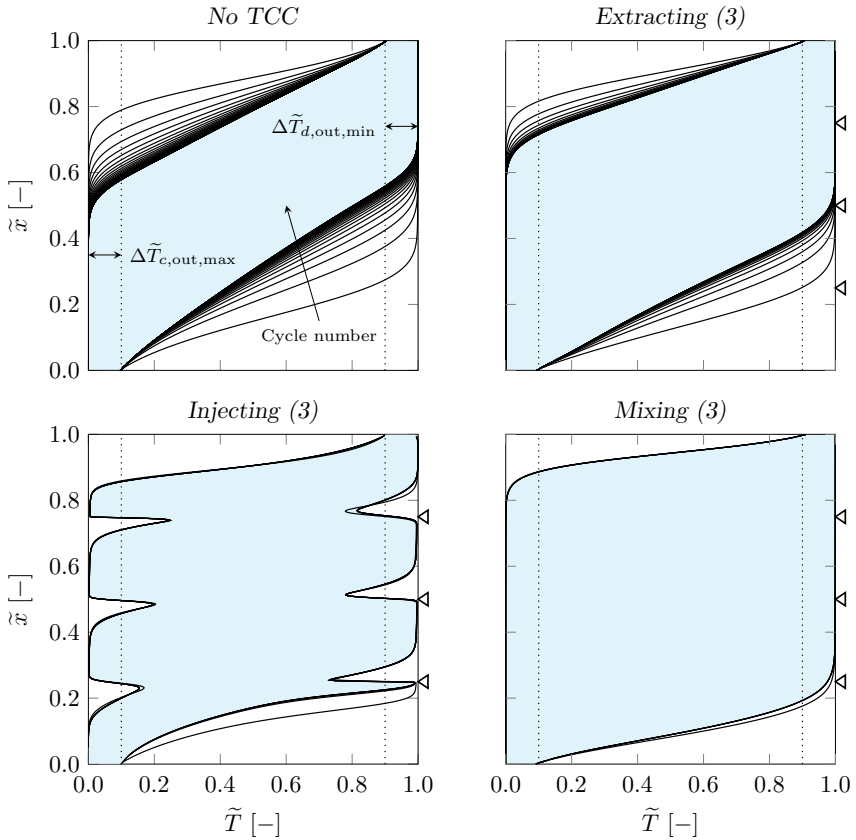
Figure 4.8: Thermoclines at the ends of charging and discharging phases until the quasi-steady state is reached for CA. The number of ports is given in parentheses after the method name and the position of the ports is indicated by triangles on the right border of each plot.

at the top. Fourth, the thermocline steepness decreases with cycling, as expected. Finally, the number of cycles required to reach a quasi-steady state is highest without TCC and lowest for the mixing method. To reach a quasi-steady state without TCC, 40 and 39 cycles are required with MS

and CA, respectively. For the mixing method with three ports, the quasi-steady state is reached after as few as two cycles. Requiring fewer cycles to reach the quasi-steady state could be an important advantage of using TCC methods in CSP plants because it suggests that the plants might approach their nominal electricity output more quickly if the TES was completely discharged following extended cloudy periods or plant shutdowns.

Figures 4.9 and 4.10 present the outflow temperatures during charging and discharging as a function of non-dimensional time for MS and CA, respectively. The non-dimensional time for charging/discharging is obtained by normalizing with the charging/discharging durations attained without TCC and the same HTF. Before listing separate observations for the three TCC methods, two observations are made that apply to all methods. First, the steeper thermoclines mean that the charging and discharging durations are longer with TCC than without it. The longest discharging durations are obtained by the mixing method with relative increases of 52% and 90% for MS and CA, respectively. Second, there is an asymmetry between charging and discharging. This is attributed to the different thermocline shapes at the top and bottom, as discussed above.

For the extracting method, Figs. 4.9 and 4.10 show clearly that port switching results in spikes in the outflow temperatures. These spikes will be damped by thermal losses and thermal inertias of pipes and valves as well as any heat exchangers that might be used in a power block. It is interesting to note that although the results shown were obtained with three ports, the outflow temperature shows only two spikes during discharging with MS and during charging and discharging with CA. This can be explained using Figs. 4.7 and 4.8. For example, for MS at the end of charging, the non-dimensional temperature at the bottommost port is already below $\widetilde{T}_{d,\text{out,min}}$. Therefore, at the start of the discharging phase, MS is extracted not through the bottommost, but directly through the second port, leading to only two spikes. A further observation can be made about the non-dimensional outflow temperature during charging, which becomes negative briefly due to thermal losses near the bottom of the storage. The part of the thermocline
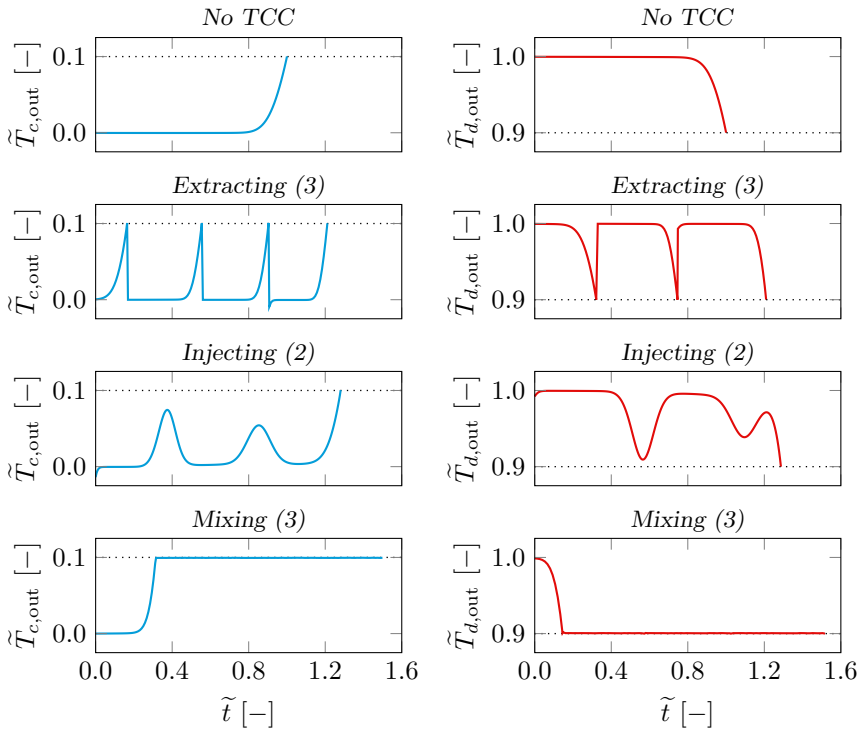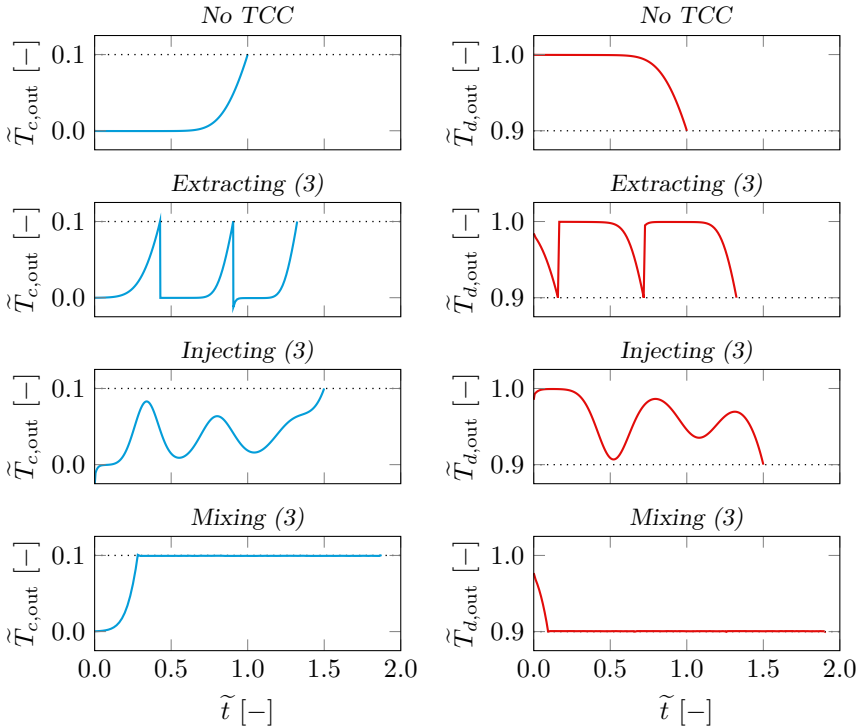
Figure 4.9: Outflow temperatures as a function of the non-dimensional time during charging (left) and discharging (right) phases at the quasi-steady state for MS. The dotted lines correspond to $\widetilde{T}_{c,\text{out,max}}$ and $\widetilde{T}_{d,\text{out,min}}$, respectively. The non-dimensional charging/discharging times are obtained by normalizing with the charging/discharging times attained without TCC, i.e., $\widetilde{t} = t/\Delta t_{\text{NC}}$ with $\Delta t_{\text{NC}} = \Delta t_{c,\text{NC}} = \Delta t_{d,\text{NC}} = 6.24$ h.

with negative non-dimensional temperatures is extracted once the outflow is switched to the bottom.

Figures 4.9 and 4.10 indicate that the injecting method leads to less pronounced spikes in the outflow temperatures than the extracting method.

Figure 4.10: Outflow temperatures as a function of the non-dimensional time during charging (left) and discharging (right) phases at the quasi-steady state for CA. The dotted lines correspond to $\widetilde{T}_{c,\text{out,max}}$ and $\widetilde{T}_{d,\text{out,min}}$, respectively. The non-dimensional charging/discharging times are obtained by normalizing with the charging/discharging times attained without TCC, i.e., $\widetilde{t} = t/\Delta t_{\text{NC}}$ with $\Delta t_{\text{NC}} = \Delta t_{c,\text{NC}} = \Delta t_{d,\text{NC}} = 4.66$ h.

Furthermore, the figures show that the non-dimensional outflow temperatures at the beginning of the charging phase are negative. The reason are thermal losses as discussed above for the extracting method.

For the mixing method, Figs. 4.9 and 4.10 demonstrate that the outflow

temperatures during charging and discharging rise and fall at the beginning of the charging and discharging phases, respectively. This is in contrast to the rise and fall of the outflow temperatures at the ends of the charging and discharging phases without TCC. Due to the asymmetric thermoclines, the temperature limit during discharging is reached sooner than that during charging.[8]

The detailed operation of the mixing method is illustrated in Fig. 4.11, which shows the non-dimensional temperatures (solid lines) and mass flow rates (dashed lines) for the top and bottom inlet/outlet and the three ports as a function of the non-dimensional time during charging (left) and discharging (right) for CA. The ports are numbered from top to bottom. For simplicity, the temperatures and mass flow rates are only shown if the corresponding inlet/outlet is active. The blue and red backgrounds indicate that a given outlet is active as a primary outlet during charging (with $\widetilde{T}_{\text{ext}} < \widetilde{T}_{c,\text{out,max}}$) or discharging (with $\widetilde{T}_{\text{ext}} > \widetilde{T}_{d,\text{out,min}}$), respectively. The yellow background indicates that a given outlet is active as a secondary outlet. The figure shows clearly how the primary and secondary outlets are switched and the corresponding mass flow rates are controlled such that the temperature of the mixed outlet streams do not rise above $\widetilde{T}_{c,\text{out,max}}$ or fall below $\widetilde{T}_{d,\text{out,min}}$ during charging and discharging, respectively.

Utilization factor

Figure 4.12 shows the utilization factor as a function of the number of ports for MS and CA. Without TCC, the utilization factors are 65.4% and 49.0% for MS and CA, respectively. With TCC, the highest utilization factors of 90.8% and 85.1% for MS and CA, respectively, are obtained with the mixing

---

[8]It is possible to eliminate the rise and fall of the outflow temperatures produced by the mixing method by combining it with bypassing of the TES, see [115, pp. 160-162] and [116]. Bypassing is based on mixing the inflow and outflow streams to control the temperature of the mixed outflow stream. In combination with the mixing method, bypassing would need to be applied only at the beginning of the charging and discharging phases. In this study, bypassing by itself was not considered as it does not steepen the thermocline.
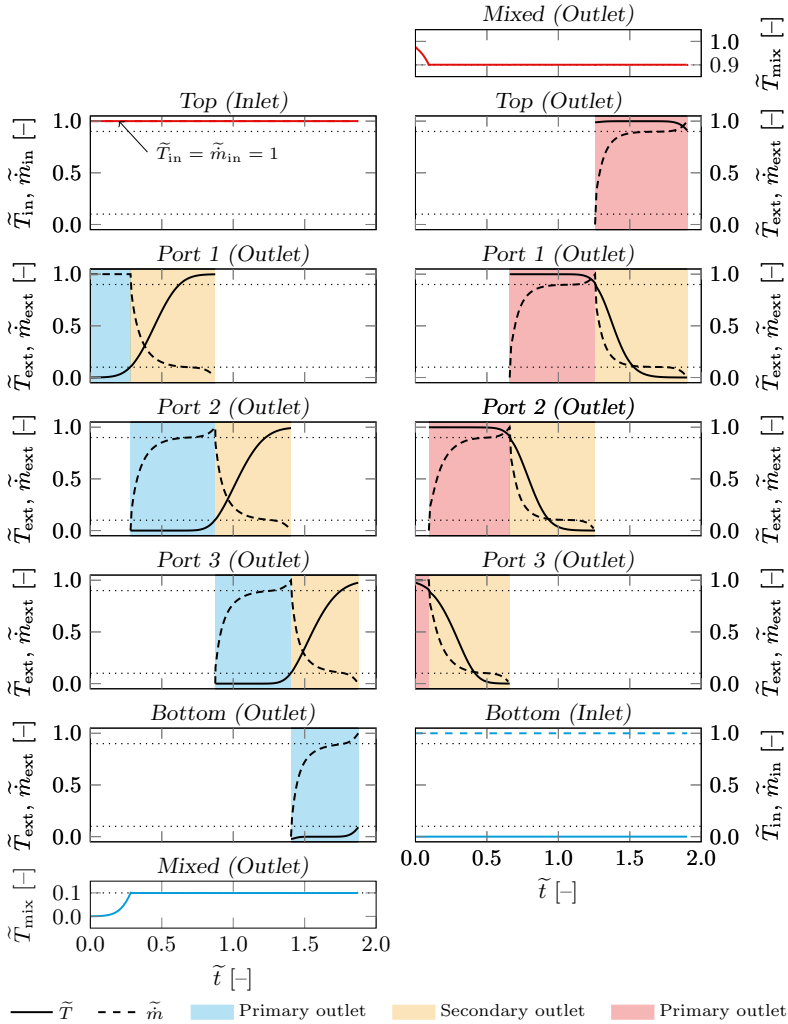
Figure 4.11: Inflow/outflow temperatures (solid) and mass flow rates (dashed) of the active inlets/outlets as a function of non-dimensional time during charging (left) and discharging (right) phases for the mixing method with three ports at the quasi-steady state using CA. The mass flow rate is normalized with the inlet mass flow rate: $\widetilde{\dot{m}} = \dot{m}/\dot{m}_{\text{in}}$.
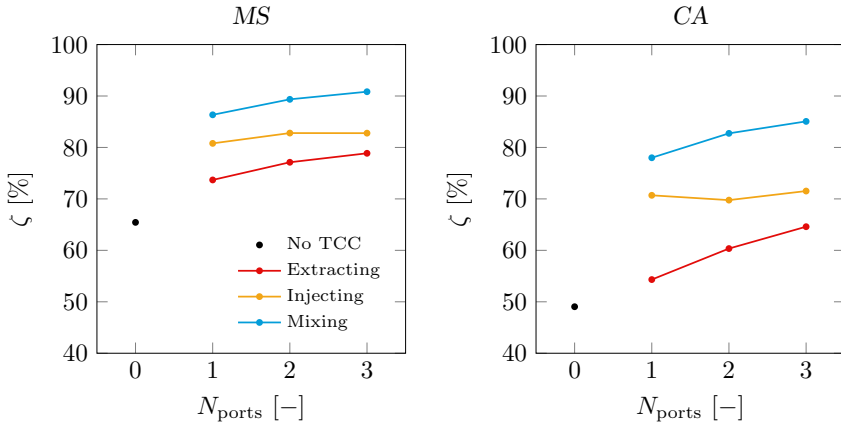
Figure 4.12: Utilization factor at the quasi-steady state as a function of the number of ports using MS and CA.

method and three ports. These utilization factors correspond to relative increases of 38.8% and 73.4% compared to no TCC, respectively.[9]

The figure also shows that the utilization factor increases with the number of ports for the extracting and mixing methods. For the injecting method, the trend is unclear, which is attributed to the fact that the temperature differences that were used in the port-switching criteria were not optimized for each port individually. As switching to the bottommost/topmost port is performed shortly before the end of the charging/discharging phase, the outflow temperature oscillations in the following discharging/charging phase that originate from switching to that bottommost/topmost port cannot be kept within the desired outflow temperature restrictions, leading to an earlier ending of the phase.

---

[9]Note that even higher increases of the utilization factor are expected if air at ambient pressure was used as HTF instead of CA. The reason is that with air at ambient pressure the rock diameter would have to be increased to avoid a significant efficiency penalty due to pumping, leading to shallower thermoclines without TCC and therefore a larger benefit from TCC.
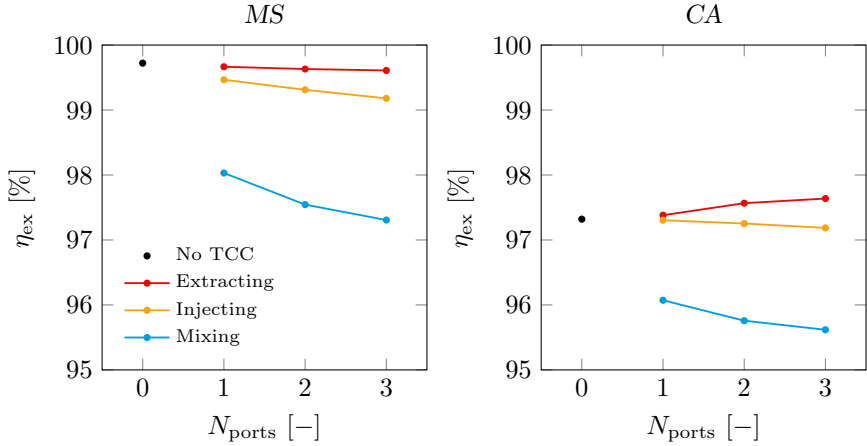
Figure 4.13: Exergy efficiencies as a function of the number of ports at the quasi-steady state using MS and CA.

Exergy efficiency

The exergy efficiencies of the TCC methods as a function of the number of ports are compared to the exergy efficiency without TCC for MS and CA in Fig. 4.13. The figure shows that the exergy efficiencies attained by the extracting and injecting methods are comparable to those obtained without TCC and that the mixing method attains the lowest exergy efficiencies. Furthermore, for a given method, the exergy efficiencies are seen to be lower for CA than for MS. Nevertheless, for all methods and both HTFs the exergy efficiencies meet the target of $\eta_{\mathrm{ex}} > 95\%$ set by the SunShot Initiative [23].

    The reasons for the differences in the exergy efficiencies are revealed in Fig. 4.14, which presents the exergy-loss fractions attributed to internal heat transfer, thermal losses through the insulation, pumping work, and mixing for the best-performing configurations of each TCC method.[10] Pumping work is seen to be the main reason for the lower exergy efficiencies attained

---

[10]The calculation of the exergy-loss fractions is explained in Appendix B.
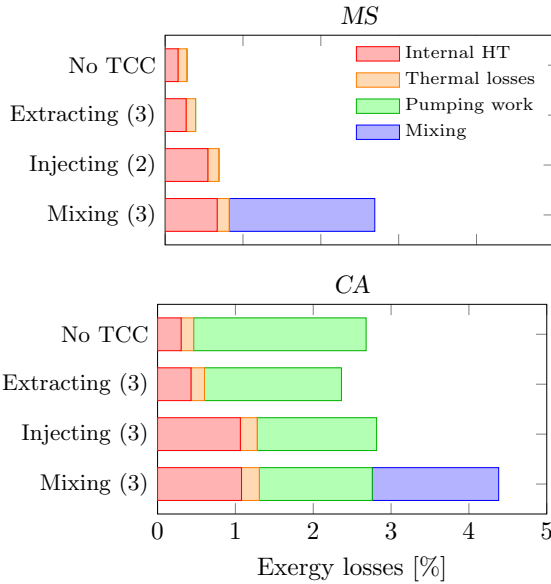
Figure 4.14: Exergy-loss breakdown at the quasi-steady state for MS and CA. For each HTF, four selected cases are shown. The number of ports is given in parentheses.

with CA. The exergy-loss fractions for CA show that the pumping work for all TCC methods is lower than that without TCC. The reason is that with TCC, the CA does not flow through the whole packed bed during the entire charging and discharging phases.

It is important to note that for all TCC methods, the fractional exergy loss due to internal heat transfer is higher than that without TCC. This is attributed to the steeper thermoclines and makes clear that reduced exergy efficiencies are a consequence of increased utilization factors. The increased exergy losses due to steeper thermoclines, together with the exergy losses caused by mixing of HTF streams, are why the mixing method has the lowest exergy efficiencies of all TCC methods.

A summary of the results for $\Delta \widetilde{T}_{\text{out,max}} = 10\%$ is given in Appendix C.

Effects of $\Delta\widetilde{T}_{\text{out,max}}$

The results presented so far were obtained for $\Delta\widetilde{T}_{\text{out,max}} = 0.1$ and have shown that TCC can provide greatly increased utilization factors at comparable or slightly reduced exergy efficiencies. In the following, we assess the performance of the mixing method with three ports for a greater range of maximum allowed outflow temperature differences.

Figure 4.15 shows that the effect of the mixing method on the utilization factor is more pronounced for smaller temperature differences because they result in shallower thermoclines without TCC. For example, for $\Delta\widetilde{T}_{\text{out,max}} = 2.5\%$, the mixing method increases the utilization factor by 331% and 744% for MS and CA, respectively, whereas for $\Delta\widetilde{T}_{\text{out,max}} = 10\%$, the increases are 38.8% and 73.4% for MS and CA, respectively. The figure also shows that for both MS and CA, the utilization factor attained by the mixing method for $\Delta\widetilde{T}_{\text{out,max}} = 2.5\%$ is larger than that without TCC for $\Delta\widetilde{T}_{\text{out,max}} = 10\%$. In other words, the mixing method allows higher utilization factors and smaller maximum allowed outflow temperature difference to be attained simultaneously.

The exergy efficiency increases with smaller allowed outflow temperature differences. For the mixing method with three ports, decreasing the maximum outflow temperature difference from $\Delta\widetilde{T}_{\text{out,max}} = 10\%$ to 2.5% increases the exergy efficiency from 97.3% to 99.2% and from 95.6% to 97.4% for MS and CA, respectively. The corresponding increases in the exergy efficiency without TCC are from 99.7% to 99.8% and from 97.3% to 97.4% for MS and CA, respectively.

Figure 4.16 shows the specific material costs as a function of the maximum allowed outflow temperature difference for no TCC and the mixing method with three ports for MS and CA, respectively. The mixing method is seen to lead to specific material costs that are nearly independent of the temperature difference, whereas without TCC the specific material costs rise sharply for small values of the temperature difference because of small utilization factors. The mixing method is therefore particularly cost-effective
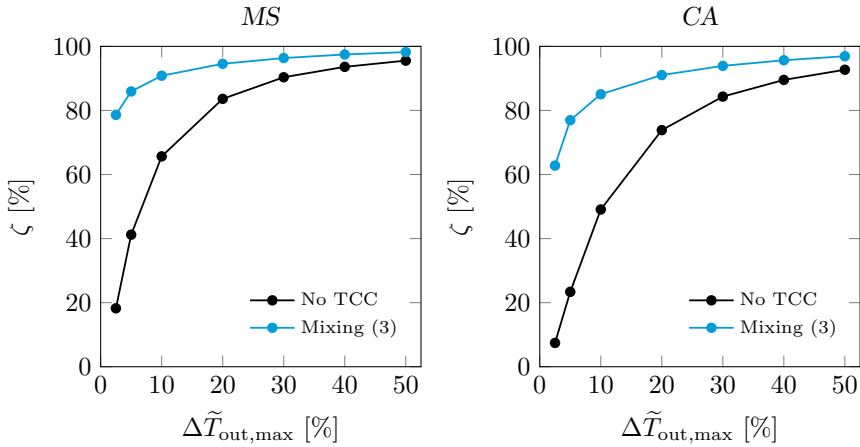
Figure 4.15: Utilization factor as a function of the maximum allowed outflow temperature difference $\Delta\widetilde{T}_{\mathrm{out,max}} = \Delta\widetilde{T}_{c,\mathrm{out,max}} = \Delta\widetilde{T}_{d,\mathrm{out,max}}$ for no TCC and for the mixing method with three ports at the quasi-steady state for MS and CA.

for small temperature differences. For instance, for $\Delta\widetilde{T}_{\mathrm{out,max}} = 2.5\%$, the specific material costs for the mixing method are as low as 5.6 \$/kWh$_{\mathrm{th}}$ and 5.0 \$/kWh$_{\mathrm{th}}$ for MS and CA, respectively.[11] These figures represent reductions by factors of about 8.5 and 4.3 compared to the corresponding costs without TCC.

The specific material costs attained by the mixing method can be compared to those for a conventional two-tank MS storage. Assuming two tanks of the same design as that used in this work, each filled with MS only, results in estimated material costs of 19.9 \$/kWh$_{\mathrm{th}}$. This shows that the mixing method applied to a packed bed of rocks is an attractive alternative to two-tank MS storage in that the mixing method can also provide constant MS

---

[11] Given that air has zero cost, it may be surprising that the specific material costs for CA are only slightly lower than for MS. The explanation is that the zero cost of air is outweighed by the smaller net energy output per cycle.
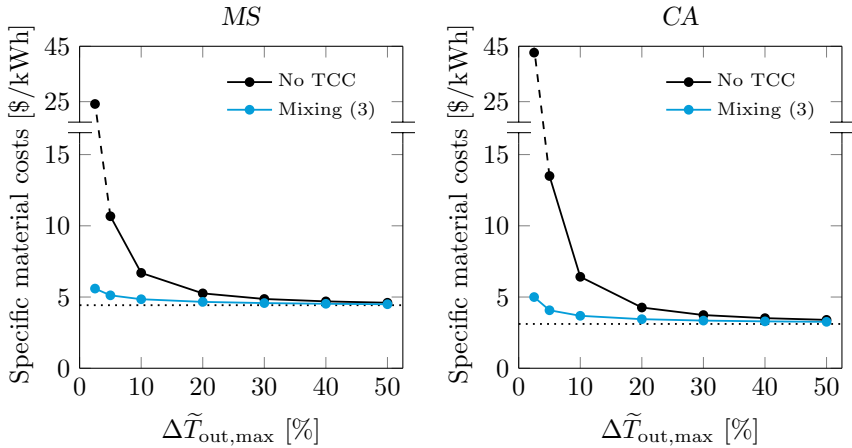
Figure 4.16: Specific material costs as a function of the maximum allowed outflow temperature difference $\Delta \widetilde{T}_{\text{out,max}} = \Delta \widetilde{T}_{c,\text{out,max}} = \Delta \widetilde{T}_{d,\text{out,max}}$ for no TCC and for the mixing method with three ports for MS and CA. The dotted lines correspond to the minimum possible material costs of 4.4 \$/kWh$_{\text{th}}$ and 3.1 \$/kWh$_{\text{th}}$ for MS and CA, respectively, based on assuming $E_{\text{out,net}} = E_{\text{max}}$.

outflow temperatures, albeit slightly different from the charging/discharging temperatures, but at significantly lower specific material costs.

4.4 Assessment of TCC for TES integrated into CSP plant

The assessment of TCC for a stand-alone TES has shown that significant increases in the utilization factor can be attained at the expense of relatively small decreases in the exergy efficiency. This positive result indicates that a more extensive assessment is warranted in which we investigate the effect of TCC for a TES that is integrated into a CSP plant. The investigation

is performed using annual simulations with a plant model that couples the previously described TES model with models of a power block and a receiver. The simulations assume MS as the HTF and use measured data for the direct normal irradiation (DNI).

The assessment includes a TES without TCC and those configurations of each TCC method that performed best for the stand-alone TES, namely the extracting method with three ports, the injecting method with two ports, and the mixing method with three ports. For comparison, the assessment includes also the mixing method with one port and a TES without TCC that is oversized by 37.5% in volume through an increase of its diameters.

In the following, the key components of the CSP plant are described and the operating conditions are specified. Thermal losses in the piping between the components are assumed to be negligible.

4.4.1 CSP plant model

Power block

The power block is assumed to operate on a Rankine steam cycle and is modeled following [117]. Hot MS is assumed to flow from the receiver or the TES to a heat exchanger in which superheated steam is generated. The superheated steam is expanded in a turbine to generate electricity. The MS is assumed to exit the heat exchanger at 300°C and to flow back to the receiver or the TES.

The Rankine cycle may be operated in either rated or derated mode. In rated operation, the MS coming from the receiver or the TES is at 600°C. Note that the MS temperature coming from the receiver is always at 600°C. The rated net generation rate is $\dot{W}_{\mathrm{el,rated}} = 109.8$ MW$_{\mathrm{el}}$ at a MS mass flow rate of $\dot{m}_{\mathrm{PB,rated}} = 594$ kg/s and a turbine efficiency of $\eta_{\mathrm{PB,rated}} = 40.5\%$.

Derated operation is allowed through sliding-pressure operation, which is needed when MS from the TES enters the heat exchanger at a temperature that is lower than 600°C. In this assessment, the minimum molten salt temperature leaving the TES during discharging is fixed at $\widetilde{T}_{d,\mathrm{out,min}} = 0.9$

or $T_{d,\text{out,min}} = 570°\text{C}$, which corresponds to the minimum derated operation of the power block. The parameters corresponding to the minimum derated operation are a net generation rate of 91.1 MW_{el}, a MS mass flow rate of 560 kg/s, and a turbine efficiency of 39.7%.

Receiver

A central receiver is used to collect solar energy. The solar multiple is SM = 2.7, which corresponds to a nominal power of

$$Q_{\text{rec,nom}} = \text{SM}\frac{\dot{W}_{\text{el,rated}}}{\eta_{\text{PB,rated}}} = 731 \text{ MW}_{\text{th}} . \tag{4.19}$$

Assuming a nominal solar irradiation of $I_{\text{nom}} = 1 \text{ kW/m}^2$, an annual receiver efficiency of $\eta_{\text{rec}} = 80\%$, an annual optical efficiency of $\eta_{\text{opt}} = 60\%,$[12] the required area of the solar field is

$$A_{\text{sf}} = \frac{Q_{\text{rec,nom}}}{\eta_{\text{rec}}\eta_{\text{opt}}I_{\text{nom}}} = 1.524 \text{ km}^2 . \tag{4.20}$$

The time-dependent power absorbed by the receiver is

$$Q_{\text{rec}}(t) = \eta_{\text{rec}}\eta_{\text{opt}}I(t)A_{\text{sf}} , \tag{4.21}$$

where $I(t)$ is the time-dependent DNI. In the simulations, it was assumed that the CSP plant was located in Billings, OK, USA and measured values of the DNI were used with a time resolution of one minute from 2009 [119].

The temperature of the MS flowing into the receiver, denoted by $T_{\text{rec,in}}(t)$, is calculated as the adiabatic mixing temperature of the MS streams coming from the heat exchanger and the TES. The nominal receiver inflow temperature is 300°C. To keep the receiver outflow temperature constant at $T_{\text{rec,out}} = 600°\text{C}$, the MS mass flow rate through the receiver adjusted,

$$\dot{m}_{\text{rec}}(t) = \frac{Q_{\text{rec}}(t)}{c_{p,\text{ms}}(T_{\text{rec,out}} - T_{\text{rec,in}}(t))} . \tag{4.22}$$

---

[12] The relatively low value reflects decreases due to atmospheric attenuation and higher spillages typical of large-scale CSP plants [118].

To run the turbine directly with solar energy, a minimum DNI of

$$I_{\min} = \frac{\dot{W}_{\mathrm{el,rated}}}{\eta_{\mathrm{PB,rated}}\eta_{\mathrm{rec}}\eta_{\mathrm{opt}}A_{\mathrm{sf}}} = 370 \ \mathrm{W/m}^2 \tag{4.23}$$

is required.

TES

The maximum capacity of the TES is determined from

$$E_{\max} = \frac{\dot{W}_{\mathrm{el,rated}}\Delta t_{d,\mathrm{nom}}}{\eta_{\mathrm{PB,rated}}\zeta} = 2549 \ \mathrm{MWh_{th}} \,, \tag{4.24}$$

for a ratio between the nominal discharge duration and the utilization factor of $\Delta t_{d,\mathrm{nom}}/\zeta = 9.41$. For utilization factors typical of the operation with and without TCC of $\zeta = 0.85$ and 0.65, the ratio corresponds to nominal discharging durations of $\Delta t_{d,\mathrm{nom}} = 8$ h and 6.1 h, respectively.

The geometric and operational parameters of the TES are given in Tables 4.1 and 4.2. Note that the outflow temperature restrictions are identical to those used in the quasi-steady state simulations, i.e., $\widetilde{T}_{c,\mathrm{out,max}} = 0.1$ and $\widetilde{T}_{d,\mathrm{out,min}} = 0.9$.

4.4.2 CSP plant operation

The plant operates in four modes depending on the DNI and the temperatures of the MS flowing out of the TES, see Fig. 4.17.

Mode 1: The DNI exceeds $I_{\min}$ and the outflow temperature of the MS is less than $T_{c,\mathrm{out,max}}$. Therefore, the TES is being charged with a mass flow rate of

$$\dot{m}_c(t) = \dot{m}_{\mathrm{rec}}(t) - \dot{m}_{\mathrm{PB,rated}} \tag{4.25}$$

and the turbine runs in rated operation.

Mode 2: The DNI exceeds $I_{\min}$ but the outflow temperature of the MS would not be less than $T_{c,\mathrm{out,max}}$. Therefore, the TES is considered to be fully charged and not being supplied with MS. The turbine runs in rated operation and the surplus thermal energy is dumped.
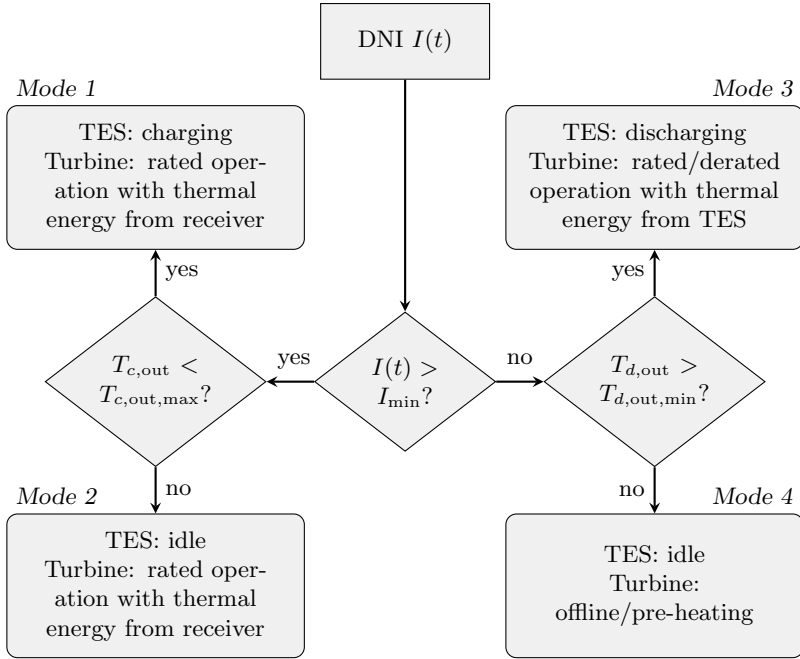
Figure 4.17: Flow chart of the four operation modes of the CSP plant.

Mode 3: The DNI is less than $I_{\min}$ and the outflow temperature of the MS is not less than $T_{d,\text{out,min}}$. Therefore, the TES is being discharged. If $\widetilde{T}_{d,\text{out}} = 1$, the turbine runs in rated mode and the mass flow rate through the TES is

$$\dot{m}_d = \dot{m}_{\text{PB,rated}} . \tag{4.26}$$

Conversely, if $\widetilde{T}_{d,\text{out,min}} < \widetilde{T}_{d,\text{out}} < 1$, the turbine runs in derated mode and the mass flow rate through the TES is a function of the MS outflow temperature, see [117].

Mode 4: The DNI is less than $I_{\min}$ and the outflow temperature of the MS would be less than $T_{d,\text{out,min}}$. Therefore, the TES is considered to be fully discharged and not being supplied with MS. The turbine is offline and the surplus thermal energy is dumped.

4.4.3 Assessment criteria

The performance of the CSP plant is assessed based on the annually generated electricity

$$W_{\text{el}} = \int_{\text{year}} \dot{W}_{\text{el}}(t) \ \mathrm{d}t \tag{4.27}$$

and the annually averaged efficiency

$$\overline{\eta}_{\text{plant}} = \frac{W_{\text{el}}}{\int_{\text{year}} A_{\text{sf}} I(t) \, \mathrm{d}t} \ . \tag{4.28}$$

The performance of the TES is assessed by the annually generated electricity with thermal energy coming solely from the TES,

$$W_{\text{el,TES}} = \int_{\text{year}, \, \dot{m}_d > 0} \dot{W}_{\text{el}}(t) \ \mathrm{d}t \, , \tag{4.29}$$

by the non-dimensional instantaneously stored energy,

$$\widetilde{E}(t) = \frac{E(t)}{E_{\text{max}}} \, , \tag{4.30}$$

by the maximum utilization factor throughout a day and its following night,

$$\zeta^*_{\text{max},i} = \max_{\substack{\text{day } i \\ \text{daytime}}} \widetilde{E}(t) - \min_{\substack{\text{day } i \\ \text{nighttime}}} \widetilde{E}(t) \, , \tag{4.31}$$

by the average maximum utilization factor throughout a year,

$$\overline{\zeta}^*_{\text{max}} = \frac{1}{365} \sum_{i=1}^{365} \zeta^*_{\text{max,day},i} \, , \tag{4.32}$$

and by the annually averaged exergy efficiency,

$$\overline{\eta}_{\text{ex}} = \frac{\int_{\text{year}} \dot{\Xi}_{d,\text{net}} \, \mathrm{d}t}{\int_{\text{year}} \dot{\Xi}_{c,\text{net}} \, \mathrm{d}t} \, , \tag{4.33}$$

where the pumping work was neglected, which is justified for MS as can be seen from Fig. 4.14.

4.4.4 Results and discussion

Comparison of TCC methods

Figure 4.18 shows the DNI, the non-dimensional instantaneously stored energy $\widetilde{E}(t)$, and the corresponding plant modes for five exemplary days. For brevity, this figure shows only the results obtained without TCC and with the mixing method with three ports. Three general observations can be made. First, during the first and second days, spikes in $\widetilde{E}(t)$ can be observed. These spikes are caused by cloudy periods during which the DNI fluctuates between values that exceed and fall below $I_{\min}$. These fluctuations force the plant operation to switch between mode 1, in which the TES is charging, and mode 3, in which it is discharging.

Second, the following three days are nearly entirely sunny and allow the TES to be fully charged, i.e., until the MS outflow temperature exceeds $T_{c,\text{out,max}}$. The fully charged states are visible in the figure when $\widetilde{E}(t)$ reaches constant values of around 78% and 94% without TCC and with the mixing method, respectively. Consequently, the plant operation switches from mode 1, in which the TES is charging, to mode 2, in which the surplus thermal energy is dumped.

Third, at sunset, as the DNI falls below $I_{\min}$, the TES is being fully discharged, i.e., until the MS outflow temperature cannot be kept above $T_{d,\text{out,min}}$. The fully discharged states are visible in the figure when $\widetilde{E}(t)$ reaches constant values of around 18% and 4% without TCC and with the mixing method, respectively. As a result, the plant operation switches from mode 3, in which the TES is discharged and the turbine is in rated/derated operation, to mode 4, in which the TES and turbine are idle.

Comparing the results obtained without TCC and with the mixing method, one can observe that the benefit of the mixing method is mainly present on sunny days, the last three days depicted in Fig. 4.18. This can be seen from the larger differences between the highest and lowest values of $\widetilde{E}(t)$ and the longer durations of modes 1 and 3 for the mixing method, which means more thermal energy is stored and released by the TES.
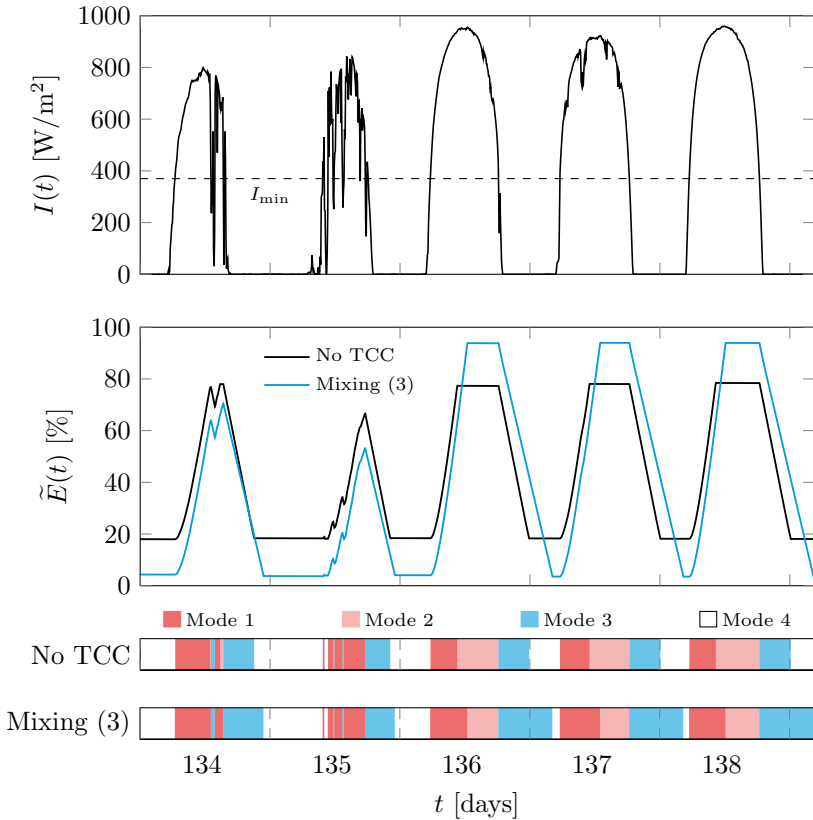
Figure 4.18: DNI (top), non-dimensional instantaneously stored energy (middle), and plant modes (bottom) for five exemplary days without TCC and with the mixing method with three ports.

The comparison of the results obtained without TCC and with the mixing method also shows that the slopes of $\widetilde{E}(t)$ are the same during charging, while during discharging the mixing method leads to slightly slower decreases of $\widetilde{E}(t)$. During charging the slopes are equal because the MS mass flow rate through the receiver is adjusted according to Eq. (4.22) such that all the solar energy is absorbed and the TES is charged with all the excess solar
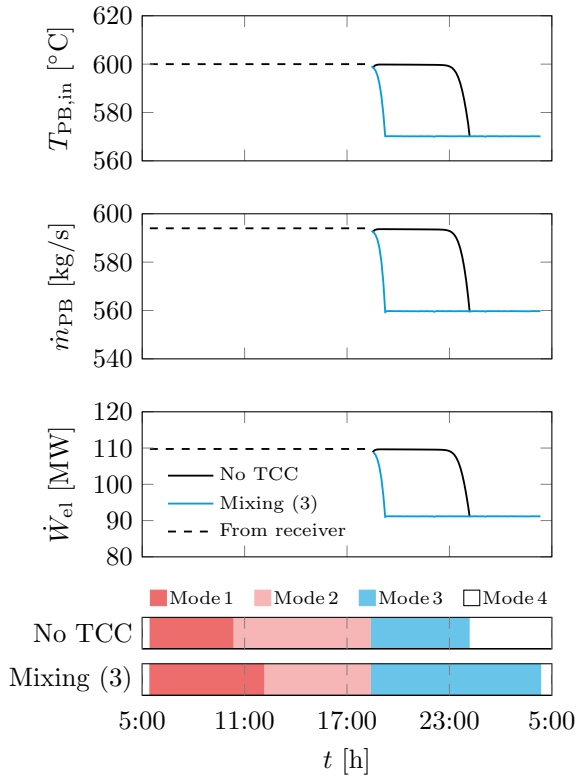
Figure 4.19: MS inflow temperature to power block (top), MS mass flow rate to power block (middle), and power output (bottom) during day 138 without TCC and the mixing method with three ports.

energy that is not needed for the rated turbine operation. The reason for the different slopes of $\widetilde{E}(t)$ during discharging is seen in Fig. 4.19, which illustrates the operation of the power block during day 138 in terms of the temperature and mass flow rate of the MS flowing into the power block and the power output. Starting at about 18:25, the plant operates using thermal energy provided from the TES, i.e., it operates in mode 3. With the mixing method, because of the lower MS temperature and mass flow rate
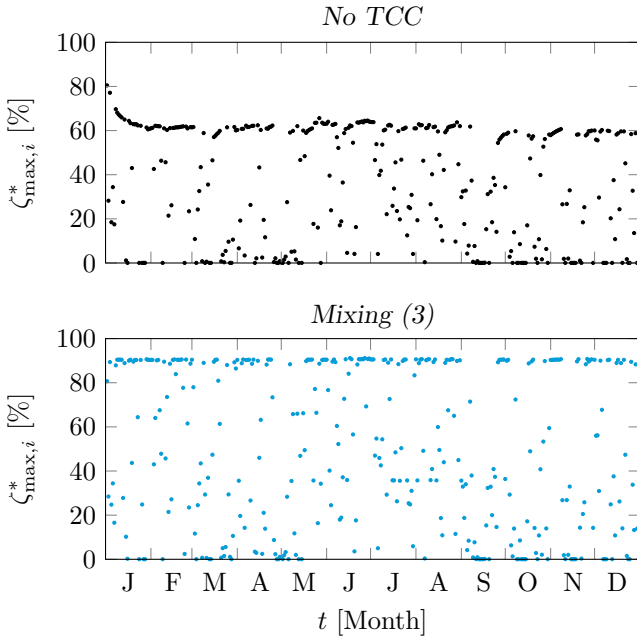
Figure 4.20: Maximum daily utilization factor over the whole year. The case without TCC is shown on top and the case with the mixing method with three ports is shown at the bottom.

coming from the TES, the power block operates mostly at minimum derated conditions. Conversely, without TCC, because of the higher MS temperature and mass flow rate, the power block operates mostly in rated conditions. The lower power output obtained with the TCC method is outweighed by the significantly longer discharging duration.

Figure 4.20 shows scatterplots of the maximum utilization factor for each day over a year without TCC and with the mixing method. We make three observations. First, both without TCC and with the mixing method, the maximum utilization factors can be seen to form a trendline. The scattered points that are below this trendline originate from cloudy days, which prevent

complete charging of the TES.

Second, the maximum utilization factor without TCC is seen to drop from about 80% to about 61% within the first month. The reason for this drop is that the TES is assumed to be completely discharged at the beginning of the year, so the thermoclines degrade and the utilization factor decreases in a manner that is very similar to what can be observed in Figs. 4.7 and 4.8 for the stand-alone simulations prior to the attainment of the quasi-steady state. By contrast, the mixing method does not lead to a drop in the maximum utilization factor, once again similar to the stand-alone simulations, in which the mixing method exhibited much reduced thermocline degradation.

Third, the last day of the year where the TES is charged up to the maximum outflow temperature limit results in utilization factors of 59.6% and 90.4% without TCC and with the mixing method, respectively. Comparing these values to the utilization factors of 65.4% and 90.8% attained in the stand-alone simulations, one can observe that the values for the mixing method are very close, whereas without TCC, the value is around 10% lower. The decreased utilization factor without TCC is caused by partial charging and discharging phases that accentuate thermocline degradation.

A summary of the simulation results, ncluding those obtained with the other TCC methods, is presented in Table 4.4. Four points can be made. First, the annual plant efficiency is increased from 14.6% without TCC to 16.1% with mixing and three ports. It is interesting to note that the relative trend in the annual plant efficiency matches the relative trend in the utilization factor from the stand-alone simulations. Second, the relative increases in annual plant efficiency appear to be relatively limited. For the extracting method the relative increase is only 6.3%, whereas for the mixing method, the relative increase is 10.3%. However, if one assesses the TCC methods based on the electricity that is produced with thermal energy coming solely from the TES, larger relative increases are observed, ranging from 15.9% for extracting to 26.0% for mixing with three ports. Third, it is interesting to note that the annually averaged exergy efficiencies of the TES are nearly identical to the exergy efficiencies of the TES in the stand-alone

Table 4.4: Summary of CSP plant simulation results: Annual plant efficiency $\overline{\eta}_{\text{plant}}$, annual TES exergy efficiency $\overline{\eta}_{\text{ex,TES}}$, average maximum utilization factor $\overline{\zeta}_{\text{max}}^{*}$, annual net generated electricity W_{el}, annual net electricity generated solely through thermal energy from the TES $W_{\text{el,TES}}$, and relative increase of the latter with respect to the case without TCC $\Delta W_{\text{el,TES}}/W_{\text{el,TES,NC}}$.

TCC method	$\overline{\eta}_{\text{plant}}$ [%]	$\overline{\eta}_{\text{ex,TES}}$ [%]	$\overline{\zeta}_{\text{max}}^{*}$ [%]	W_{el} [GWh]	$W_{\text{el,TES}}$ [GWh]	$\frac{\Delta W_{\text{el,TES}}}{W_{\text{el,TES,NC}}}$ [%]
No TCC	14.6	99.4	37.4	396.8	154.7	0.0
Extracting (3)	15.5	99.4	44.0	422.0	179.2	15.9
Injecting (2)	15.6	99.2	45.5	425.9	183.6	18.7
Mixing (1)	15.8	97.9	47.9	430.4	187.8	21.4
Mixing (3)	16.1	97.3	50.7	437.4	194.9	26.0
No TCC, oversized	16.0	99.4	34.9	435.2	193.1	24.8

simulations shown in Fig. 4.13. The largest difference is observed without TCC, where the exergy efficiency decreased from 99.7% for the quasi-steady state to 99.4% when averaged annually. Finally, the decreased annually averaged exergy efficiencies of the TES with TCC have no clear effect on the annually averaged plant efficiency. The explanation for this result appears to be that the decreases in the exergy efficiency of the TES are small enough to be outweighed by the significant increases in the utilization factor and the attendant substantial increases in electricity generation.

Comparison of mixing method with oversizing

Equation (4.10) shows that the utilized energy can be increased in two ways. The first is by increasing the utilization factor for a given maximum storage capacity, which can be achieved through TCC. The second is by increasing the maximum storage capacity by oversizing the TES, provided that the increased capacity is not outweighed by a reduced utilization factor.

To assess the performance of an oversized TES in the CSP plant, addi-

tional simulations were carried out. The TES was oversized such that the increase in the utilized capacity was similar to the increase of 38.8% obtained by the mixing method with three ports in the stand-alone simulations, see Fig. 4.12. Assuming for simplicity that the quasi-steady state utilization factor is unaffected by oversizing, the utilized capacity was increased by 37.5% through enlarged storage diameters of $d_{\mathrm{top}} = 39.04\,\mathrm{m}$ and $d_{\mathrm{bottom}} = 32.06\,\mathrm{m}$.

Table 4.4 shows that relative to the mixing method with three ports, oversizing the TES leads to a slightly lower annually averaged plant efficiency, a higher exergy efficiency of the TES, and a slightly lower annual net electricity generation. This confirms the previously discussed result that the utilized energy has a stronger impact on the annually averaged plant efficiency than the exergy efficiency.

Oversizing the TES increased the material cost by 33%. Therefore, if the costs of the ports, pipes, valves, and sensors required by TCC methods amount to less than about a third of the material cost of a TES, equipping it with TCC not only increases its performance but is also cheaper than an oversized TES.

4.5   Conclusions and future work

The extracting, injecting, and mixing TCC methods were assessed through simulations of a stand-alone TES using MS or CA as HTF and a TES integrated into a CSP plant using MS as HTF. The assessment leads to the following conclusions:

1. The simulations of the stand-alone TES showed that for given maximum allowed non-dimensional outflow temperature differences of $\Delta \widetilde{T}_{\mathrm{out,max}} = 10\%$, the TCC methods led to significant increases in the utilization factor at the expense of small decreases in the exergy efficiency.

2. The largest utilization factors were attained by the mixing method, a new method proposed in this work. For MS and CA, the utilization factors with three ports were 90.8% and 85.1%, which represent relative

increases of 38.8% and 73.4% with respect to the baseline configurations that were operated without TCC.

3. The smallest exergy efficiencies were attained by the mixing method with three ports with 97.3% and 95.6% for MS and CA, respectively. These values represent relative decreases of 2.4% and 1.7% with respect to the baseline configurations.

4. The benefits of TCC increased significantly for smaller values of the maximum outflow temperature differences. For the mixing method with three ports and $\Delta\widetilde{T}_{\text{out,max}} = 2.5\%$, the relative increases in the utilization factors were 331% and 744% for MS and CA, respectively. The exergy efficiency of the mixing method with three ports for $\Delta\widetilde{T}_{\text{out,max}} = 2.5\%$ was similar to the one without TCC yielding 99.2% and 97.4% for MS and CA, respectively.

5. For the mixing method, the specific material costs were almost independent of the maximum outflow temperature differences at $4.4 - 5.6$ \$/kWh and $3.1 - 5.0$ \$/kWh for MS and CA, respectively. This is in contrast to the specific material costs without TCC, which rose to 24.2 \$/kWh and 42.7 \$/kWh for MS and CA for $\Delta\widetilde{T}_{\text{out,max}} = 2.5\%$.

6. Because TCC methods reduce thermocline degradation, in general fewer charging-discharging cycles are required to reach quasi-steady conditions. This may be an important advantage of TCC methods in CSP plants because the nominal electricity output may be attained more quickly following extended cloudy periods or plant shutdowns.

7. The simulations of the TES integrated into the CSP plant showed that TCC increased the annually averaged plant efficiency and the annual net electricity generated solely from thermal energy supplied by the TES. The mixing method with three ports performed best with an efficiency of 16.1% compared to 14.6% without TCC and a relative increase in the annual net electricity generated solely from thermal energy supplied by the TES of 26.0%.

8. The beneficial effect of TCC on the performance of the CSP plant

  indicates that the small decreases in the exergy efficiency of the TES
  are outweighed by the large increases in the utilization factor.

9. Compared with the mixing method with three ports, oversizing the
  TES by 37.5% led to a slightly lower annually averaged plant efficiency
  and a slightly lower annual net electricity.

The simulations were carried out with a model that did not take into account
the void spaces near the ports, the flow of the HTF through the ports, pipes,
and valves, and two- and three-dimensional flow effects near the ports. Future
work will therefore require more detailed and multi-dimensional simulations
to obtain more accurate estimates of the increases in the utilization factor
and the decreases in the exergy efficiency. With the more accurate estimates,
it will be possible to estimate the cost of the ports, pipes, valves, and sensors.
The future simulations should also be used to design a laboratory-scale TES
to allow an experimental assessment of TCC.

PILOT-SCALE DEMONSTRATION OF ADVANCED ADIABATIC COMPRESSED AIR ENERGY STORAGE: PLANT DESCRIPTION AND TESTS WITH SENSIBLE THERMAL ENERGY STORAGE[1]

5.1 Introduction

The growing share of intermittent renewable-energy sources such as wind and solar requires short- and long-term energy storage to guarantee the power supply. At present, pumped hydroelectric storage (PHS) accounts for more than 99% of worldwide bulk storage capacity [120]. The large contribution of

PHS is explained by the simplicity of the underlying technology and by the large storage capacities and high efficiencies that can be attained by PHS plants. The construction of additional plants is hampered by high capital costs and restrictive site requirements. These requirements include the need for substantial elevation differences between the two reservoirs, which usually requires the flooding of valleys in mountainous regions [121].

Advanced adiabatic compressed air energy storage (AA-CAES) is so far the only alternative to PHS that can compete in terms of capacity and efficiency and has the advantages of lower expected capital costs and less strict site requirements [37, 120]. Because CAES plants do not require elevation differences, they can be built in non-mountainous regions also. Furthermore, CAES in its simpler diabatic form (D-CAES) is the only storage technology other than PHS that has been proven at the utility scale with the plants in Huntorf, Germany (321 MW$_{el}$, since 1978) [122, 123] and McIntosh, USA (110 MW$_{el}$, since 1991) [124, 125].

The working principle of CAES is straightforward: During periods of low demand, surplus electrical energy is used to drive a compressor operating with ambient air and the compressed air is stored in a cavern. During periods of high demand, electrical energy is generated by expanding the stored air in a turbine. To reduce the required cavern volume for a given storage capacity and to reduce thermal stresses in the cavern wall, the air flowing into the cavern should be at a low temperature. In D-CAES, this is achieved by rejecting the thermal energy generated by the compression. This necessitates that the air flowing out of the cavern during discharging is reheated to prevent ice buildup in the turbine during expansion. In the existing D-CAES plants, the reheating is achieved by burning fossil fuels. It is the need to reheat the air prior to expansion in the turbine that is responsible for the relatively low cycle efficiencies of about 45-50% of D-CAES plants. By contrast, in AA-CAES the thermal energy generated by the compression is stored in a thermal energy storage (TES), which increases cycle efficiencies to about 60-75% [39, 40].

The D-CAES plants in Huntorf and McIntosh use caverns that were

solution-mined from salt deposits. Because suitable salt deposits are not ubiquitous, the use of acquifers and rock caverns has been studied [126, 127, 128]. Rock caverns are of particular interest because rock formations are more prevalent than salt deposits and would allow reusing decommissioned tunnels and mines. In addition, rock caverns can be accessed more easily than solution-mined salt caverns, which leads to two advantages. First, in principle CAES plants could be built entirely underground. Second, and perhaps more importantly, the TES can be placed inside the cavern. This simplifies the construction of the TES considerably because its structure does not need to sustain a pressure difference, in contrast to plants in which the TES is placed above ground, see, e.g., [129]. The main disadvantage of rock caverns compared to salt caverns relates to tightness. Salt caverns are often considered to be virtually airtight because of very low permeability and self-healing nature of rock salt, see, e.g., [130, 131]. Conversely, for rock caverns, based on the experience with the storage of compressed natural gas, the use of linings or hydrodynamic containment is advocated to ensure tightness, see, e.g., [132, 133, 134, 135].

Rock caverns constructed in two former mines were investigated in Japan. Experimental data was presented for a cavern lined with backfilling concrete, reinforced concrete, and a rubber sheet [136]. The cavern had a volume of about 1600 m^3 and was located at a depth of about 450 m. Starting from a maximum pressure of about 0.9 MPa, leakage rates of about 0.5% per day were observed and traced to cracks in the concrete lining and the air tightness of the rubber sheet. Experimental data was also reported for an unlined blast-excavated cavern with a volume of about 200 m^3 located at a depth of about 1000 m [137]. The pressure in the cavern, starting from 0.6 MPa, reduced to ambient pressure within about five hours. The leaks were traced to the piping. Because of the above-mentioned advantages, rock caverns continue to be of interest despite the leaks. This interest is reflected in a growing number of studies of rock caverns for CAES from geological and geomechanical perspectives, see, e.g., [138, 139, 140, 141, 142].

So far, AA-CAES has not been demonstrated at the utility scale. An

above-ground pilot plant was tested with five compressor and three expansion stages [143]. The compressed air was stored in two steel tanks with a combined volume of 100 m^3 and with pressures ranging from 2.5 MPa to 9.5 MPa. Two pressurized water tanks with a volume of 12 m^3 were used as a TES. The water was used to cool/heat the air between the compression/expansion stages, respectively. An average round-trip energy efficiency of 22.6% was reported. The low efficiency was ascribed to the unsteady operation of the compressor, to mass flow rates during expansion that were lower than expected, and to heat losses from the TES that were larger than expected.

In this chapter, experimental data obtained with the world's first underground AA-CAES pilot plant are presented. The specific objectives of the pilot plant were:

1. Demonstrate the ability of rock caverns to withstand the stresses induced by cyclic charging/discharging of the cavern.

2. Evaluate the tightness of a mostly unlined rock cavern: Reducing the area covered by a lining simplifies the construction and reduces the cost.

3. Investigate the performance of a sensible TES using a packed bed of rocks placed inside the cavern.

4. Investigate the performance of a combined sensible/latent TES at the pilot scale: Adding a layer of encapsulated phase-change material on top of the packed bed of rocks decreases the drop in the outflow temperature during discharging [24, 25, 97].

The pilot plant was built in a mountain tunnel that was used during the excavation of the Gotthard base tunnel near Biasca in southern Switzerland. The tunnel has a length of 3.16 km and a diameter of 4.9 m. Further information on the geological and geotechnical conditions at the plant site as well as information on a preliminary design of the pilot plant were presented in [144]. Two experimental campaigns were performed with the pilot plant. The first campaign was performed with a sensible TES and is described

in this chapter. The second campaign was performed with a combined sensible/latent TES and is described in a companion paper [145].

5.2 Plant description

A schematic of the pilot plant is shown in Fig. 5.1. During charging, hot compressed air enters the cavern through an insulated pipe that directs the air to the top of the TES. By flowing through the thermocline TES, the air is cooled. The cooled air then exits the TES at the bottom and enters the cavern. During discharging, the flow is reversed: cold air from the cavern enters the TES at the bottom, is heated, leaves the TES at the top, and exits the cavern through the insulated tube. As can be seen from Fig. 5.1, the pilot plant does not include a turbine because none was necessary to meet the plant's objectives. Therefore, the hot air that exits the cavern is routed through a silencer (not indicated in Fig. 5.1 for simplicity) and released to the ambient. In the following, the various components of the plant are described in more detail.

5.2.1 Cavern

The cavern is located approximately 800 m from the northeasterly portal of the tunnel and has an average rock overburden of about 450 m. The cavern is 120 m long and confined by two concrete plugs and steel doors, see Fig. 5.1. The plugs are 5 m thick and have a double-conical shape to
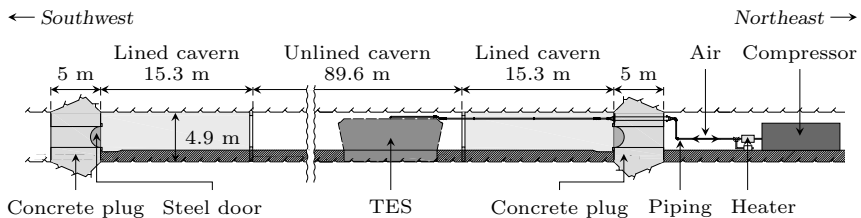
Figure 5.1: Schematic of the pilot plant.

Figure 5.2: Picture of one of the concrete plugs and the associated steel door.

transfer the cavern pressure to the surrounding rock. A picture of one of the plugs and the associated steel door is shown in Fig. 5.2. The volume and surface area of the cavern are estimated to be about 1942 m^3 and 1991 m^2, respectively. Note that the volume includes the void space inside the TES.

The cavern surface exposed to rock is covered with about 5 cm of shotcrete that had been applied during the construction of the tunnel. With the exception of the cavern surface near the two plugs, no lining is used and therefore the cavern is referred to as "mostly unlined." Near the two plugs, the shotcrete is lined with an impermeable high-strength glass-fiber membrane, see Fig. 5.3. The objective of the lining was to reduce the likelihood of air leakages near the plugs by forcing the air to travel a longer path through the rock to reach the ambient. The plant and the components have been designed for a maximum operating pressure of 33 bar.

Figure 5.3: Picture of the impermeable high-strength glass-fiber membrane that was used to line the cavern near the concrete plugs. The insulated pipe through which the hot air enters and exits the cavern is visible at the top.

5.2.2   TES

The packed-bed thermocline TES is located inside the cavern and built against the cavern wall as can be seen from Figs. 5.4 and 5.5. As indicated in Fig. 5.5, the TES is charged from top to bottom with hot air from the compressor and discharged from bottom to top with cold air from the cavern. The TES has a height of about 3.1 m and an average length and average width of about 9.9 m and 2.4 m, respectively. From inside to outside, the walls consist of 1 cm of ultra-high performance concrete (UHPC), 4 cm of low density concrete (LDC), 10 cm of microporous thermal insulation and 25 cm of reinforced concrete. In the wall adjacent to the cavern surface, the

Figure 5.4: Picture of the TES inside the cavern. The red cables connect the resistance temperature detectors (RTDs) inside the TES to the data acquisition system. The positions of the RTDs inside the TES are shown in Fig. 5.5.

thickness of the reinforced concrete is 39 cm. The walls facing the tunnel axis are angled outward to reduce the stresses exerted by the rocks on each other and on the UHPC due to thermal cycling, see [22]. The TES rests on a foundation of reinforced concrete. A steel cover lined with 15 cm microporous thermal insulation is placed on top of the TES.

The TES is filled to a height of about 2.7 m with a packed bed of rocks with a mean diameter of about 2 cm. The packed bed comprises various rock types (mafic rocks, felsic rocks, limestones, sandstones, and quartz-rich conglomerates) obtained from a fluvial deposit near Zurich, Switzerland.

Previous studies used rocks from the same deposit in lab- and pilot-scale storages [22, 51, 97]. Flow distributors are mounted above and below the packed bed; they were designed and optimized via CFD to ensure uniform air flow conditions. The fully-charged capacity of the TES is 12 MWh$_{th}$. The TES was over-dimensioned on purpose to protect the cavern and its measurement equipment from high temperatures.

5.2.3 Compressor train

A high-pressure compressor train (Atlas Copco, ZD 800-1200 & ZD 1200 VSD air-cooled) was used to provide pressurized air at ambient temperature. To simulate adiabatic compression, the air was then heated to 550 °C with an electrical heater.

5.2.4 Sensors

The gauge pressure in the cavern was measured by two sensors. The air mass flow rate was measured between the compressor and the inlet to the cavern and, therefore, was measured for the air flowing into the TES during charging and for the air flowing out from the TES during discharging. The temperature in the cavern was measured by two resistance temperature detectors (RTDs). Since one RTD was placed near the TES and found to be affected by heat losses, we only report the temperature measured by the other RTD that was placed in the middle of the cavern. The temperature of the rock was measured by two RTDs located about 10 cm inside the rock. The temperatures in the TES were measured by 19 RTDs whose locations are shown by the symbols in Fig. 5.5. The deformation of the cavern and the displacement and deformation of the concrete plugs was monitored using extensometers, tachymeters, and strain gauges.
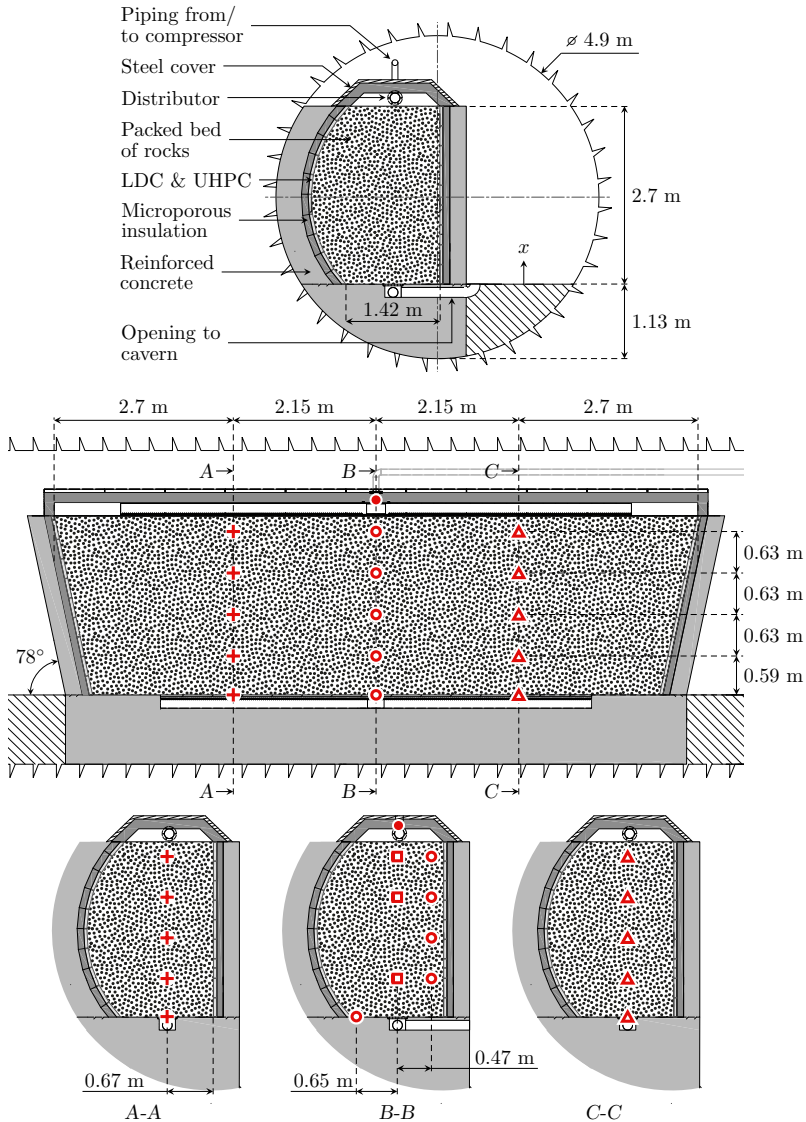
Figure 5.5: Schematic of the dimensions and structure of the TES. The cross, circle, square, and triangle symbols indicate the locations of resistance temperature detectors (RTDs).

5.3 Numerical model

A numerical model was developed to assist in the design of the experiments
carried out with the pilot plant and to simulate larger plants. This model
couples a model for the TES with a simple model for the evolution of the
air in the cavern.

5.3.1 TES

The model for the TES is based on the model presented in Chapter 2 that
solves one-dimensional (axial) energy equations in a packed bed of circular
cross-section and two-dimensional (axial and radial) energy equations in the
annular insulation and structure. To simulate the pilot plant, the model
was adapted in two ways. First, modifications were made to account for
the specific TES configuration. The rectangular cross-section is represented
in the model by considering transient heat conduction in linear instead of
circular geometries for the structure and insulation. Natural convection
is assumed on the outer walls of the TES using the correlations of [146]
and neglecting that one side of the storage abuts the cavern wall.   The
second modification relates to the coupling between the TES and the cavern.
During charging, the temperature of the air entering the cavern is equal to the
temperature of the air exiting the TES. Conversely, during discharging, the
temperature of the air entering the TES is approximated by the temperature
of the air in the cavern. During both charging and discharging, the pressure
at the bottom of the TES is assumed to be equal to the cavern pressure. To
compute thermal losses from the TES, the ambient temperature is assumed
to be the simulated temperature of the air in the cavern.

In the simulations presented in Section 5.4, the flow distributors at
the top and the bottom of the TES were neglected. The convective heat-
transfer coefficient in the packed bed was calculated from the correlation
of [147]. Natural convection on the lateral walls and the cover was modelled
using the correlation of [146]. At the bottom, conduction losses through
the reinforced concrete were considered based on a mean thickness of 0.6 m.

Table 5.1: Thermophysical properties of various materials. Ranges indicate temperature-dependent properties for $15°\text{C} \leqslant T \leqslant 550°\text{C}$.

Material	c [J/kgK]	ρ [kg/m^3]	k [W/mK]	Source
Rocks	860-1249	2635	1.61-3.70	[148]
Reinforced concrete	784	2400	0.765	[149]
Microporous insulation	1050	270	Eq. (5.1)	[150]
LDC	663	1500	0.37-0.64	[81]
UHPC	500	2500	1.66-2.20	[81]

The properties of the rocks were taken from [148] and the properties of reinforced concrete and microporous insulation are given in Table 5.1, where the thermal conductivity of the microporous insulation is given by

$$k_{\text{ins}}(T) = 2.151 \cdot 10^{-3} + 9.219 \cdot 10^{-5}T - 1.421 \cdot 10^{-7}T^2 + 8.333 \cdot 10^{-11}T^3, \quad (5.1)$$

where the temperature is in K. The material properties for LDC and UHPC are taken from [81]. Air was considered to be an ideal gas and thermophysical properties were taken from [52].

5.3.2 Cavern

The cavern model is based on the equations for the conservation of mass and energy for an open control volume. Assuming that the air in the cavern can be treated as an ideal gas, the conservation equations simplify to

$$V_{\text{cav}} \frac{\mathrm{d}\rho_{\text{cav}}}{\mathrm{d}t} + \dot{m} = 0 \,, \quad (5.2)$$

$$c_v V_{\text{cav}} \frac{\mathrm{d}\rho_{\text{cav}}T_{\text{cav}}}{\mathrm{d}t} + \dot{m}c_p T_t = -Q'' A_{\text{cav}} \,, \quad (5.3)$$

where V_{cav} and A_{cav} are the volume and surface area of the cavern, ρ_{cav} is the average density of the air in the cavern, $\dot{m}$ is the mass flow rate of the air, c_v and c_p are the specific heat capacities of the air, T_{cav} is the average temperature of the air in the cavern, T_t is the total temperature of the air

flowing into/out of the cavern, and Q'' is the wall heat flux. It is assumed that the wall heat flux can be expressed as

$$Q'' = h(T_{\mathrm{cav}} - T_w)\,, \tag{5.4}$$

where h is a convective heat-transfer coefficient and T_w is the cavern wall temperature. Zaugg [151] appears to have been the first to present the analytical solution of Eqs. (5.2) and (5.3) for charging at constant mass flow rate, inflow total temperature, wall temperature, and air properties. In the Appendix D, Zaugg's solution is extended to simultaneous charging and discharging. With the extended solution, the evolution of the density and temperature of the air in the cavern can be described if some of the air escapes through a leak during charging. If the mass flow rate, the total inlet and wall temperatures, or the air properties are not constant, Eqs. (5.2) and (5.3) can either be solved numerically or the analytical solution can be applied for small time steps. In the simulations, the cavern wall temperature was approximated by the average of the measured rock temperatures.

5.4 Results and discussion

Two sets of experiments were conducted with the pilot plant. In the first set, the cavern was charged with compressed air at ambient temperature to assess the tightness of the cavern. In the second set, the cavern was charged with compressed air at about 525-550 °C. In both tests, the deformation of the cavern walls and the plugs was found to be negligible. This is not further discussed as it was not the focus of this paper.

5.4.1 Ambient-temperature tests

The tests revealed discrepancies between the measured cavern gauge pressure and that predicted by the cavern model using the measured charging mass flow rate. The discrepancy was ascribed to leaks through the plugs and/or the unlined portion of the cavern. In Fig. 5.6, the measured cavern gauge pressure $\tilde{p}_{\mathrm{cav}} = p_{\mathrm{cav}} - p_{\mathrm{amb}}$, the measured mass flow rate, and the estimated total
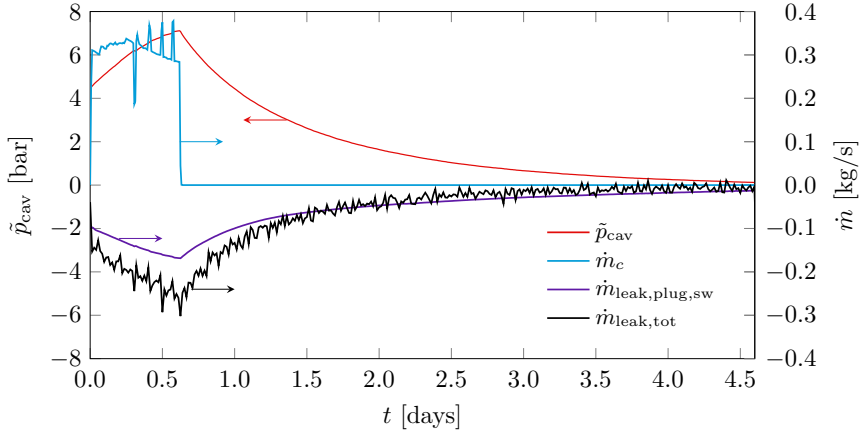
Figure 5.6: Results from ambient-temperature tests showing the measured cavern gauge pressure (red), the measured charging mass flow rate (blue), the estimated total leakage mass flow rate (black), and the estimated leakage mass flow rate through the southwesterly plug (purple).

leakage mass flow rate $\dot{m}_{\text{leak,tot}}$ are shown as a function of time. The total leakage mass flow rate was estimated by subtracting the measured mass flow rate from that necessary to reproduce the measured cavern gauge pressure. Once the cavern was no longer being charged, the pressure approached the ambient within about 4 days.

The leakage through the southwesterly plug could be estimated thanks to an anemometer in an antechamber located adjacent to the plug. (The antechamber is not shown in Fig. 5.1 for simplicity.) Comparing the estimated leakage mass flow rate $\dot{m}_{\text{leak,plug,sw}}$ with the total leakage mass flow rate indicates that at least at high gauge pressures, around 60% of the total leakage can be attributed to the southwesterly plug. Although the leakage rate through the northeasterly plug could not be measured, it is unlikely that the behavior of that plug is considerably different. Therefore it can be concluded that leakages originated mainly from the concrete plugs and that

losses through the unlined portion of the cavern could be considered to be small or even negligible. Since the tightness of the concrete plugs depends on their design, and improved designs will be considered for future plants, the results are encouraging concerning the tightness of unlined rock caverns.

The measurements from all the ambient-temperature tests were used to derive a correlation for the total leakage mass flow rate,

$$\dot{m}_{\text{leak,tot}} = -2.746 \cdot 10^{-2} \tilde{p}_{\text{cav}} + 2.989 \cdot 10^{-3} \tilde{p}_{\text{cav}}^2 - 6.210 \cdot 10^{-4} \tilde{p}_{\text{cav}}^3 \,, \quad (5.5)$$

where $\dot{m}_{\text{leak,tot}}$ is in kg/s and $\tilde{p}_{\text{cav}}$ in bars. The fit was used in the simulation of the high-temperature pressure tests to account for the leakage.

5.4.2 High-temperature tests

Two test runs were conducted, each consisting of up to five days of operation. Run 1 and 2 consisted of six and seven charging/discharging cycles, respectively. A so-called pre-charging was performed before the first charging of each run to approach steady cycling behavior of the TES more quickly, see [81] and the comments below. The durations of the pre-charging, charging, and discharging phases of each cycle are given in Table 5.2. The table also lists the figures in which the mass flow rates, the charging temperature, and the cavern gauge pressure are shown. In general, cycles of equal charging and discharging times were performed, except for cycles B1, B2, and B3 of run 1, which were performed after a re-charge phase in a constant gauge pressure range between 3.5 and 4 bar.

Figures 5.7 and 5.8 show the measured charging temperature, the measured mass flow rates, and the measured and simulated cavern gauge pressures during the pre-charging phases of the two runs, respectively. In these and the following figures, light blue, white, and gray backgrounds indicate pre-/re-charging, charging, and discharging phases, respectively. The charging temperature was measured inside the tube just above the distributor, as indicated by the filled black circle in Fig. 5.5. During both pre-charging phases, the plant was charged at the maximum mass flow rate, which in-

Table 5.2: Operating conditions of the high-temperature test runs.

Run	Cycle	Δt_{pc} [h]	Δt_c [h]	Δt_d [h]	$\dot{m}$, $T_{c,\text{in}}$, $\tilde{p}_{\text{cav}}$
	A1	40:10	2:45	2:45	Figs. 5.7 & 5.9
	A2		2:45	2:45	Fig. 5.9
	A3		2:45	2:45	Fig. 5.9
1	B1	4:59	4:00	1:07	Fig. 5.9
	B2		3:22	1:01	Fig. 5.9
	B3		3:34	1:05	Fig. 5.9
	A1	42:00	2:45	2:45	Figs. 5.8 & 5.10
	A2		2:45	2:45	Fig. 5.10
	B1		1:22	1:22	Fig. 5.10
2	B2		1:22	1:22	Fig. 5.10
	C1		4:07	4:07	Fig. 5.10
	C2		4:07	4:07	Fig. 5.10
	C3		4:07	4:07	Fig. 5.10

creased with increasing back pressure from the cavern. The maximum mass flow rate was limited to protect measurement equipment and the steel cover.

As can be seen from Fig. 5.7, during the pre-charging phase of run 1 the plant was charged with cold compressed air for the first five hours. Afterwards, the charging temperature was rapidly increased and kept constant at $T_{c,\text{in}} \approx 525\,^{\circ}\text{C}$. During the pre-charging phase of run 2, the inlet temperature was ramped slowly from $20\,^{\circ}\text{C}$ to about $550\,^{\circ}\text{C}$ and then kept constant. The temporal evolution of the inflow temperature results in a spatial temperature distribution in the TES due to the flow. The ramp, which was designed with the numerical model, therefore leads to a shallower thermocline than if the inflow temperature were immediately set to its maximum of $550\,^{\circ}\text{C}$. Because the shallower thermocline more closely resembles the thermocline at quasi-steady conditions, pre-charging allows quasi-steady cycling conditions of the TES to be reached more quickly. There was a short interruption during pre-charging where the plant was switched to discharge mode. In both runs, the cavern gauge pressure increased to about 6 bar.

One can make three observations about the agreement between the
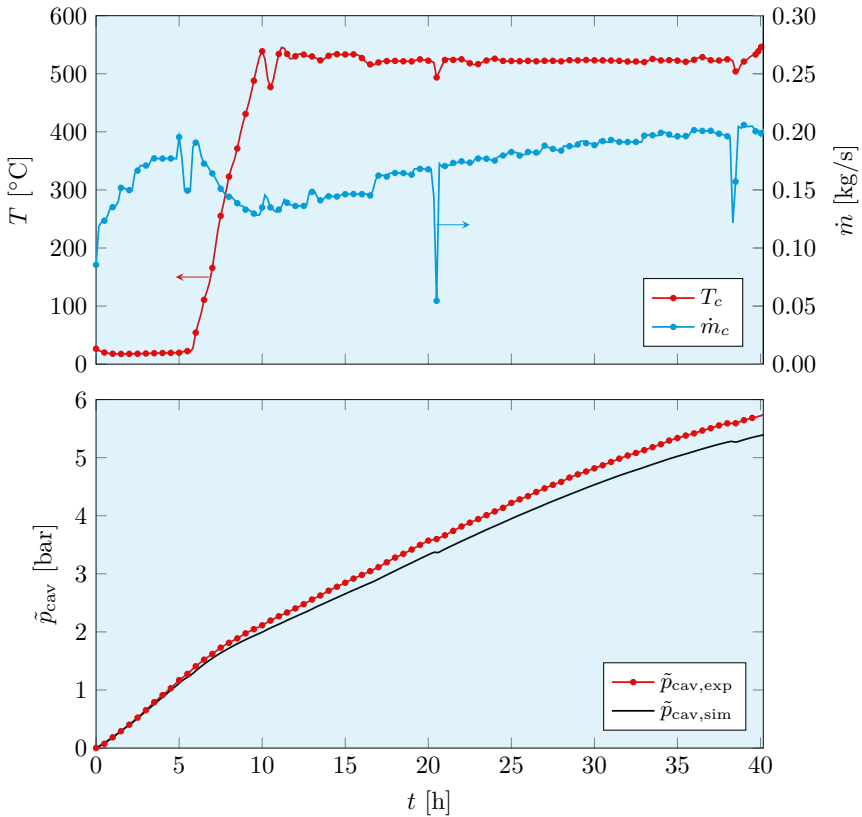
Figure 5.7: Measured charging temperature, measured mass flow rate, and comparison of measured and simulated cavern gauge pressures during pre-charging phase of run 1 of the high-temperature tests.
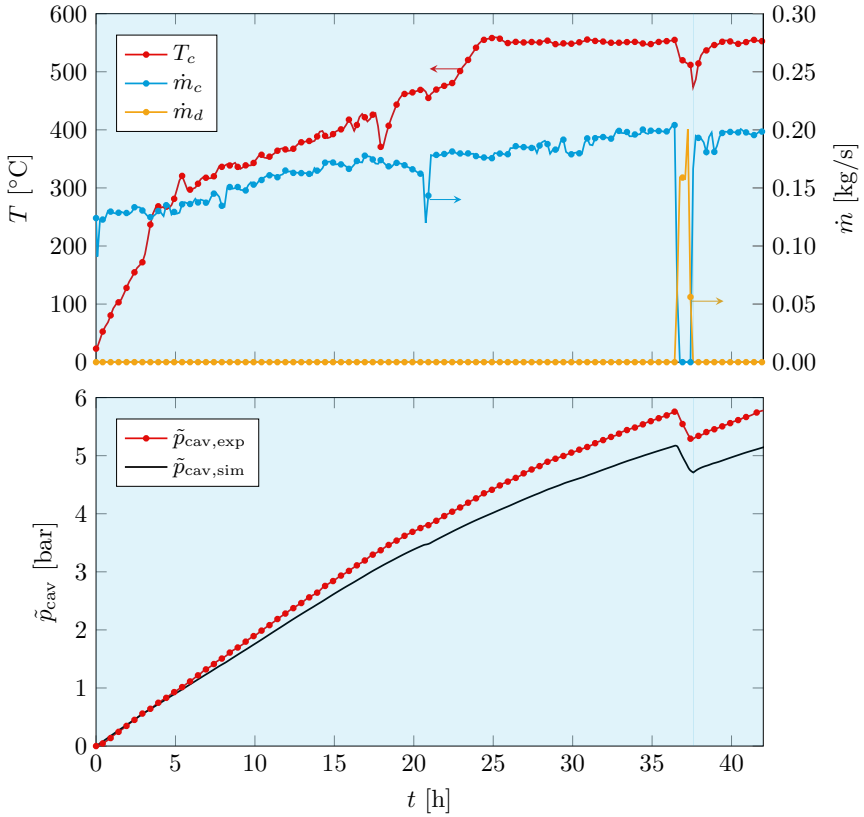
Figure 5.8: Measured charging temperature, measured mass flow rate, and comparison of measured and simulated cavern gauge pressures during pre-charging phase of run 2 of the high-temperature tests.

measured and simulated cavern gauge pressures. First, the agreement is seen to be fairly good overall, with better agreement at lower gauge pressures. Second, the agreement worsens from run 1 to run 2. These two observations may indicate that the leakage rate changes with time. Finally, it should be noted that perfect agreement between the measured and simulated cavern gauge pressures can be obtained by extracting for each run a separate correlation for the total leakage mass flow rate. This was omitted because it causes the comparison with experimental data to degenerate into a curve-fitting exercise.

Cavern

Figures 5.9 and 5.10 show the measured and simulated temperatures at the top of the TES, the measured mass flow rates, and the measured and simulated cavern gauge pressure during the cycles of run 1 and run 2, respectively. The charging temperature for all cycles was $T_{c,\text{in}} \approx 550\ °\text{C}$.

The measured and simulated temperatures coincide during the charging and re-charging phases because the former were used as boundary conditions in the simulations. The simulations were carried out for two values of the bypass flow fraction in the TES, 0% and 15%. The agreement between the measured and simulated outflow temperatures during discharging is better for the bypass flow fraction of 15%. Reasons for bypassing in the TES are the increased void fraction in the packed bed near the walls and air losses in the steel cover due to deformation of steel components. The deformation of the steel cover resulted from the pressure difference between the inside of the steel cover and the cavern because of the pressure drop across the packed bed. Considering the size of the TES, the wall bypassing is assumed to be small. During run 2, the agreement between the simulated and measured temperatures for the bypass flow fraction of 15% is good during the first discharging phase. In the subsequent discharging phases, the agreement becomes worse, which is thought to be due to increasing air losses from the piping and the steel cover.

The measured and simulated cavern gauge pressures agree quite well.
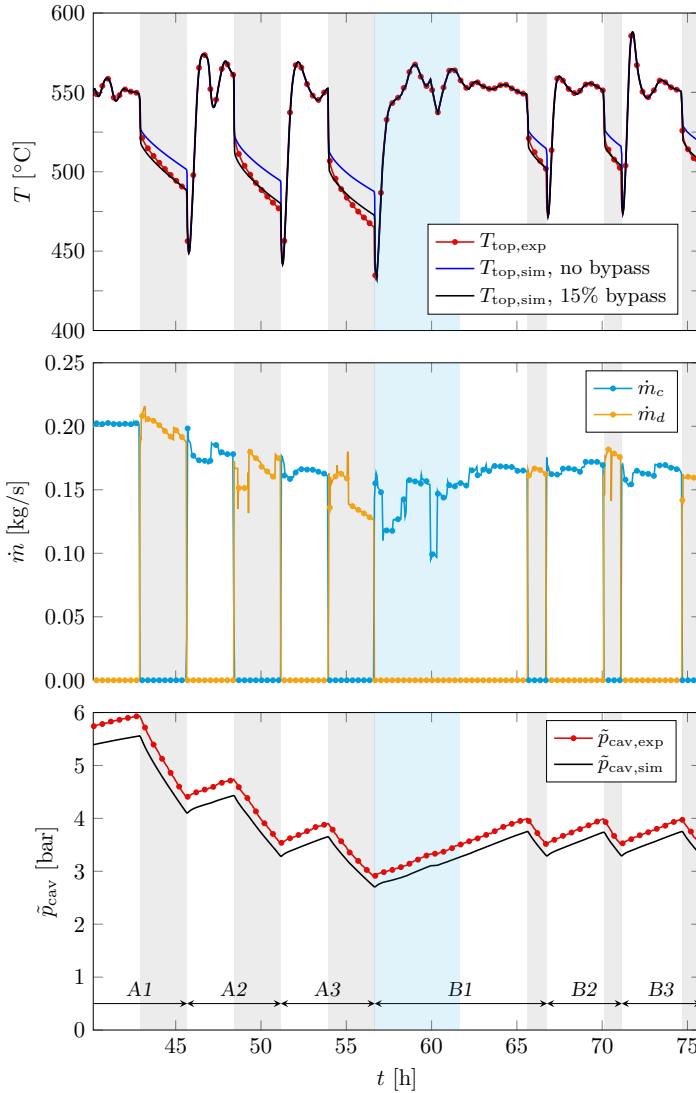
Figure 5.9: Measured and simulated temperature at the top of the TES, measured mass flow rates, and measured cavern gauge pressure during cycles for run 1 of high-temperature tests (excluding pre-charging phase shown in Fig. 5.7).
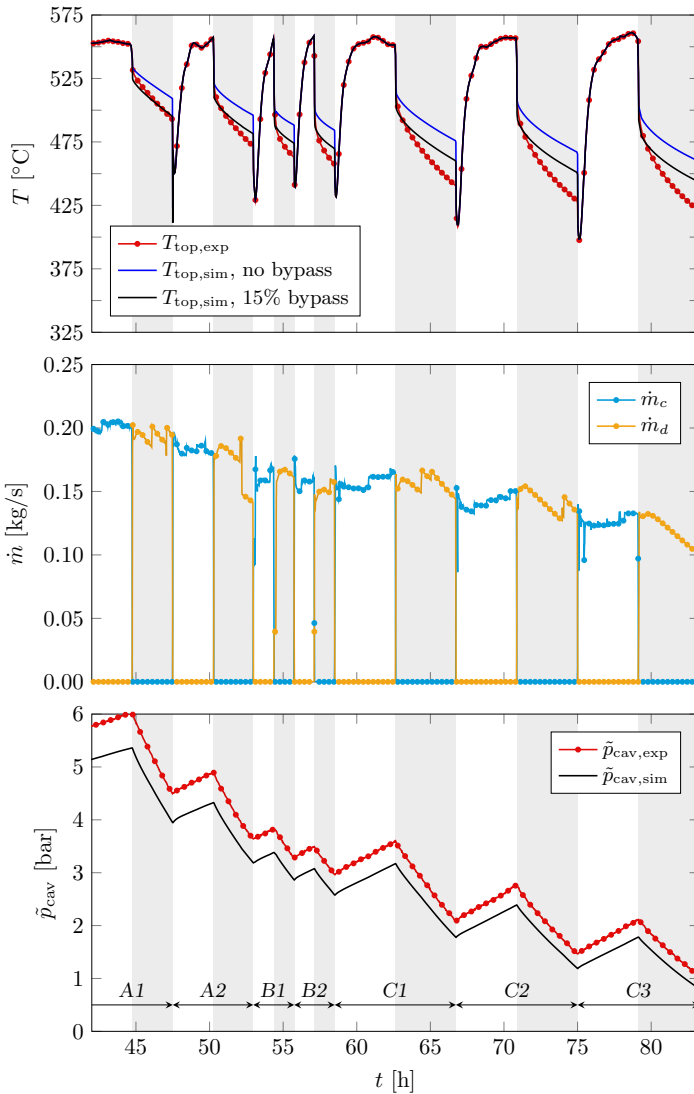
Figure 5.10: Measured and simulated temperature at the top of the TES, measured mass flow rates, and measured cavern gauge pressure during cycles for run 2 of high-temperature tests (excluding pre-charging phase shown in Fig. 5.8).
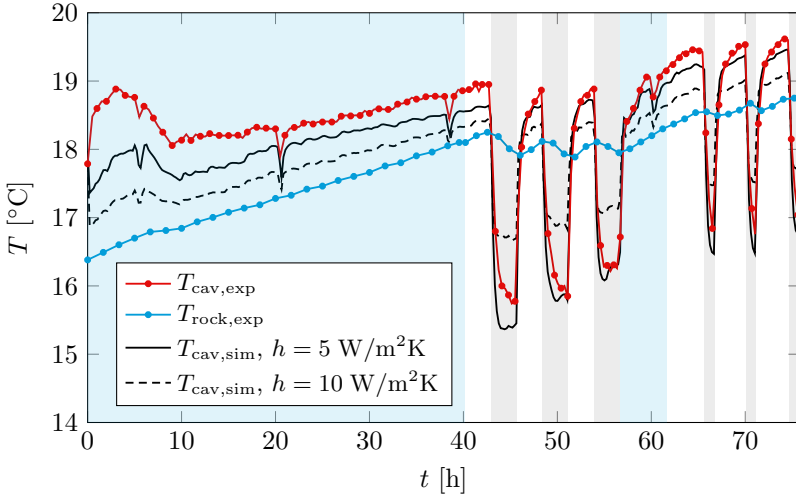
Figure 5.11: Measured and simulated cavern temperatures and measured rock temperature for run 1 of the high-temperature tests.

The overall decrease in the gauge pressures is a consequence of the above-mentioned air leaks. It is interesting to note that the relative errors between the measured and simulated absolute cavern pressures remains approximately constant. The relative errors at the beginning and at the end of the first run are 5.4% and 4.5%, and 10.3% and 13.0% for the second run, respectively. This means that the difference between the pressures during cycling is determined mostly by the difference at the end of the pre-charging phase.

In Figs. 5.11 and 5.12, the measured and simulated cavern temperatures and the measured rock temperature are presented. The simulations were performed with heat-transfer coefficients of $h = 5$ W/m^{2}K and 10 W/m^{2}K. For the former, good agreement was obtained between the simulated and measured cavern temperatures with maximum temperature differences of around 1 °C for both runs. The value of $h = 5$ W/m^{2}K is somewhat smaller than previously used values for modeling of the salt cavern of the Huntorf plant [152, 153]. This is attributed to the different cavern shapes
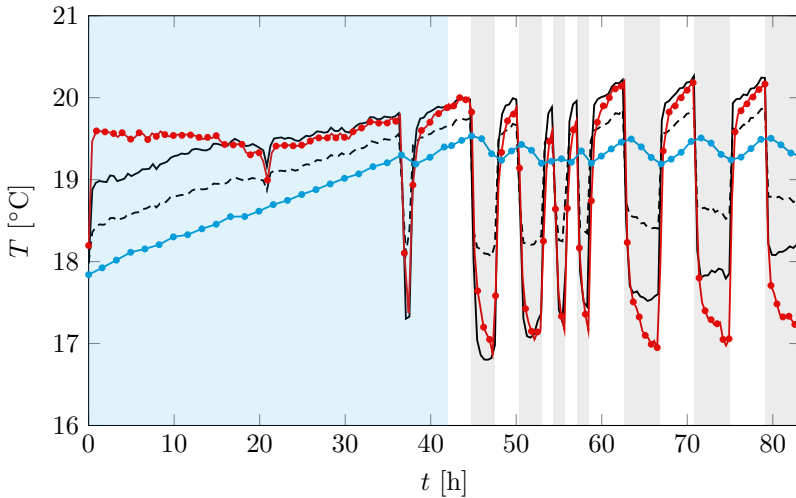
Figure 5.12: Measured and simulated cavern temperatures and measured rock temperature for run 2 of the high-temperature tests. See the legend in Fig. 5.11 for an explanation of the lines and symbols.

and materials as well as the location of the temperature measurement (inside the rock and therefore affected by its thermophysical properties).

TES

The measured temperatures and the simulated thermoclines are shown in Figs. 5.13 and 5.14 at four times during the pre-charging phases. The symbols indicate the measurement locations in Fig. 5.5 and the solid and dashed lines represent the averages of the simulated air and rock temperatures with 0% bypass and 15% bypass fractions, respectively.

Although the TES is relatively large and wall effects are therefore not expected to be significant, measurements at equal axial positions nevertheless differ by up to 75 °C. These differences may be attributed to the following causes. First, the steep thermoclines mean that even small differences in axial placement of the RTDs can result in relatively large temperature differences.
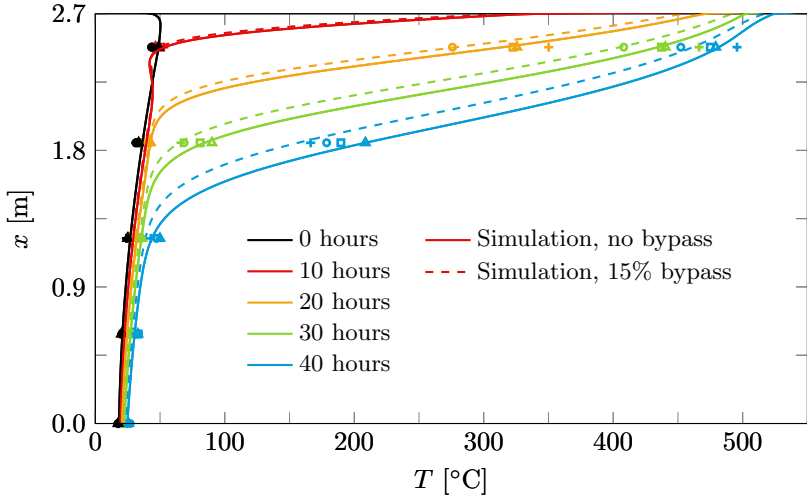
Figure 5.13: Measured temperatures and simulated thermoclines during pre-charging for run 1 of high-temperature tests. The symbols correspond to the measurement locations in Fig. 5.5. The simulated temperature is the average of the air and rock temperatures.

For example, the average thermocline slopes extracted from the simulations are approximately 1227 °C/m and 545 °C/m after 10 and 40 hours of run 1, respectively. Assuming that the vertical inaccuracy in placing the RTDs is 5 cm, the corresponding differences in the temperature would be 61 °C and 27 °C, respectively. The second cause might be non-uniform flow distribution at the top of the packed bed, perhaps partially due to the distributor and partially due to the leaks from the steel cover. This explanation appears plausible given that the differences between the measured temperatures are somewhat larger near the top of the packed bed. Finally, measurement errors are expected to contribute to the differences. The maximum error of the RTD measurement at 550 °C is ±3.1 °C.

The agreement between the measured temperatures and the simulated thermoclines is considered to be good, given that the latter mostly fall in
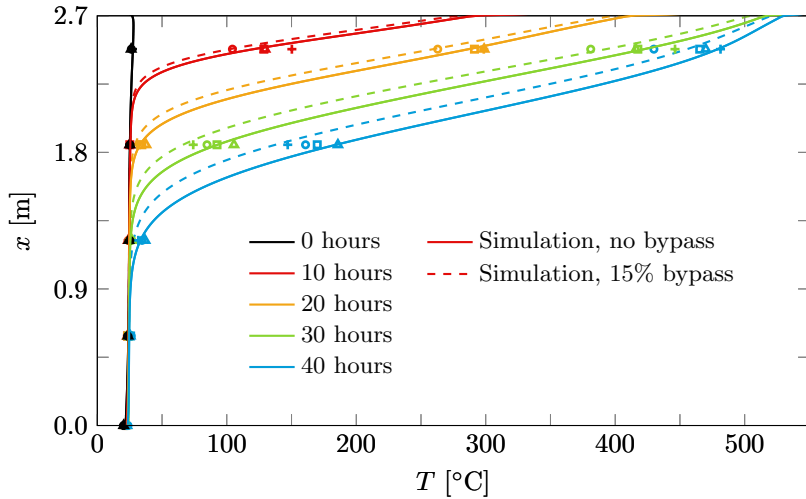
Figure 5.14: Measured temperatures and simulated thermoclines during pre-charging for run 2 of high-temperature tests. The symbols correspond to the measurement locations in Fig. 5.5. The simulated temperature is the average of the air and rock temperatures.

the ranges of the former at the various axial locations. For the larger bypass fraction of 15%, the agreement is slightly better at later times and further down in the TES.

Figures 5.15 and 5.16 present the measured and simulated temperatures as a function of time at three axial positions in the TES. The experimental data is an average of all measurements at the same axial position and the simulated data is an average of the air and rock temperatures assuming a bypass fraction of 15%. The agreement between the measured and simulated temperatures improves with time for run 1, whereas it becomes worse for run 2.
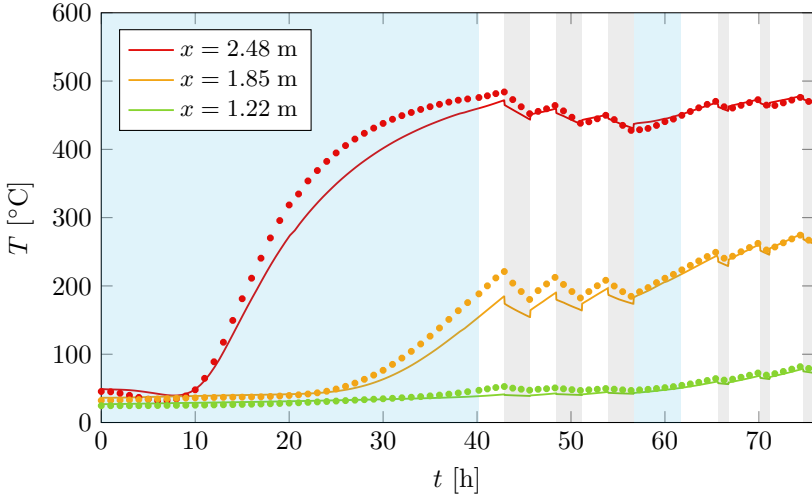
Figure 5.15: Comparison of measured (symbols) and simulated (lines) temperatures in TES as a function of time for run 1 of the high-temperature tests. Measured temperatures are averaged over all RTDs at the same height and simulated temperatures are averages of air and rock temperatures.

TES and plant efficiencies

The cycle energy efficiency of the TES is defined as

$$\eta_{\text{TES}} = \frac{E_{\text{th},d}}{E_{\text{th},c}}, \tag{5.6}$$

where $E_{\text{th},d}$ and $E_{\text{th},c}$ are the thermal energies provided to and recovered from the TES,

$$E_{\text{th},d} = \int_0^{\Delta t_d} \dot{m}_d(t) \left[e(T_{d,\text{out}}(t)) - e(T_{d,\text{in}}(t)) \right] \mathrm{d}t, \tag{5.7}$$

$$E_{\text{th},c} = \int_0^{\Delta t_c} \dot{m}_c(t) \left[e(T_{c,\text{in}}(t)) - e(T_{c,\text{out}}(t)) \right] \mathrm{d}t, \tag{5.8}$$

where Δt_d and Δt_c are the discharging and charging durations, respectively, and $e(T)$ is the specific internal energy of the air, computed from the
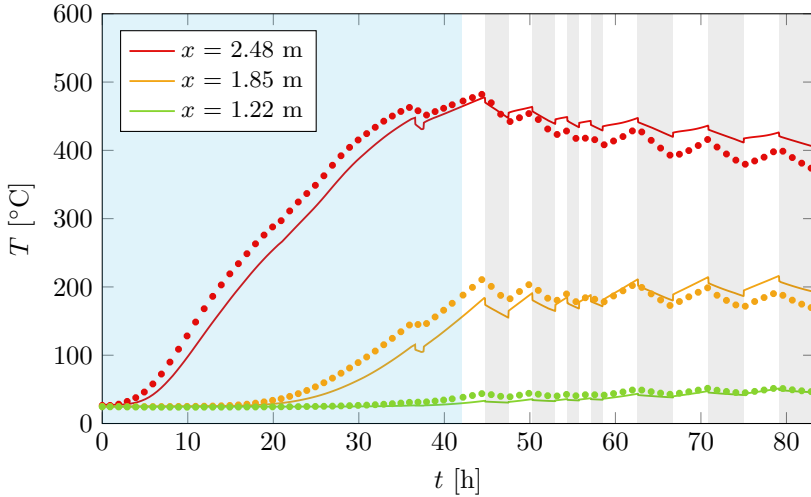
Figure 5.16: Comparison of measured (symbols) and simulated (lines) temperatures in TES as a function of time for run 2 of the high-temperature tests. Measured temperatures are averaged over all RTDs at the same height and simulated temperatures are averages of air and rock temperatures.

indicated measured time-dependent temperatures.

The cycle exergy efficiency of the TES is defined as

$$\eta_{\mathrm{ex,TES}} = \frac{\Xi_{\mathrm{th},d}}{\Xi_{\mathrm{th},c}}, \tag{5.9}$$

where $\Xi_{\mathrm{th},d}$ and $\Xi_{\mathrm{th},c}$ are the thermal exergies provided to and recovered from the TES,

$$\Xi_{\mathrm{th},d} = \int_0^{\Delta t_d} \dot{m}_d(t) \left\{ h(T_{d,\mathrm{out}}(t)) - h(T_{d,\mathrm{in}}(t)) \right.$$
$$\left. - T_0 \left[s(T_{d,\mathrm{out}}(t)) - s(T_{d,\mathrm{in}}(t)) \right] \right\} \mathrm{d}t, \tag{5.10}$$

$$\Xi_{\text{th},c} = \int_0^{\Delta t_c} \dot{m}_c(t) \left\{ h(T_{c,\text{in}}(t)) - h(T_{c,\text{out}}(t)) \right.$$
$$\left. - T_0 \left[s(T_{c,\text{in}}(t)) - s(T_{c,\text{out}}(t)) \right] \right\} \mathrm{d}t, \quad (5.11)$$

where $h(T)$ and $s(T)$ are the specific enthalpy and exergy of the air. The reference state was taken as $T_0 = 15\ °\text{C}$.

The cycle efficiency of AA-CAES plants is usually defined as

$$\eta_{\text{plant}} = \frac{W_{\text{el,gen}}}{W_{\text{el,mot}}}, \quad (5.12)$$

where $W_{\text{el,gen}}$ and $W_{\text{el,mot}}$ are the electricity produced by the generator and the electricity consumed by the motor, respectively. To apply this definition to the pilot plant, it was assumed (1) that the motor drove an adiabatic compressor instead of an isothermal compressor and an electric heater and (2) that the pilot plant was equipped with a turbine and a generator. Then

$$W_{\text{el,gen}} = \eta_{\text{gen}} \int_0^{\Delta t_d} \dot{m}_d(t) c_{p,\text{air}} T_{d,\text{out}}(t) \eta_{\text{turb},s} \left[1 - \left(\frac{p_{\text{amb}}}{p_{\text{cav}}(t)} \right)^{\frac{\gamma-1}{\gamma}} \right] \mathrm{d}t,$$
$$(5.13)$$

$$W_{\text{el,mot}} = \frac{1}{\eta_{\text{mot}}} \int_0^{\Delta t_c} \frac{\dot{m}_c(t) c_{p,\text{air}} T_{\text{amb}}}{\eta_{\text{comp},s}} \left[\left(\frac{p_{\text{cav}}(t)}{p_{\text{amb}}} \right)^{\frac{\gamma-1}{\gamma}} - 1 \right] \mathrm{d}t, \quad (5.14)$$

where $\eta_{\text{turb},s} = 0.9$ and $\eta_{\text{comp},s} = 0.85$ are representative isentropic turbine and compressor efficiencies, respectively, $\eta_{\text{gen}} = \eta_{\text{mot}} = 0.97$ are representative generator and motor efficiencies, the ambient pressure p_{amb} was assumed to be 1 bar, and $\gamma = 1.4$ is the ratio of the specific heats of air. The specific heat capacity at constant pressure of the air was assumed to be constant at $c_{p,\text{air}} = 1041\ \text{J/kg K}$, which corresponds to its value at the average temperature between $T_{\text{amb}} = 15\ °\text{C}$ and the typical measured TES inlet temperature of $T_{c,\text{in}} \approx 550\ °\text{C}$.

As indicated in Eqs. (5.13) and (5.14), it was assumed that the compressor and turbine operate between ambient and time-dependent cavern pressures and that the temperature of the air flowing into the turbine is equal to the

measured time-dependent temperature of the air flowing out of the TES. The time-dependent cavern pressure was not taken from the experiments because of the leaks. Instead, the model presented in Section 5.3.2 was used to simulate an airtight cavern with the measured mass flow rates, a constant rock temperature of 15 °C, and a wall heat-transfer coefficient of h = 5 W/m^{2}K.

In estimating the plant efficiency, the pre-charging operation was modified from that used in the experiments so that the cavern pressure is consistent with the typical measured TES inlet temperature of $T_{c,\text{in}} \approx 550$ °C. Using

$$\frac{p_{\text{comp,out}}}{p_{\text{amb}}} = \left(\frac{T_{\text{comp,out},s}}{T_{\text{amb}}}\right)^{\frac{\gamma}{\gamma-1}} \tag{5.15}$$

and

$$T_{\text{comp,out},s} = T_{\text{amb}} + \eta_{\text{comp},s}(T_{\text{comp,out}} - T_{\text{amb}}) \tag{5.16}$$

and assuming that $T_{\text{comp,out}} = T_{c,\text{in}} \approx 550$ °C, one obtains $p_{\text{comp,out}} =$ 27.52 bar. Therefore, pre-charging was simulated until the cavern pressure reached this value, assuming a constant mass flow rate of $\dot{m}_{pc} = 0.2$ kg/s. Together with the air temperature in the cavern after pre-charging of 16.6 °C, subsequent charging-discharging cycles were then simulated using the cavern model to obtain $p_{\text{cav}}(t)$ and the plant efficiency was computed.

The TES and plant efficiencies are given in Table 5.3. Because efficiencies are only meaningful for cycles with $\Delta t_d = \Delta t_c$, the efficiencies of cycles B1, B2, and B3 of run 1 are not reported. The TES efficiency is seen to range from 76.7% to 90.9%. These are already fairly high efficiencies and it can be expected that they further increase for large-scale TES. The plant efficiency lies between 62.7% and 73.8%, which compares favorably with the usually quoted range of 60-75%. The impact of thermal losses from the TES and the cavern on the plant efficiency can be estimated by comparing it to the theoretical plant efficiency in the absence of thermal losses [154],

$$\eta_{\text{plant,max}} = \eta_{\text{gen}}\eta_{\text{mot}}\eta_{\text{turb},s}\left(1 - \frac{1 - \eta_{\text{comp},s}}{(p_{\text{comp,out}}/p_{\text{amb}})^{\frac{\gamma-1}{\gamma}}}\right), \tag{5.17}$$

Table 5.3: TES and plant cycle efficiencies of pilot-plant configuration, computed from experimentally measured mass flow rates and temperatures and assuming an airtight cavern.

Run	Cycle	η_{TES}	$\eta_{\mathrm{ex,TES}}$	$\eta_{\mathrm{plant,est}}$
	A1	90.9%	88.7%	73.8%
1	A2	83.7%	80.0%	68.4%
	A3	76.7%	72.8%	62.7%
	A1	88.1%	85.7%	70.2%
	A2	82.8%	79.7%	66.2%
	B1	89.7%	86.3%	69.6%
2	B2	87.5%	82.9%	69.7%
	C1	85.1%	79.2%	70.4%
	C2	85.1%	78.5%	70.2%
	C3	78.7%	71.9%	65.2%

which was derived assuming constant and equal charging and discharging durations and mass flow rates. For the assumed isentropic efficiencies and the pressure ratio of 27.52, one obtains $\eta_{\mathrm{plant,max}} = 79.8\%$, indicating that thermal losses cause reductions in the efficiency of 6.0-17.1%.

5.5   Summary, conclusions, and further work

A pilot-scale AA-CAES plant was built in an unused tunnel. The cavern of 120 m length and 4.9 m diameter was confined by two concrete plugs and was mostly unlined. The TES consisting of a packed bed of rocks was placed inside the cavern to avoid pressure forces acting on its structure and had a maximum capacity of 12 $\mathrm{MWh_{th}}$. The pilot plant did not include a turbine.

Tests were carried out with charging temperatures of 550 °C, cavern gauge pressures between 0-7 bar, and various pre-charging, charging and discharging durations. The main conclusions from these tests are:

1. The deformation of the cavern induced by cyclic charging/discharging was found to be negligible.

2. The cavern suffered from leaks. The leaks were traced mostly to the concrete plugs. The unlined portion of the cavern was determined to have small or even negligible leaks. With an empirical correlation for the leakage mass flow rate as a function of the cavern gauge pressure, good agreement between simulated and measured cavern gauge pressures was obtained.

3. The TES performed well with energy efficiencies between 77% and 91% and exergy efficiencies between 72% and 89%. Good agreement was found between simulated and measured thermoclines, with discrepancies attributed partly to the deformation of the steel cover. The concrete structure, the insulation, and the rocks withstood the thermal cycling at high pressures.

4. Plant efficiencies were estimated using the measured mass flow rates and TES inflow/outflow temperatures and assuming isentropic compressor and turbine efficiencies as well as an airtight cavern. The estimated efficiencies were between 63% and 74%, consistent with the usually quoted values of AA-CAES plant efficiencies of 60-75%.

Further work will first focus on addressing the leaks from the concrete plugs. This work will evaluate proven techniques used for the storage of compressed gas in unlined caverns, see, e.g., [132, 133, 134]. Hydrodynamic containment appears to be a particularly attractive option. Attention will then shift toward the construction of a larger-scale pilot plant that includes a turbine.

EFFICIENT SOLAR-THERMOCHEMICAL FUEL PRODUCTION USING SENSIBLE HEAT RECUPERATION IN A DUAL-STORAGE REACTOR[1,2]

6.1 Introduction

Solar-thermochemical redox cycles allow liquid fuels to be produced from renewable energy, H_2O, and CO_2 [155, 41]. This conversion of intermittent solar energy into fuels allows not only for the long-term storage and long-

---

[1] Material in this chapter has been disclosed in A. Steinfeld, P. Furler, A. Haselbacher, and L. Geissbühler, "A thermochemical reactor system for a temperature swing cyclic process with integrated heat recovery and a method for operating the same," Pat. Appl. Nr. EP16194074, 2016.

[2] Material in this chapter is to be submited as L. Geissbühler, A. Pedretti, A. Haselbacher, A. Steinfeld, "Efficient solar-thermochemical fuel production using sensible heat recuperation in a dual-storage reactor," *Energy & Environmental Science*, to be submitted for publication, 2018.

range transport of solar energy, it may also be one path toward a sustainable energy future free of fossil fuels. Most commonly, solar-thermochemical redox cycles are two-step cycles using a metal oxide as an intermediate [156].

In this study, ceria is selected as the redox material because of its morphological stability and rapid kinetics [157]. In the endothermic reduction step, ceria is reduced at temperatures > 1573 K using concentrated solar energy,

$$CeO_2 \rightarrow CeO_{2-\delta} + \frac{\delta}{2}O_2\,, \tag{6.1}$$
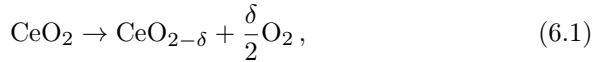
where δ is the oxygen nonstoichiometry. In the exothermic oxidation step, ceria is oxidized at temperatures < 1373 K, thereby splitting H_2O and CO_2 to produce syngas, a mixture of H_2 and CO,

$$CeO_{2-\delta} + \delta H_2O \rightarrow CeO_2 + \delta H_2, \tag{6.2}$$

$$CeO_{2-\delta} + \delta CO_2 \rightarrow CeO_2 + \delta CO\,. \tag{6.3}$$
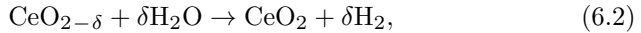
The syngas can be converted to liquid fuels using the well-established Fischer-Tropsch process [158].

The solar-to-fuel efficiency of the two-step redox cycle can be defined as

$$\eta_{\text{solar-to-fuel}} = \frac{\text{HHV}_{H_2} n_{H_2} + \text{HHV}_{CO} n_{CO}}{Q_{\text{solar}} + Q_{\text{penalties}}}, \tag{6.4}$$

where HHV is the higher heating value of the product gas, n is the number of moles produced, Q_{solar} is the solar energy input, and $Q_{\text{penalties}}$ is any additional energy required, such as for pumping or gas separation.

To assess the potential efficiencies of two-step redox cycles, thermodynamic analyses can be applied [157, 42, 159, 160, 161, 162]. The comparison of pure pressure swing (isothermal) cycles with combined pressure and temperature swing cycles revealed that the maximum efficiencies of the former are limited irrespective of the redox material [160, 161]. The low efficiencies are caused by thermodynamically limited product-gas concentrations during oxidation. Cycles with combined pressure and temperature swings have been demonstrated in experiments and observed to lead to the highest efficiencies. To the best knowledge of the author, the highest efficiency

demonstrated so far is $\eta_{\text{solar-to-fuel}} = 5.25\%$, obtained with a 4 kW single-cavity laboratory-scale reactor using non-stoichiometric ceria as the redox material [163]. The reduction and oxidation temperatures were about 1773 K and 1173 K, respectively, and the total pressure during reduction was 10 mbar.

For economically viable production using the solar-thermochemical redox cycles, higher efficiencies are necessary. The main improvements required to reach higher efficiencies with the single-cavity reactor design were identified to be [164]:

1. Recuperation of the sensible heat of the redox material between the reduction and oxidation temperatures.

2. Recuperation of the sensible heat carried by the hot gases exiting the reactor.

3. Reduction of reradiation losses through the reactor aperture.

4. Reduction of conduction losses through the reactor insulation.

Conduction losses through the insulation generally decrease with increasing reactor size and are therefore less significant for pilot- and industrial-scale reactors. Reradiation losses decrease with higher solar concentration ratios and operation at lower temperatures, and therefore depend on the design of the solar field and the reaction characteristics of the redox material, respectively. By contrast, sensible-heat recuperation is a matter of reactor design. Sensible-heat recuperation is the most promising way to increase the solar-to-fuel efficiency because the energy needed to heat the redox material from the oxidation to the reduction temperature is typically significantly larger than the reaction energy as well as the reradiation losses [157]. By increasing the sensible-heat recuperation of the redox material and the reaction gases from 0% to 100%, the maximum predicted solar-to-fuel efficiency using ceria as the redox material rises from less than 20% to almost 60% [42].

Several reactor concepts that incorporate sensible-heat recuperation from the redox material have been proposed:

1. A concept consisting of counter-rotating redox material rings was proposed, where one side is exposed to concentrated solar radiation and held at reduction temperature while the other side is held at oxidation temperature [43]. The counter-rotating rings act as solid-solid heat recuperators.

2. A concept with two concentric counter-rotating cylinders was developed, where the hollow outer cylinder is made from ceria and the inner cylinder is made from an inert ceramic to provide a heat-recuperation mechanism [44].

3. A concept based on a continuously moving packed bed of redox material particles [45]. Using a solid-solid heat exchanger, the sensible energy is exchanged between the oxidized and reduced particles.

4. Another concept based on redox material particles was proposed by [46]. However, instead of a solid-solid heat exchanger, a solid-phase heat-transfer medium consisting of small particles is mixed with the redox material and used to recover the sensible energy. The more mixing stages are used, the more effective is the heat recovery.

5. A concept using liquid metal as a heat-transfer fluid (HTF) to absorb solar energy in the receiver and exchange heat between reactors [47]. The maximum heat-recovery effectiveness ε scales with the number of reactors N as $\varepsilon = 1 - 1/N$.

Because reactor concepts 1 to 4 require the redox material to be rotated or transported at very high temperatures, challenging problems such as material attrition, obstruction of moving parts, and/or material storage must be addressed. Reactor concept 5 avoids moving of the redox material by using liquid metal as a HTF. However, the pumping of liquid metals requires that high-temperature pumps based on graphite or ceramics be developed.

In this chapter, a new solar-thermochemical redox reactor concept is presented that includes sensible-heat recuperation from the redox material but avoids the need to rotate or transport the redox material or to develop

pumps for liquid metals.   The so-called dual-storage reactor concept is based on two thermocline thermal energy storages that allow for heat recuperation between the oxidation and reduction steps [165].

The objectives of this chapter are to explain the dual-storage reactor concept, to demonstrate the concept through laboratory-scale experiments, and to assess the performance of a large-scale dual-storage reactor.

6.2   Dual-storage reactor concept

The dual-storage reactor consists of two vertically oriented packed beds of inert material on top of which the redox material is placed as shown in Fig. 6.1. The packed beds serve as thermal energy storage (TES) units in which axial temperature profiles (thermoclines) are established [166, 18, 22]. The TES units are oriented vertically to exploit stratification and to ensure that the inert material occupies the entire cross section of the units. By pumping a HTF through the TES units, the thermoclines are moved up and down. Therefore, the redox-material sections are alternately exposed to the reduction and oxidation temperatures and hence sensible heat is recuperated between the reduction and oxidation steps. In Fig. 6.1, ideal temperature profiles are indicated by black and blue lines. The ideal temperature profiles have plateaus at the reduction, oxidation, and ambient temperatures. The blue temperature profiles show the reaction zone in the left/right tank undergoing reduction/oxidation, respectively, and vice versa for the black temperature profiles.

A heating zone increases the HTF temperature between the reaction zones to provide the reduction enthalpy and to compensate for thermal losses and the degradation of the thermoclines. As suggested in Fig. 6.1, the heating zone could consist of a receiver that concentrates solar radiation. Because the redox material is not exposed to direct irradiation, local hot spots that can induce material attrition are avoided. Furthermore, because heat is transferred to the redox material by convection instead of radiation, more conventional reactor and redox material geometries can be chosen. For
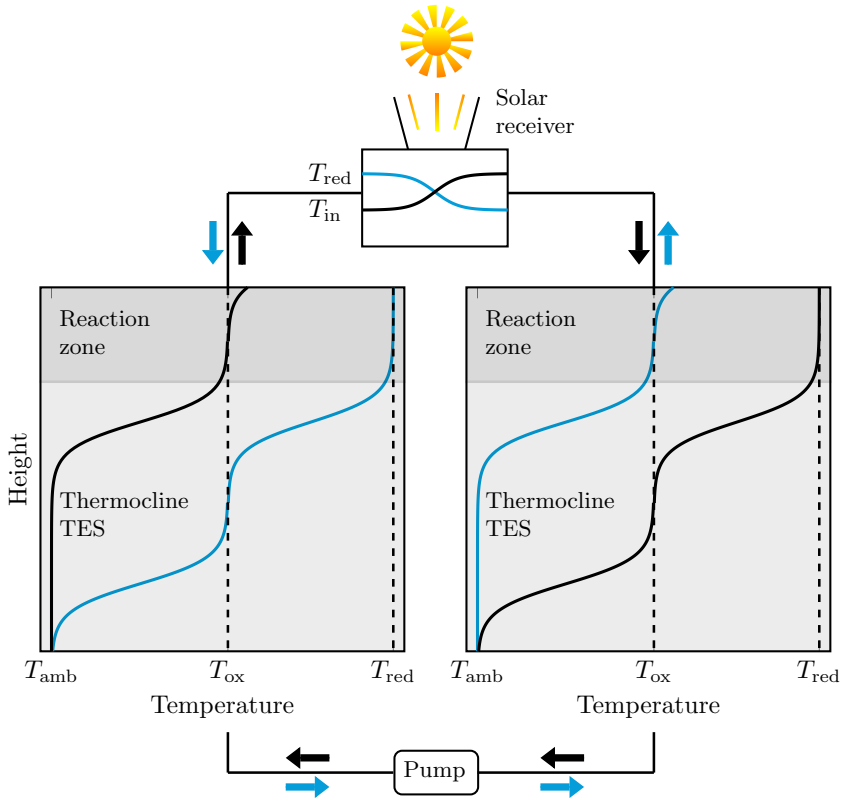
Figure 6.1: Ideal temperature plateaus inside the two tanks of the dual-storage reactor. The reaction zones and the thermocline TES are shaded in darker and lighter grays, respectively. Blue lines correspond to the operation in which the left tank is brought to reduction temperatures and the right tank to oxidation temperatures. Black lines correspond to the reverse operation.

example, the ceria RPC (reticulated porous ceramic) structures that are typically used in single-cavity reactors can be replaced by a packed bed of ceria particles.

To support the reduction of the redox material, the reactor is either flushed with inert gas or a vacuum is pulled. During oxidation of the redox material, H_2O and CO_2 are injected into the reaction zone to produce syngas.

Figure 6.1 indicates that the pump for the HTF is located at the bottom of the TES units, where the temperature is close to ambient. This has the advantages that high-temperature pumps are not needed and that the pumping work is reduced.

In the following, the key components of the dual-storage reactor are described in more detail.

6.2.1   Reaction zone

Reactions zones with direct and indirect contact between the HTF and the redox material can be used in the dual-storage reactor. Figure 6.2 shows a schematic of the reaction zone where the redox material is in direct contact with the HTF. Direct contact has the advantages of good heat transfer and no additional piping requirements to connect the reactor zone with the reaction-gas supplies (e.g., H_2O and CO_2). The main disadvantage is that the HTF needs to be inert with the redox material. During reduction, oxygen needs to be flushed away by the HTF, thereby polluting inert HTF. If the polluted HTF cannot be recycled, the energy efficiency of the process is reduced significantly [45]. Using a second, lower temperature redox cycle, the inert HTF can be cleaned and recycled [167]. This complicates the concept but may keep the efficiency of the whole process high.

Figure 6.3 shows a schematic of the reaction zone where the redox material is in indirect contact with the HTF. The disadvantages are an additional thermal resistance between HTF and redox material, as well as demanding requirements on the encapsulation material. The material should not react with the redox material or the HTF, withstand very high temperatures, and suppress diffusion of oxygen and other gases. Despite these complications, encapsulation is interesting as it confers several advantages:

- The HTF does not need to be inert with the redox material and can
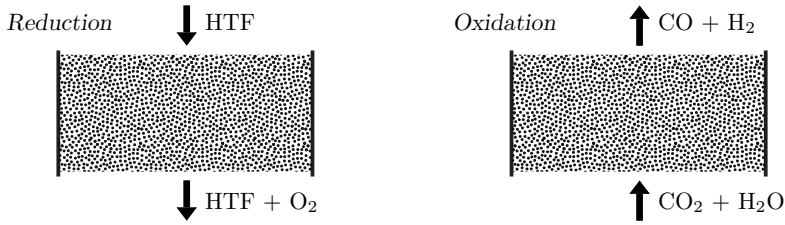
Figure 6.2: Schematic of the reaction zone with direct contact between redox material and HTF.
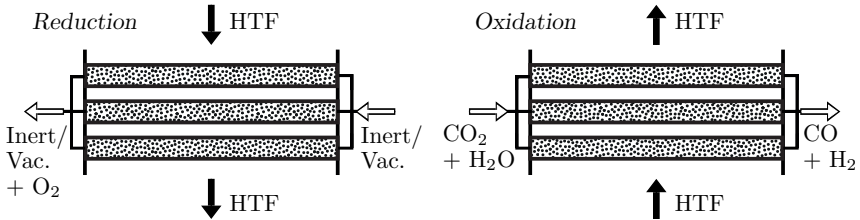
Figure 6.3: Schematic of the reaction zone with indirect contact between redox material and HTF.

be, e.g., air.

- Inert HTF cleaning is not needed.

- To decrease the pumping work, the HTF can be pumped at high pressures.

- The required HTF atmosphere for the chemical reaction during reduction and oxidation needs to be adjusted only locally inside the encapsulation. The vacuum can be pulled locally during reduction for efficient removal of oxygen as only a small volume needs to be evacuated.

For simplicity, in the laboratory-scale experimental setup, the ceria is in

direct contact with the HTF. The potential of encapsulated ceria is studied with the numerical model and will be presented in Section 6.4.

6.2.2   TES

The storage material at the top of the TES has to withstand temperatures as high as the reduction temperature of the redox material, i.e., about 1773 K. Such very high temperatures are not common in concentrated solar power (CSP) plants, in which TES units are important components [6, 7]. However, such temperatures are common in industrial applications such as steel production, in which regenerators containing ceramic bricks are employed to preheat air to 1573-1873 K [17]. Experimental data on the performance of TES units at high to very high temperatures are quite limited. An experimental facility using ceramics-based checkerwork that could be charged at up to 1573 K was described in [15]. Experimental data for a packed bed of ZrO_2 pellets tested between 298 and 1253 K was presented by [14].

In this study, the TES units were chosen to be packed beds of alumina spheres. Packed beds are of interest because their high convective heat-transfer rates. Alumina is used because it is compatible with the elevated temperatures and because of its high storage density [168].

It is important to note that the thermocline TES units in the dual-storage reactor differ from typical (single-media) thermocline TES units for CSP plants. In the latter, there are usually two plateaus at the charging and discharging temperatures, whereas in the former, there are three desired plateaus at the reduction, oxidation, and ambient temperatures.[3]

6.2.3   Solar receiver

As shown schematically in Fig. 6.1, the purpose of the solar receiver is to upgrade the left/right tank outlet HTF temperature to the reduction

---

[3]The reduction and ambient temperatures can be interpreted as the charging and discharging temperatures of the TES units in the dual-storage reactor.

temperature before it enters the right/left tank. For a highly efficient fuel
production cycle, a large portion of this energy input originates from the
consumed heat of reaction. The rest of the required energy originates
from irreversibilities such as thermal losses and thermocline degradation.
For a well designed dual-storage reactor using ceria as redox material, the
corresponding temperature upgrade would be around $\Delta T_{\mathrm{rec}} = 50$ to 200 K
(see Section 6.4 for an example). In order to obtain a stable receiver outflow
temperature, the mass flow rate would need to be adjusted depending on
the present solar irradiation and the inlet temperature.

The operation of a windowless pressurized air receiver was demonstrated
at pressures up to 6 bar and gas exit temperatures up to 1479 K [169].
Receiver gas exit temperatures up to 1573 K were demonstrated using CO_2
as HTF at pressures of $p_{\mathrm{HTF}} = 10$–30 bar in a receiver with window [170].
Although no receiver has been demonstrated with HTF exit temperatures
up to 1773 K, the requirements appear to be feasible considering the low
ΔT_{rec}, which is up to one order of magnitude smaller than the ΔT_{rec} in the
mentioned alternative concepts in Section 6.1.

6.2.4   Thermocline control

To maximize the syngas production, the entire reaction zones should be
operated alternately at the reduction and oxidation temperatures. Therefore,
the ideal thermoclines should have plateaus at these temperatures, as shown
in Fig. 6.1. As the thermoclines are moved up and down by pumping of the
HTF, the axial extents of the plateaus reduce and hence the temperature
gradients between the plateaus reduce also. These changes in the thermo-
clines are commonly referred to as thermocline degradation. Typical reasons
for thermocline degradation are (1) limited heat-transfer rates between the
HTF and storage material, (2) axial heat conduction along the storage, (3)
heat exchange between the storage material and the storage container and
insulation, and (4) mixing of HTF at different temperatures due to vortical
flows at the inlet and outlet and bypass flows adjacent to the container wall.

To counteract thermocline degradation, it is necessary to resort to either

passive or active thermocline control (TCC). An overview of passive and active TCC methods is provided in Section 4.1. TCC in the dual-storage reactor is achieved partly by controlling the outflow temperature of the HTF leaving the solar receiver, leading to the plateau at the reduction temperature. To create and maintain the temperature plateau at the oxidation temperature, further TCC is necessary. The form of TCC used in this chapter consists of extracting and injecting HTF at certain axial positions and may be viewed as the reverse of the siphoning method [32], which is used to create (intermediate) temperature plateaus. In addition, a part of the thermocline of one tank is periodically expelled at approximately the oxidation temperature.

6.3 Experimental demonstration of the dual-storage reactor

A laboratory-scale experimental setup was used to demonstrate the dual-storage reactor concept with three main objectives:

1. Demonstration of thermocline TES at temperatures relevant to solar-thermochemical fuel production, i.e., $T > 1573$ K.

2. Demonstration of heat recovery between the reduction and oxidation temperatures by shifting of thermoclines in two adjacent TES.

3. Comparison of experimental data with simulation results prior to simulating a large-scale dual-storage reactor.

As mentioned earlier, for the laboratory-scale dual-storage reactor, the redox material is in direct contact with the HTF. Air was used as the HTF because the production of CO and H_2 was not an objective of the experiment.

6.3.1 Reactor configuration

For simplicity, the laboratory-scale reactor, shown in Fig. 6.4, differed from the reactor concept described in Section 6.2 in four ways: (1) The two TES units were arranged horizontally instead of vertically, with the heating and
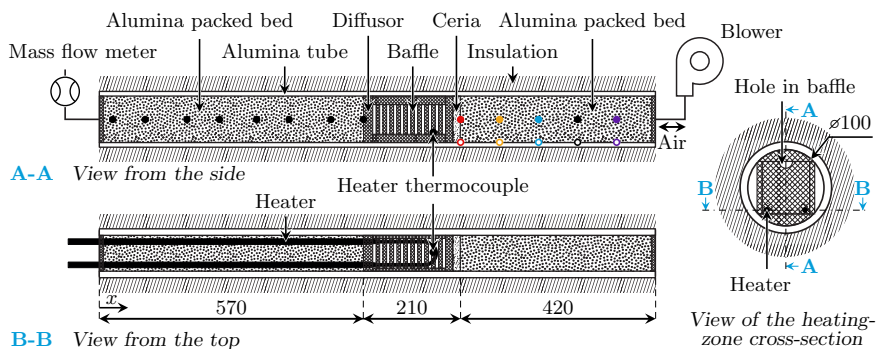
Figure 6.4: Schematic of the laboratory-scale dual-storage reactor. Only part of the actual insulation is shown. Insulation materials and corresponding thicknesses vary and are shown in Fig. 6.5. The colored circles indicate positions of thermocouples. Dimensions are given in mm.

reaction zones in-between, (2) the heating zone consisted of an electrical heater instead of a solar receiver, (3) only one reaction zone was used, where the reaction itself was neither studied nor driven, and (4) no TCC was performed. The last difference means that instead of three temperature plateaus shown in Fig. 6.1, only two plateaus could be established.

The packed beds, the heating zone, and the redox material were placed in a horizontal alumina tube, which had a length of 1200 mm and inner and outer diameters of 100 mm and 110 mm, respectively. The packed beds consisted of porous alumina spheres with a diameter of 1–3 mm, a density of 1073 kg/m^3 (corresponding to an internal porosity of 0.73), and a packed-bed solid-volume fraction of 0.686. Ceria was used as redox material in the form of a dual-scale RPC [171]. It had a thickness of 16 mm and a mean pore size of 2.25 mm. The strut-scale solid-volume fraction was 0.7 and the RPC-scale solid-volume fraction was 0.22. The heating zone consisted of a 1.3 kW$_{el}$ MoSi$_2$ electrical heating element and 10 square porous ceramic baffles to enhance the heat transfer. The baffles had openings alternately

at the top or bottom. The heating zone was separated from the packed bed and the RPC by porous ceramic diffusors that allowed the flow to pass only through the square section of the baffles. The insulation adjacent to the alumina tube consisted of rigid porous ceramic insulation boards from Schupp®, surrounded by microporous insulation panels from BIFIRE®. Fig. 6.5 shows the cross section of the insulation at various axial positions. The cross section of the porous ceramic insulation was cylindrical while that of the microporous insulation was annular with a square outer shape.

Air was pumped through the dual-storage reactor using a blower and valves were used to switch the flow direction. The heater temperature was PID-controlled using a pulse-width-modulated solid-state relay. The AC voltage and AC current of the heater were measured and used for the calculation of the RMS power. The mass flow was measured by a Bronkhorst® mass-flow meter. The temperature distribution along the reactor was measured using K- and B-type thermocouples.

6.3.2 Operation strategy

The operation of the laboratory-scale dual-storage reactor was divided into cycles, each of which consisted of three phases:

1. Heating/reduction phase: The electrical heater power was controlled such that the maximum heater temperature was never exceeded ($T_{\text{heater,max}} = 1893$ K) and air was pumped through the reactor. The flow direction was periodically alternated at intervals of about 20-30 s to prevent significant motion of the thermoclines in the packed beds. The resulting temperature profile in the entire dual-storage reactor was similar to a Gaussian, with a maximum temperature close to the reduction temperature and minimum temperatures close to the ambient temperature. Towards the end of the heating phase, air was pumped from left to right to shift the opposing thermoclines across the setup and to bring the ceria to reduction temperatures.

2. Cooling/oxidation phase: Air was pumped from right to left to shift
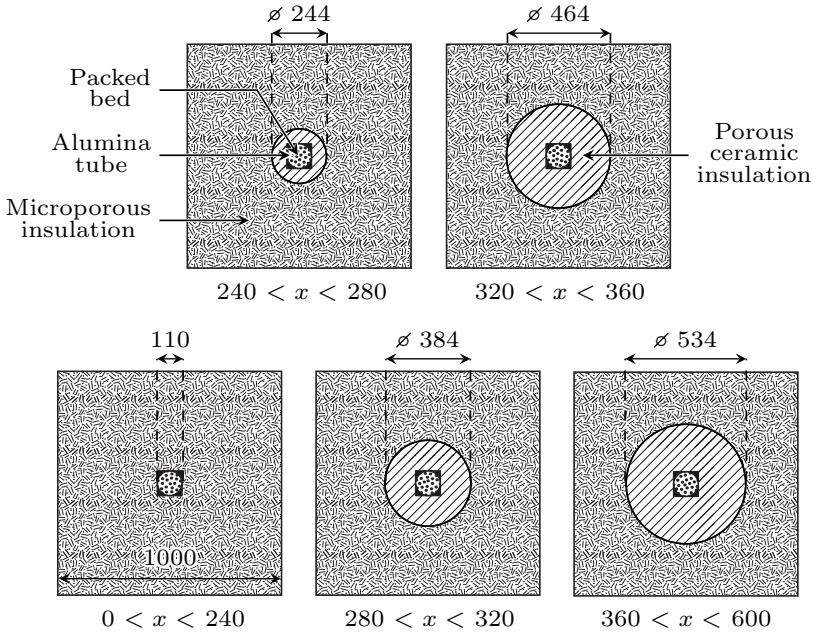
Figure 6.5: Schematic of the insulation cross sections for various axial positions of the laboratory-scale dual-storage reactor. Dimensions are given in mm. The axial coordinate x is defined in Figure 6.4. The insulation geometry is reflected about the middle of the alumina tube, i.e., about x = 600 mm. The gap between the circular alumina tube and the porous ceramic insulation, which had square shape towards the inside, was filled with alumina powder from the porous ceramic insulation (shaded in black).

the opposing thermoclines to the left and to bring the ceria to the oxidation temperature. The heater was turned off after approximately half of the cooling phase.

3. Heat-recovery phase: Air was pumped from left to right to recover the heat stored in the left packed bed. The heater was off during this

phase.

Figure 6.6 shows the measured power input from the electrical heater as well as the air mass-flow rates from the right and left for several consecutive cycles. During the alternating flow of the heating phase it was observed that although the blower power was kept constant, the mass flow rate was larger if the flow came from the right side (the blower pushing the air through the reactor) than if the flow came from the left side (the blower pulling the air through the reactor). This was observed from the temperature readings inside the reactor, in particular that of the heater. Therefore, to keep the temperature profile in the middle during the alternating flow, the time interval of the flow coming from the right was chosen to be $\Delta t_{r\rightarrow l} = 20$ s, while the time interval of the flow coming from the left had to be increased to $\Delta t_{l\rightarrow r} = 30$ s, or in other words $\Delta t_{r\rightarrow l} = 0.67\Delta t_{l\rightarrow r}$.

Since the mass-flow rate was only measured when the air came from the right ($\dot{m}_{r\rightarrow l}$), the mass-flow rate coming from the left ($\dot{m}_{l\rightarrow r}$) had to be estimated. According to the adjustments that had to be made to the time intervals during the alternating flow, the mass-flow rate coming from the left can be estimated to be around 67% of the one coming from the left. This would lead to equal amounts of air masses being injected from the left and right sides during the alternating time intervals.

After comparison with the simulation, it was found that a ratio of $\dot{m}_{l\rightarrow r} = 0.6\dot{m}_{r\rightarrow l,\mathrm{prev}}$ yielded good agreement with the simulation, which is similar to the estimated ratio. The previous mass flow rate $\dot{m}_{r\rightarrow l,\mathrm{prev}}$ was taken as the last measured value of the mass-flow rate coming from the right before switching of the flow direction.

The lower mass flow is attributed mainly to the fact that when the flow comes from the left the blower operates at underpressure as it has to suck the air through the dual-storage. This is explained in the following. The blower power was constant and is proportional to

$$P_{\mathrm{blower}} \propto \int \dot{V}\mathrm{d}p = \int \frac{\dot{m}_{r\rightarrow l}}{\rho_{\mathrm{right}}}\mathrm{d}p = \int \frac{\dot{m}_{l\rightarrow r}}{\rho_{\mathrm{left}}}\mathrm{d}p\,. \qquad (6.5)$$

where ρ_{right} and ρ_{left} are the air densities seen by the blower. For the flow
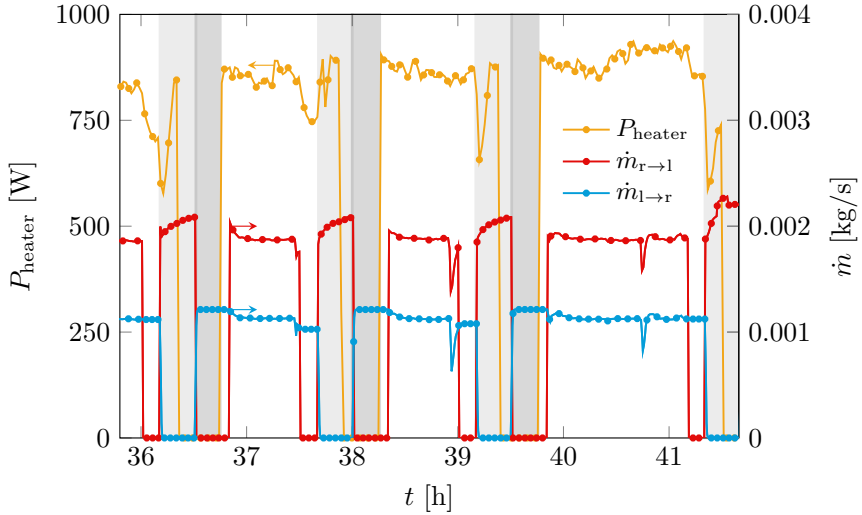
Figure 6.6: Heater power and mass-flow rates in the laboratory-scale dual-storage reactor as a function of time. The heating, cooling, and heat recovery phases are indicated by the white, lighter gray, and darker gray areas, respectively.

velocities of this setup, the pressure drop, based on Ergun's equation, is approximately proportional to the velocity (and not to the mass flow rate). Therefore, for a constant blower power, both the volume-flow rate and the pressure drop had to be approximately constant. Hence, from Eq. (6.5), a constant pressure drop, and assuming air densities of $\rho_{\text{right}} = 0.75\rho_{\text{amb}}$ and $\rho_{\text{left}} = 1.25\rho_{\text{amb}}$ one obtains $\dot{m}_{\text{l}\rightarrow\text{r}} = 0.6\dot{m}_{\text{r}\rightarrow\text{l,prev}}$.

6.3.3 Results and comparison with simulations

In Fig. 6.7, the simulated temperature distributions are compared with the measured temperatures along the centerline and the wall of the dual-storage reactor during the heating/reduction phase at $t = 37.68$ h, during
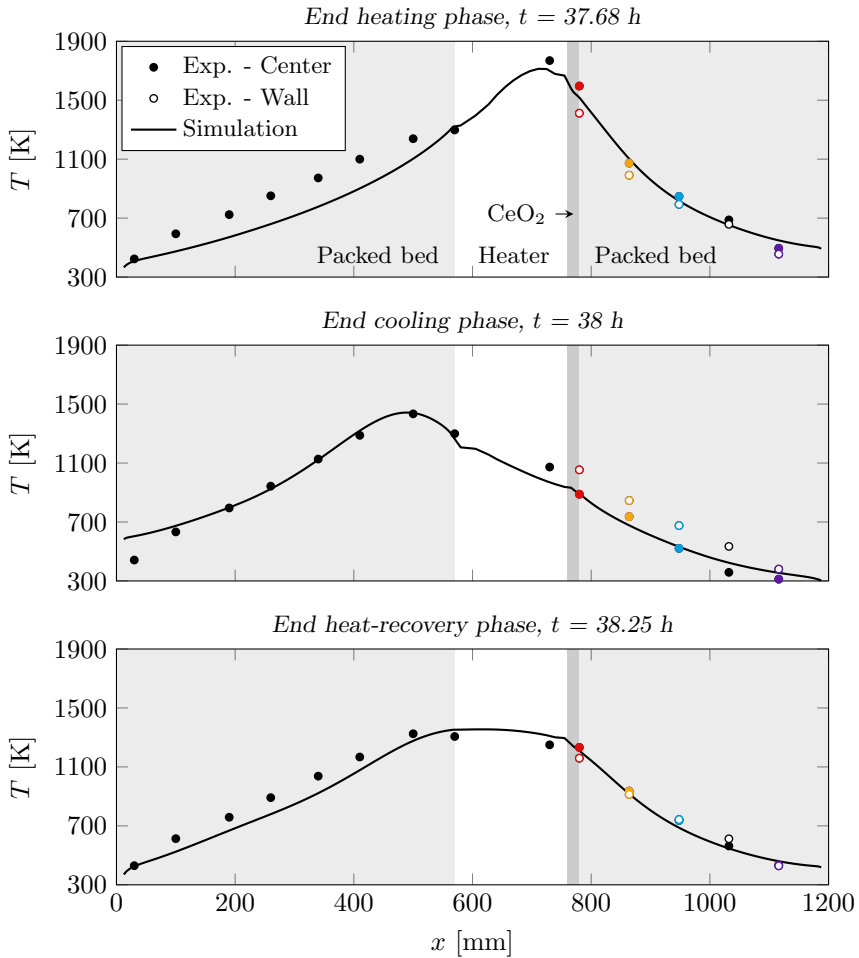
Figure 6.7: Comparison of simulated and measured temperatures in the laboratory-scale dual-storage reactor. Solid lines correspond to the simulation and symbols correspond to thermocouple measurements, whose locations are indicated in Fig. 6.4. The alumina packed beds and the ceria RPC are indicated by lighter and darker gray shading, respectively.

the cooling/oxidation phase at $t = 38$ h, and during the heat-recovery phase at $t = 38.25$ h. Between the heating and cooling phases, the average temperature of the ceria drops from $T_{\text{ceria,red}} = 1596$ K to $T_{\text{ceria,ox}} = 888$ K in less than 20 minutes, while during the heat-recovery phase, the average temperature rises from $T_{\text{ceria,ox}} = 888$ K to $T_{\text{ceria,hr}} = 1233$ K. From these temperatures, a heat-recovery effectiveness can be estimated as

$$\varepsilon_{\text{hr}} = \frac{e_{\text{ceria}}(T_{\text{ceria,hr}}) - e_{\text{ceria}}(T_{\text{ceria,ox}})}{e_{\text{ceria}}(T_{\text{ceria,red}}) - e_{\text{ceria}}(T_{\text{ceria,ox}})} = 49\% \,. \tag{6.6}$$

Given the small scale and the simplicity of the laboratory-scale setup, this result is considered to be promising.

Considering the agreement between the simulated and the measured temperatures, one has to keep in mind that the one-dimensional heat-transfer model does not consider radial gradients in the packed bed (see Appendix E for further details). It can therefore not be expected to deliver perfect agreement for the laboratory-scale dual-storage reactor. Nevertheless, it can be seen from Fig. 6.7 that the agreement is good in general. In the left packed bed the agreement is a little bit worse. This is attributed mainly to the heater that passes through the left packed bed and conducts heat, thereby disturbing the shape of the thermocline. An additional reason might be that the left packed bed could have larger air gaps at the top and therefore more pronounced bypassing.

Figure 6.8 shows the comparison of the simulated and measured temperatures as a function of time in the right packed bed. The colors indicate the thermocouple positions shown in Fig. 6.4. One can make two observations. First, differences exist between the measured temperatures in the center and at the wall of the packed bed. It can be seen that these radial differences are more pronounced the closer the thermocouples are to the heater. Furthermore, it is interesting to note the behavior of the measured temperatures for the three thermocouple positions closest to the heater during the cooling phases. At the beginning of the cooling phases, the temperatures at the center are higher than those at the wall, but the cooling rates at the center are larger, resulting in temperatures at the center that are lower than those
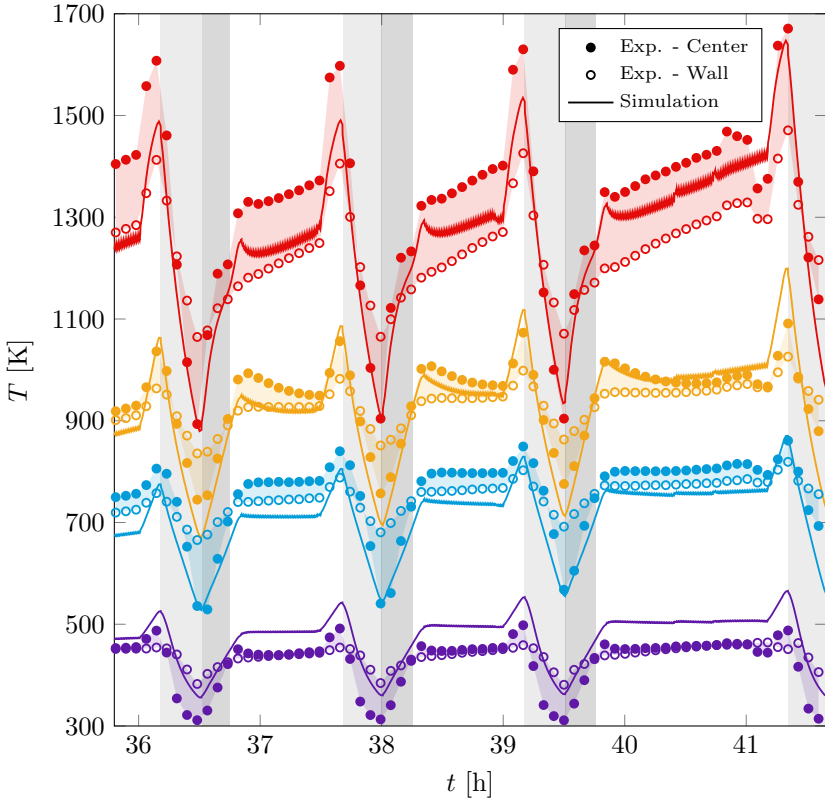
Figure 6.8: Comparison of simulated and measured temperatures in the right packed bed of the laboratory-scale dual-storage reactor as a function of time. Colors and symbols correspond to thermocouple locations as indicated in Fig. 6.4. The heating, cooling, and heat recovery phases are indicated by the white, lighter gray, and darker gray areas, respectively.

at the wall at later stages of the cooling phase. The differences in the cooling rates in the center and at the wall are caused by differences in the thermal inertia of the packed bed and the insulation. The differences in the measured temperatures in the center and at the wall of the packed bed could also be

caused by a bypass flow, which is likely to be non-negligible at the top of the packed bed due to imperfect filling of the horizontal alumina tube.

The second observation concerns the differences between the simulated and measured temperatures. It can be seen from Fig. 6.8 that the agreement between simulated and measured temperatures is good and that the simulated temperatures lie mostly between the measured wall and center temperatures.

The experimental demonstration of the dual-storage reactor concept is judged to be successful because the three objectives were met: (1) Packed-bed temperatures of up to 1673 K were reached, (2) a heat-recovery effectivenesses of 49% was obtained, and (3) the comparison of the experimental and numerical results showed good agreement, especially considering experimental uncertainties and the simplicity of the model.

6.4 Simulations of large-scale dual-storage reactor

A numerical model was used to assess the potential of a large-scale dual-storage reactor, with the aim of reaching high solar-to-fuel efficiencies. The redox material was assumed to be in indirect contact with the HTF. Steady cycling conditions were deemed to have been reached if the relative difference in the solar-to-fuel efficiency between consecutive cycles was smaller than 10^{-3}. Details of the model are given in Appendix E.

6.4.1 Reactor configuration

The large-scale dual-storage reactor consists of two adjacent identical tanks, each containing a thermocline TES and a reaction zone, as shown in Fig. 6.1. The tanks are oriented vertically to enable complete filling and to exploit natural convection and thereby enhance stratification. The radius of each tank is 12 m and the heights of the TES and the reaction zones are 4.6 m and 1.4 m, respectively. Tables 6.1 and 6.2 list all design parameters of the reactor. The TES consist of packed beds of alumina spheres of 5 mm diameter. The reaction zone contains alumina tubes filled with packed beds of ceria spheres, arranged in layers as shown in Fig. 6.9. The ceria spheres
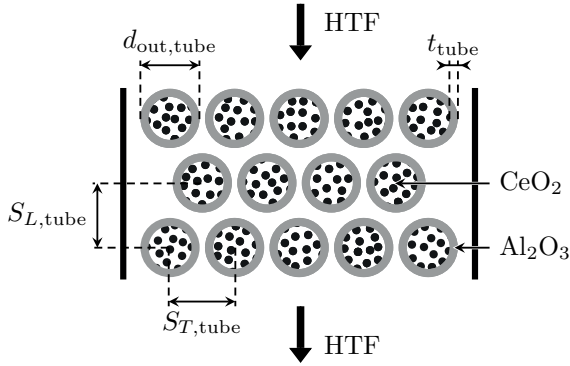
Figure 6.9: Cross section of the tube arrangement in the reaction zone of the large-scale dual-storage reactor.

have a micro-porous structure to enhance oxidation kinetics. Their micro-scale solid fraction is equal to that of the RPC struts in [172]. The HTF outlet temperature of the solar receiver is $T_{rec} = 1773$ K, which is therefore the maximum achievable reduction temperature T_{red} of the encapsulated ceria.

Several insulation materials are used depending on their limits on maximum temperatures. The insulation thicknesses of porous ceramic insulation, ceramic felt and microporous insulation are listed in Table 6.3.

The solar-receiver efficiency is assumed to be equal to the ideal absorption efficiency, assuming a typical solar irradiation of $I = 1$ kW and a concentration ratio of $C = 3000$ suns. Such concentration ratios are attainable with solar concentrating systems [174].

6.4.2 Reaction gases and heat-transfer fluid

The oxygen partial pressure inside the reactor tubes is decreased during reduction by means of a vacuum pump, such that the use of inert gas is avoided. Oxidation is controlled to take place at $T_{ox} = 1273$ K using pure CO_2 as oxidation agent. Oxidation with pure CO_2 without water

Table 6.1: Simulation parameters of the large-scale dual-storage reactor: General, TES and solar receiver.

Component	Quantity	Value	Units
General	$Q_{\text{solar,cycle}}$	89-103	MWh
	T_{amb}	298	K
	$T_{\text{HTF,rec,out}}$	1773	K
	p_{HTF}	2.5-20	bar
	$\dot{m}_{\text{HTF,air}}$	537.5	kg/s
	$\dot{m}_{\text{HTF,CO}_2}$	537.5	kg/s
	$\dot{m}_{\text{HTF,He}}$	110	kg/s
	N_{tank}	2	−
	r_{tank}	12	m
	H_{TES}	4.6	m
	H_{reactor}	1.4	m
	$\eta_{\text{pump,HTF}}$	95	%
	$\eta_{\text{pump,vacuum}}$	[173]	−
	$\eta_{\text{heat-to-electricity}}$	40	%
TES	$d_{\text{particle,alumina}}$	5	mm
	$\phi_{s,\text{Al}_2\text{O}_3}$	0.63	−
	$\tilde{\phi}_{s,\text{particle,Al}_2\text{O}_3}$	0.7	−
Receiver	I	1	kW
	C	3000	−
	T_{rec}	1773	K
	η_{abs}	81.3	%

has particular interest, as described in [163]. Although the dual-storage reactor could also be applied for pure H_2O or combined H_2O and CO_2 splitting, this is not further discussed in this thesis for brevity. The CO_2 inlet temperature into the reactor tubes is chosen to be 1173 K, which corresponds to approximately 90% gas-to-gas heat recovery since the outlet temperature is close to the solid temperature (1273 K).

Simulations are performed at various pressures for three HTFs (Air, CO_2 and helium). The advantage of using CO_2 instead of air or helium is its higher density which leads to smaller pressure drops and therefore

Table 6.2: Simulation parameters of the large-scale dual-storage reactor: Reaction zone.

Quantity	Value	Units
$p_{O_2,\text{reduction,max}}$	100	Pa
$p_{O_2,\text{reduction,min}}$	10	Pa
T_{red}	1773	K
T_{ox}	1273	K
T_{in,CO_2}	1173	K
$\dot{m}_{\text{in,tube},CO_2}$	1.44	kg/h
$d_{\text{out,tube,HTF=air}}$	27.5	mm
$d_{\text{out,tube,HTF}=CO_2}$	27.5	mm
$d_{\text{out,tube,HTF=He}}$	27	mm
$l_{\text{tube,mean}}$	18.8	m
t_{tube}	1.5	mm
$S_{\text{T,tube}}$	28	mm
$S_{\text{L,tube}}$	28	mm
$d_{\text{particle,ceria}}$	5	mm
$\phi_{\text{s,ceria,PB}}$	0.63	–
$\tilde{\phi}_{\text{s,particle,ceria}}$	0.7	–
$\tilde{\phi}_{\text{s,tube,alumina}}$	1	–
$N_{\text{tube−rows,tank}}$	50	–
$N_{\text{tube,row}}$	857	–

less pumping work. The advantage of using helium is its higher thermal conductivity leading to improved convective heat-transfer with the tubes. However, due to the low density of helium the pressure drop is higher. To keep the pumping work low with helium, the tubes are put further apart from each other by decreasing the tube diameter while the number of layers and the number of tubes per layer are kept the same (see Table 6.2). This means that the total amount of ceria is slightly reduced in the simulations with He. The HTF mass flow rate delivered by the pump is assumed constant throughout the whole cycle.

Table 6.3: Insulation thicknesses for the large-scale dual-storage reactor (in m, the origin of x is at the bottom of the two (equivalent) tanks.

Position					Porous ceramic insulation	Ceramic felt	Microporous insulation
0	<	x	<	3.45	0	0	1.0
3.45	<	x	<	7.15	0.1	0.25	0.65

6.4.3 Operation strategy

For the dual-storage reactor to be efficient, it is crucial to employ a carefully designed operation strategy. The operation strategy specifies the phases of each cycle, what operations are carried out in the phases, and the durations of the phases. For the laboratory-scale reactor, devising a strategy was straightforward because of the reactor's simplicity (only one reaction zone, the redox material was in direct contact with the HTF, no TCC) and because attaining high efficiencies was not a concern. By contrast, the large-scale reactor is more complex and attaining high solar-to-fuel efficiencies is the main objective.

The operation strategy was determined using simulations in a trial-and-error approach, which aimed at reaching high solar-to-fuel efficiencies while keeping the cycle time relatively low. The chosen strategy consists of 12 phases per cycle irrespective of the HTF and the HTF pressure, compared to only three phases for the laboratory-scale reactor. (While the simulations predict that the chosen strategy results in high solar-to-fuel efficiencies, it is likely that even higher efficiencies can be obtained with further optimization of the strategies.)

The simulated temperature distributions during the first six phases of each cycle at the quasi-steady state are presented in Fig. 6.10, assuming CO_2 at 10 bar as HTF. The second six phases are not shown because they are identical to the first six, except that the phases are switched between the two tanks. In Fig. 6.10, the reaction zones and the TES are indicated by the dark gray and light gray shading, respectively. The temperature

distributions at the start and end of each phase are shown as red and blue lines, respectively, while those after one and two thirds of the duration of each phase are shown as yellow and green lines, respectively. Flowing HTF is indicated by gray arrows, while flows through the reaction zone are indicated by framed white arrows.

The first six phases of each cycle are:

1. Reduction in right tank: HTF is pumped through the left tank from the bottom, shifting the thermocline in the left tank upwards and leading to a temperature decrease in the left reaction zone. The HTF leaving the left tank at the top is upgraded to T_{red} in the solar receiver. After exiting the solar receiver, the HTF enters the right tank from the top, shifting the thermocline in the right tank downwards and leading to a temperature increase in the right reaction zone. Simultaneously, a vacuum pump gradually decreases the total pressure in the tubes of the right reaction zone from 100 Pa to 10 Pa, favoring the reduction of ceria and the resulting oxygen is removed. (Since the pressure in all tubes of the right tank is the same, one vacuum pump is sufficient for the system.) The HTF leaves the right tank at the bottom at a temperature of about T_{amb}. The duration of the phase is $\Delta t_1 = 33.3$ min.

2. Further cooling of left tank: Although the right reaction zone is at sufficiently high temperatures for reduction, the left reaction zone is not at sufficiently low temperatures for oxidation. Therefore, HTF continues to be pumped through the left tank from the bottom. Now, however, it bypasses the solar receiver and instead directly enters the right tank from the top. The bypassing is required to prevent expanding the spatial extent of temperatures close to the reduction temperature in the right tank. The HTF exiting the right tank at the bottom is at a temperature close to T_{amb}. The total pressure in the tubes of the right reaction zone is kept at 10 Pa to favor reduction. The duration of the phase is $\Delta t_2 = 20$ min.

3. Partial expulsion of thermocline in left tank: The HTF is pumped from the bottom to the top of the left tank without passing through the right tank, resulting in the partial expulsion of the thermocline in the left tank. The partial expulsion is necessary to remove the heat released by the exothermic oxidation step. If this heat were not be expelled, the temperature profile would widen continuously and thereby make it impossible to operate the dual-storage reactor efficiently. Beyond its necessity, the partial expulsion is beneficial because it steepens the thermocline in the left tank and because the expelled high-temperature heat can, after conversion to electrity, be used to power the pumps required for the operation of the dual-storage reactor.[4] The duration of the phase is $\Delta t_3 = 2$ min.

4. TCC in left tank: TCC is performed in the left reaction zone to obtain a plateau at the oxidation temperature. HTF is extracted at the lower boundary of the reaction zone and the top of the tank, mixed, and then injected in the middle of the reaction zone. Pumping is performed after the mixing of the streams. The mass flow of HTF flowing in each direction of the reactor is assumed to be half of the nominal mass flow rate. The duration of the phase is $\Delta t_4 = 16.7$ min.

5. TCC and oxidation in left tank: While the actions of phase 4 continue, oxidation is performed by injecting CO_2 at a mass flow rate of $\dot{m}_{\text{in},CO_2}$ into each tube of the left reaction zone. The duration of the phase is $\Delta t_5 = 20$ min.

6. Shifting of temperature profiles: HTF is pumped through the right tank from the bottom, shifting the thermocline in the right tank upwards and leading to an increase in the average temperature of the right reaction zone. The HTF leaving the right tank bypasses the receiver, enters the left tank, shifts the thermocline in the left tank downwards, and thereby increases the temperature in the left reaction zone. At

---

[4]The expelled heat could be stored in an additional TES to enable the continuous conversion of this heat to electricity. The additional TES was not simulated within this thesis.

the end of this phase, the temperature profile in the left (right) tank is equal to the temperature profile in the right (left) tank at the beginning of phase 1. The duration of the phase is $\Delta t_6 = 20$ min.

The total time of a half-cycle is 1 h 52 min.

Note that solar energy is used only in the first and seventh phases of a complete cycle for a total of 1 h 7 min. To use solar energy during an entire day, it will be necessary to operate more than one dual-storage reactor. To allow operation during the night or during periods of insufficient insolation, additional TES units could be used.

6.4.4 Results

Having explained the phases with the aid of Fig. 6.10, we return to the figure to focus on a more detailed discussion of the results. As already stated, the figure shows the results for CO_2 at 10 bar as HTF. For brevity, results for other HTFs and pressures will not discussed in detail because they are qualitatively similar.

Inside the void part, the fluid temperature changes only marginally, mainly due to thermal losses. This is the case for all phases.

During phase 1 of the first half-cycle, the total pressure in the right reaction zone is reduced to favor reduction. This can be seen more clearly in Fig. 6.11, which shows the ceria temperature, the reduction extent, and the partial pressure of oxygen in two tube layers each of the left and right reaction zones as a function of time for one complete cycle. The black and blue curves correspond to the 10th tube layers from the bottom and the top, respectively.

Although the solar receiver is bypassed during phase 2, the temperature in the lower part of the right reaction zone still increases initially, leading to further increase of the reduction extent, as shown by Fig. 6.11. The reduction extent at the end of phase 2 of the whole reaction zone of the right tank ranges from 0.027 to 0.037. At the end of phase 2, the temperature profile in the right tank is pushed down to its lowest position, see Fig. 6.10.
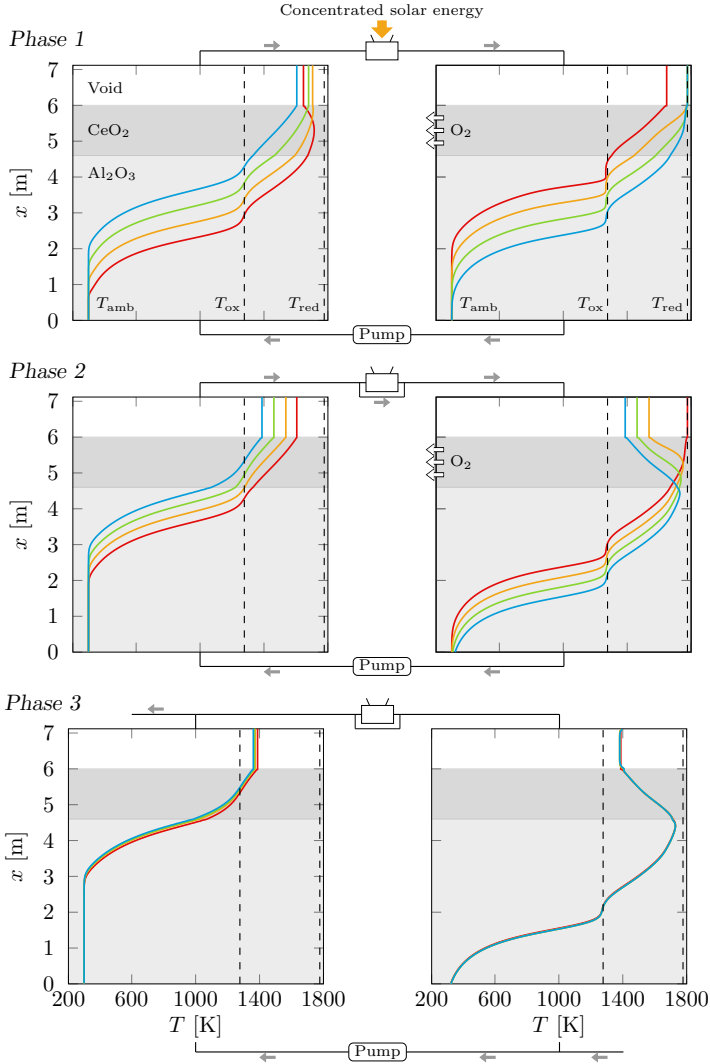
Figure 6.10: Simulated HTF temperature distributions in the large-scale dual-storage reactor for the six phases of one half-cycle, assuming CO_2 at 10 bar as HTF. The temperature distributions at the start and end of each phase are shown as red and blue lines, respectively, while those after one and two thirds of the duration of each phase are shown as yellow and green lines, respectively. Descriptions of the phases are given in the text.
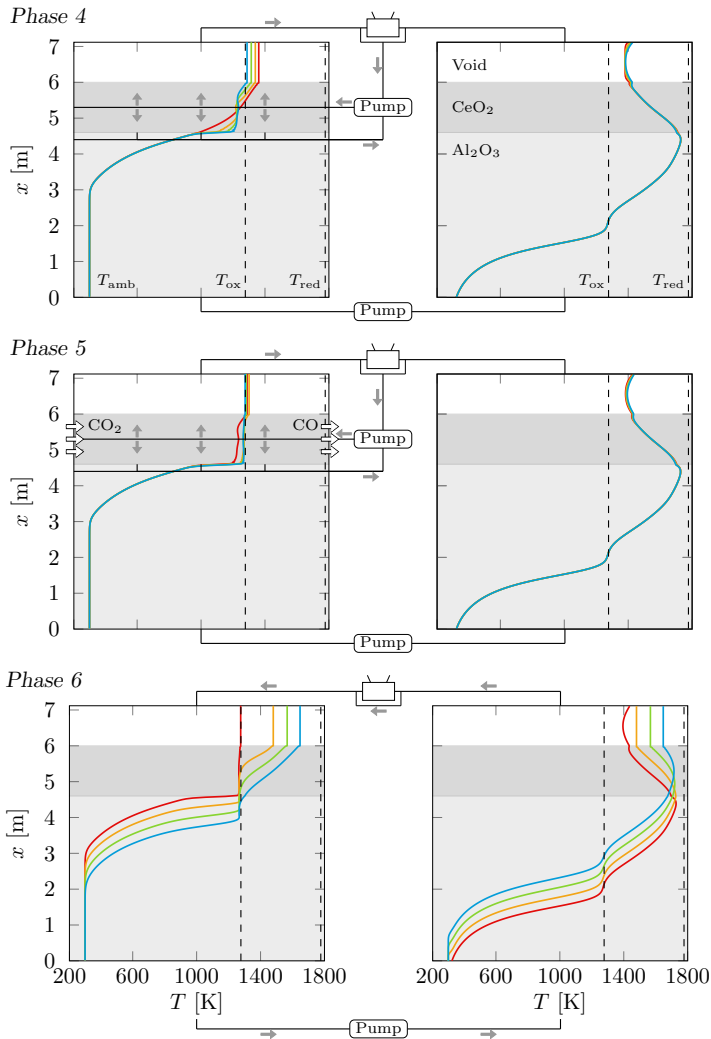
Figure 6.10: (continued) Simulated HTF temperature distributions in the large-scale dual-storage reactor for the six phases of one half-cycle, assuming CO_2 at 10 bar as HTF. The temperature distributions at the start and end of each phase are shown as red and blue lines, respectively, while those after one and two thirds of the duration of each phase are shown as yellow and green lines, respectively. Descriptions of the phases are given in the text.
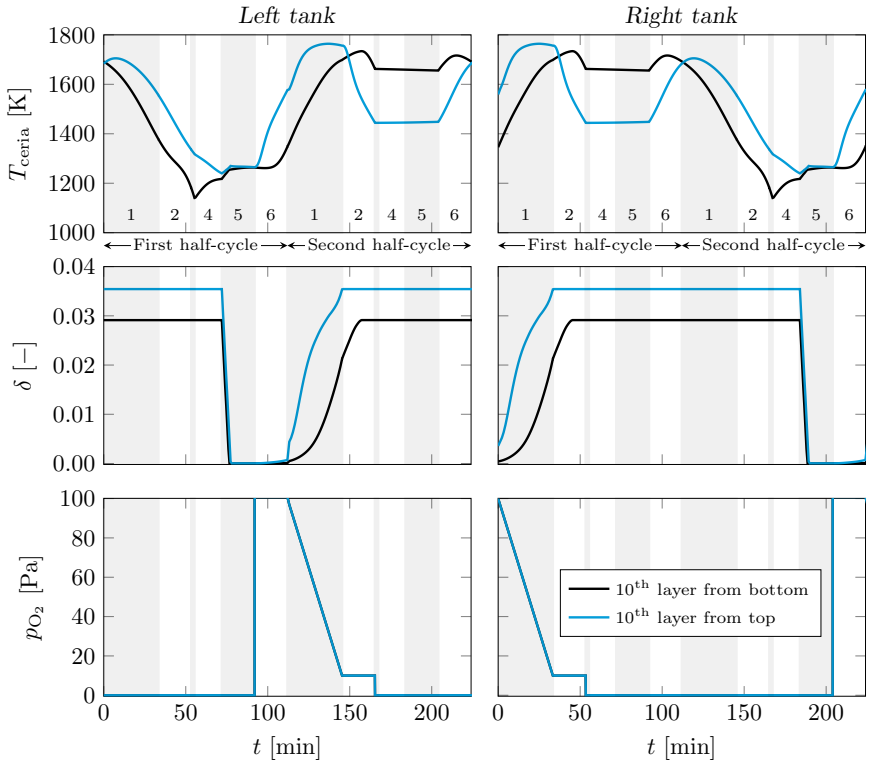
Figure 6.11: Evolution of the the ceria temperature T_{ceria}, the reduction extent δ, and the oxygen partial pressure p_{O_2} over one complete cycle of the large-scale dual-storage reactor. Values are averages of the 10th tube row (counted from the bottom) of each tank. The thin shaded area indicates phase 3.

Nevertheless, it is remarkable that the HTF outflow temperature reaches a temperature of only 318.5 K, corresponding to a maximum increase of 20.5 K over the ambient (initial) temperature. This modest increase, which enables the use of conventional pumps, is attributed to the relatively steep

thermocline.

During phase 3, the thermocline is partially expelled at the top of the left tank at an outlet temperature of around 1373 K by pumping cold HTF from the bottom of the left tank, see Fig. 6.10. It is an important advantage of the design and operation of the dual-storage reactor that high-temperature heat that was accumulated at approximately the oxidation temperature (from exothermic oxidation and thermocline degradation) can be extracted in this fashion and potentially reused as discussed above. The extracted thermal energy is used to charge an additional TES that was not simulated. The cold outflow temperature from this additional TES is the inlet temperature to the pump of the dual-storage reactor during this phase.

The application of TCC in the left tank during phase 4 creates a plateau at the oxidation temperature in the reaction zone, as can be seen from Fig. 6.10. This favors high conversion of CO_2 to CO and favorable reaction kinetics throughout the reaction zone during the oxidation in phase 5. In Fig. 6.11, one can see that the ceria temperature of the left tank increases during phase 5 due to the exothermic oxidation at 1273 K. The rapid decrease of the reduction extent is controlled by mass transfer since thermodynamic equilibrium is assumed during oxidation. After the end of oxidation, when the flow of CO_2 through the tubes has ceased, the partial pressure of oxygen increases rapidly. This is because the material starts to reduce already, and as there is no flow, the released oxygen accumulates. However, due to the relatively low temperatures, the reduction extent stays close to zero.

Note that throughout phases 3 to 5, the temperature profile inside the right tank barely changes (Fig. 6.10). This is remarkable because one might suppose that temperatures equilibrate faster due to the high temperatures and the resulting radiation inside the packed bed and the reactor. These effects are accounted for in the simulations and have only a small effect due to (1) the rather short duration of phases 3 to 5 and (2) blocking of radiation due to many tube/particle layers. Natural convection inside the tanks is not accounted for in the simulations. However, if temperatures are higher at the top of the vertical tanks, natural convection will support thermocline

steepness.

Because the receiver in the dual-storage reactor connects two reaction zones, it needs to impart only comparatively small temperature increases to the HTF. During a complete cycle, the minimum and maximum HTF inflow temperatures are 1592 K and 1701 K, respectively. Consequently, the HTF temperature increases in the receiver range from 72 K to 181 K. Because these increases are much smaller than those in receivers for CSP plants, receivers for dual-storage reactors can be based on simpler designs. During plant start-up, such simpler designs may need to periodically switch the HTF flow direction during a pre-heating phase to reach HTF outflow temperaturs equal to the reduction temperature (see Section 6.3.2).

6.4.5 Efficiency

The solar-to-fuel energy efficiency of a complete cycle of the dual-storage reactor is computed from Eq. (6.4). The energy required to heat the HTF, Q_{solar}, is computed as twice the energy consumed during phase 1 of the half-cycle,

$$Q_{\mathrm{solar}} = \frac{2}{\eta_{\mathrm{abs}}} \int_0^{\Delta t_1} \dot{m}_{\mathrm{HTF}} \left[h_{\mathrm{HTF}}(T_{\mathrm{red}}) - h_{\mathrm{HTF}}(T_{\mathrm{rec,in}}(t)) \right] \mathrm{d}t \,, \qquad (6.7)$$

where h_{HTF} is the enthalpy of the HTF at the indicated temperature and η_{abs} is the ideal absorption efficiency given by

$$\eta_{\mathrm{abs}} = 1 - \frac{\sigma T_{\mathrm{rec}}^4}{IC} \,, \qquad (6.8)$$

where σ is the Stefan-Boltzmann constant.

For the calculation of $Q_{\mathrm{penalties}}$, it is assumed that the high-temperature heat extracted during phase 3 of the half-cycle can be used to produce electricity. Therefore, $Q_{\mathrm{penalties}}$ is the concentrated solar energy required to provide the electricity for pumping that is not covered by the extracted

heat,

$$\begin{aligned}Q_{\text{penalties}} &= Q_{\text{pump,HTF}} + Q_{\text{pump,vacuum}} - Q_{\text{extracted}} \\ &= \frac{W_{\text{el,pump,HTF}} + W_{\text{el,pump,vacuum}}}{\eta_{\text{abs}}\eta_{\text{heat-to-electricity}}} - Q_{\text{extracted}}\,,\end{aligned} \quad (6.9)$$

where $\eta_{\text{heat-to-electricity}} = 40\%$, $W_{\text{el,pump,HTF}}$ is the electrical work required to pump the HTF, and $W_{\text{el,pump,vacuum}}$ is the electrical work required to pull the vacuum in the tubes. One can write

$$W_{\text{el,pump,HTF}} = \frac{1}{\rho_{\text{HTF}}(T_{\text{amb}})\,\eta_{\text{pump,HTF}}} \int_0^{\Delta t_{\text{cycle}}} \dot{m}\Delta p\,\mathrm{d}t\,, \quad (6.10)$$

assuming that pumping is performed at ambient temperature (which requires a counter-flow heat-exchanger for phases 4 and 5), and $W_{\text{el,pump,vacuum}}$ is calculated following [173]. The extracted high-temperature heat is given by

$$Q_{\text{extracted}} = 2 \int_0^{\Delta t_3} \dot{m}_{\text{HTF}}\big[h_{\text{HTF}}(T_{\text{out}}(t)) - h_{\text{HTF}}(T_{\text{in}}(t))\big]\,\mathrm{d}t\,, \quad (6.11)$$

where T_{out} and T_{in} are the outflow and inflow temperatures of the receiver, respectively. If $Q_{\text{extracted}}$ is sufficient to cover all pumping needs, $Q_{\text{penalties}}$ is set to zero and the remaining high-temperature heat is unused.

Figure 6.12 shows the energy flows determined from the simulations using CO_2 at 10 bar as HTF. The reradiation losses from the solar receiver and the extracted high-temperature heat amount to 18.7% and 42.7% of the concentrated solar energy input, respectively. In this case, the extracted high-temperature heat covers all pumping needs and 6.7% of that heat remains unused. Thermal losses at low temperature amount to 3.1%. These losses are caused by imperfect recovery of heat from the product gases, losses through the insulation, and heat flowing out with the HTF at the bottom of the tanks. The remainder of the concentrated solar energy input of 35.1% is stored in the fuel CO and hence the solar-to-fuel energy efficiency of the large-scale dual-storage reactor is

$$\eta_{\text{solar-to-fuel}} = 35.1\%. \quad (6.12)$$

This a highly promising value considering that the simulations are not just based on thermodynamic considerations but on detailed simulations of the whole dual-storage reactor concept.

It should be noted that although the loss through the insulation at only 0.1% is very small, its impact is not negligible. The insulation layers, in particular the more conductive porous ceramic and ceramic felt, take up heat when the reaction zones are heated to the reduction temperature and then return it when the reaction zone is cooled to the oxidation temperature. In the process, this leads to undesired disturbances of the thermoclines. The net heat loss towards from the insulation to the surroundings is very small due to the excellent performance of the microporous insulation.

6.4.6 Heat-recovery effectiveness

The heat-recovery effectiveness $\varepsilon_{\mathrm{hr}}$ cannot be extracted readily from the energy breakdown shown in Fig. 6.12. This is because the sum of thermal energy losses (without reradiation losses) and extracted high temperature heat can be ascribed to two effects: (1) imperfect heat recovery and (2) exothermic heat of oxidation. To determine the heat-recovery effectiveness of the dual-storage reactor simulations, the simulated efficiency is compared to the theoretical solar-to-fuel energy efficiency for a certain heat-recovery effectiveness.

The theoretical solar-to-fuel energy efficiency is limited by (1) the reradiation losses of the solar receiver, (2) the exothermic heat released during oxidation, and (3) the heat-recovery effectiveness between reduction and oxidation temperatures. The solar to fuel energy conversion efficiency can then be written as follows, assuming that the sensible heat of the reaction gas CO_2 is fully recovered [42]:

$$\eta_{\text{solar-to-fuel}} = \eta_{\text{abs}} \frac{\mathrm{HHV}_{\mathrm{CO}}\delta}{(1 - \varepsilon_{\mathrm{hr}})M_{\mathrm{ceria}}\int_{T_{\mathrm{ox}}}^{T_{\mathrm{red}}} c_{p,\mathrm{ceria}}\mathrm{d}T + \Delta H_{\mathrm{red}}\delta}, \qquad (6.13)$$

where M_{ceria} is the molar mass of ceria. For the values stated in Table 6.1, one can determine the corresponding maximum reduction extent ($\delta = 0.041$)
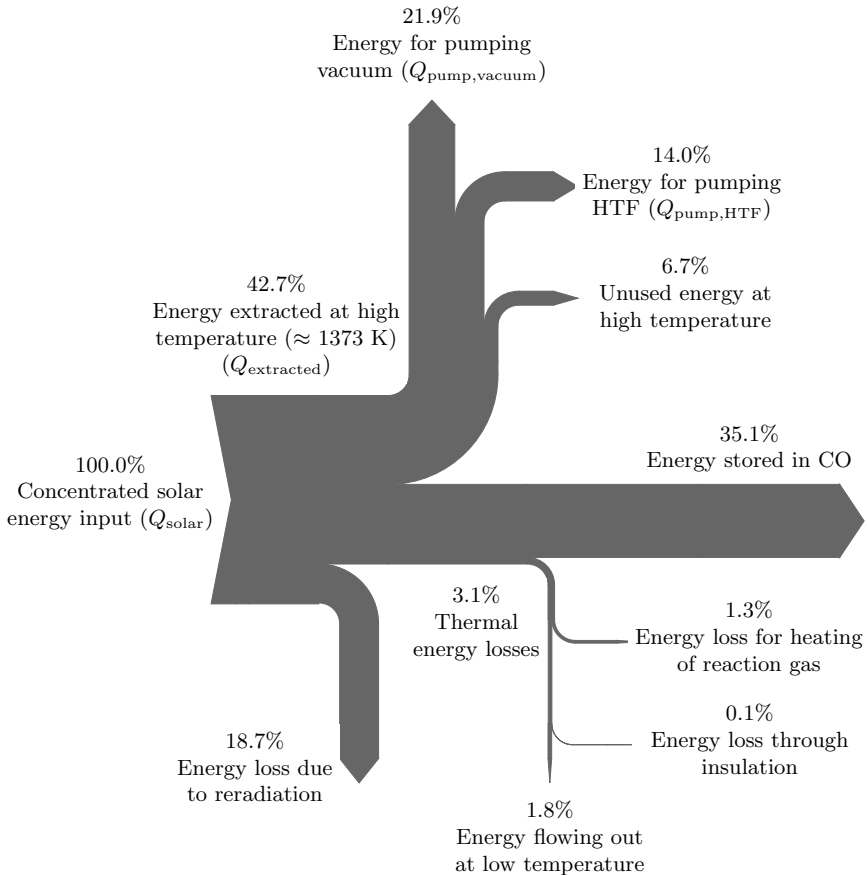
Figure 6.12: Energy flows determined from the simulations of the large-scale dual-storage reactor using CO_2 at 10 bar as HTF. All energy values are given in terms of thermal energy. Electric pumping work is converted to the corresponding heat using $\eta_{\text{heat-to-electricity}} = 40\%$.

and η_{abs}. The theoretical $\eta_{\text{solar-to-fuel}}$ is plotted in Fig. 6.13 as a function of the heat-recovery effectiveness ε_{hr}. The reradiation losses are shaded in red
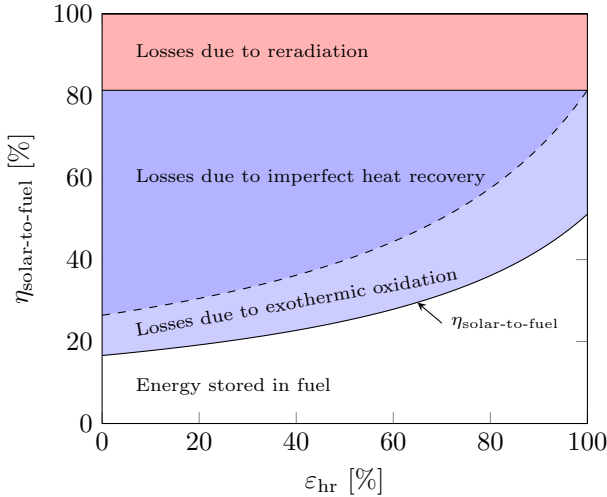
Figure 6.13: Theoretical solar-to-fuel energy efficiency for ceria and breakdown of energy losses as a function of the heat-recovery effectiveness for p_{O_2} = 10 Pa, T_{ox} = 1273 K, T_{red} = T_{rec} = 1773 K, C = 3000, and I = 1 kW.

and the sum of the losses due to imperfect heat recovery and exothermic oxidation are shaded in blue.[5] One can see that the solar-to-fuel energy efficiency strongly depends on the heat-recovery effectiveness as it increases from $\eta_{solar-to-fuel}$ = 16.6% for ε_{hr} = 0% to $\eta_{solar-to-fuel}$ = 51.1% for ε_{hr} = 100%. The ratio between the losses due to the exothermic heat of oxidation and the energy stored in the fuel is constant and equals to 0.59. The fraction of reradiation losses from the solar receiver is constant and amounts to 18.7%.

The heat-recovery effectiveness for the case shown in Fig. 6.12 can now be

---

[5]Note that in Eq. (6.13) reradiation losses lead to a decreasing value of the nominator, while losses due to imperfect heat recovery and exothermic oxidation lead to an increasing denominator. Therefore, splitting of the losses is not intuitive. To separate the losses originating from imperfect heat recovery and exothermic oxidation heat, their sum was split proportionally to the respective loss, which lead to the dashed line indicated in Fig. 6.13. The exothermic heat of oxidation is given by the difference $\Delta H_{red}\delta - HHV_{CO}\delta$.
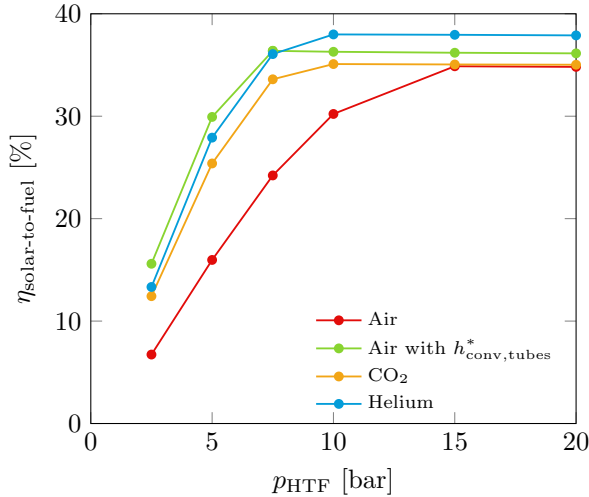
Figure 6.14: Simulated solar-to-fuel energy efficiency of large-scale dual-storage reactor for various HTFs as a function of p_{HTF}.

determined by comparing the simulated efficiency of 35.1% to the theoretical efficiency plotted in Fig. 6.13, resulting in $\varepsilon_{\mathrm{hr}} = 78\%$. Note that this value of $\varepsilon_{\mathrm{hr}}$ incorporates also all thermal losses and (potential) parasitic losses related to the reaction zone and the TES.

Figure 6.14 shows the resulting $\eta_{\mathrm{solar\text{-}to\text{-}fuel}}$ for various HTFs as a function of p_{HTF}. In addition to the simulations with the mentioned HTFs, results are shown for air with an artificially increased convective heat transfer coefficient around the tubes of $h^*_{\mathrm{conv,tubes}} = 5 \cdot h_{\mathrm{conv,tubes}}$ to show its sensitivity.[6] One can observe a strong dependence of the efficiency on p_{HTF}. At lower HTF pressures (p_{HTF}) the HTF pumping work increases significantly due to higher flow velocities. As soon as the sum of the required energies for HTF

---

[6]This could be achieved by increasing the surface area of the encapsulation, using other geometries than tubes or adding fins to the tubes. Due to the improved convective heat transfer it is possible to decrease the tube diameter to place the tubes further apart ($d^*_{\mathrm{out,tube,HTF=air}} = 26.5$ mm) as described for helium in Section 6.4.1.

and vacuum pumping is larger than the extracted high temperature heat ($Q_{\text{penalties}} > 0$), $\eta_{\text{solar-to-fuel}}$ decreases rapidly. The plateau of maximum efficiency is reached at different pressures for the respective HTF. For helium and CO_2 it is reached at 10 bar while for air and air with modified heat transfer coefficient it is reached at 15 and 7.5 bar, respectively.

The maximum solar-to-fuel energy efficiencies are $\eta_{\text{solar-to-fuel,max}} = 34.9\%$ for air, 35.1% for CO_2, 36.4% for air with modified heat transfer coefficient, and 38.0% for helium.

Comparing these values to the ideal $\eta_{\text{solar-to-fuel}}$ shown in Fig. 6.13 they correspond to heat-recovery effectivenesses between 78% and 83%. Furthermore, considering that for this case the theoretical maximum solar-to-fuel efficiency is $\eta_{\text{solar-to-fuel}} = 51.1\%$, the relative efficiency of the dual-storage reactor is 68.3% to 74.4% with respect to the maximum achievable value.

6.5 Summary, conclusions, and further work

Reaching high efficiencies when producing fuels using solar-thermochemical redox cycles requires effective heat recovery. In this chapter, the so-called dual-storage reactor, a new reactor concept that incorporates heat recovery, was presented. The concept is based on two vertical tanks, each of which contains a reaction zone placed on top of a thermocline TES. The temperature profiles in the tanks are shifted up and down by pumping a HTF through the tanks. As the temperature profiles are shifted, the redox material in the reaction zones is alternately exposed to oxidation or reduction temperatures. The HTF is heated in a solar receiver to supply the heat of reaction and to compensate for thermocline degradation and thermal losses. Temperature plateaus at oxidation and reduction temperatures are established and maintained by TCC.

In addition to incorporating heat recovery, the dual-storage reactor concept has other advantages. First, the redox material can be in direct or indirect contact with the HTF. With indirect contact, the use of inert

gases can be avoided and operation under vacuum during reduction becomes possible. Second, by placing the HTF pump at the bottom of the tanks, the pump is only exposed to temperatures close to the ambient. This avoids the need to develop high-temperature pumping technology and lowers the required pumping work.

A simplified version of the dual-storage reactor concept was assessed experimentally in a 1.3 kW$_{el}$ laboratory-scale setup with maximum temperatures of 1673 K. Ceria was used as the redox material and air was used as the HTF. The two thermocline TES consisted of alumina spheres with a diameter of 3 mm. The setup demonstrated the shifting of the temperature profiles between the two thermocline TES and yielded a heat-recovery effectiveness of 49%. Good agreement was obtained between measured and simulated temperature profiles.

The performance of a large-scale dual-storage reactor with a solar input per cycle of up to 103 MWh was assessed using simulations. Ceria was used as redox material, encapsulated in alumina tubes. Air, carbon dioxide, and helium at various pressures were investigated as HTFs. The simulations predicted solar-to-fuel efficiencies of more than 35% for HTF pressures of at least 10 bar and sufficiently good heat transfer. The largest contribution to the losses of about 43% arises from the need to extract high-temperature energy to reject the heat of oxidation and to preserve a temperature plateau at the oxidation temperature. However, about 36% of the rejected energy can be used to generate electricity required to pull the vacuum during reduction and to pump the HTF.

Considering the large number of operation and design parameters that characterize the dual-storage reactor concept, it is expected that systematic numerical optimization will lead to increased solar-to-fuel efficiencies. Future studies may also consider the following adaptations:

- Minimizing the work for vacuum pumping: Combinations of pumping and injecting small amounts of inert gas during reduction should be investigated [175].

- Connecting reactor tube outlets/inlets to maximize conversion during oxidation: Since conversion is maximum at lower temperatures, reactor tubes that are exposed to higher temperatures during oxidation could have their outlet connected to reactor tubes that are exposed to lower temperatures during oxidation.

- Cascaded dual-storage reactor: Multiple redox materials that react at different temperatures could be arranged such that their reaction temperatures match the temperature profile of the thermoclines, reducing the need for TCC.

- Using a liquid metal instead of a gas as HTF may boost the solar-to-fuel efficiency. However, this adaptation relies on the development pumps for liquid metals. Furthermore, the minimum temperature of the process would need to be higher than ambient temperature to prevent solidification of the metal.

7

Experimental Demonstration of Heat Recovery and Splitting of CO_2 in a Dual-Storage Reactor

7.1 Introduction

The dual-storage reactor is a novel heat-recovery concept for solar thermochemical fuel production via two-step redox cycles. The reader is referred to Section 6.1 for a background on solar fuels and existing heat recovery concepts. The novel concept of the dual-storage reactor was described in detail in Section 6.2. Simulations of the concept were presented in Section 6.4 and showed remarkably high solar-to-fuel energy conversion efficiencies of $\eta_{\text{solar-to-fuel}} > 35\%$ for encapsulated ceria.[1] In Section 6.3, experimental results were presented for a simplified laboratory-scale dual-storage reactor, which proved the basic principle of heat recovery. However, the redox re-

---

[1] The encapsulation was also referred to as indirect contact between the redox material and the HTF.

action was not driven within this setup because large amounts of inert gas
would have been needed as the ceria was in direct contact with the HTF.

This chapter aims at the experimental demonstration of both chemical
reaction and heat recovery within the same setup with encapsulated ceria.
Thanks to the encapsulation, reaction gases and ceria are physically separated
from the HTF, which has two advantages. First, the amount of inert gas
required during reduction can either be reduced as the inert gas has to
be provided only in the encapsulation as opposed to the entire reactor, or
it can even be omitted entirely by using a vacuum pump for the oxygen
removal. Second, the HTF does not need to be inert with the reacting
material and therefore its choice is much less restricted and can be, e.g.,
air. The main disadvantages of the encapsulation are (1) lower heat-transfer
rates between the HTF and the redox material due to the additional thermal
resistance, (2) potential reactions/corrosion between the redox material and
the encapsulation, and (3) increased complexity of the reactor design.

7.2   Experimental setup

7.2.1   Configuration

Figure 7.1 shows a schematic of the dual-storage reactor setup. The setup
was designed using simulations and the experience gained with the simplified
experimental setup that was presented in Section 6.3. Similar to the previous
setup, the heat was provided electrically, only one reaction zone was used,
air was used as HTF, and no TCC was performed.

The experimental setup differs from that described in Section 6.3 in three
respects. First, the ceria was encapsulated and therefore in indirect contact
with the HTF. The encapsulation was made of a cylindrical alumina tube.

Second, the redox reaction of ceria was driven. During reduction, argon
was injected and during oxidation, CO_2, or for simplicity air, was injected
into the encapsulation. The reduction and oxidation reactions are as follows,
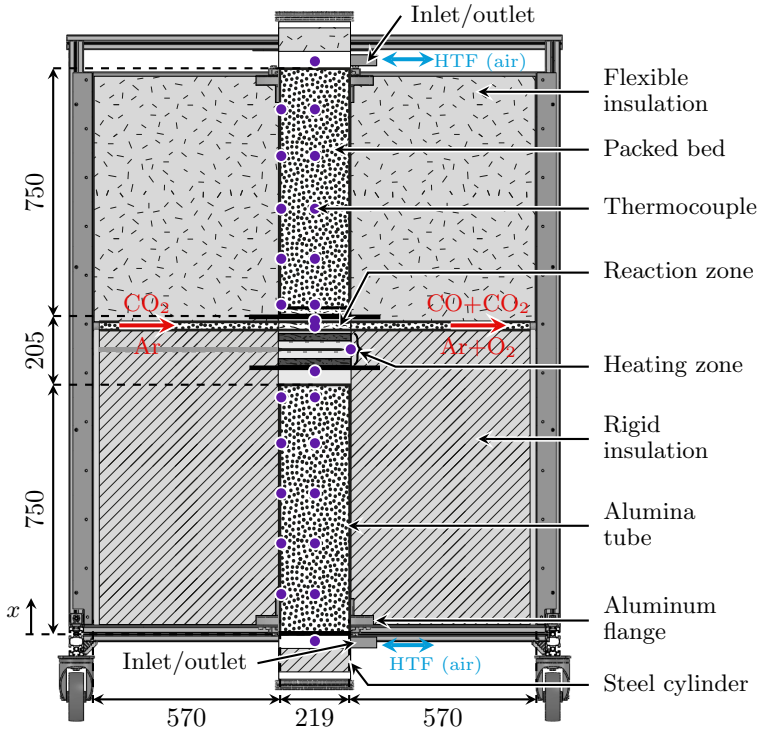
Figure 7.1: Schematic of the dual-storage reactor setup. The blue arrows correspond to the flow of the HTF (air). The red arrows on the left and right sides correspond to the flow of gases at the inlet and outlet of the reactor, respectively. The labeling above the red arrows ($CO_2 \rightarrow CO_2 + CO$) and below the red arrows ($Ar \rightarrow Ar + O_2$) correspond to the oxidation and reduction reactions, respectively. The violet circles indicate the locations of thermocouples. Dimensions are given in mm.

assuming that oxidation with CO_2 may be incomplete,

$$CeO_{2-\delta_{ox}} \rightarrow CeO_{2-\delta_{red}} + \frac{\Delta\delta}{2}O_2, \tag{7.1}$$

$$CeO_{2-\delta_{red}} + \Delta\delta CO_2 \rightarrow CeO_{2-\delta_{ox}} + \Delta\delta CO, \tag{7.2}$$
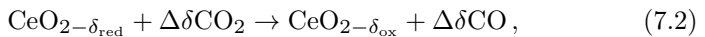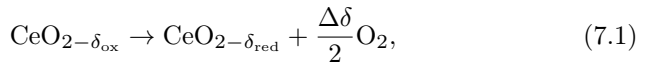
where $\Delta\delta = \delta_{\mathrm{red}} - \delta_{\mathrm{ox}}$.

The third difference is the arrangement of the packed beds. Due to the difficulties that were experienced with the horizontal placement of the packed beds, in this setup the storage tanks were arranged vertically. To decrease the need for air piping and to reduce thermal losses between the two tanks, the tanks were placed on top of each other. This means that the top tank was placed upside down, with the hot zone at its bottom and the cold zone at its top. The associated natural convection forces inside the packed bed were estimated to be negligible for this particular case according to the theory for stagnant flow [176].

The two packed beds had a length of 750 mm each and consisted of porous alumina spheres, which had a diameter of 3-5 mm, a density of 1073 kg/m^3 (corresponding to an internal porosity of 0.73), and a packed-bed solid-volume fraction of 0.686. The packed beds were enclosed mostly by two alumina tubes, which had a length of 700 mm and inner and outer diameters of 203 mm and 218 mm, respectively, see Fig. 7.2(a). To prevent the alumina tubes from experiencing thermal shocks when switching the HTF flow direction, the length of the packed beds was enlarged by 50 mm towards the HTF inlet/outlet using steel cylinders that were attached to the alumina tube using an aluminum flange. The steel cylinders had a length of 178 mm, a diameter of 219 m diameter and a thickness of 3 mm. The aluminum flanges had a thickness of 25 mm and inner and outer diameters of 220 mm and 360 mm, respectively.

Further precautions were taken to avoid damaging the two alumina tubes due to thermal expansion: Space was left between the lower alumina tube and the heating zone to keep the alumina tube free from any weight from the upper part. The upper cylinder was suspended by springs (not shown in Fig. 7.1) that took most of the cylinder's weight while still allowing the top alumina tube to expand freely.

Pictures of the reaction and heating zones are shown in Fig. 7.2(b-d). Figure 7.3 shows an enlarged schematic of the reaction and heating zones. The reaction zone consisted of seven alumina tubes of inner and outer

(a) Bottom packed bed

(b) Reaction zone

(c) Ceria and thermocouple

(d) Heating zone
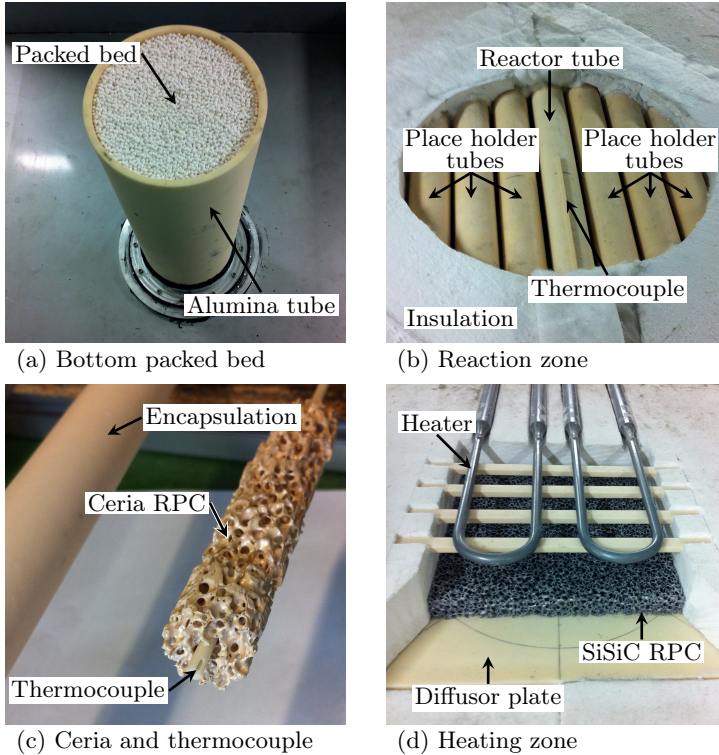
Figure 7.2: Pictures of the dual-storage reactor setup. (a) packed bed of alumina spheres inside the bottom alumina tube, (b) reaction zone with the reactor tube (the tube in the middle), the thermocouple on top of the encapsulation, and the place-holder tubes (three tubes on each side next to the middle tube), (c) the encapsulation and the ceria RPC with the thermocouple, and (d) electrical heaters that are supported by alumina rods.
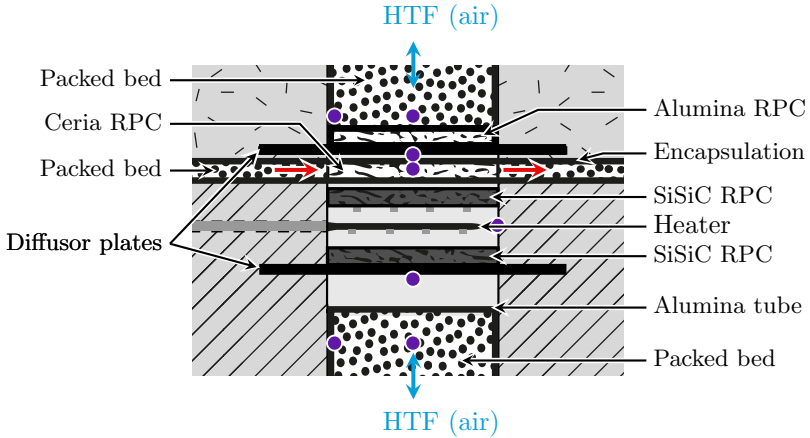
Figure 7.3: Schematic of the heating and reaction zones. The blue and red arrows denote the streams of HTF (air) and reaction/inert gases, respectively. The violet circles indicate the locations of thermocouples.

diameters of 19 mm and 25 mm, respectively, see Fig. 7.2(b). They were placed next to each other with a spacing of around 2 mm. For simplicity, only the middle tube contained ceria and was fed by reaction/inert gases, while the other tubes were placeholders. Ceria was inserted into the encapsulation in the form of eight small cylinders of dual-scale reticulated porous ceramic (RPC) [171], see Fig. 7.2(c). They had a total length of 200 mm, a diameter of 19 mm, and total masses of either 76.9 g or 73.5 g, depending on the experimental run. The mean pore size was 2.25 mm, the strut-scale solid-volume fraction was 0.7, and the RPC-scale solid-volume fraction was 0.255.

The heating zone consisted of two 2 kW $MoSi_2$ electrical heating elements that were supported by four small alumina rods of 250 mm length, 12 mm width, and 6 mm height. The total height of the heating zone was 100 mm. Due to the size of the heating elements, the heating zone did not have a circular cross section but a square cross section of 200 mm width, see Fig. 7.2(d). The heating power was controlled via a pulse-width-modulated

solid-state relay. Below and above the heating elements, SiSiC RPCs were placed to absorb the radiation emitted by the heaters and transfer it through convection to the air. The RPCs had 10 pores per inch (PPI), a square cross-section of 200 mm width, a height of 20 mm, and a weight of 328 g. The upper RPC was also supported by four small alumina rods of the same dimensions as those that supported the heating elements.

Two square diffusor plates separated the heating and reaction zones from the packed beds. Each diffusor plate had two purposes. The first purpose was the same for both diffusor plates, namely to generate a homogeneous air flow. The second purpose of the top diffusor plate was to transfer the weight of the top alumina tube and its packed bed to the rigid insulation. The second purpose of the bottom diffusor plate was to support the bottom SiSiC RPC of the heating zone. The diffusor plates had a thickness of 7 mm, a width of 300 mm, and had 52 holes of 3 mm diameter, which were evenly distributed inside a disk of 200 mm diameter. To prevent alumina spheres in the top packed bed from falling into the reaction and heating zone, a 10 PPI alumina RPC was placed above the top diffusor plate, which had a diameter of 200 mm, a height of 20 mm, and a weight of 304 g.

Figure 7.4 shows schematics of the cross section of the insulation at various axial positions. To sustain the weight of the upper packed bed (transferred by the top diffusor plate), the insulation of the lower part of the reactor (0 mm $< x <$ 955 mm) was rigid. The upper insulation (955 mm $< x <$ 1655 mm) was flexible to have a close fitting between the insulation and the alumina tube, and between the insulation layers themselves to reduce natural convection. Natural convection streams are only favored by the upside-down arrangement of the upper TES (hot at the bottom, cold at the top), while for the lower TES this was not an issue. The rigid insulation consisted of porous ceramic and microporous insulation. The flexible insulation consisted of ceramic felt, flexible microporous insulation, and rockwool.

The flow paths of the reaction/inert gas and the HTF are indicated in Fig. 7.5 with red and blue lines, respectively. Air was used as HTF and
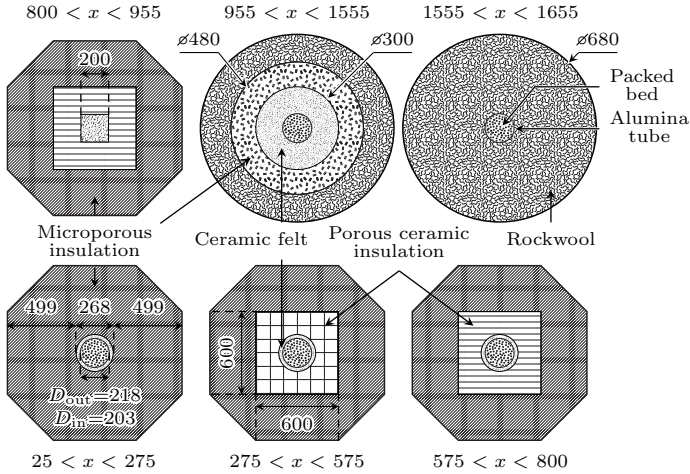
Figure 7.4: Schematic of the cross section of the insulation at various axial positions x, where x is defined in Fig. 7.1. Dimensions are given in mm.

pumped through the dual-storage reactor using a blower. The mass flow rate was PID controlled using an inverter. An air-to-water heat exchanger was placed before the blower to extract any accumulated heat from the outflow stream of the dual-storage reactor. Additional outflow temperature cooling before the heat exchanger was possible using an additional air stream that bypassed the dual-storage reactor (orange) and was then mixed with the air outflow stream of the dual-storage reactor. Valves were used to switch the flow direction.

The whole piping and pumping system was designed to be airtight. The only place where air could potentially escape was through the insulation of the heating and reaction zone. However, since the rest of the setup (packed beds, air piping, flanges, valves, and blower) was airtight, any air leaving/entering the bottom packed bed at its top had to be equal to that entering/leaving the top packed bed at its bottom. Furthermore, since the resistance to the flow passing through the heating and reaction zones was much smaller than the resistance to the flow passing through the insulation,
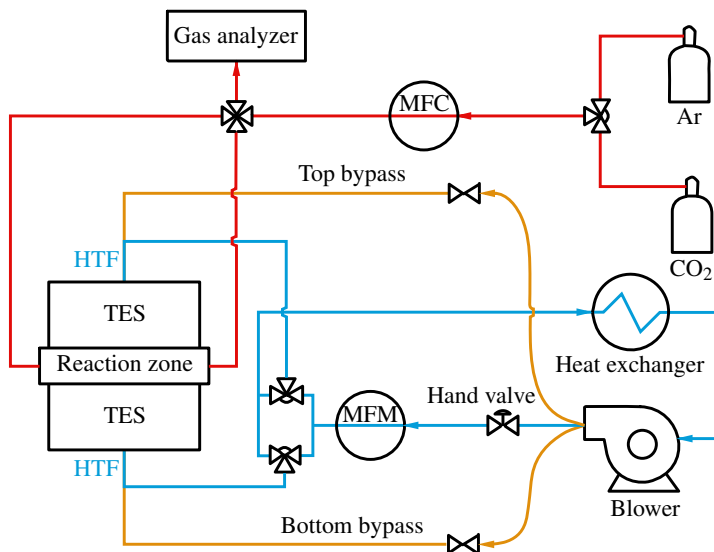
Figure 7.5: Schematic of the flow paths of the dual-storage reactor setup. The flow paths of the HTF and the bypass air are indicated with blue and orange lines, respectively. The flow path of the reaction/inert gas is indicated with red lines. MFM and MFC denote mass flow meters and mass flow controllers, respectively.

it is very unlikely that air bypassed the heating and reaction zones. Because of this particular design of the flow system, a pressure of around 1 bar evolved at the position of the heating and reaction zones.

A mass-flow controller was used to regulate the mass flow rates of the reaction/inert gases that were supplied from gas bottles. During reduction a flow of argon was injected into the reactor to decrease the oxygen partial pressure surrounding the ceria RPC. During oxidation, CO_2 was injected.

The AC voltage and AC current of both electrical heating elements were measured to determine the electrical power input. A mass-flow meter was used to measure the mass flow rate of the air flowing through the packed beds.

K- and B-type thermocouples were used to measure the temperature in the dual-storage reactor and piping. The packed-bed temperature distribution was measured at the center and at the wall of the alumina tube. The latter was measured by attaching the thermocouples to the inner surface of the alumina tube. The thermocouple locations are shown in Figs. 7.1 and 7.3. The axial distance between the thermocouples in the packed bed was around 150 mm and the distance between the end of the packed bed and the first thermocouples in the packed bed was around 125 mm. The concentrations of CO, CO_2, and O_2 in the reaction/inert gases were measured by a Siemens® Ultramat 23 gas analyzer. The setup was controlled by a computer and pre-defined cycles could be performed automatically.

7.2.2   Operation strategy

Various operation strategies were used to test heat recovery. Cycles were performed either with or without chemical reaction. For the cycles with chemical reaction, reduction of ceria was favored by decreasing the oxygen partial pressure using a flow of argon. During oxidation, ceria was oxidized either with CO_2 or, for simplicity, with air.

Cycles could be performed either symmetrically or asymmetrically. Symmetric cycles mean that the reduction temperature plateau/peak is moved, using a HTF, alternately to each of the tanks/packed beds. Asymmetric cycles mean that the reduction temperature plateau/peak is moved only to one of the tanks/packed beds and then back. While the original concept presented in Section 6.2 had two reaction zones and therefore a symmetric operation was meaningful, for this setup an asymmetric operation was also considered since there was only one reaction zone.

With this setup, three different operation strategies were performed: (1) asymmetric cycles with chemical reaction, (2) asymmetric cycles without chemical reaction, and (3) symmetric cycles without chemical reaction. Note that before the cycles could be performed, all experiments were initiated with a preheating phase to heat the insulation and the packed beds. During the preheating phase, the HTF was alternately injected from the top or

Table 7.1: Five phases of a typical cycle with the laboratory-scale dual-storage reactor. RG denotes the reactant gas, which is the gas that is injected into the reactor tube. Air is used as HTF. Phases 1 and 3 are stopped as soon as the ceria temperature reaches the reduction and oxidation temperatures, respectively.

	1. Heating	2. Reduction	3. Cooling	4. Oxidation	5. Heat recov.
	$\dot{m}_{HTF}$	$\dot{V}_{RG}$	$\dot{m}_{HTF}$	$\dot{V}_{RG}$	$\dot{m}_{HTF}$
Δt_i	Δt_{heat}	Δt_{red}=10 min	Δt_{cool}	Δt_{ox}=10 min	$\Delta t_{hr}=\Delta t_{cool}$
Δt_{alt}	120-300 s	-	-	-	-
$\dot{m}_{HTF}$	15-30 kg/h	-	15-30 kg/h	-	15-30 kg/h
	Alternating	-	From top	-	From bottom
$\dot{V}_{RG}$	-	1.5 l/min	-	0.5/1.5 l/min	-
RG	-	Argon	-	CO_2/air	-
P_{heater}	Max: 3.15 kW	-	-	-	-

bottom to increase the heat transfer between the air and the heater and between the air and the RPCs.

In the following, the first and the third operation strategy are presented in detail. The second operation strategy is the same as the first, just leaving out the phases of chemical reaction. Results of the first and third operation strategy are discussed in detail in Sections 7.3.1 and 7.3.2, while Section 7.3.3 summarizes the results of all three operation strategies for various HTF mass flow rates, reduction temperatures, and oxidation temperatures.

Asymmetric cycles with chemical reaction

These cycles were operated asymmetrically as there was only one reaction zone above the heating zone. To perform heat recovery and the redox reaction with one reaction zone, five operation phases were needed with this setup,

which are listed in Table 7.1. Note that the operation was not optimized for performance. Instead, the operation was split into basic actions, for example via separating cooling and oxidation as well as heating and reduction phases. Short descriptions of each phase follow.

1. Heating: The heating power was ramped to the desired maximum power. The maximum power cannot be reached immediately because the electrical resistance of the heating element increases as it heats up. Otherwise, the current through the heating elements cannot be kept below the limit of 250 A. During the heating phase, the HTF is alternately injected from the top or bottom to increase the convective heat transfer between the air and the heater and between the air and the RPCs. The duration of the heating phase (Δt_{heat}) is given by the requirement that the ceria thermocouple (inside the encapsulation) reaches the desired reduction temperature.

2. Reduction: The HTF flow is turned off. Argon (99.999% purity) is injected into the reactor with a volume flow of 1.5 l/min to favor the reduction of ceria. The oxygen concentration in the argon stream is measured by the gas analyzer. The duration of this phase is $\Delta t_{\text{red}} = 10$ min.

3. Cooling: HTF is injected from the top to cool the ceria. The phase stops when the temperature of the ceria reaches the desired oxidation temperature (Δt_{cool}).

4. Oxidation: CO_2 (or air for simplicity) is injected with a volume flow of 0.5 or 1.5 l/min to oxidize the ceria and produce CO. The time duration of this phase is $\Delta t_{\text{ox}} = 10$ min.

5. Heat recovery: HTF is injected from the bottom to re-heat the ceria. To shift the temperature profile back to the position at the beginning of the cooling phase, the time duration is set to the duration of the cooling phase, $\Delta t_{\text{hr}} = \Delta t_{\text{cool}}$.

Symmetric cycles without chemical reaction

Symmetric operation would be preferred if there was a second reaction zone below the heating zone. Since there was only a reaction zone above the heating zone, these experiments were performed without driving the redox reaction. The cycles consisted of two symmetric half-cycles, one in which the temperature profile was first shifted downwards and then back upwards and one in which the temperature profile was first shifted upwards and then back downwards. The first half-cycle was similar to the asymmetric cycle described above, just without chemical reaction and consisted therefore only of phases 1, 3, and 5 (see Table 7.1). The second half-cycle consisted also of phases 1, 3, and 5, with the difference that during phase 3 the HTF was injected from the bottom instead of from the top, and during phase 5 the HTF was injected from the top instead of from the bottom. The times of the phases 1, 3, and 5 of the second half-cycle were chosen to be equal to the respective times of the first half-cycle.

7.3   Results[2]

In the following two sections, two specific heat-recovery experiments are discussed in detail. The first experiment consisted of a preheating phase and four asymmetric cycles with chemical reaction. The second experiment consisted of a preheating phase and four symmetric cycles without reaction. Further experiments are summarized in Section 7.3.3.

7.3.1   Asymmetric cycles with chemical reaction

Figure 7.6 shows the ceria temperature T_{ceria}, the accumulated electrical energy input by the heater E_{heater}, and the integrated mass flows from the top and the bottom ($m_{\text{HTF,top}}$ and $m_{\text{HTF,bottom}}$) during the preheating

---
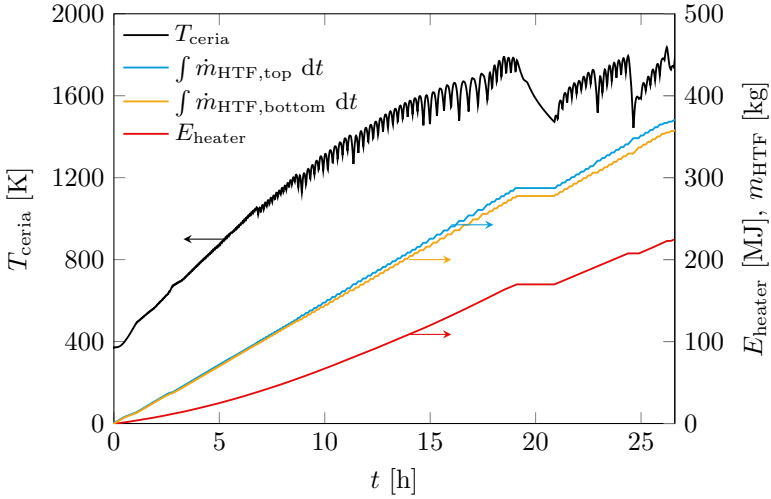
Figure 7.6: Preheating phase for the asymmetric cycles with chemical reaction. The ceria temperature T_{ceria} is shown in black, the accumulated electrical energy input by the heater E_{heater} is shown in red, and the integrated HTF mass flows from the top and the bottom ($m_{\mathrm{HTF,top}}$ and $m_{\mathrm{HTF,bottom}}$) are shown in blue and yellow, respectively. The mass flow rate was kept constant at $\dot{m}_{\mathrm{HTF}} = 30$ kg/h and the maximum heater power was $P_{\mathrm{heater,max}} = 3.3$ kW. The flow direction was alternated at intervals of $\Delta t_{\mathrm{alt}} = 120 - 800$ s.

phase. Note that the measured ceria temperature was inaccurate in the beginning of the pre-heating phase as in the beginning the temperature was close to ambient temperature ($\sim$298 K), which is below the lower measurement limit of B-Type thermocouples ($\sim$373 K). The air mass flow rate was constant at $\dot{m}_{\mathrm{HTF}} = 30$ kg/h. The oscillations seen in $m_{\mathrm{HTF,top}}$ and $m_{\mathrm{HTF,bottom}}$ originate from the fast alternation of the HTF flow direction. The alternating time interval ranged from $\Delta t_{\mathrm{alt}} = 120$ s to 800 s. Small Δt_{alt} lead to a faster heating of the heating zone and steeper temperature profiles, while larger Δt_{alt} lead to flatter temperature profiles as the heat is spread
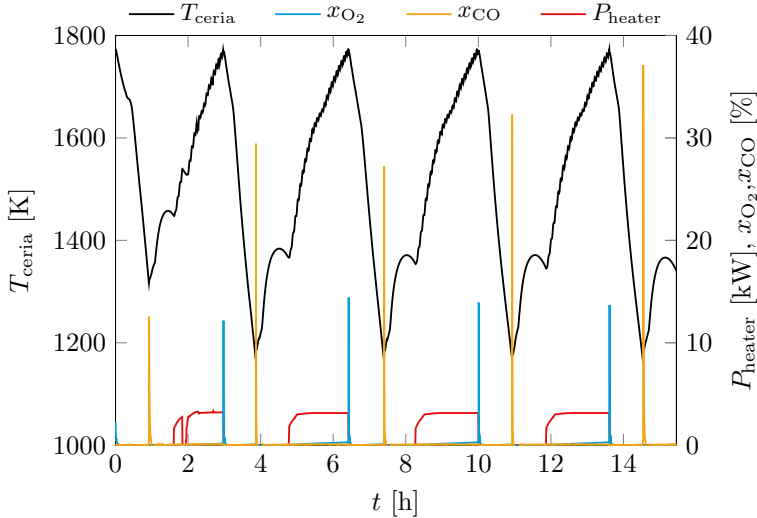
Figure 7.7: Four asymmetric cycles with chemical reaction. The ceria temperature is shown in black, the accumulated energy by the heater is shown in red, and the O_2 and CO concentrations are shown in blue and yellow, respectively. The reduction and oxidation temperatures were T_{red} = 1773 K and T_{ox} = 1173 K, respectively. The mass flow rate was kept constant at $\dot{m}_{HTF}$ = 15 kg/h and the maximum heater power was P_{heater} = 3.15 kW. The alternating time interval during heating was Δt_{alt} = 120 s.

over a larger range. Although in theory steep thermoclines are desired to decrease the cycle time and thereby thermal losses, in this setup they were flattened intentionally for two reasons: First, to have a good preheating of the insulation, and second, to avoid large axial temperature gradients in the alumina tube that contained the packed bed to avoid breaking of the tube. The whole preheating phase consumed 225 MJ of electrical heating energy over 26.5 h.

After the preheating phase, multiple consecutive cycles were performed. Figure 7.7 shows the ceria temperature, the heating power, and the concen-
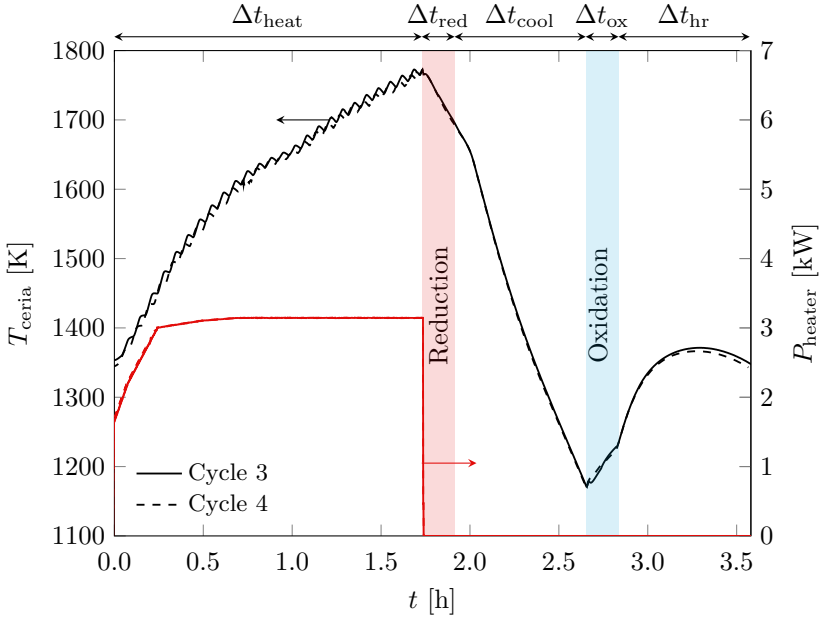
Figure 7.8: Ceria temperature (black) and heater power (red) for the third and fourth asymmetric cycles with chemical reaction.

trations x_{O_2} and x_{CO} for four consecutive cycles. The cycles were performed with $T_{red} = 1773$ K and $T_{ox} = 1173$ K and a HTF mass flow rate of $\dot{m}_{HTF}$ $= 15$ kg/h. The O_2 and CO concentrations are only seen by sharp peaks because of the relatively short time of the reduction and the oxidation with respect to the total cycle time. The ceria temperature and the integrated heating power are already close to a quasi-steady state after the second cycle, which is attributed to the long preheating phase.

The similarity of the cycles can be seen also in Fig. 7.8 where the ceria temperature and the heater power of the third and fourth cycles are plotted on top of each other while their differences are barely visible. Each cycle is comprised of the five phases described in Section 7.2.2. In the following, observations are listed separately for the five phases:

1. The oscillations during the heating phase were again due to alternating of the HTF flow direction with $\Delta t_{\text{alt}} = 120$ s. The heater power was ramped up to 3.15 kW. The heating phase was stopped when the ceria temperature reached $T_{\text{ceria}} = 1773$ K, which ocurred after $\Delta t_{\text{heat}} = 105$ min.

2. During the subsequent reduction phase, the HTF flow and the heater were turned off, causing the ceria temperature to drop due to thermal losses and thermocline degradation. The reduction took $\Delta t_{\text{red}} = 10$ min, during which argon was injected with 1.5 l/min into the reactor tube to reduce the partial pressure of oxygen and remove the evolved oxygen from the ceria.

3. During the cooling phase, HTF was injected from the top to cool the ceria temperature until it reached the oxidation temperature $T_{\text{ceria}} = 1173$ K after $\Delta t_{\text{cool}} = 45$ min. (Due to temperature limits of some thermocouples, the cooling phase of the first cycle had to be interrupted before the ceria reached the desired oxidation temperature.)

4. After cooling, the HTF flow was turned off and CO_2 was injected into the reactor tube during $\Delta t_{\text{ox}} = 10$ min to oxidize the ceria and produce CO. The CO_2 volume flow rate was 1.5 l/min for the first three cycles, while for the fourth cycle it was 0.5 l/min. The CO peak concentrations seen in Fig. 7.7 differ between the first three cycles, which is attributed to the fact that the oxidation with CO_2 was the only setup input that was controlled manually for safety reasons.

5. During the heat-recovery phase, HTF was injected from the bottom, to heat the ceria. The duration was equal to the cooling phase, i.e. $\Delta t_{\text{hr}} = \Delta t_{\text{cool}} = 45$ min. The peak in the ceria temperature is reached before the completion of the heat-recovery phase.

The reason for the last observation is a counter-intuitive result, but it becomes more clear when looking at Fig. 7.9. It shows the temperature distribution at the start of the reduction phase, at the start of the oxidation phase, and at the end of the heat-recovery phase. The temperatures measured
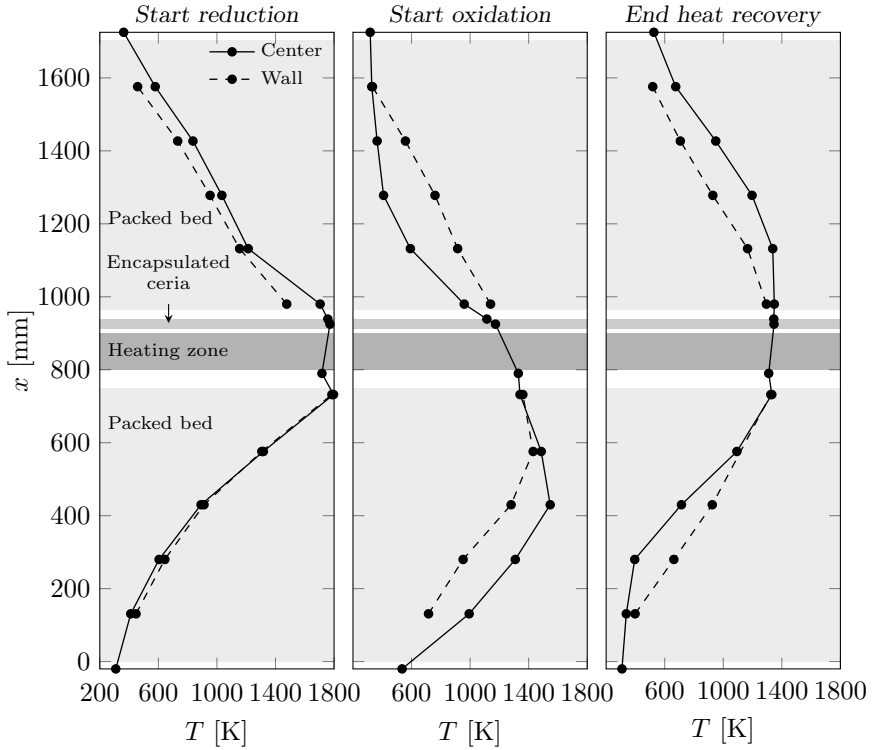
Figure 7.9: Temperature distributions during the fourth asymmetric cycle with chemical reaction as a function of the height. The left, middle, and right plots correspond to the temperature distributions along the dual-storage reactor at the start of reduction, at the start of oxidation, and at the end of heat recovery, respectively. The temperatures measured along the centerline and the wall are shown as solid and dashed lines, respectively.

along the centerline and the wall are shown as solid and dashed lines, respectively. At the start of the oxidation phase, the wall is hotter than the center in the upper part of the bottom packed bed and the top packed bed,

while in the lower part of the bottom packed bed the insulation is considerably cooler. This leads to an apparent upwards shift of the temperature profile during the oxidation phase due to conduction. The same effect is present during the cooling and the heat-recovery phases. This effect is the reason why the temperature profile along the centerline is not symmetric along the setup at the end of the heat-recovery phase, which was approximately the case at the start of the reduction phase. Instead, at the end of the heat-recovery phase the temperature profile is shifted too much upwards. This also explains why the ceria temperature reaches its peak before the end of the heat-recovery phase.

One can make two further observations. First, the inertia of the thermal insulation causes the temperature profiles along the wall to move significantly less than the temperature profiles along the center. Second, the temperature peak at the start of reduction disperses during the cooling phase of the ceria. This is a result of thermal losses and thermocline degradation. Furthermore, the actual amount of thermal energy stored inside the heating and reaction zones is rather small because the void fraction is much larger than inside the packed beds. Therefore, shifting this peak down into the packed bed leads consequently to a contraction of the peak and thereby to a faster dissipation of the high-temperature thermal energy.

To calculate the heat-recovery effectiveness, the maximum ceria temperature that was measured throughout the heat recovery phase was used:

$$\varepsilon_{\text{hr}} = \frac{e_{\text{ceria}}(T_{\text{ceria,hr,max}}) - e_{\text{ceria}}(T_{\text{ceria,ox}})}{e_{\text{ceria}}(T_{\text{ceria,red}}) - e_{\text{ceria}}(T_{\text{ceria,ox}})} \ . \tag{7.3}$$

For the second, third and fourth cycle, the heat-recovery effectiveness was 33%. This value is smaller than the value reported for the setup in Section 6.3, which was 49%. The smaller value is due to three main reasons. First, additional heat losses and thermocline degradation occurred with this setup due to the additional oxidation and reduction phases where the HTF flow was turned off. Second, the ceria was encapsulated and therefore an additional thermal resistance was present between the air and the ceria. Third, reduction
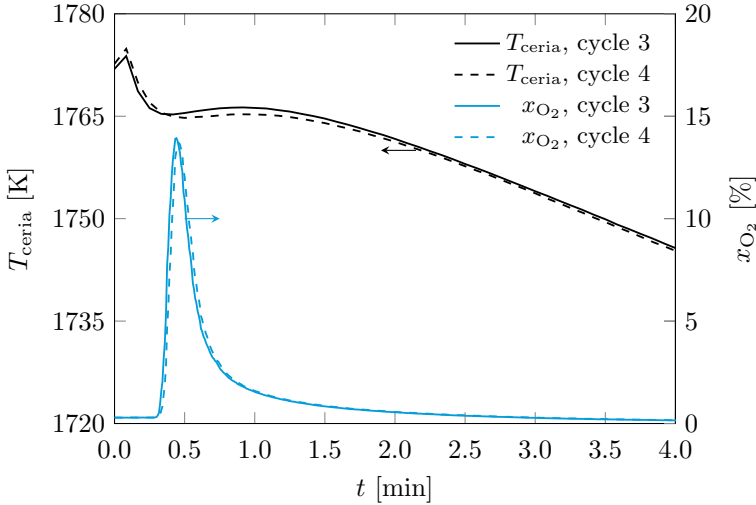
Figure 7.10: Ceria temperature (black) and O_2 concentration after the reactor tube outlet (blue) during the reduction phases of the third (solid lines) and fourth (dashed lines) asymmetric cycles with chemical reaction.

temperatures were higher with $1500°C$ instead of $1400°C$, leading to higher thermocline degradation due to radiation. Nevertheless, considering the small scale of the setup, a heat-recovery effectiveness of 33% with chemical reaction is an encouraging result.

Figure 7.10 shows the O_2 concentration and the ceria temperature as a function of time during the reduction phases of the third and fourth cycles. One can observe that the two cycles are quite repeatable, which supports the previous observation that the system is close to a quasi-steady state after the first two cycles. The ceria temperature does not show a continuous decrease in temperature. Instead, it exhibits a dip in the first half-minute that is attributed to the endothermic reduction of ceria. Based on the O_2 evolution, the volume flow of argon, and the mass of ceria, one can calculate the mean difference between the reduction extent before and after reduction. For the four cycles, the resulting reduction extent differences were $\Delta \delta_1 =$
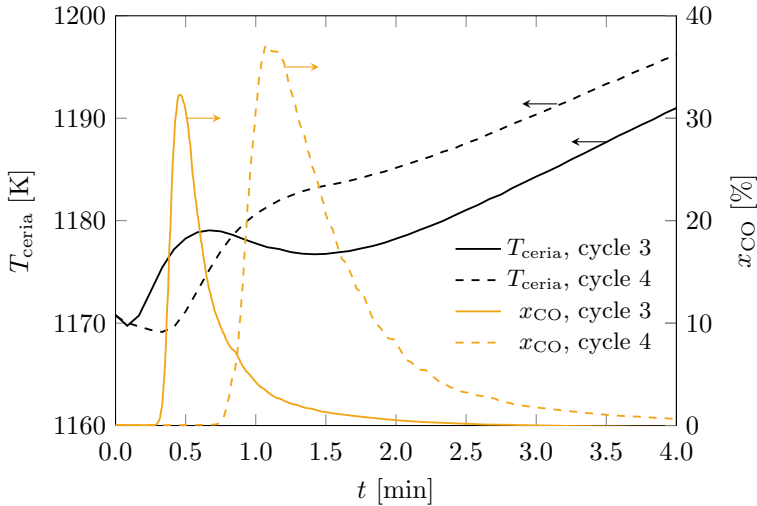
Figure 7.11: Ceria temperature (black) and CO concentration after the reactor tube outlet (yellow) during the oxidation phases of the third (solid lines, $\dot{V}_{CO_2} = 1.5$ l/min) and fourth (dashed lines, $\dot{V}_{CO_2} = 0.5$ l/min) asymmetric cycle with chemical reaction.

0.016, $\Delta\delta_2 = 0.017$, $\Delta\delta_3 = 0.017$, and $\Delta\delta_4 = 0.018$.

Figure 7.11 shows the CO concentration and the ceria temperature as a function of time during the oxidation phases of the third and fourth cycles. The exothermic oxidation of the ceria causes the rise in temperature in the first 1-2 minutes. The temperature rises earlier for the oxidation with $\dot{V}_{CO_2} = 1.5$ l/min due to the shorter duration between the start of injection of CO_2 until the CO_2 reaches the ceria. Based on the CO evolution and the volume flow of CO_2, one can calculate the mean difference between the reduction extent before and after oxidation. For the four cycles, the resulting reduction extent differences were $\Delta\delta_1 = 0.016$, $\Delta\delta_2 = 0.018$, $\Delta\delta_3 = 0.02$, and $\Delta\delta_4 = 0.016$. These values are relatively close to the values obtained from the O_2 evolution during reduction, especially considering the limited accuracy of the gas analyzer. Since the setup served as a demonstration of
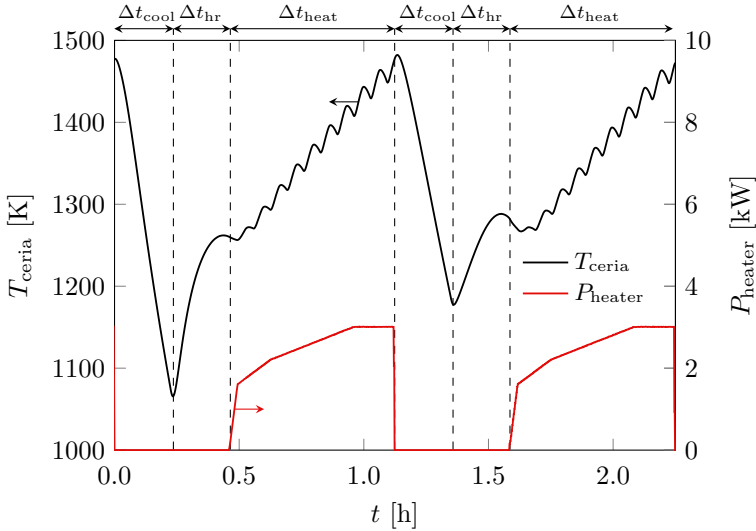
Figure 7.12: Ceria temperature (black) and heater power (red) for one symmetric cycle without chemical reaction. The reduction and oxidation temperatures were $T_{red} = 1473$ K and $T_{ox} = 1073$ K, respectively. The mass flow rate was kept constant at $\dot{m}_{HTF} = 30$ kg/h and the maximum heater power was $P_{heater} = 3$ kW. The alternating time interval during heating was $\Delta t_{alt} = 240$ s.

the dual-storage reactor concept, this amount of accuracy was considered to be sufficient. Since the accuracy of the O_2 concentration sensor is better than that of the CO sensor, in the following the $\Delta\delta$ is calculated from the O_2 evolution during reduction.

7.3.2 Symmetric cycles without chemical reaction

For brevity, only one representative symmetric cycle without chemical reaction is discussed. Figure 7.12 shows the ceria temperature evolution and the electrical power input as a function of time for one complete symmetric cycle. The three phases of each half-cycle were described in Section 7.2.2.

The mass flow rate of the HTF was kept constant at 30 kg/h and the heater power was ramped up to 3 kW in phase 1 of each half-cycle. The targeted reduction and oxidation temperatures were $T_{\mathrm{red}} = 1473$ K and $T_{\mathrm{ox}} = 1073$ K, which were used for the operation strategy of the first half-cycle. The time of the heating phases of both half-cycles was $\Delta t_{\mathrm{heat}} = 38$ min. The time of the cooling and heat-recovery phases of both half-cycles was $\Delta t_{\mathrm{cool}} = 14$ min. The temperature evolution of the ceria is not symmetric because the ceria is not in the center of the dual-storage reactor.

Figure 7.13 shows the temperature profile along the dual-storage reactor at at the end of heating and cooling of the first and second half-cycle. The center and wall temperatures are shown in the left and right plots, respectively. Although the setup itself was not completely symmetric, the symmetric operation lead to reasonably symmetric temperature distributions. This is seen from the fact that the temperature distributions at the end of the heating phase of both half-cycles are similar (solid and dashed blue lines), while the temperature distributions at the end of the cooling phases of the two half-cycles (red and yellow lines) are approximately reflected at the location of the heating zone. The most significant temperature difference is seen in the wall temperatures of each packed bed closest to the heating zone. The wall temperature of the top packed bed is lower, which could originate from the upside-down arrangement of the top packed bed and an imperfect fitting between the insulation and the alumina tube, favoring natural convection at the outside of the alumina tube. Apart from that, natural convection seems to have only a marginal effect on the behavior of the top packed bed.

The heat-recovery effectiveness based on the ceria temperature measurement during the first half-cycles was between $\varepsilon_{\mathrm{hr}} = 0.48$ and $\varepsilon_{\mathrm{hr}} = 0.49$ for all four cycles that were performed. These values are higher than the ones from the asymmetric experiment. This is because (1) there were no oxidation and reduction phases with stagnant HTF, (2) thermal losses were smaller due to the lower temperatures, (3) the mass flow rate was higher, leading also to smaller thermal losses as the phase time is decreased, and
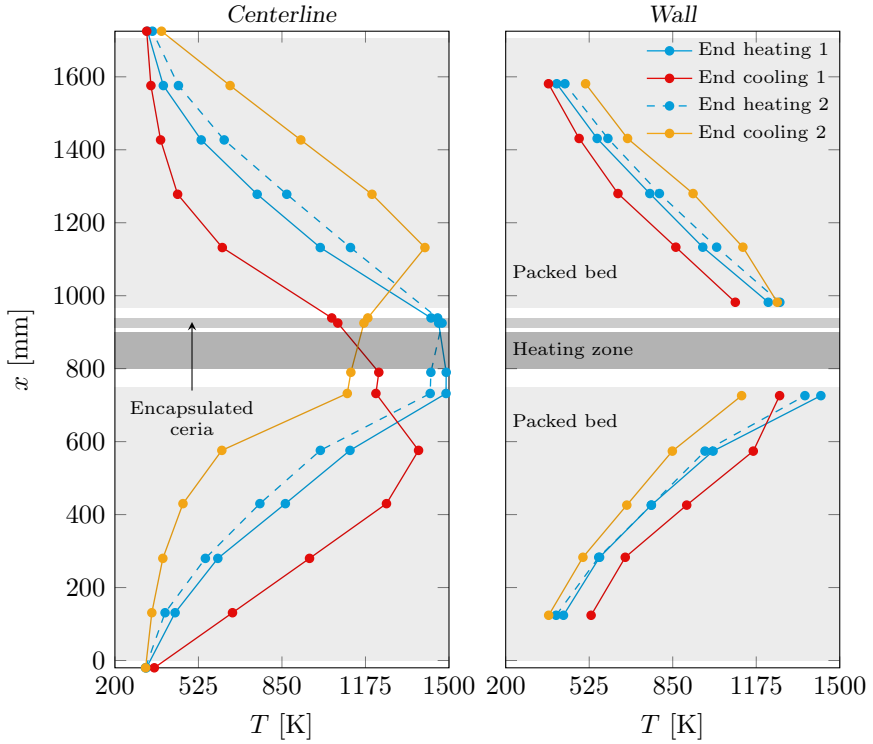
Figure 7.13: Temperature distributions along the centerline (left) and the wall (right) during the fourth symmetric cycle without chemical reaction. The solid and dashed blue lines correspond to the temperature distributions along the dual-storage reactor at the end of the heating phase of the first and second half-cycles, respectively. The red and yellow lines correspond to the temperature distribution at the end of the cooling phases of the first and second half-cycles, respectively.

(4) the thermocline steepness was more uniform along the packed bed. The obtained heat-recovery effectiveness is promising and shows that also for encapsulated ceria and symmetric operation the dual-storage reactor concept

Table 7.2: Summary of asymmetric cycles with chemical reaction and oxidation with CO_2. The following parameters were the same for all cycles: T_{red} = 1773 K, T_{ox} = 1173 K, Δt_{alt} = 120 s, $\dot{m}_{HTF}$ = 15 kg/h, m_{ceria} = 76.9 g.

Cycle [−]	E_{heater} [MJ]	Δt_{heat} [min]	Δt_{cool} [min]	ε_{rec} [%]	$\Delta \delta$ [−]
1	13.3	81.5	43.3	36	0.016
2	17.9	100.2	47.9	33	0.017
3	18.9	104.7	45.1	33	0.017
4	18.9	105.1	44.9	33	0.018

is performing well.

7.3.3 Summary of results

Table 7.2 shows a summary of the four asymmetric cycles that included the redox reaction using CO_2 during the oxidation, as described in Section 7.3.1. One can see that the values barely change between the third and the fourth cycles.

Table 7.3 shows a summary of the two asymmetric cycles that also included the redox reaction but oxidation was performed with air. Different reduction temperatures and mass flows were used for the two experiments. The results of the last two cycles are again very similar, indicating that the experiments were close to a quasi-steady state. The results of the first experiment with T_{red} = 1773 K are similar to those shown in Table 7.2. For the former, slightly higher reduction extents and heat-recovery effectivenesses were found.

Table 7.4 shows the summary of the asymmetric cycles that did not include the redox reaction. Therefore, only phases 1, 3, and 5 (see Section 7.2.2) were performed for these cycles. One can see that with a lower mass flow rate of 15 kg/h instead of 30 kg/h, the heat-recovery effectiveness was smaller for the same reaction temperatures at 36%-39% vs. 46%-49%. Furthermore, also the integrated heating power and the heating time were smaller for the experiment with the lower mass flow rate. Therefore, the

Table 7.3: Summary of asymmetric cycles with chemical reaction and oxidation with air. The mass of ceria was $m_{\text{ceria}} = 73.5$ g.

Cycle [−]	T_{red} [K]	T_{ox} [K]	$\dot{m}_{\text{HTF}}$ [kg/h]	Δt_{alt} [s]	E_{heater} [MJ]	Δt_{heat} [min]	Δt_{cool} [min]	ε_{rec} [%]	$\Delta \delta$ [−]
1	1773	1173	15	240	11.3	61.5	37.5	38	0.026
2	1773	1173	15	240	14.8	79.4	38.0	36	0.022
3	1773	1173	15	240	15.2	81.3	38.1	36	0.022
1	1673	1173	30	120 − 360	16.1	94.5	20.8	41	0.011
2	1673	1173	30	120 − 360	18.3	107.1	18.5	43	0.011
3	1673	1173	30	120 − 360	15.2	89.4	20.3	42	0.011
4	1673	1173	30	120 − 360	15.5	91.4	20.6	41	0.011

Table 7.4: Summary of asymmetric cycles with heat recovery and without chemical reaction. The mass of ceria was $m_{\text{ceria}} = 73.5$ g.

Cycle [−]	T_{red} [K]	T_{ox} [K]	$\dot{m}_{\text{HTF}}$ [kg/h]	Δt_{alt} [s]	E_{heater} [MJ]	Δt_{heat} [min]	Δt_{cool} [min]	ε_{rec} [%]
1	1473	1073	15	240	5.8	39.7	20.8	39
2	1473	1073	15	240	6.0	40.4	22.7	37
3	1473	1073	15	240	5.9	40.3	23.7	36
1	1473	1073	30	120	7.0	46.2	10.9	49
2	1473	1073	30	120	7.0	46.0	13.0	47
3	1473	1073	30	120	6.7	44.4	14.0	46
1	1573	1173	30	240 − 300	8.3	49.5	13.1	48
2	1573	1173	30	240 − 300	8.0	47.9	13.8	47
3	1573	1173	30	240 − 300	7.9	47.8	14.3	48
1	1673	1173	30	240 − 300	11.0	61.9	19.2	50
2	1673	1173	30	240 − 300	12.6	69.2	19.1	52

lower heat-recovery effectiveness of the experiment with lower mass flow rate is attributed to (1) the smaller heating power input and (2) the increased heat losses due to a longer duration of the cooling and heat-recovery phases. The other experiments were performed at different temperatures but all yielded similar heat-recovery effectivenesses between 46% and 52%. This shows that the heat-recovery effectiveness of the concept does not strongly depend on the reduction and oxidation temperatures.

Table 7.5: Summary of symmetric cycles with heat recovery and without chemical reaction. The mass of ceria was $m_{\mathrm{ceria}} = 73.5$ g. Results are only shown for the first half-cycle. For the second half-cycle, the values are equal for the mass flow rate, the alternating time, the integrated heating power, the duration of heating, and the duration of cooling.

Cycle	T_{red}	T_{ox}	$\dot{m}_{\mathrm{HTF}}$	Δt_{alt}	E_{heater}	Δt_{heat}	Δt_{cool}	$\varepsilon_{\mathrm{rec}}$
[−]	[K]	[K]	[kg/h]	[s]	[MJ]	[min]	[min]	[%]
1	1473	1073	30	240	6.6	44.2	12.1	48
2	1473	1073	30	240	5.9	39.8	13.8	48
3	1473	1073	30	240	5.4	37.1	14.4	49
4	1473	1073	30	240	5.6	38.4	14.4	49

Table 7.5 shows the summary of the symmetric cycles, which were discussed in Section 7.3.2. The values are only shown for the first half-cycle, the second half-cycle has the same values for the mass flow rate, the alternating time, the integrated heating power, the duration of heating and the duration of cooling. The reduction and oxidation temperatures and the heat-recovery effectivenesses are not stated for the second half-cycle because there was only one reaction zone which was used to define the first half-cycle. The performance, namely the heating power, heat-recovery effectiveness, and durations of the phases, is seen to be relatively stable throughout all four cycles.

7.4   Summary and conclusions

A laboratory-scale dual-storage reactor setup using ceria as redox material was designed, built, and tested. Similar to the setup presented in Section 6.3, one of the goals was to demonstrate sensible-heat recovery of the redox material. In contrast to the setup presented in Section 6.3, this setup had the additional goal of demonstrating CO production in combination with heat recovery for encapsulated ceria.

The setup consisted of two packed beds, which served as thermocline thermal energy storages to recover the thermal energy between reduction

and oxidation temperatures. The filler material of the packed beds was alumina spheres of 3-5 mm diameter. The packed beds were vertically arranged and stacked on top of each other. The height and diameter of the packed beds were 750 mm and 203 mm, respectively. The thermoclines were moved upwards and downwards using air as HTF. Between the packed beds there was an electrical heating zone and a reaction zone. The reaction zone consisted of ceria RPCs that were encapsulated in an alumina tube. Reaction gases could be injected at the inside of the encapsulation. Thereby, the reaction gases could be separated from the HTF.

The setup successfully demonstrated both heat recovery and the generation of CO from CO_2. Temperatures of the encapsulated ceria and the packed beds reached up to 1773 K. Multiple cycles for different operating strategies, mass flow rates (15-30 kg/h) and reduction (1473-1773 K) and oxidation (1073-1173 K) temperatures were performed. Reduction extents of up to $\delta_{red} = 0.026$ were obtained (average over the reaction zone) and CO concentrations during oxidation were above 35%. The heat-recovery effectivenesses of all experiments ranged from 33% to 52%. The heat-recovery effectiveness was more strongly affected by the mass flow rates than by the reduction and oxidation temperatures. The effect of natural convection was small for the top packed bed although it was arranged upside-down.

OUTLOOK

8.1 Combined sensible/latent thermal energy storage

The option of placing PCM not only at the top but also at the bottom of sensible-heat TES was proposed in previous studies [24, 26]. This can limit the outflow temperature increase during charging. Studying the benefit of this concept in more detail for the application in AA-CAES plants is particularly interesting because there the maximum outflow temperature from the TES into the cavern is strongly limited to protect the cavern [177]. Using a suitable PCM at the bottom can therefore reduce the need for oversizing a sensible-only TES.

Performance and cost may be optimized using numerical optimization tools to assist in the selection of the most suitable PCMs considering their melting temperature, heat of fusion, and other thermo-physical properties, and to assist in choosing the amount as well as the dimensions of the tubes or the spheres. While numerical optimization studies were published for sensible-only [178] and for latent-only [72] TES concepts, no numerical

optimization studies were published for combined sensible/latent TES.

Furthermore, to realize the use of encapsulated PCM at industrial-scale, an efficient encapsulation process needs to be developed. Future cost comparisons between combined sensible/latent TES and sensible-only TES should consider the cost of the encapsulation process and the related labour cost.

Finally, corrosion at the interface between the encapsulation material and the PCM can be a major issue. While there exist many corrosion studies mainly on salt PCMs, only little work was published on the corrosion between metallic PCMs and steel. The formation of an intermetallic layer between solid iron and liquid aluminum is well known and was previously studied [179, 73]. The intermetallic layer formation between $AlSi_{12}$ as PCM and steel AISI 316L as encapsulation was studied in [180] and a ceramic coating was proposed to inhibit its formation. Further studies of corrosion in encapsulated metallic PCMs are required to guarantee the performance and the mechanical stability over thousands of cycles.

8.2   Thermocline control

The TCC methods that were analyzed in this thesis (extracting, injecting, and mixing) rely either on having multiple smaller TES units or on having ports at intermediate heights of the TES. For the latter, CFD simulations are required to carefully design the ports and guarantee an approximately one-dimensional flow. Furthermore, the design needs to consider that the port should not affect significantly the flow of the HTF when the port is not in use and the HTF has to flow around the port. Finally, the design should keep the labour and material costs low. Within this project, first steps were undertaken for the design of the ports using CFD simulations in a semester project [181].

The functionality of the studied TCC methods and the functionality of the port design needs to be tested experimentally to validate numerical models. With the aim of model validation, air could be used as HTF in

a laboratory-scale setup and the experimental charging and discharging temperatures could be chosen to be relatively low to simplify the setup design and construction.

To decide whether TCC methods make economic sense, a cost analysis is necessary. In this cost analysis it is crucial to look not only at the material cost but also include the cost of the turbine. The cost of the turbine should depend on the maximum accepted TES outflow temperature drop during discharging. This requires taking into account the interaction between the various types of power cycles and the TES.

Furthermore, the literature lacks a comprehensive comparison between all proposed passive and active methods that address thermocline degradation. Such a comparison preferably assesses the performance as well as the estimated costs of each method.

8.3 Advanced adiabatic compressed air energy storage

The operation of the thermocline TES inside the cavern was successful and its behavior was as expected except for the leaks from the steel cover. In a future plant these leaks should be eliminated by using a more robust steel cover. In terms of material degradation, more cycles are necessary to gain confidence in the robustness and reliability of the concept at larger scales.

The rock cavern based AA-CAES technology needs further studies and improvements to make the technology a reliable alternative to PHS. Tests at higher pressures are necessary to gain further knowledge about the tightness of unlined rock caverns. To perform these tests with the existing pilot plant, it is necessary to redesign and reconstruct the concrete plugs. In addition, due to the temperature restrictions of the rock and salt caverns, it would be interesting to test the pilot plant TES with additional PCM at the bottom.

Furthermore, an integral need for the AA-CAES technology is the integration of all key components with the cavern and the TES, namely an adiabatic compressor and a turbine.

As an alternative to the one-stage compression and expansion concept, two- and three-stage compression and expansion concepts may be considered, which would require multiple TES units that store/release the heat between compression/expansion stages. This would simplify the design of the adiabatic compressors. Numerical studies are needed to properly design and optimize the components and the operation procedure. First steps were undertaken in a semester project where the TES model was coupled to models of the compressors and turbines [182].

8.4 Dual-storage reactor

Experimental and numerical work is needed to further improve and/or simplify the dual-storage reactor concept.

8.4.1 Improvements of numerical model

The chemical reaction should be modeled in more detail, considering oxidation reaction kinetics and hence maximum conversion.

8.4.2 Laboratory-scale setup of dual-storage reactor with redox reaction

The numerical model can be further validated with data from the second laboratory-scale dual-storage reactor (Chapter 7), where temperatures up to 1773 K were reached in the packed beds.

The experimental setup may be used to test different redox materials, storage materials or encapsulation materials. The operation of the setup may be optimized to reach higher performance, e.g., injecting argon already during heating phases and injecting CO_2 already during cooling phases. The operation of the reactor during reduction may also be tested with a vacuum pump instead of an inert gas.

8.4.3 Improvements and extensions of dual-storage reactor concept

Tank containment

It was shown that solar-to-fuel efficiencies are increased by using higher operation pressures of the HTF. Pressurized containers are typically made of steel. However, the maximum operation temperature of steel is significantly lower than the operation temperatures of the dual-storage reactor. Therefore, the insulating material should be placed between the tank filler materials and the containment. This requires a careful design to avoid bypassing of the HTF through the insulation and experimental testing to see what the consequences are for the insulation, e.g., to what extent it is contracted due to the expansion of the particles.

Reaction zone

For the concept of indirect contact between HTF and redox material, future work should focus on improving the heat transfer between HTF and redox material while keeping the pressure drop small. Typically this can be achieved by increasing the specific surface area of the encapsulation. This could, e.g., be realized via fins or the use of RPC structures in the void space of the reaction zone. However, since the encapsulation is most probably made from ceramics, experimental verification is necessary to demonstrate the stability of the improved encapsulation geometry at high temperatures.

To optimize the conversion during oxidation, tube layers that are exposed to different oxidation temperatures can be connected. For example, CO_2 is first injected into tubes of highest oxidation temperature, since there the lowest maximum conversion of CO is reached. The outlet of those tubes is connected to an inlet of tubes where the oxidation temperature is lower and therefore higher maximum conversions are reached. Such an operation leads to higher conversion and total fuel yield and reduces the need for TCC before oxidation. The benefit could be assessed by simulations.

To reduce the work for vacuum pumping, combinations of pulling vacuum and injecting small amounts of inert gas during reduction can be considered [175].

For economical reasons, it may be important to shorten the cycle time. The cycle time could be shortened by using, e.g., only one reaction zone instead of two or by decreasing the height of the TES and the reactor.

Considerable efforts have been made to find redox materials other than ceria in order to decrease the reduction temperature. Although several materials reduce at lower temperatures, they typically come with the drawbacks of higher temperature differences between reduction and oxidation temperatures and lower CO_2 to CO conversions, as seen for perovskites [183] or zirconia-doped ceria [162]. However, assuming that the alternative materials are mechanically and chemically stable, these materials can be interesting for the dual-storage reactor for two reasons. On the one hand, thanks to the efficient heat recovery, the higher temperature differences between reduction and oxidation temperatures are not that much of an issue. On the other hand, multiple redox materials that react at different temperatures could be combined in a cascaded dual-storage reactor.

A schematic of a cascaded dual-storage reactor is shown in Fig. 8.1. Multiple redox materials are stacked on top of each other with the redox materials of highest reduction and oxidation temperatures at the top and the redox materials of lowest reduction and oxidation temperatures at the bottom of the reaction zone. Such a cascade suits the dual-storage reactor particularly well because a certain gradient of the thermoclines is desired to expose the redox materials to the corresponding reaction temperatures. Therefore thermocline degradation is expected to be less of an issue. For encapsulated redox materials, conversion is maximized via connecting the outlet of reactor tubes that lead to low conversions with the inlet of reactor tubes that lead to high conversions, as discussed above.

Considering the material selection for the cascaded dual-storage reactor, particular attention may be given to variable dopant concentrations in ceria. Using zirconia as dopant, it was shown that the higher the zirconia
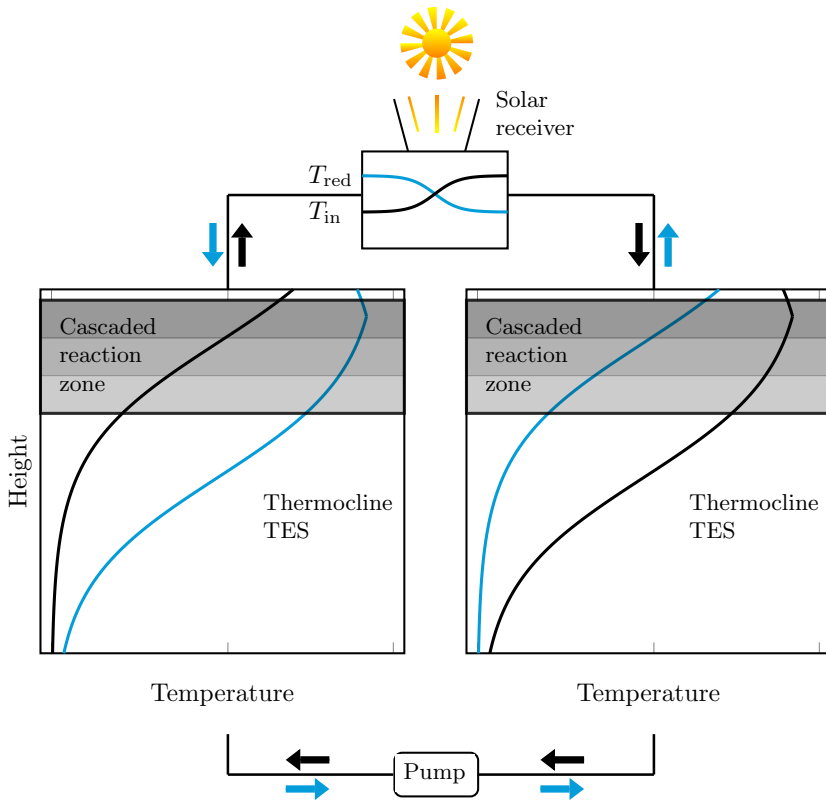
Figure 8.1: Schematic temperature profiles inside the two tanks of the cascaded dual-storage reactor. The darkest gray corresponds to the redox material with the highest reduction and oxidation temperatures and the lightest gray corresponds to the redox material with the lowest reduction and oxidation temperatures. Blue lines correspond to operation when the left tank is brought to reduction temperatures and the right tank to oxidation temperatures. Black lines correspond to the inverse operation.

dopant concentration, the more the reduction and oxidation temperatures decrease [162]. A gradual increase of the dopant concentration from the top

towards the bottom of the reaction zone would therefore be a well-suited option for cascaded redox materials. Another benefit would be that the complexity is not substantially increased, as only one dopant needs to be studied. Considering that less TCC will be necessary, this can potentially decrease the complexity of the system.

Long-term experimental studies are required to test the compatibility of the encapsulation material with the redox material at elevated temperatures, as, e.g., also alumina and ceria are known to react at high temperatures [184].

Receiver

The receiver needs to deliver very high temperatures, however it needs to upgrade the temperature of the HTF only relatively little. The receiver should be capable of handling pressurized HTFs. Such receivers are not reported in the literature and require substantial research for their realization.

Heat-transfer fulid

As an alternative to using gaseous HTFs, previous work proposed using liquid metals [47]. This relies on the development of pumps for liquid metals and the compatibility of the HTF with the containment, the storage material, and the encapsulation needs to be considered. The benefit of using liquid metals instead of gases is that the receiver design would be simpler, pumping work would be less of an issue, and the system could operate efficiently at ambient pressure. In a first step, numerical simulations could assess these benefits for the dual-storage reactor.

Inert-gas cleaning

If the dual-storage reactor is operated with direct contact between the redox material and the HTF, a large amount of inert gas gets contaminated by oxygen. Oxygen removal from inert gases can be performed with perovskite redox cycles [167]. These redox cycles could also be executed with a dual-storage reactor configuration. Furthermore, it would theoretically be possible

to incorporate the inert-gas cleaning within the cascaded dual-storage re-
actor shown in Fig. 8.1 by replacing a part of the thermocline TES with
encapsulated perovskites that are operated to clean inert gas, since the
corresponding reaction occurs typically at lower temperatures (200-500°C).
This concept would need to be simulated to assess its potential.

8.4.4   Numerical optimization

Given that the operation and design parameters are based on trial-and-error
so far, numerical optimization tools could be used to further boost the
efficiency or to decrease the cycle time.

ADAPTATIONS OF THE MODEL FOR TCC SIMULATIONS

The numerical model of the TES is based on a quasi-one-dimensional heat-transfer model [97]. A few changes were made to adapt it to the TES configurations considered in this study.

The convective heat-transfer coefficient is adapted to make it valid for molten salt as well using the correlation from [185]. A variable packed bed void fraction is implemented as described in [22].

The representation of the temperature and velocity fields near the ports is restricted by the one-dimensional model. Using a one-dimensional model assumes that the flow exiting a port is well-distributed over the entire cross-section. This assumption seems reasonable given the large flow resistance imposed by the packed bed.

Natural convection is assumed on the outer walls of the TES [146], while on the cover a constant convective heat-transfer coefficient of 5 W/m^2 is assumed, and ambient temperature is assumed below the concrete at the

bottom. The material properties of the insulation and the structure are given in [97]. The temperature-dependent properties of the rocks and air are taken from [148] and [52], respectively. The temperature-dependent molten-salt properties are adopted from [117], except for the density, which was assumed to be constant at 1803.8 kg/m^3.

A quasi-steady state is judged to have been reached when the relative changes in the utilization factor and the exergy efficiency meet predetermined convergence criteria. In this work, the criteria were $|\Delta\zeta|/\zeta < 10^{-4}$ and $|\Delta\eta_{\mathrm{ex}}|/\eta_{\mathrm{ex}} < 8 \cdot 10^{-4}$, where the utilization factor and the exergy efficiency are defined by Eqs. (4.10) and (4.13), respectively.

APPENDIX B

EXERGY BALANCE

The exergy-loss breakdown shown in Fig. 4.14 is based on the following considerations. Assuming quasi-steady state, the net thermal exergy accumulated in the TES (including rocks and HTF) during charging has to balance the net thermal exergy leaving the TES during discharging, i.e.,

$$\Xi_{c,\text{TES,net}} = \Xi_{d,\text{TES,net}} \,. \tag{B.1}$$

The net exergies can be split into contributions from the HTF streams entering and exiting the TES as well as exergetic losses,

$$\Xi_{c,\text{in}} - \Xi_{c,\text{out}} - \Xi_{c,\text{loss}} = \Xi_{d,\text{out}} - \Xi_{d,\text{in}} + \Xi_{d,\text{loss}} \tag{B.2}$$

or

$$1 - \frac{\Xi_{d,\text{out}} - \Xi_{d,\text{in}}}{\Xi_{c,\text{in}} - \Xi_{c,\text{out}}} = \frac{\Xi_{c,\text{loss}} + \Xi_{d,\text{loss}}}{\Xi_{c,\text{in}} - \Xi_{c,\text{out}}} \,. \tag{B.3}$$

Adding $\Xi_{\text{pump}}/(\Xi_{c,\text{in}} - \Xi_{c,\text{out}})$ on both sides and using Eq. 4.13 results in

$$1 - \eta_{\text{ex}} = \frac{\Xi_{c,\text{loss}} + \Xi_{d,\text{loss}}}{\Xi_{c,\text{in}} - \Xi_{c,\text{out}}} + \frac{\Xi_{\text{pump}}}{\Xi_{c,\text{in}} - \Xi_{c,\text{out}}} \,. \tag{B.4}$$

Equation (B.4) underlies the exergy-loss breakdown presented in Fig. 4.14 once the exergy losses during charging and discharging are split into contributions from internal heat transfer, thermal losses through the structure and insulation, and mixing of HTF streams. For example, during charging,

$$\Xi_{c,\mathrm{loss}} = \Xi_{c,\mathrm{int}} + \Xi_{c,\mathrm{ins}} + \Xi_{c,\mathrm{mix}} . \tag{B.5}$$

Summary of TCC Results for a Maximum Outflow Temperature Variation of 10%

Table C.1 summarizes the results in terms of the number of cycles required to reach a quasi-steady state, utilization factors, exergy efficiencies, and relative differences in the utilization factors and exergy efficiencies with respect to the values without TCC for $\Delta \widetilde{T}_{\text{out,max}} = 10\%$. Note that the exergy efficiency of all methods may further decrease if the heat and pressure losses of the piping, valves, and ports were included. The relative increase of ζ is generally higher for compressed air than for molten salt. This is due to the more pronounced thermocline degradation with the compressed air simulations and therefore TCC is more effective. It appears evident that the more thermocline degradation occurs, the less steep becomes the thermocline and therefore the more pronounced the effect of TCC.

Table C.1: Summary of results for MS and CA at quasi-steady state. N_{cycles} is the number of cycles required to reach a quasi-steady state.

HTF	Method	N_{ports} [−]	N_{cycles} [−]	η_{ex} [%]	$\frac{\Delta\eta_{\text{ex}}}{\eta_{\text{ex,NC}}}$ [%]	ζ [%]	$\frac{\Delta\zeta}{\zeta_{\text{NC}}}$ [%]
	No TCC	0	40	99.7	0.0	65.4	0.0
		1	22	99.7	−0.1	73.7	12.6
	Extracting	2	19	99.6	−0.1	77.1	17.9
		3	14	99.6	−0.1	78.9	20.5
MS		1	7	99.5	−0.3	80.8	23.5
	Injecting	2	4	99.3	−0.4	83.3	27.3
		3	4	99.2	−0.5	82.8	26.5
		1	5	98.0	−1.7	86.3	31.9
	Mixing	2	3	97.5	−2.2	89.4	36.5
		3	2	97.3	−2.4	90.8	38.8
	No TCC	0	39	97.3	0.0	49.0	0.0
		1	43	97.4	0.1	54.3	10.8
	Extracting	2	36	97.6	0.3	60.3	23.0
		3	19	97.6	0.3	64.6	31.7
CA		1	7	97.3	0.0	70.7	44.1
	Injecting	2	5	97.3	−0.1	69.8	42.2
		3	5	97.2	−0.1	71.5	45.8
		1	5	96.1	−1.3	78.0	59.0
	Mixing	2	5	95.8	−1.6	82.7	68.7
		3	2	95.6	−1.7	85.1	73.4

Analytical Solution of Cavern Model

Presented is the analytical solution for the cavern temperature at diabatic and simultaneous charge and discharge conditions with constant inlet and wall temperatures as well as constant mass flow rates. Mass conservation yields

$$\frac{\rho_{\text{cav}}(t)}{\rho_{\text{cav},0}} = 1 + \frac{(\dot{m}_c - \dot{m}_d)t}{m_0} \, ,$$

where $\rho_{\text{cav},0}$ and m_0 are the initial air density and mass inside the cavern. Energy conservation gives

$$\frac{T_{\text{cav}}(t)}{T_{\text{cav},0}} = \left(1 + \frac{(\dot{m}_c - \dot{m}_d)t}{m_0}\right)^{\alpha}$$

$$- \left[\left(1 + \frac{(\dot{m}_c - \dot{m}_d)t}{m_0}\right)^{\alpha} - 1\right] \frac{\gamma \dot{m}_c \dfrac{T_{t,c}}{T_{\text{cav},0}} + \dfrac{hA_{\text{cav}}}{c_v} \dfrac{T_w}{T_{\text{cav},0}}}{\dot{m}_c + (\gamma - 1)\dot{m}_d + \dfrac{hA_{\text{cav}}}{c_v}} \, , \quad \text{(D.1)}$$

where $T_{\text{cav},0}$ is the initial cavern temperature, $T_{t,c}$ is the total inlet temperature to the cavern during charging and α is given by

$$\alpha = -\left(\frac{\dot{m}_c}{\dot{m}_c - \dot{m}_d} + (\gamma - 1)\frac{\dot{m}_d}{\dot{m}_c - \dot{m}_d} + \frac{hA_{\text{cav}}}{(\dot{m}_c - \dot{m}_d)c_v} \right).$$

The cavern pressure $p_{\text{cav}}(t)$ follows from the equation of state of an ideal gas.

ADAPTATIONS OF THE MODEL FOR DUAL-STORAGE REACTOR SIMULATIONS

To study the effectiveness of the proposed heat-recovery concept, a numerical heat- and mass-transfer model was developed. The heat-transfer model is based on the model presented in Chapter 2. It solves the 1D energy-conservation equations for the fluid and solid phases in the packed bed and in the tube rows, as well as the 2D energy-conservation equation in the insulation. Adaptations were made to solve the heat- and mass-transfer equations of the encapsulated ceria. The ceria is considered to be inserted as a packed bed of spheres inside a cylindrical encapsulation. These cylindrical reactors are arranged in stacked, parallel-shifted tube rows. The pressure drop through the packed bed is calculated with the Ergun equation for a packed bed of spheres. The pressure drop correlation for shifted parallel tube rows in cross flow is taken from [86]. In the void sections, Darcy's law is applied to calculate the pressure drop for laminar flow. Inside the reactor tubes, a uniform pressure is assumed during operation with the vacuum

pump. The receiver is not modeled in detail. Its efficiency is based on the ideal absorption efficiency (see Eq. 6.8) and a constant outflow temperature is assumed.

E.1   Reaction zone heat-transfer model and coupling of solutions

Since the shape of the reactors is cylindrical, the 1D model from Chapter 2 was reapplied to solve the heat transfer equations of the ceria (1D axial; two-phase) and the encapsulation (2D axial and radial; one-phase). For each row of tubes, the model is solved individually. Note that the (axial) flow direction of the reactors is transversal to the main flow of the HTF around the tubes. For each time step, the coupling between the tubes and the main flow, the packed bed and the insulation is performed as follows:

- In each row, a heat source term is added to the energy equation of the outermost encapsulation layer, accounting for (1) convection between the HTF and the encapsulation, (2) conduction and radiation between tube rows and (3) conduction from the tubes to the lateral walls. Additional heat source terms are added in the energy equations of the tube row next to the packed bed of the TES as well as in the top tube row, to account for radiation to the top layer of packed bed and to the lid, respectively. All terms are described in [97]. For the calculation of (3) it is assumed that the lateral insulation is in touch with the whole cross section of each tube.

- In each row, the calculated mean temperature of the outermost encapsulation layer is used as boundary condition in the energy equations of the HTF and the insulation. The outermost encapsulation temperatures of the top and bottom rows are used as boundary condition for the calculation of the radiation to the adjacent lid and to the adjacent packed bed layer, respectively.

E.2   Chemical reaction

For the simulation of the chemical reaction inside the reactor, the oxygen-conservation equation is solved:

$$\frac{\partial c_{O_2}}{\partial t} + u \, \frac{\partial c_{O_2}}{\partial x} = S_{\text{reaction}} \tag{E.1}$$

where c_{O_2} is the oxygen concentration and u is the interstitial flow velocity. The source term S_{reaction} denotes the oxygen released/consumed by the ceria

$$S_{\text{reaction}} = \frac{\partial c_{O_2,\text{reaction}}}{\partial t} = \frac{1}{2} \frac{\partial \delta}{\partial t} \frac{\phi_{CeO_2} \rho_{CeO_2}}{M_{CeO_2}(1 - \phi_{CeO_2})} \,, \tag{E.2}$$

where δ is the reduction extent, ϕ_{CeO_2} is the volume fraction, ρ_{CeO_2} is the density and M_{CeO_2} is the molar mass of ceria. The reduction extent is modeled assuming thermodynamic equilibrium, which is a function of oxygen partial pressure p_{O_2} and temperature T_{CeO_2} as given in [186]. The oxygen partial pressure p_{O_2} is determined from the ideal gas law:

$$p_{O_2} = c_{O_2} R T_f \,, \tag{E.3}$$

where R is the universal gas constant. During reduction, thermodynamic equilibrium is assumed as previous studies showed that the overall kinetics were controlled by heat transfer [187]. During oxidation, mass conservation is considered only, leaving out a detailed kinetic model. Complete re-oxidation of the redox material is assumed while exposing it to a CO_2 stream during 20 min. This oxidation time was also used in previous work [186].

    The energy conservation equation for the redox material is given by

$$\phi_{CeO_2} \frac{\partial \rho_{CeO_2} e_{CeO_2}}{\partial t} = \frac{\partial}{\partial x} \left(k_{\text{eff}} \frac{\partial T_{CeO_2}}{\partial x} \right) + h_v(T_f - T_{CeO_2})$$

$$+ h_{v,w,\text{cond}-\text{rad}}(T_w - T_{CeO_2}) + \frac{\phi_{CeO_2} \rho_{CeO_2}}{M_{CeO_2}}(\Delta H_{\text{red}} - \Delta H_{\text{splitting}}) \,, \tag{E.4}$$

where e_{CeO_2} is the internal energy of ceria, T_w is the tube wall temperature at the inner side of the encapsulation, h_v is the volumetric convective

heat-transfer coefficient, $h_{v,w,\text{cond}-\text{rad}}$ is the volumetric wall heat transfer coefficient, k_{eff} is the effective conductivity and $\Delta H_{\text{splitting}}$ and ΔH_{red} are the CO_2 splitting enthalpy per mole of ceria and the redox reaction enthalpy per mole of ceria, respectively. The latter can be calculated as follows [162]:

$$\Delta H_{\text{red}} = \frac{\int_{\delta_1}^{\delta_2} \Delta H_O(\delta)d\delta}{\delta_2 - \delta_1}(\delta_2 - \delta_1) = \frac{\int_{\delta_1}^{\delta_2} \Delta H_{O_2}(\delta)d\delta}{2}, \qquad \text{(E.5)}$$

for a given change of the reduction extent from δ_1 to δ_2. The reaction enthalpy per mole of oxygen, $\Delta H_{O_2}(\delta)$, is calculated based on the correlation given in [186]. $\Delta H_{\text{splitting}}$ is calculated based on the higher heating value of CO and the decrease in the reduction extent during oxidation:

$$\Delta H_{\text{splitting}} = \Delta\delta \; \text{HHV}_{\text{CO}}, \qquad \text{(E.6)}$$

where $\Delta\delta = \delta_2 - \delta_1$. The heat transfer parameters h_v, $h_{v,w,\text{cond}-\text{rad}}$, and k_{eff} are calculated as described in [97], except that the convective heat-transfer coefficient h_v is based on a correlation from [60] to account for the spherical shape of the ceria particles. This correlation is also used in the alumina packed bed of the thermocline TES.

The energy-conservation equation for the fluid surrounding the redox material is given by

$$(1 - \phi_{\text{CeO}_2})\frac{\partial(\rho_f e_f)}{\partial t} + (1 - \phi_{\text{CeO}_2})\frac{\partial(u\rho_f h_f)}{\partial x} = \\ h_v(T_{\text{CeO}_2} - T_f) + h_{v,w,\text{conv}}(T_w - T_f), \qquad \text{(E.7)}$$

where ρ_f is the density, e_f is the internal energy and h_f is the enthalpy of the fluid. $h_{v,w,\text{conv}}$ is the convective wall heat-transfer coefficient per unit volume.

E.3 Thermocline control

When HTFs are mixed, extracted or injected at certain positions, the following assumptions are made:

- The mixing is performed adiabatically.

- A uniform flow distribution is assumed when the HTF is injected or extracted. This can be achieved by a careful design of the flow distributors.

E.4 Laboratory-scale simulations

The heat-transfer model was adapted for the simulation of the heating section and the ceria RPC, which is in direct contact with the HTF.

Heat released by the heater was assumed to be completely absorbed by the adjacent porous ceramic baffles. Conductive heat transfer between the porous ceramic and the alumina tube is considered where they are in touch (at the top and the bottom, see Fig. 6.4 on the right side). Radiation heat transfer is considered where the porous ceramic and the alumina tube are not in touch with each other. Parallel plate radiation heat transfer is considered between the adjacent baffles and the diffusors. The convective heat-transfer coefficient between the air and the diffusors was assumed to be $h_{\text{diffusors}} = 20$ W/m^2 and the convective heat-transfer coefficient between the air and the baffles was taken from [52] for a laminar flow with combined entry length. The specific surface area of the diffusors and the baffles are $a_{\text{diffusors}} = 71.3$ m^2/m^3 and $a_{\text{baffles}} = 109$ m^2/m^3, respectively.

The volume-averaged model of the RPC is based on correlations from [172] for the calculation of the effective conductivity, the convective heat-transfer coefficient and the extinction coefficient. Radiation inside the RPC is modeled using the Rosseland diffusion model. Parallel plate radiation heat transfer is considered at the interface to the packed bed and the diffusor plate.

Natural convection from the insulation to the surroundings is modeled using the correlation for an isothermal cuboid from [188]. The insulation geometry is assumed to be cylindrical. The increased thickness due to the cuboid shape are neglected at the outside and the minimal radial thickness is used instead, see the schematic in Fig. 6.5. The gap between the alumina

tube and the porous ceramic insulation, which was filled with alumina powder, was modeled with its effective radius (converting the rectangular outer diameter of the gap to an effective outer diameter) with properties of porous ceramic insulation, except for its thermal conductivity: Since the high thermal resistance due to the structure of the porous ceramic insulation is no longer given for powder, the conductivity of alumina was assumed within this gap. The losses from each end of the packed bed towards the surrounding are based on conduction through a porous ceramic disc of 1 cm thickness.

E.5 Material properties

Solid material properties are listed in Table E.1, referring to the following fitted equations:

$$k_{\text{micro}}(T) = 2.151 \cdot 10^{-3} + 9.219 \cdot 10^{-5}T - 1.421 \cdot 10^{-7}T^2 + 8.333 \cdot 10^{-11}T^3 \tag{E.8}$$

$$k_{\text{porous ceramic}}(T) = \begin{cases} 0.14, & \text{if } T < 1073.15 \\ -0.1137 + 2.81 \cdot 10^{-4} \cdot T - \\ 4.17 \cdot 10^{-8} \cdot T^2, & \text{if } T > 1073.15 \end{cases} \tag{E.9}$$

$$k_{\text{felt}}(T) = \begin{cases} 0.18, & \text{if } T < 1073.15 \\ 0.4875 - 8.23 \cdot 10^{-4} \cdot T + 5.0 \cdot 10^{-7} \cdot T^2, & \text{if } T > 1073.15 \end{cases} \tag{E.10}$$

Solid material properties are given in Table E.1. Since the ceramic insulation consists mainly of alumina, its specific heat capacity is assumed to be equal to the one of pure alumina. The microporous insulation is from BIFIRE® and the rigid porous ceramic insulation (UltraBoard 1750/400P) is from Schupp®. The latter material was also used to make the baffles and diffusors.

Table E.1: Material properties used in the dual-storage reactor simulations. Ranges indicate temperature-dependent properties, T in K. "n/a" is inserted where the value is not required for the simulations.

Material	c_p [J/kgK]	ρ [kg/m^3]	k [W/mK]	ϵ [$-$]	Source
Alumina	$c_{p,\mathrm{alumina}}(T)$	3990	$k_{\mathrm{alumina}}(T)$	0.45	[189, 190]
Ceria	$c_{p,\mathrm{ceria}}(T)$	7220	$k_{\mathrm{ceria}}(T)$	0.7	[186]
Microporous insulation	1050	270	Eq. E.8	n/a	[150]
Porous ceramic insulation	$c_{p,\mathrm{alumina}}(T)$	400	Eq. E.9	0.28	[189, 191] [186]
Ceramic felt	$c_{p,\mathrm{alumina}}(T)$	130	Eq. E.10	n/a	[189, 192]

Properties of the HTFs are taken from [193, 194] for air, from [195] for CO_2, and from [196] for helium.

LIST OF FIGURES

LIST OF TABLES

Bibliography

[1] IPCC, 2007: Summary for policymakers. In *Climate Change 2007: The Physical Science Basis. Contribution of Working Group I to the Fourth Assessment Report of the Intergovernmental Panel on Climate Change.* Cambridge University Press, Cambridge, United Kingdom and New York, NY, USA, 2007.

[2] D. Etheridge, L. Steele, R. Langenfelds, R. Francey, J. Barnola, and V. Morgan. Natural and anthropogenic changes in atmospheric CO_2 over the last 1000 years from air in antarctic ice and firn. *J. Geophys. Res. - Atmos.*, 101(D2):4115–4128, 1996.

[3] International Energy Agency. *Key world energy statistics.* Paris, 2016.

[4] BP. Statistical review of world energy. 2016.

[5] V. Quaschning. *Understanding renewable energy systems.* Routledge, 2016.

[6] R. Sioshansi and P. Denholm. The value of concentrating solar power and thermal energy storage. *IEEE Transactions on Sustainable Energy*, 1(3):173–183, 2010.

[7] P. Denholm, M. Hand, T. Mai, R. Margolis, G. Brinkman, E. Drury, M. Mowers, and C. Turchi. The potential role of concentrating solar power in enabling high renewables scenarios in the united states.

Technical report, National Renewable Energy Laboratory, Golden, Colorado, 2012.

[8] A. Gil, M. Medrano, I. Martorell, A. Lázaro, P. Dolado, B. Zalba, and L. Cabeza. State of the art on high temperature thermal energy storage for power generation. Part 1—Concepts, materials and modellization. *Renew. Sust. Energy Rev.*, 14(1):31–55, 2010.

[9] S. Kuravi, J. Trahan, Y. Goswami, M. Rahman, and E. Stefanakos. Thermal energy storage technologies and systems for concentrating solar power plants. *Prog. Energy Combust. Sci.*, 39(4):285–319, 2013.

[10] M. Liu, W. Saman, and F. Bruno. Review on storage materials and thermal performance enhancement techniques for high temperature phase change thermal storage systems. *Renew. Sust. Energy Rev.*, 16:2118–2132, 2012.

[11] R. Bradshaw and D. Meeker. High-temperature stability of ternary nitrate molten salts for solar thermal energy systems. *Sol. Energy Mater.*, 21(1):51–60, 1990.

[12] P. Poživil and A. Steinfeld. Integration of a pressurized-air solar receiver array to a gas turbine power cycle for solar tower applications. *J. Sol. Energy Eng.*, 139(4):041007, 2017.

[13] U.S. Department of Energy's Sunshot Iniative: Thermal storage research and development for CSP systems. http://energy.gov/eere/sunshot/thermal-storage-rd-csp-systems, November 5, 2015.

[14] A. Jalalzadeh-Azar, W. Glenn Steele, and G. Adebiyi. Performance comparison of high-temperature packed bed operation with pcm and sensible-heat pellets. *Int. J. Energy Res.*, 21(11):1039–1052, 1997.

[15] A. Glück, R. Tamme, H. Kalfa, and C. Streuber. Investigation of high temperature storage materials in a technical scale test facility. *Sol. Energy Mater.*, 24(1):240–248, 1991.

[16] P. Good, G. Zanganeh, G. Ambrosetti, M. Barbato, A. Pedretti, and A. Steinfeld. Towards a commercial parabolic trough CSP system using air as heat transfer fluid. *Energy Procedia*, 49:381–385, 2014.

[17] D. Laing and S. Zunft. Using concrete and other solid storage media in thermal energy storage (TES) systems. *Advances in Thermal Energy Storage Systems: Methods and Applications*, page 65, 2014.

[18] J. Pacheco, S. Showalter, and W. Kolb. Development of a molten-salt thermocline thermal storage system for parabolic trough plants. *J. Sol. Energy Eng.*, 124:153–159, 2002.

[19] S. Saeed Mostafavi Tehrani, R. Taylor, K. Nithyanandam, and A. Shafiei Ghazani. Annual comparative performance and cost analysis of high temperature, sensible thermal energy storage systems integrated with a concentrated solar power plant. *Sol. Energy*, 153:153–172, 2017.

[20] S. Flueckiger, Z. Yang, and S. Garimella. An integrated thermal and mechanical investigation of molten-salt thermocline energy storage. *Appl. Energy*, 88(6):2098–2105, 2011.

[21] K. Wang, R. West, F. Kreith, and P. Lynn. High-temperature sensible-heat storage options. *Energy*, 10(10):1165–1175, 1985.

[22] G. Zanganeh, A. Pedretti, S. Zavattoni, M. Barbato, and A. Steinfeld. Packed-bed thermal storage for concentrated solar power – Pilot-scale demonstration and industrial-scale design. *Sol. Energy*, 86(10):3084 – 3098, 2012.

[23] J. Stekli, L. Irwin, and R. Pitchumani. Technical challenges and opportunities for concentrating solar power with thermal energy storage. *J. Thermal Sci. Eng. Appl.*, 5(2):021011, 2013.

[24] E. Hahne, U. Taut, and U. Gross. Salt ceramic thermal energy storage for solar thermal central receiver plants. *Solar World Congress*, 2:1937–1941, 1991.

[25] G. Zanganeh, M. Commerford, A. Haselbacher, A. Pedretti, and A. Steinfeld. Stabilization of the outflow temperature of a packed-bed thermal energy storage by combining rocks with phase change materials. *Appl. Therm. Eng.*, 70(1):316 – 320, 2014.

[26] P. Galione, C. Pérez-Segarra, I. Rodríguez, A. Oliva, and J. Rigola. Multi-layered solid-PCM thermocline thermal storage concept for CSP plants. Numerical analysis and perspectives. *Appl. Energy*, 142:337–351, 2015.

[27] M. Farid. Solar energy storage with phase change. *J. Sol. Energy Res.*, 4(11), 1986.

[28] M. Farid and A. Kanzawa. Thermal performance of a heat storage module using pcm's with different melting temperatures: mathematical modeling. *J. Sol. Energy Eng.*, 111(2):152–157, 1989.

[29] G. Adebiyi, B. Hodge, W. Steele, A. Jalalzadeh-Azar, and E. Nsofor. Computer simulation of a high-temperature thermal energy storage system employing multiple families of phase-change storage materials. *J. Energy Resour. Technol.*, 118:102–111, 1996.

[30] K. Nithyanandam, R. Pitchumani, and A. Mathur. Analysis of a latent thermocline energy storage system for concentrating solar power plants. In *ASME 2012 6th International Conference on Energy Sustainability collocated with the ASME 2012 10th International Conference on Fuel Cell Science, Engineering and Technology*, pages 519–528. American Society of Mechanical Engineers, 2012.

[31] C. Agrafiotis, M. Roeb, and C. Sattler. Exploitation of thermochemical cycles based on solid oxide redox systems for thermochemical storage of solar heat. Part 4: Screening of oxides for use in cascaded thermochemical storage concepts. *Sol. Energy*, 139:695–710, 2016.

[32] M. Walmsley, M. Atkins, and J. Riley. Thermocline management of stratified tanks for heat storage. *Proceedings of 12th International*

Conference on Process Integration, Modelling and Optimisation for Energy Saving and Pollution Reduction, 2009.

[33] H. Bindra and P. Bueno. Optimum process design of packed bed type thermal storage systems and other applications, 2016. US Patent App. 14/234,286.

[34] A. Mathur and R. Kasetty. Thermal energy storage system comprising optimal thermocline management, October 2013. US Patent 8,554,377.

[35] C. Bullough, C. Gatzen, C. Jakiel, M. Koller, A. Nowi, and S. Zunft. Advanced adiabatic compressed air energy storage for the integration of wind energy. In *Proceedings of the European Wind Energy Conference, EWEC*, 2004.

[36] S. Zunft, C. Jakiel, M. Koller, and C. Bullough. Adiabatic compressed air energy storage for the grid integration of wind power. In *Sixth international workshop on large-scale integration of wind power and transmission networks for offshore windfarms*, pages 26–28, 2006.

[37] H. Chen, T. Cong, W. Yang, C. Tan, Y. Li, and Y. Ding. Progress in electrical energy storage system: a critical review. *Prog. Natural Sci.*, 19(3):291–312, 2009.

[38] E. Barbour, D. Mignard, Y. Ding, and Y. Li. Adiabatic compressed air energy storage with packed bed thermal energy storage. *Appl. Energy*, 155:804–815, 2015.

[39] M. Budt, D. Wolf, R. Span, and J. Yan. A review on compressed air energy storage: Basic principles, past milestones and recent developments. *Appl. Energy*, 170:250–268, 2016.

[40] A. Sciacovelli, Y. Li, H. Chen, Y. Wu, J. Wang, S. Garvey, and Y. Ding. Dynamic simulation of adiabatic compressed air energy storage (A-CAES) plant with integrated thermal storage–Link between

components performance and plant performance. *Appl. Energy*, 185:16–28, 2017.

[41] W. Chueh, C. Falter, M. Abbott, D. Scipio, P. Furler, S. Haile, and A. Steinfeld. High-flux solar-driven thermochemical dissociation of CO_2 and H_2O using nonstoichiometric ceria. *Science*, 330(6012):1797–1801, 2010.

[42] J. Scheffe and A. Steinfeld. Thermodynamic analysis of cerium-based oxides for solar thermochemical fuel production. *Energy Fuels*, 26(3):1928–1936, 2012.

[43] R. Diver, J. Miller, N. Siegel, and T. Moss. Testing of a CR5 solar thermochemical heat engine prototype. In *ASME 2010 4th International Conference on Energy Sustainability*, pages 97–104. American Society of Mechanical Engineers, 2010.

[44] J. Lapp, J. Davidson, and W. Lipiński. Heat transfer analysis of a solid-solid heat recuperation system for solar-driven nonstoichiometric redox cycles. *J. Sol. Energy Eng.*, 135(3):031004, 2013.

[45] I. Ermanoski, N. Siegel, and E. Stechel. A new reactor concept for efficient solar-thermochemical fuel production. *J. Sol. Energy Eng.*, 135(3):031002, 2013.

[46] J. Felinks, S. Brendelberger, M. Roeb, C. Sattler, and R. Pitz-Paal. Heat recovery concept for thermochemical processes using a solid heat transfer medium. *Appl. Therm. Eng.*, 73(1):1006–1013, 2014.

[47] C. Yuan, C. Jarrett, W. Chueh, Y. Kawajiri, and A. Henry. A new solar fuels reactor concept based on a liquid metal heat transfer fluid: Reactor design and efficiency estimation. *Sol. Energy*, 122:547–561, 2015.

[48] K. Ismail and R. Stuginsky. A parametric study on possible fixed bed models for PCM and sensible heat storage. *Appl. Therm. Eng.*, 19(7):757–788, 1999.

[49] T. Schumann. Heat transfer: a liquid flowing through a porous prism. *J. Franklin Inst.*, 208(3):405–416, 1929.

[50] A. Anzelius. Über Erwärmung vermittels durchströmender Medien. *Z. Angew. Math. Mech.*, 6(4):291–294, 1926.

[51] G. Zanganeh, R. Khanna, C. Walser, A. Pedretti, A. Haselbacher, and A. Steinfeld. Experimental and numerical investigation of combined sensible-latent heat for thermal energy storage at 575 °C and above. *Sol. Energy*, 114:77 – 90, 2015.

[52] F. Incropera, D. Dewitt, T. Bergman, and A. Lavince. *Fundamentals of Heat and Mass Transfer*. John Wiley & Sons, Hoboken, NJ, 6th edition, 2007.

[53] A. Gupta and G. Thodos. Direct analogy between mass and heat transfer to beds of spheres. *AIChE J.*, 9(6):751–754, 1963.

[54] J. Beek. Design of packed catalytic reactors. *Adv. Chem. Eng.*, 3:203 – 271, 1962.

[55] K. Ofuchi and D. Kunii. Heat-transfer characteristics of packed beds with stagnant fluids. *Int. J. Heat Mass Transfer*, 8(5):749 – 757, 1965.

[56] D. Kunii and J. Smith. Heat transfer characteristics of porous rocks. *AIChE J.*, 6(1):71–78, 1960.

[57] S. Ergun. Fluid flow through packed columns. *Chem. Eng. Prog*, 48, 1952.

[58] I. Macdonald, M. El-Sayed, K. Mow, and F. Dullien. Flow through porous media-the ergun equation revisited. *Ind. Eng. Chem. Fund.*, 18(3):199–208, 1979.

[59] D. Beasley, C. Ramanarayanan, and H. Torab. Thermal response of a packed bed of spheres containing a phase-change material. *Int. J. Energy Res.*, 13(3):253–265, 1989.

[60] T. Galloway and B. Sage. A model of the mechanism of transport in packed, distended, and fluidized beds. *Chem. Eng. Sci.*, 25(3):495–516, 1970.

[61] A. Žukauskas. Heat transfer from tubes in crossflow. volume 8 of *Advances in Heat Transfer*, pages 93 – 160. Elsevier, 1972.

[62] R. Ratzesberger. *Regeneratoren in Parabolrinnen-Solarkraftwerken.* VDI-Verlag, 1995.

[63] V. Voller. Fast implicit finite-difference method for the analysis of phase change problems. *Numer. Heat Transfer B*, 17(2):155–169, 1990.

[64] H. Klein and G. Eigenberger. Approximate solutions for metallic regenerative heat exchangers. *Int. J. Heat Mass Transfer*, 44(18):3553 – 3563, 2001.

[65] S. Madaeni, R. Sioshansi, and P. Denholm. How thermal energy storage enhances the economic viability of concentrating solar power. *Proc. IEEE*, 100(2):335–347, 2011.

[66] M. Hänchen, S. Brückner, and A. Steinfeld. High-temperature thermal storage using a packed bed of rocks – heat transfer analysis and experimental validation. *Appl. Therm. Eng.*, 31(10):1798 – 1806, 2011.

[67] G. Zanganeh, A. Pedretti, A. Haselbacher, and A. Steinfeld. Design of packed bed thermal energy storage systems for high-temperature industrial process heat. *Appl. Energy*, 137:812 – 822, 2015.

[68] G. Adebiyi. A second-law study on packed bed energy storage systems utilizing phase-change materials. *J. Sol. Energy Eng.*, 113(3):146–156, 1991.

[69] A. Jalalzadeh-Azar, W. Steele, and G. Adebiyi. Performance comparisons of high-temperature packed bed operation with PCM and sensible-heat pellets. *Int. J. Energy Res.*, 21(11):1039–1052, 1997.

[70] S. Flueckiger and S. Garimella. Latent heat augmentation of thermocline energy storage for concentrating solar power – a system-level assessment. *Appl. Energy*, 116:278–287, 2013.

[71] H. Michels and R. Pitz-Paal. Cascaded latent heat storage for parabolic trough solar power plants. *Sol. Energy*, 81(6):829–837, 2007.

[72] K. Nithyanandam and R. Pitchumani. Optimization of an encapsulated phase change material thermal energy storage system. *Sol. Energy*, 107:770–788, 2014.

[73] G. Pasche, M. Scheel, R. Schäublin, C. Hébert, M. Rappaz, and A. Hessler-Wyser. Time-resolved X-ray microtomography observation of intermetallic formation between solid Fe and liquid Al. *Metall. Mater. Trans. A*, 44:4119–4123, 2013.

[74] M. Kenisarin. High-temperature phase change materials for thermal energy storage. *Renew. Sust. Energy Rev.*, 14(3):955–970, 2010.

[75] B. Cárdenas and N. León. High temperature latent heat thermal energy storage: Phase change materials, design considerations and performance enhancement techniques. *Renew. Sust. Energy Rev.*, 27:724–737, 2013.

[76] R. Ratzesberger, B. Beine, and E. Hahne. Regeneratoren mit Beton und Phasenwechselmaterial als Speichermasse. *VDI Berichte*, 1168:467–481, 1994.

[77] Properties of microtherm®. www.microtherm.be, June 15, 2015.

[78] Properties of felt. www.promat-ap.com, June 15, 2015.

[79] Properties of rockwool. www.isolmec.com, June 15, 2015.

[80] Heat capacity of rockwool. www.siper-bg.com, June 15, 2015.

[81] G. Zanganeh. *High-temperature thermal energy storage for concentrated solar power with air as heat transfer fluid*. PhD thesis, ETH Zurich, 2014.

[82] D. Meyer. *Foamed cement based materials, manufacture, material structure, properties relations*. PhD thesis, ETH Zurich, 2009.

[83] W. Pitts, E. Braun, R. Peacock, H. Mitler, E. Johnsson, P. Reneke, and L. Blevins. Temperature uncertainties for bare-bead and aspirated thermocouple measurements in fire environments. *ASTM Spec. Tech. Publ.*, 1427:3–15, 2003.

[84] M. Q. Brewster. *Thermal radiative transfer and properties*. John Wiley & Sons, 1992.

[85] D. Collis and M. Williams. Two-dimensional convection from heated wires at low Reynolds numbers. *J. Fluid Mech.*, 6(3):357–384, 1959.

[86] VDI-Gesellschaft. *VDI-Wärmeatlas*. Springer, 10th edition, 2006.

[87] G. Zanganeh, G. Ambrosetti, A. Pedretti, S. Zavattoni, M. Barbato, P. Good, A. Haselbacher, and A. Steinfeld. A 3 MWth parabolic trough CSP plant operating with air at up to 650 °C. *Proceedings of the 2nd International Renewable and Sustainable Energy Conference*, 2014.

[88] W. Steinmann. Thermal energy storage systems for concentrating solar power (CSP) plants. In K. Lovegrove and W. Stein, editors, *Concentrating solar power technology*, pages 362–394. Woodhead Publishing, 2012.

[89] I. Dincer and M. Rosen. *Thermal Energy Storage: Systems and Applications*. John Wiley & Sons, 2nd edition, 2010.

[90] J. Kotzé, T. von Backström, and P. Erens. High temperature thermal energy storage utilizing metallic phase change materials and metallic heat transfer fluids. *J. Sol. Energy Eng.*, 135(3):035001, 2013.

[91] Costs of AISI 316L. www.fastop.it, 12/15/2014.

[92] L. Geissbühler, M. Kolman, G. Zanganeh, A. Haselbacher, and A. Steinfeld. Analysis of industrial-scale high-temperature combined sensible/latent thermal energy storage. *ASME-ATI-UIT Conference on Thermal Energy Systems: Production, Storage, Utilization and the Environment*, 2015.

[93] M. Biencinto, R. Bayón, E. Rojas, and L. González. Simulation and assessment of operation strategies for solar thermal power plants with a thermocline storage tank. *Sol. Energy*, 103:456–472, 2014.

[94] C. Libby. Solar thermocline storage system–preliminary design study. *Electric Power Research Institute*, Palo Alto, CA, 2010.

[95] M. Geyer, W. Bitterlich, and K. Werner. The dual medium storage tank at the IEA/SSPS project in Almeria (Spain); Part I: experimental validation of the thermodynamic design model. *J. Sol. Energy Eng.*, 109(3):192–198, 1987.

[96] F. Dinter, M. Geyer, and R. Tamme. *Thermal energy storage for commercial applications.* Springer-Verlag, Berlin, 1991.

[97] L. Geissbühler, M. Kolman, G. Zanganeh, A. Haselbacher, and A. Steinfeld. Analysis of industrial-scale high-temperature combined sensible/latent thermal energy storage. *Appl. Therm. Eng.*, 101:657–668, 2016.

[98] A. Mathur, R. Kasetty, J. Oxley, J. Mendez, and K. Nithyanandam. Using encapsulated phase change salts for concentrated solar power plant. *Energy Procedia*, 49:908–915, 2014.

[99] R. Copeland. Method and apparatus for operating an improved thermocline storage unit, 1985. US Patent 4,523,629.

[100] A. Slocum, J. Buongiorno, C. Forsberg, D. Codd, and A. Paxson. Concentrated solar power system, 2011. WO Patent App. PCT/US2010/049,474.

[101] J. Lataperez and J. Lorenzo. Dual thermal energy storage tank. US Patent App. 13/001,759, 2011.

[102] P. Querol, J. Olano, A. Pereña, T. Velasco, J. Arevalo, and J. Lata. Single tank thermal storage prototype. In *Proceedings of the 12th SolarPACES International Conference*, 2012.

[103] D. Codd. Experimental investigation of divider plate assisted thermocline storage. In *ASME 2015 9th International Conference on Energy Sustainability*, pages V001T05A002–V001T05A002. American Society of Mechanical Engineers, 2015.

[104] D. Crandall and E. Thacher. Segmented thermal storage. *Sol. energy*, 77(4):435–440, 2004.

[105] J. Howes, J. Macnaghten, and R. Hunt. Improved heat storage apparatus, 2012. WO Patent App. PCT/GB2011/051,595.

[106] H. Bindra, P. Bueno, and J. Morris. Sliding flow method for exergetically efficient packed bed thermal storage. *Appl. Therm. Eng.*, 64(1):201–208, 2014.

[107] A. White, J. McTigue, and C. Markides. Analysis and optimisation of packed-bed thermal reservoirs for electricity storage applications. *Proceedings of the Institution of Mechanical Engineers, Part A: Journal of Power and Energy*, 230(7):739–754, 2016.

[108] S. Ströhle, A. Haselbacher, Z. Jovanovic, and A. Steinfeld. Upgrading sensible-heat storage with a thermochemical storage section operated at variable pressure: An effective way toward active control of the heat-transfer fluid outflow temperature. *Appl. Energy*, 196:51–61, 2017.

[109] J. Howes, J. MacNaghten, and R. Hunt. Layered thermal store with selectively alterable gas flow path, 2017. US Patent 9,658,004.

[110] H. Benoit, L. Spreafico, D. Gauthier, and G. Flamant. Review of heat transfer fluids in tube-receivers used in concentrating solar thermal systems: Properties and heat transfer coefficients. *Renew. Sust. Energy Rev.*, 55:298–315, 2016.

[111] Solar Millennium. The parabolic trough power plants Andasol 1 to 3. *Tech. Solar Millennium AG*, 2008.

[112] A. Fernandez, M. Lasanta, and F. Perez. Molten salt corrosion of stainless steels and low-Cr steel in CSP plants. *Oxid. Met.*, 78(5-6):329–348, 2012.

[113] J. Schulte-Fischedick, R. Tamme, and U. Herrmann. CFD analysis of the cool down behaviour of molten salt thermal storage systems. In *ASME 2008 2nd International Conference on Energy Sustainability collocated with the Heat Transfer, Fluids Engineering, and 3rd Energy Nanotechnology Conferences*, pages 515–524. American Society of Mechanical Engineers, 2008.

[114] C. Turchi, P. Kurup, S. Akar, and F. Flores. Domestic material content in molten-salt concentrating solar power plants. Technical report, National Renewable Energy Laboratory, Golden, Colorado, 2015.

[115] F. W. Schmidt and A. J. Willmott. *Thermal energy storage and regeneration*. Hemisphere Publishing Corporation, Washington, 1981.

[116] A. El-Halwagi and M. El-Rifai. Simulation of variable flow fluidized bed heat regenerators. *Chem. Eng. Commun.*, 91(1):235–240, 1990.

[117] S. Flueckiger, B. Iverson, S. Garimella, and J. Pacheco. System-level simulation of a solar power tower plant with thermocline thermal energy storage. *Appl. Energy*, 113:86–96, 2014.

[118] A. Avila-Marin, J. Fernandez-Reche, and F. Tellez. Evaluation of the potential of central receiver solar power plants: configuration, optimization and trends. *Appl. Energy*, 112:274–288, 2013.

[119] A. Ohmura, H. Gilgen, H. Hegner, G. Müller, M. Wild, E. Dutton, B. Forgan, C. Fröhlich, R. Philipona, A. Heimo, G. König-Langlo, B. McArthur, R. Pinker, C. Whitlock, and K. Dehne. Baseline surface radiation network (BSRN/WCRP): New precision radiometry for climate research. *Bull. Am. Meteorol. Soc.*, 79(10):2115–2136, 1998.

[120] X. Luo, J. Wang, M. Dooner, and J. Clarke. Overview of current development in electrical energy storage technologies and the application potential in power system operation. *Appl. Energy*, 137:511–536, 2015.

[121] G. Venkataramani, P. Parankusam, V. Ramalingam, and J. Wang. A review on compressed air energy storage–a pathway for smart grid and polygeneration. *Renew. Sust. Energy Rev.*, 62:895–907, 2016.

[122] F. Crotogino and P. Quast. Compressed-air storage caverns at Huntorf. In M. Bergman, editor, *Subsurface Space*, volume 2, pages 593–600, Oxford, 1980. Pergamon Press.

[123] F. Crotogino, K.-U. Mohmeyer, and R. Scharf. Huntorf CAES: More than 20 years of successful operation. In *Proceedings of Solution Mining Research Institute Spring Meeting*, pages 351–362, 2001.

[124] M. Nakhamkin, L. Anderson, E. Swensen, J. Howard, R. Meyer, R. Schainker, R. Pollak, and B. Mehta. AEC 110 MW CAES plant: Status of project. *Journal of Engineering for Gas Turbines and Power*, 114:695–700, 1992.

[125] J. Daly, R. Loughlin, M. DeCorso, D. Moen, and L. Davis. CAES–reduced to Practice. ASME GT2001-397, 2001.

[126] R. Allen, T. Doherty, and A. Fossum. Geotechnical issues and guidelines for storage of compressed air in excavated hard rock caverns.

Technical Report PNL-4180, Pacific Northwest Laboratory, Richland, WA, 1982.

[127] R. Allen, T. Douherty, R. Erikson, and L. Wiles. Factors affecting storage of compressed air in porous rock reservoirs. Technical Report PNL-4707, Pacific Northwest Laboratory, Richland, WA, 1983.

[128] S. Bauer, K. Gaither, S. Webb, and C. Nelson. Compressed air energy storage in hard rock feasibility study. Technical Report SAND2012-0540, Sandia National Laboratories, Albuquerque, NM, 2012.

[129] S. Zunft, M. Krüger, V. Dreißigacker, P.-M. Mayer, C. Niklasch, and C. Bertsch. Adiabate Druckluftspeicher für die Elektrizitäts-versorgung — der ADELE-Wärmespeicher. In M. Beckmann and A. Hurtado, editors, *Kraftwerkstechnik - Sichere und nachhaltige Energieversorgung*, volume 4, pages 749–757, Neuruppin, Germany, 2012. TK-Verlag.

[130] P. Bérest and B. Brouard. Safety of salt caverns used for underground storage. *Oil & Gas Science and Technology*, 58(3):361–384, 2003.

[131] J. Chen, S. Ren, C. Yang, D. Jiang, and L. Li. Self-healing characteristics of damaged rock salt under different healing conditions. *Materials*, 6(8):3438–3450, 2013.

[132] D. Goodall, B. Åberg, and T. Brekke. Fundamentals of gas containment in unlined rock caverns. *Rock Mech. Rock Eng.*, 21:235–258, 1988.

[133] K. Kovári. Basic consideration on storage of compressed natural gas in rock chambers. *Rock Mech. Rock Eng.*, 26(1):1–27, 1993.

[134] M. Lu. Rock engineering problems related to underground hydrocarbon storage. *Journal of Rock Mechanics and Geotechnical Engineering*, 2(4):289–297, 2010.

[135] J. Rutqvist, H.-M. Kim, D.-W. Ryu, J.-H. Synn, and W.-K. Song. Modeling of coupled thermodynamic and geomechanical performance

of underground compressed air energy storage in lined rock caverns. *Int. J. Rock Mech. Min. Sci.*, 52:71–81, 2012.

[136] T. Ishihata. Underground compressed air storage facility for CAES-G/T power plant utilizing an airtight lining. *News Journal, International Society for Rock Mechanics*, 5(1):17–21, 1997.

[137] M. Nakata, H. Yamachi, A. Nakayama, S. Sakurai, and T. Shidahara. Thermo-dynamical approach to compressed air energy storage system. *Doboku Gakkai Ronbunshu*, 1998(610):31–42, 1998.

[138] T. Shidahara, T. Oyama, K. Nakagawa, K. Kaneko, and A. Nozaki. Geotechnical evaluation of a conglomerate for compressed air energy storage: the influence of the sedimentary cycle and filling minerals in the rock matrix. *Engineering Geology*, 56:125–135, 2000.

[139] H. Kim, D. Park, D. Ryu, and W. Song. Parametric sensitivity analysis of ground uplift above pressurized underground rock caverns. *Engineering Geology*, 135-136:60–65, 2012.

[140] P. Perazelli, G. Anagnostou, and J. Amberg. Uplift analysis for CAES tunnels. In F. Oka, A. Murakami, R. Uzuoka, and S. Kimoto, editors, *Computer Methods and Recent Advances in Geomechanics*, pages 1691–1696. CRC Press, Leiden, Netherlands, 2015.

[141] P. Perazzelli and G. Anagnostou. Design issues for compressed air energy storage in sealed underground cavities. *Journal of Rock Mechanics and Geotechnical Engineering*, 8:314–328, 2016.

[142] C. Carranza-Torres, D. Fosnacht, and G. Hudak. Geomechanical analysis of the stability conditions of shallow cavities for compressed air energy storage (CAES) applications. *Geomechanics and Geophysics for Geo-Energy and Geo-Resources*, 3:131–174, 2017.

[143] S. Wang, X. Zhang, L. Yang, Y. Zhou, and J. Wang. Experimental study of compressed air energy storage system with thermal energy storage. *Energy*, 103:182–191, 2016.

[144] A. Pedretti, D. Vietti, M. Bazzi Pedrazzini, and M. Neuenschwander. Reuse of abandoned underground structures – the compressed air energy storage test plant in Switzerland. In G. Anagnostou and H. Ehrbar, editors, *Underground - the way to the future!*, pages 35–42, London, 2013. Taylor & Francis.

[145] V. Becattini, L. Geissbühler, G. Zanganeh, A. Haselbacher, and A. Steinfeld. Pilot-scale demonstration of advanced adiabatic compressed air energy storage, Part 2: Tests with combined sensible/latent thermal-energy storage. *In preparation*, 2017.

[146] T. Fujii and H. Imura. Natural-convection heat transfer from a plate with arbitrary inclination. *Int. J. Heat Mass Transfer*, 15(4):755–767, 1972.

[147] E. Alanís, L. Saravia, and L. Rovetta. Measurement of rock pile heat transfer coefficients. *Sol. Energy*, 19(5):571–572, 1977.

[148] V. Becattini, T. Motmans, A. Zappone, C. Madonna, A. Haselbacher, and A. Steinfeld. Experimental investigation of the thermal and mechanical stability of rocks for high-temperature thermal-energy storage. *Appl. Energy*, 203:373–389, 2017.

[149] G. Zanganeh. Reinforced concrete properties: Average between C25/C30, Personal communication. April 28, 2016.

[150] Properties of microporous insulation. www.bifire.it, April 18, 2017.

[151] P. Zaugg. Centrales a accumulation pneumatiques. *11th international congress in combustion engines*, 1975.

[152] R. Kushnir, A. Dayan, and A. Ullmann. Temperature and pressure variations within compressed air energy storage caverns. *Int. J. Heat Mass Transfer*, 55(21):5616–5630, 2012.

[153] C. Xia, Y. Zhou, S. Zhou, P. Zhang, and F. Wang. A simplified and unified analytical solution for temperature and pressure variations in

compressed air energy storage caverns. *Renew. Energy*, 74:718–726, 2015.

[154] I. Glendenning. Long-term prospects for compressed air storage. *Appl. Energy*, 2:39–56, 1976.

[155] A. Steinfeld and R. Palumbo. Solar thermochemical process technology. *Encyclopedia of physical science and technology*, 15(1):237–56, 2001.

[156] J. Scheffe and A. Steinfeld. Oxygen exchange materials for solar thermochemical splitting of H_2O and CO_2: a review. *Materials Today*, 17(7):341–348, 2014.

[157] W. Chueh and S. Haile. A thermochemical study of ceria: exploiting an old material for new modes of energy conversion and CO_2 mitigation. *Philos. T. Roy. Soc. A*, 368(1923):3269–3294, 2010.

[158] C. Graves, S. Ebbesen, M. Mogensen, and K. Lackner. Sustainable hydrocarbon fuels by recycling CO_2 and H_2O with renewable or nuclear energy. *Renew. Sust. Energy Rev.*, 15(1):1–23, 2011.

[159] J. Lapp, J. Davidson, and W. Lipiński. Efficiency of two-step solar thermochemical non-stoichiometric redox cycles with heat recovery. *Energy*, 37(1):591–600, 2012.

[160] R. Bader, L. Venstrom, J. Davidson, and W. Lipiński. Thermodynamic analysis of isothermal redox cycling of ceria for solar fuel production. *Energy Fuels*, 27(9):5533–5544, 2013.

[161] I. Ermanoski, J. Miller, and M. Allendorf. Efficiency maximization in solar-thermochemical fuel production: challenging the concept of isothermal water splitting. *Phys. Chem. Chem. Phys.*, 16(18):8418–8427, 2014.

[162] M. Takacs, J. Scheffe, and A. Steinfeld. Oxygen nonstoichiometry and thermodynamic characterization of Zr doped ceria in the 1573–1773 K temperature range. *Phys. Chem. Chem. Phys.*, 17:7813–7822, 2015.

[163] D. Marxer, P. Furler, M. Takacs, and A. Steinfeld. Solar thermochemical splitting of CO_2 into separate streams of CO and O_2 with high selectivity, stability, conversion, and efficiency. *Energy Environ. Sci.*, 2017.

[164] D. Marxer, P. Furler, J. Scheffe, H. Geerlings, C. Falter, V. Batteiger, A. Sizmann, and A. Steinfeld. Demonstration of the entire production chain to renewable kerosene via solar thermochemical splitting of H_2O and CO_2. *Energy Fuels*, 29(5):3241–3250, 2015.

[165] A. Steinfeld, P. Furler, A. Haselbacher, and L. Geissbühler. A thermochemical reactor system for a temperature swing cyclic process with integrated heat recovery and a method for operating the same, 2016. Pat. Appl. Nr. EP16194074.

[166] A. Meier, C. Winkler, and D. Wuillemin. Experiment for modelling high temperature rock bed storage. *Sol. Energy Mater.*, 24(1):255–264, 1991.

[167] M. Ezbiri, K. Allen, M. Gàlvez, R. Michalsky, and A. Steinfeld. Design principles of perovskites for thermochemical oxygen separation. *ChemSusChem*, 8(11):1966–1971, 2015.

[168] S. Khare, M. Dell'Amico, C. Knight, and S. McGarry. Selection of materials for high temperature sensible energy storage. *Sol. Energy Mater. Sol. Cells*, 115:114–122, 2013.

[169] P. Poživil, N. Ettlin, F. Stucker, and A. Steinfeld. Modular design and experimental testing of a 50 kW_{th} pressurized-air solar receiver for gas turbines. *J. Sol. Energy Eng.*, 137(3):031002, 2015.

[170] J. Karni, A. Kribus, P. Doron, R. Rubin, A. Fiterman, and D. Sagie. The DIAPR: a high-pressure, high-temperature solar receiver. *J. Sol. Energy Eng.*, 119(1):74–78, 1997.

[171] P. Furler, J. Scheffe, D. Marxer, M. Gorbar, A. Bonk, U. Vogt, and A. Steinfeld. Thermochemical CO_2 splitting via redox cycling of ceria reticulated foam structures with dual-scale porosities. *Phys. Chem. Chem. Phys.*, 16(22):10503–10511, 2014.

[172] S. Ackermann, M. Takacs, J. Scheffe, and A. Steinfeld. Reticulated porous ceria undergoing thermochemical reduction with high-flux irradiation. *Int. J. Heat Mass Transfer*, 107:439–449, 2017.

[173] S. Brendelberger and C. Sattler. Concept analysis of an indirect particle-based redox process for solar-driven H_2O/CO_2 splitting. *Sol. Energy*, 113:158–170, 2015.

[174] M. Romero and A. Steinfeld. Concentrating solar thermal power and thermochemical fuels. *Energy Environ. Sci.*, 5(11):9234–9245, 2012.

[175] B. Bulfin, F. Call, M. Lange, O. Lubben, C. Sattler, R. Pitz-Paal, and I. Shvets. Thermodynamics of CeO_2 thermochemical fuel production. *Energy Fuels*, 29(2):1001–1009, 2015.

[176] D. Nield and A. Bejan. Internal natural convection: Heating from below. In *Convection in Porous Media, fourth ed.*, chapter 6. Springer, 2006.

[177] J. Park, D. Park, D. Ryu, B. Choi, and E. Park. Analysis on heat transfer and heat loss characteristics of rock cavern thermal energy storage. *Eng. Geol.*, 181:142–156, 2014.

[178] J. Marti, L. Geissbühler, V. Becattini, A. Haselbacher, and A. Steinfeld. Constrained multi-objective optimization of thermocline packed-bed thermal-energy storage. *Appl. Energy*, 216:694–708, 2018.

[179] V. Yeremenko, Y. Natanzon, and V. Dybkov. The effect of dissolution on the growth of the $Fe_2 Al_5$ interlayer in the solid iron-liquid aluminium system. *J. Mater. Sci.*, 16(7):1748–1756, 1981.

[180] D. Perraudin, S. Binder, E. Rezaei, A. Ortonaa, and S. Haussener. Phase change material systems for high temperature heat storage. *CHIMIA International Journal for Chemistry*, 69(12):780–783, 2015.

[181] B. Leistner. CFD-based designing of injectors for thermocline control in thermal energy storages. Semester Thesis. ETH Zürich, 2017.

[182] A. Schuller. Process simulation of an AA-CAES plant. Semester Thesis. ETH Zürich, 2017.

[183] M. Takacs, M. Hoes, M. Caduff, T. Cooper, J. Scheffe, and A. Steinfeld. Oxygen nonstoichiometry, defect equilibria, and thermodynamic characterization of $LaMnO_3$ perovskites with Ca/Sr A-site and Al B-site doping. *Acta Mater.*, 103:700–710, 2016.

[184] M. Mizuno, R. Berjoan, J. Coutures, and M. Foex. Phase diagram of the system Al_2O_3-CeO_2 at liquidus temperature. *J. Ceram. Assoc. Jpn.*, 83(954):90–96, 1975.

[185] N. Wakao and S. Kagei. *Heat and Mass Transfer in Packed Beds*, volume 1. Taylor & Francis, 1982.

[186] P. Furler and A. Steinfeld. Heat transfer and fluid flow analysis of a 4kW solar thermochemical reactor for ceria redox cycling. *Chem. Eng. Sci.*, 137:373–383, 2015.

[187] P. Furler, J. Scheffe, M. Gorbar, L. Moes, U. Vogt, and A. Steinfeld. Solar thermochemical CO_2 splitting utilizing a reticulated porous ceria redox system. *Energy Fuels*, 26(11):7051–7059, 2012.

[188] E. Radziemska and W. Lewandowski. Natural convective heat transfer from isothermal cuboids. *Int. J. Heat Mass Transfer*, 46(12):2169–2178, 2003.

[189] Y. Touloukian. *Thermophysical Properties of High Temperature Solid Materials*, volume 4. Macmillan, 1967.

[190] M. Chase. NIST-JANAF thermochemical tables. *J. Phys. Chem. Ref. Data. Monograph*, 1998.

[191] Properties of ultraboard. www.schupp-ceramics.com, March 15, 2017.

[192] Properties of felt. www.schupp-ceramics.com, March 15, 2017.

[193] E. Lemmon, R. Jacobsen, S. Penoncello, and D. Friend. Thermodynamic properties of air and mixtures of nitrogen, argon, and oxygen from 60 to 2000 K at pressures to 2000 MPa. *J. Phys. Chem. Ref. Data*, 29(3):331–385, 2000.

[194] K. Kadoya, N. Matsunaga, and A. Nagashima. Viscosity and thermal conductivity of dry air in the gaseous phase. *Journal of physical and chemical reference data*, 14(4):947–970, 1985.

[195] Y. Cengel. *Introduction to Thermodynamics and Heat Transfer*. McGraw-Hill New York, 1997.

[196] H. Petersen. The properties of helium: density, specific heats, viscosity, and thermal conductivity at pressures from 1 to 100 bar and from room temperature to about 1800 K. Report 224, Danish Atomic Energy Commission, 1970.

LIST OF PUBLICATIONS

Journal articles

L. Geissbühler, S. Zavattoni, M. Barbato, G. Zanganeh, A. Haselbacher, and A. Steinfeld, "Experimental and numerical investigation of combined sensible/latent thermal energy storage for high-temperature applications," *CHIMIA*, vol. 69(12), pp. 799-803, 2015. doi: 10.2533/chimia.2015.799.

L. Geissbühler, M. Kolman, G. Zanganeh, A. Haselbacher, and A. Steinfeld, "Analysis of industrial-scale high-temperature combined sensible/latent thermal energy storage," *Applied Thermal Engineering*, vol. 101, pp. 657-668, 2016. doi: 10.1016/j.applthermaleng.2015.12.031.

L. Geissbühler, V. Becattini, G. Zanganeh, S. Zavattoni, M. Barbato, A. Haselbacher, and A. Steinfeld, "Pilot-scale demonstration of advanced adiabatic compressed air energy storage, Part 1: Plant description and tests with sensible thermal-energy storage," *Journal of Energy Storage*, vol. 17, pp. 129-139, 2018. doi: 10.1016/j.est.2018.02.004.

L. Geissbühler, A. Mathur, A. Mularczyk, A. Haselbacher, and A. Steinfeld, "An assessment of thermocline-control methods for packed-bed thermal-energy storage in CSP plants," *Solar Energy*, to be submitted for publication, 2018.

L. Geissbühler, A. Pedretti, A. Haselbacher, and A. Steinfeld, "Efficient solar-thermochemical fuel production using sensible heat recuperation in a dual-storage reactor," *Energy & Environmental Science*, to be submitted for publication, 2018.

J. Marti, L. Geissbühler, V. Becattini, A. Haselbacher, and A. Steinfeld, "Constrained multi-objective optimization of thermocline packed-bed thermal-energy storage," *Applied Energy*, vol. 216, pp. 694-708, 2018. doi: 10.1016/j.apenergy.2017.12.072.

V. Becattini, L. Geissbühler, G. Zanganeh, A. Haselbacher, and A. Steinfeld, "Pilot-scale demonstration of advanced adiabatic compressed air energy storage, Part 2: Tests with combined sensible/latent thermal-energy storage," *Journal of Energy Storage*, submitted for publication, 2018.

Conference proceedings

L. Geissbühler, M. Kolman, G. Zanganeh, A. Haselbacher, and A. Steinfeld. Analysis of industrial-scale high-temperature combined sensible/latent thermal energy storage. *ASME-ATI-UIT Conference on Thermal Energy Systems: Production, Storage, Utilization and the Environment*, 2015.

J. Marti, L. Geissbühler, V. Becattini, A. Haselbacher, and A. Steinfeld, "Multi-objective optimization of thermocline thermal energy storage systems," *11th ISES EuroSun Conference*, 2016.

S. Zavattoni, L. Geissbühler, M. Barbato, G. Zanganeh, A. Haselbacher, and A. Steinfeld, "High-temperature thermocline TES combining sensible and latent heat-CFD modeling and experimental validation," *AIP Conference Proceedings*, vol. 1850, p. 080028, 2017. doi: 10.1063/1.4984449.

Patent

A. Steinfeld, P. Furler, A. Haselbacher, and L. Geissbühler, "A thermochemical reactor system for a temperature swing cyclic process with integrated heat recovery and a method for operating the same," Patent Application Nr. EP16194074, 2016.